UNIVERSIDAD CARLOS III DE MADRID

ESCUELA POLITÉCNICA SUPERIOR

DEPARTAMENTO DE TEORÍA DE LA SEÑAL Y COMUNICACIONES

TESIS DOCTORAL

Metamaterial-Loaded Printed Antennas: Design and Applications

Autor:
Francisco Javier Herraiz Martínez

Director:
Daniel Segovia Vargas

Leganés, Madrid, Febrero de 2010

TESIS DOCTORAL

Metamaterial-Loaded Printed Antennas: Design and Applications

Autor:
Francisco Javier Herraiz Martínez

Director:
Daniel Segovia Vargas

Departamento de Teoría de la Señal y Comunicaciones
Universidad Carlos III de Madrid
Leganés, Madrid, Febrero de 2010

A mi familia

Caminante, son tus huellas
el camino y nada más;
Caminante, no hay camino,
se hace camino al andar.
Al andar se hace el camino,
y al volver la vista atrás
se ve la senda que nunca
se ha de volver a pisar.
Caminante no hay camino
sino estelas en la mar.
Antonio Machado

Abstract

Wireless communication systems have grown dramatically during the last few years. Moreover, these systems have achieved a great popularity in society. Several examples can be mentioned: cellular communications (GSM, DCS, UMTS), personal area networks (Bluetooth), local area wireless networks (WiFi), radionavigation systems (GPS), etc. The current trend consists of using only one user terminal for several standards (e. g. GSM and UMTS terminals) and for more than one service (e. g. cellular communications, radionavigation systems and personal area networks). In addition, it is also important to note that current user terminals are more and more compact. For these reasons, it would be desirable to use only one antenna for all the standards and/or services covered by the terminal. However, it is important to note that each standard or service requires different antenna characteristics in terms of operating frequency and optimal radiation performance (radiation pattern, polarization, etc.). Hence, compact antennas with multifrequency (simultaneous operation over two or more bands) and multifunction performance (radiation pattern or polarization diversity, frequency reconfigurability, etc.) are a good solution as the radiating element of hanheld terminals. Furthermore, similar arguments can be made to justify the huge demand on multifrequency and multifunction compact antennas for the network elements such as base stations, hot-spots and other access points. Additionally, novel proposals, such as Cognitive Radio, and emerging radio applications like RFID are challenging from antenna engineering point of view.

It is important to take into account that the antennas with the optimal characteristics stated above are very difficult to achieve by using conventional

techniques. Thus, novel approaches are being developed to obtain radiating elements with the desired characteristics. One of these techniques is the use of *metamaterial structures*.

Metamaterials can be broadly defined as electromagnetic structures engineered to achieve exotic or unusual properties. These features have been used in microwave engineering to develop devices with extraordinary properties such as miniaturization or operation over multiple frequency bands. On the other hand, the effort in the antenna field has been put on the use of metamaterials for travelling-wave antennas and as substrates and superstrates for antennas. Recently, there has been a great effort on miniaturized antennas based on metamaterial concepts. Nevertheless, from the author's point of view, the possibility of achieving multifrequency and/or multifunction antennas based on metamaterials has not been fully explored.

The main goal of the proposed Thesis is the development of a novel design approach called *metamaterial-loaded printed antennas*. This solution consists of loading a conventional printed antenna with a set of metamaterial particles. Hence, the benefits of printed antennas (low cost, compactness, low profile, light weight, simplicity to integrate with circuitry and usefulness as elements for antenna arrays) are kept. Furthermore, the desired additional characteristics such as multifrequency and multifunction performance are obtained thanks to the proper design of the metamaterial loading elements. Several metamaterial-loaded printed antennas are proposed to provide solutions for a broad range of applications. In particular, two types of printed antennas are considered: printed wire antennas and microstrip patch radiators. The methodology used throughout the Thesis is the following: firstly, approximate models based on transmission line theory and equivalent circuits are developed to analyse and design the proposed antennas with low computational cost. Then, a full-wave study is carried out by making use of commercial and home-made solvers. Finally, the designed antennas are manufactured and measured to check their performance.

Two different classes of wire antennas are proposed: printed dipole antennas loaded with metamaterial particles and printed wire antennas over ground plane with *Left-Handed* (LH) metamaterial loading. Regarding the dipole antennas, a multifrequency performance is achieved because these antennas have additional working bands close to the self-resonance frequencies of the metamaterial loading particles. Moreover, miniaturization is achieved when the additional modes are placed below the resonance frequency of the unloaded dipole. On the other hand, the use of LH loading allows developing antennas over ground plane (the monopole and half-loop antenna over ground plane) with additional features and small dimensions.

The second type of antennas is microstrip patch antennas filled with metamaterial structures. Multifrequency and multifunction microstrip patch antennas are developed using this approach. In addition, this technique is extended to achieve multifunction patch antennas with polarization diversity and multifrequency performance. In particular, two applications are proposed: quad-frequency patch antennas with polarization diversity and dual-frequency circularly polarized patch antennas.

Finally, it is proposed the application of the metamaterial-loaded antennas not as isolated radiating elements, but integrated into systems or antenna arrays. Specifically, the proposed dipole antennas are used to enhance the performance of log-periodic antenna arrays. Moreover, it is shown that metamaterial-loaded antennas are a good solution to fulfil the requirements of future communications systems (Cognitive Radio) and emerging applications such us RFID.

Resumen

Los sistemas de comunicaciones inalámbricos han experimentado un enorme crecimiento en los últimos años. Prueba de ello es que varios de estos sistemas han logrado una gran popularidad. Podemos mencionar los ejemplos de la telefonía móvil (GSM, DCS, UMTS), las redes de área personal (Bluetooth), las redes locales inalámbricas (WiFi), los servicios de radionavegación (GPS), etc. La tendencia actual consiste en emplear un único terminal de usuario para diferentes normas (por ejemplo los terminales que funcionan en GSM y UMTS simultáneamente) y para varios servicios distintos (como los terminales que proporcionan los servicios de telefonía móvil, radionavegación y redes personales). Además, es importante tener en cuenta que los terminales cada vez son más compactos. Por estas razones, sería deseable emplear una única antena para todos las normas y/o servicios en los que funcione el terminal. Sin embargo, hay que tener en cuenta que cada norma o servicio requiere unas características diferentes de la antena tanto desde el punto de vista de la frecuencia de funcionamiento como de las características de radiación (diagrama de radiación, polarización, etc.) De este modo, las antenas compactas con propiedades de multifrecuencia (funcionamiento simultáneo en dos o más bandas de frecuencia) y multifunción (diversidad de diagramas de radiación, reconfigurabilidad en frecuencia, etc.) resultarían una buena solución como elementos radiantes de los terminales de usuario. Además, se pueden considerar argumentos similares para justificar la enorme demanda de antenas multifrecuencia y multifución para los elementos de red como estaciones base, *hot-spots* y otros puntos de acceso a redes inalámbricas. No podemos obviar tampoco que las nuevas propuestas como los sistemas de radio cognitiva *(Cognitive Radio)* y otras aplicaciones inalámbricas emergentes

como la identificación por radiofrecuencia (RFID) suponen una serie de retos desde el punto de vista de la ingeniería de antenas.

Debemos tener en cuenta que es muy difícil diseñar antenas con todas las características mencionadas anteriormente mediante el empleo de las técnicas convencionales. Por esta razón, se están proponiendo nuevas técnicas para el desarrollo de elementos radiantes con las características optimas deseadas. Ona de estas nuevas técnicas está basada en el empleo de las denominadas estructuras *metamateriales*.

Los metamateriales se puden definir de manera amplia como estructuras electromagnéticas diseñadas para obtener propiedades exóticas o no comunes. Estas características se han empleado en el ámbito de la ingeniería de microondas para el desarrollo de dispositivos con características extraordinarias como son la miniaturización o multifrecuencia. En cambio, en el ámbito de la ingeniería de antenas se han empleado para el diseño de antenas de onda viajera (por ejemplo *leaky-wave*) y como sustratos o superestratos para antenas. Más recientemente, se ha realizado un gran esfuerzo para obtener antenas miniaturizadas basadas en los conceptos de estructuras metamateriales. Sin embargo, desde el punto de vista del autor, la posibilidad de obtener antenas multifrecuencia y/o multifunción basadas en estructuras metamateriales no ha sido totalmente explotada.

El principal objetivo de esta tesis doctoral es el desarrollo de una novedosa técnica de diseño de antenas consistente en cargar una antena impresa convencional con partículas metamateriales. Por este motivo denominamos este conjunto *antenas impresas cargadas con partículas metamateriales*. Mediante el empleo de esta técnica se mantienen los beneficios de las antenas impresas (bajo coste, antenas compactas y de bajo perfil, bajo peso, simplicidad para integrarlas con circuitería y como elementos en agrupaciones de antenas). Además, se consiguen una serie de características deseadas como multifrecuencia y multifuncionalidad gracias al empleo de las partículas materiales que se emplean para cargar la antena. En concreto, se proponen dos clases de antenas impresas cargadas con partículas metamateriales con el objetivo de cubrir el amplio espectro de aplicaciones que requieren antenas con dichas características. Las dos clases de antenas propuestas son las antenas de hilo impresas cargadas con partículas metamateriales y las antenas de parche parcialmente rellenas de estrucutras metamateriales.

La metodología que se sigue durante el desarrollo de esta tesis doctoral es la siguiente: en primer lugar se proponen modelos aproximados de bajo coste computacional basados en la teoría de líneas de transmisión y equivalentes circuitales para el análisis y diseño de las antenas propuestas. A continuación, se realizan simulaciones de onda completa empleando simuladores

comerciales y una solución propia del método de los momentos. Finalmente, las antenas diseñadas se fabrican y se miden para comprobar sus prestaciones.

Se proponen dos tipos de antenas de hilo impresas: dipolos cargados con partículas metamateriales y antenas de hilo impresas sobre plano de masa cargadas con líneas metamateriales zurdas (conocidas como *Left-Handed* o *LH* en la bibliografía técnica). En lo que respecta a los dipolos cargados con partículas metamateriales, se obtiene la característica de multifrecuencia debido a que estas antenas presentan bandas de funcionamiento adicionales próximas a las frecuencias de resonancia de las partículas metamateriales que se emplean para cargarlas. Además, es posible obtener la característica de miniaturización ya que los modos adicionales pueden resonar por debajo de la frecuencia fundamental del dipolo convenconal sin cargar. En cambio, el empleo de estructuras LH en las antenas sobre plano de masa (como son el monopolo y el semilazo sobre plano de masa) proporcionan características adicionales y miniaturización respecto a las antenas convencionales sin cargar.

La segunda clase de antenas propuestas son los parches parcialmente rellenos de estructuras metamateriales. El empleo de esta técnica permite el diseño de antenas de parche con las propiedades de multifrecuencia y multifunción. Además, esta técnica se puede emplear también para obtener antenas multifrecuencia con diversidad de polarización. En concreto, se proponen dos aplicaciones distintas: parches de cuádruple frecuencia con diversidad de polarización y parches de doble frecuencia con polarización circular.

Finalmente, se propone el empleo de las antenas impresas cargadas con partículas metamateriales no como elementos radiantes aislados, sino integradas en sistemas y agrupaciones de antenas. Por ejemplo, los dipolos impresos multifrecuencia se utilizan para mejorar las características de las agrupaciones log-periódicas. Además, se demuestra que las antenas propuestas son unas buenas candidatas para satisfacer los requisitos de los sistemas de comunicaciones futuros (como Cognitive Radio) y las aplicaciones emergentes como RFID.

List of Acronyms

1-D	One-Dimensional or One Dimension
2-D	Two-Dimensional or Two Dimensions
3-D	Three-Dimensional or Three Dimensions
AMC	Artificial Magnetic Conductor
AR	Axial Ratio
ASIC	Application Specific Integrated Circuit
BW	Bandwidth
CLS	Capacitively Loaded Strip
COPOL	Co-Polarization
CP	Circular Polarization or Circularly Polarized
CPS	Coplanar Strip
CPW	Coplanar Waveguide
CR	Cognitive Radio
CRLH	Composite Right/Left-Handed
CSRR	Complementary Split-Ring Resonator
DCS	Digital Communication System
DNG	Double-Negative
DPS	Double-Positive
DVB-H	Digital Video Broadcasting Handheld
EBG	Electromagnetic Band-Gap
EIG	Eigenfrequency
ENG	Epsilon-Negative
FET	Field-Effect Transistor

FSS	Frequency Selective Surface
FM	Frequency Modulation
FW	Full-Wave
GF	Green's Function
GPS	Global Positioning System
GSM	Global System for Mobile communications
ISM	Industrial, Scientific and Medical
LH	Left-Handed
LHCP	Left-Handed Circular Polarization or Circularly Polarized
LW	Leaky-Wave
MIM	Metal-Insulator-Metal
MIMO	Multiple-Input Multiple-Output
MNG	Mu-Negative
MoM	Method of Moments
MPIE	Mixed Potential Integral Equation
OSRR	Open Split-Ring Resonator
PDA	Personal Digital Assistant
PIFA	Planar Inverted F Antenna
PP	Polypropylene
PRS	Partially Reflective Surface
RF	Radio-Frequency
RFID	Radio-Frequency Identification
RH	Right-Handed
RHCP	Right-Handed Circular Polarization or Circularly Polarized
SMA	SubMiniature version A
SMD	Surface Mount Device
SRR	Split-Ring Resonator
TEM	Transverse Electromagnetic
TL	Transmission Line
TM	Transverse Magnetic
TW	Thin-Wire
UMTS	Universal Mobile Telecommunications System
XPOL	Cross-Polarization
WiFi	Wireless Fidelity
WLAN	Wireless Local Area Network

Agradecimientos/Acknoledgements

En primer lugar me gustaría dar las gracias a mi director de tesis Dani Segovia porque fue quien me dio la oportunidad de trabajar en investigación y a lo largo de estos años siempre me ha ayudado a realizar este trabajo de la mejor forma posible. Siempre se ha preocupado de que pudiera trabajar en las mejores condiciones y me ha dado la oportunidad de seguir formándome y poder difundir nuestro trabajo. No puedo olvidar de la ayuda que nos han prestado Quique y Vicente en muchas partes del trabajo que aquí se resume.

Igualmente quiero agradecer a mis compañeros de laboratorio (Ogarpe, Edu Ugarte, Dani G. Doñoro, Belén, Javi Montero) toda la ayuda que me han prestado: desde montajes de medida a fotos, pasando por los buenos momentos y el buen ambiente del laboratorio. Además, tanto Edu como Javi participaron activamente en este trabajo cuando realizaron sus PFCs. Esto me hace recordar al resto de proyectandos que han trabajado conmigo (Karmele, José Romero e Isma). Tampoco me puedo olvidar del resto de amigos del departamento (Rubén, Eloy, Bertran, Rosa, etc.) con los que he compartido tan buenos momentos.

At this point, I would like to thank all the members of LEMA-EPFL. I really felt at home during my stay in Switzerland. I will not forget my friends: Roberto, Laleh, Ruzica, Fred, Gabriela, Benjamin, Edén, Francesco, ... Especialmente quiero agradecer a Juan Mosig la oportunidad de poder trabajar y aprender en el LEMA. Igualmente, Eulalia me ayudó en todo momento durante mi estancia en Suiza. Por último, quiero agradecer especialmente a Sergio, quien me enseñó y ayudó a realizar mi trabajo en Suiza. Además, en el terreno personal se portó como un como un hermano, haciendo que me

integrara totalmente en Lausanne y pasara una estancia bastante agradable.

I also want to thank Peter Hall for giving me the opportunity to work at Birmingham. I really learnt a lot during my stay in his laboratory and some interesting results of this Thesis were developed there. I want to thank my colleagues (Qing, Elham, Lida, etc.) for all the help and support during my stay in Birmingham. I cannot forget my family in Birmingham: the Weslyans!!! Pamila, Seb, Eduardo, Verónica, Leonardo, Dana, Hale, Bibi, ... (I would like to mention all of them, but it is impossible!) I had a good time at Wesley!

I would like to thank Prof. Midrio and Prof. Mazánek for reviewing this Thesis. They have provided very constructive reviews which will be useful for my future works.

Finalmente, me gustaría dar las gracias a mi familia, especialmente a mis padres, hermana y abuelos, porque sin ellos este trabajo no hubiera sido posible.

Contents

CHAPTER 1

Introduction

1.1 Motivation and Global Ojectives

Wireless communications systems have grown dramatically in the last few years. These systems have achieved a great popularity in society. Several examples can be mentioned: mobile communications (GSM, DCS, UMTS), personal area networks (Bluetooth), local area wireless networks (WiFi), radionavigation systems (GPS), etc. Related to this fact, the popularity and sells of wireless terminals have also grown. The first user terminals which become so popular were mobile phones. For example, the ratio between the number of mobile phones and population in Spain is over one which gives an idea of the success of these terminals. However, mobile phones are not the only user terminals extended in the society. We have several examples: PDAs, laptops and more recently terminals embedded inside cars.

Initially, user terminals were designed for only one service and a unique standard (e. g. GSM mobile phones [1]). After that, several communication standards and bands were defined (GMS1800/1900, UMTS, etc.) [2] and hence, the necessity of providing service for several standards with only one terminal arose (e. g. multiband mobile phones). This implies the use of antennas working at several frequencies simultaneously (multifrequency performance) [3, 4, 5, 6]. Moreover, the use of a single terminal for several communication systems is becoming more and more common [7, 8, 9]. For example, mobile phones and PDAs are currently user terminals for mobile

communication systems and GPS and they also provide Bluetooth connectivity; terminals embedded in cars provide radio-navigation services (GPS) and Bluetooth connectivity, etc. It is important to note that the requirements of the radiating elements for such different services are also different. For example, the antenna radiation patterns for mobile communications and radio-navigation systems are orthogonal [10]. In other cases, the polarization requirements for each application are different. In summary, nowadays there is a huge demand on radiating elements for user terminals working at several bands and with different requirements at each band. Antennas satisfying such properties are known as multifunction antennas [11].

In addition, it is also important to note that current terminals are more and more compact. This implies the use of small or miniaturized antennas. However, it is difficult to achieve small antennas with high efficiency and good matching [12, 13, 14, 15, 16, 17, 18].

Current solutions, such as broadband antennas and conventional resonant antennas, are not optimal. On the one hand, broadband antennas have a broad bandwidth which can cover all the working frequencies, but they also work over undesired bands receiving undesired interferences. Furthermore, broadband antennas are bigger than the space allowed in terminals for the antennas. On the other hand, conventional resonant antennas can be used at several frequencies but the ratio between them is always harmonic (an integer number equal to or larger than two) whilst the ratio between current services does not follow a harmonic ratio. Moreover, in most the cases the ratio between the working frequencies is a small number (< 2) which cannot be achieved with conventional approaches. Nowadays, the usual solution consists of a combination of different separated modules, each of them with a specific antenna [9]. For example, in current terminals there is an antenna for GSM/UMTS, another one for Bluetooth and another one for FM radios. For these reasons, great efforts are being made in the antenna field to achieve miniaturized, low-profile, multifrequency and multifunction antennas.

Up to now we have considered the importance of the radiating element from the terminal point of view, but it is also important to note that most of the wireless systems are based on two functional elements: the user terminal and the network element (base station, hot-spot, etc.) [19]. A proper selection of the antenna installed in the network element is crucial to achieve an optimal performance of the wireless system. In most cases, the requirements for these two units are different in terms of gain, radiation patterns, cost, size ... Moreover, these features are different for each application. For these reasons, a broad range of novel antennas has to be developed.

Furthermore, novel antennas must be developed in order to fulfill the

requirements of future communications systems, such as Cognitive Radio [20, 21], and satisfy the demand of emerging applications as Radio Frequency Identification systems (RFID) [22, 23]. All these requirements cannot be achieved with conventional approaches. This fact has made that novel technologies are being studied and implemented. One of these technologies is the use of metamaterial structures.

Metamaterials are one of the hot topics in the fields of physics and engineering [24, 25, 26, 27]. This is clear since the number of scientific publications, congresses and seminars related to this topic has grown exponentially during the last years. This fact has made that there is no unique definition of metamaterials. Anyway, metamaterials can be broadly defined as electromagnetic structures engineered to achieve exotic or unusual properties. These features have been used in microwave engineering to develop devices with extraordinary properties such as miniaturization or operation over multiple frequency bands [24, 25, 26, 27]. However, the effort in the antenna field has been put on the use of metamaterials for travelling-wave antennas and as substrates and superstrates for antennas (Sections 2.6.1 and 2.6.2). Recently, there has been a great effort on miniaturized antennas based on metamaterial concepts (Section 2.6.3). Nevertheless, from the author's point of view, the possibility of achieving multifrequency and/or multifunction antennas based on metamaterials has not been fully explored. Moreover, these features can be combined with the possibility of miniaturization to develop compact antennas for modern and future wireless communication systems.

During the last thirty years printed technology has been the most popular technique to manufacture antennas. Printed antennas have become so popular due to their low profile, light weight, low cost, simplicity to integrate with circuitry and usefulness as elements for antenna arrays [28, 29].

The main goal of the proposed Thesis is to model, design, manufacture and measure novel printed antennas loaded with metamaterial particles for nowadays and future wireless applications. Several metamaterial-loaded printed antennas are proposed to provide solutions for a broad range of applications. It is important to note that the radiating elements are the printed antennas and the use of metamaterial loading allows achieving multifrequency and/or multifunction performance: antennas working at two or more bands simultaneously with the possibility of achieving different radiation characteristics at each band (e. g. orthogonal radiation patterns, polarization diversity, etc.). Moreover, the proposed antennas can be designed to work at arbitrary working frequencies, even when the ratio between them is small (e. g. < 2). It is important to take into account another two facts: the first one is the use of printed technology and the second one is the size of the proposed

antennas. The use of printed technology allows the development of low-cost antennas which can be directly integrated with circuitry. Thus, the proposed antennas can be produced for mass applications as wireless systems. Related to the dimensions of the antennas, the proposed antennas do not increase the dimensions of conventional antennas but reduce the size in several cases, achieving a high degree of miniaturization in some implementations. Furthermore, the use of printed technology allows the development of low profile and light weight antennas. Thus, all the requirements of radiating elements for current and future wireless applications can be achieved with the proposed antennas.

1.2 Outline

This structure of the present Thesis is as follows:

Chapter 2 reviews the fundamentals of metamaterial structures, gives a short historic introduction and studies the state of the art of antenna applications using metamaterial structures. First, bulk metamaterials are studied. Then, the two main approaches to achieve planar implementations are summarized. The first one is based on resonant particles whilst the second one is based on Transmission Line (TL) theory. 1-D and 2-D printed implementations are described. After that, metamaterial based resonators are presented and an Eigenfrequency Method to efficiently compute the working frequencies of applications based on metamaterial resonant structures is proposed. This method reduces drastically the computation time with respect to conventional approaches, which are based on full-wave analysis. This method is used in the following Chapters because several of the proposed antennas are based on metamaterial resonators. Finally, a review of the state of the art of the application of metamaterial structures in antenna engineering is presented.

Chapter 3 presents the first set of metamaterial-loaded antennas: metamaterial-loaded printed wire antennas. Two different types of antennas are developed. The first one is multifrequency printed dipole antennas. Several implementations based on lumped LC components and metamaterial particles are designed, manufactured and measured, showing the multifrequency performance of such antennas. Additionally, the possibility of achieving miniaturization is also explained. Moreover, an equivalent circuit model for such kind of antennas is proposed. The second kind of antennas is Left-Handed (LH) wire antennas over ground plane. Two different antennas are proposed: the LH monopole antenna and the LH half-loop antenna over a finite ground

plane. The analysis, design, implementation and measurement of both types of antennas are presented.

Chapter 4 is focused on microstrip patch antennas filled with metamaterial structures. Multifrequency and multifunction microstrip patch antennas are developed using this approach. First, two different kind of microstrip patch antennas are designed, manufactured and measured, showing good performance. The first one is a dual-mode and triple-frequency microstrip patch antenna and the second one is a dual-frequency patch antenna with reduced ratio between the working frequencies. Two different analysis and design methods are proposed: an equivalent circuit model based on TL theory and a full-wave tool based on the MPIE-MoM (Mixed Potential Integral Equation - Method of Moments) approach. Finally, multifunction patch antennas with polarization diversity and multifrequency performance are developed. In particular, two applications are proposed: quad-frequency patch antennas with polarization diversity and dual-frequency circularly polarized (CP) patch antennas.

In Chapter 5, novel applications of metamaterial-loaded printed antennas are presented. The first one is the use of metamaterial-loaded dipoles as the elements of log-periodic arrays to enlarge the bandwidth of such antennas without increasing the number of dipoles. The second application consists of developing LH wire antennas with wideband tuning. Then, these antennas are integrated into a complete radiating structure for future communication terminals (Cognitive Radio). Finally, self-diplexed patch antennas based on microstrip patch antennas filled with metamaterial structures are developed. These self-diplexed antennas are two-port radiating devices with high isolation between the ports. These antennas are proposed for active RFID microwave systems application.

Finally, Chapter 6 presents the conclusions of the Thesis and proposes the future working lines.

CHAPTER 2

Metamaterial Structures and their Application to Antenna Engineering

2.1 A Brief Introduction to Metamaterial Structures

As it was stated in the Introduction (Chapter 1), metamaterials can be broadly defined as electromagnetic structures engineered to achieve exotic or unusual properties.

This is a broad definition which can include several structures usually fabricated by introducing some inclusions or inhomogeneities embedded in a host medium or connected to or embedded on a host surface. In the present Thesis we will use the term *metamaterials* associated to a more restricted group of structures: the artificial materials with negative constitutive parameters. This implies that we are considering that the inclusions and the distances between them are much smaller than wavelength and, as a consequence, such media can be described by its macroscopic constitutive parameters. This is not the case of other artificial structures (e.g. Electromagnetic Band-Gap materials, EBG) in which the distance between the inclusions are on the order of half a wavelength or more and the main behaviour is dominated by periodic concepts.

Fig. 2.1 shows the classification of the different materials as a function of their macroscopic constitutive properties: permittivity (ε) and permeability

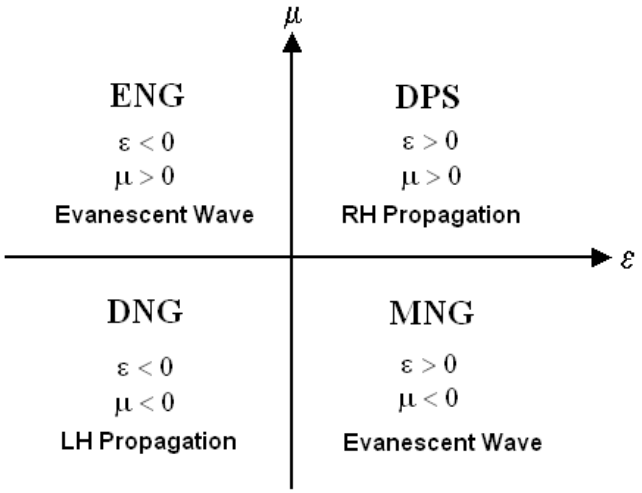

Figure 2.1: Classification of the different materials depending on their constitutive parameters.

(μ). Most of the materials we can find in nature (e. g. dielectrics) have positive constitutive parameters ($\varepsilon > 0$ and $\mu > 0$). For this reason, they are called Double-Positive materials (DPS). The materials with negative permittivity and positive permeability ($\varepsilon < 0$ and $\mu > 0$) are called Epsilon-Negative materials (ENG). In certain frequencies many plasmas exhibit these characteristics. On the other hand, a material with positive permittivity and negative permeability ($\varepsilon > 0$ and $\mu < 0$) is known as Mu-Negative medium (MNG). In certain frequencies ferrites present this behaviour. Finally, materials with both negative constitutive parameters ($\varepsilon < 0$ and $\mu < 0$) are called Double-Negative materials (DNG). Up to now, these materials have not been found in nature and they have only been obtained artificially.

It is important to note that the propagation of electromagnetic waves is only possible through DPS and DNG materials. In the first case (Fig. 2.2.a), the electric field, the magnetic field and the propagation vector form a right-handed triplet. Thus, the propagation constant β is positive ($\beta > 0$), which means a forward-wave propagation. For this reason, they are also known as Right-Handed (RH) materials. On the other hand, the propagation through DNG materials follows the left-handed rule (Fig. 2.2.b), which means that the electric field, magnetic field and propagation vector build a left-handed triplet. In this case, the propagation constant is negative $\beta < 0$, which means a backward-wave propagation. This fact has led to the fact

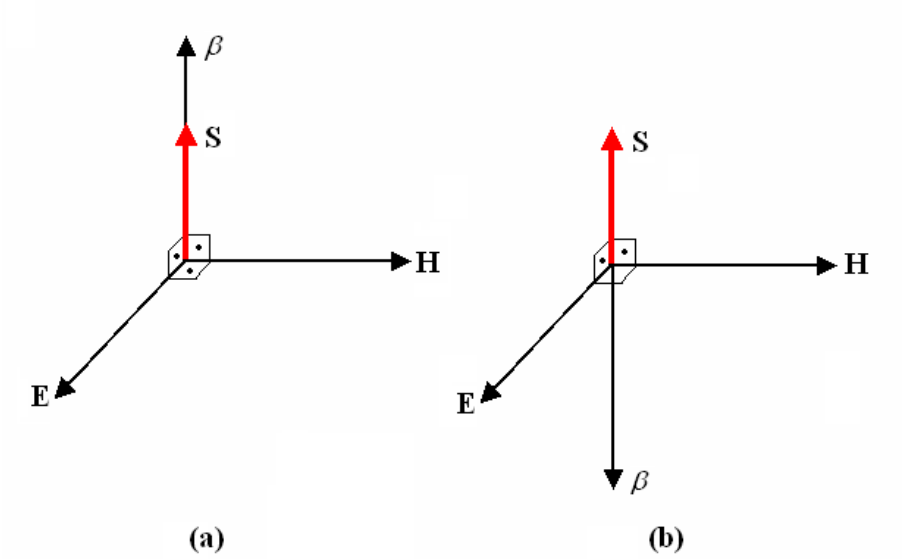

Figure 2.2: Illustration of the system of vectors $\mathbf{E}, \mathbf{H}, \mathbf{S}, \beta$ for a TEM (transverse electromagnetic) wave in (a) conventional or RH and (b) DNG or LH medium.

that DNG materials are commonly called Left-Handed (LH) materials. In both cases, the time-averaged flux of energy is determined by the real part of the Poynting vector $\mathbf{S}$ which is unaffected by a simultaneous change of the sign of ε and μ.

The Russian physicist Viktor Veselago predicted in 1967 the existence of "Substances with simultaneously values of ε and μ" [30]. Veselago used the term LH "substances" to note that these materials would allow the propagation of electromagnetic waves with a LH triplet. Moreover, Veselago also predicted some additional features of the LH materials:

- Frequency dispersion of the constitutive parameters.
- Reversal of Doppler effect.
- Reversal of Vavilov-Čerenkov radiation.
- Reversal of the boundary conditions relating to the normal components of the electric and magnetic fields at the interface between a conventional RH medium and a LH medium.
- Reversal of Snell's law.
- Negative refraction at the interface between a RH medium and a LH medium.

- Transformation of a point source into a point image by a LH slab.
- Interchange of convergence and divergence effects in convex and concave LH lenses, respectively.
- Plasmonic expressions of the constitutive parameters in resonant-type LH materials.

However, Veselago ended his paper remarking the difficulty of developing such structures, because no LH material had been discovered at that time.

The first experimental implementation and demonstration of a LH material was developed by Smith and his group at University of California San Diego (UCSD) [31] more than 30 years later. This work was inspired by the structures introduced by Pendry (Imperial College, London) [32, 33].

Pendry had introduced the ENG and MNG structures in the microwave range. Both metamaterials were periodic structures whose unit cells had a size p much smaller than the guided wavelength ($p \ll \lambda_g$). Thus, these structures can be considered as homogeneous metamaterials. ENG structures were based on Thin-Wire cells (TW), as shown in Fig. 2.3.a. MNG metamaterial unit-cell was the Split-Ring Resonator (SRR) which is shown in Fig. 2.3.b.

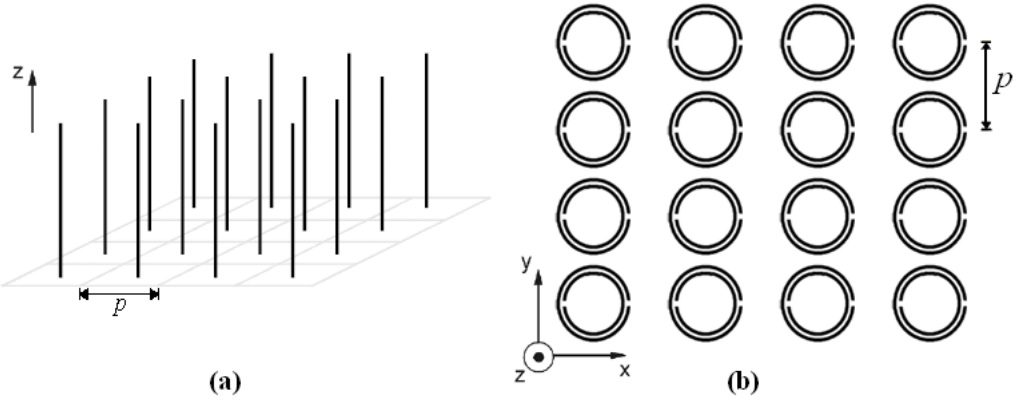

Figure 2.3: First metamaterial structures proposed by Pendry. (a) TW (Thin-Wire) structure working as ENG metamaterial [32]. (b) SRR (Split-Ring Resonator) structure constituting a MNG metamaterial [33].

Smith and his group combined Pendry's structures to develop the first LH metamaterial implementation [31], shown in Fig. 2.4.a. The arguments considered in that paper were the following:

- TW and SRR structures with overlapped negative ε and μ frequency bands were designed.

- Both structures were joined together (Fig. 2.4).
- The propagation effect of an electromagnetic wave through the new material was studied. It was concluded that the structure had a pass band in the frequency range under study with simultaneous negative constitutive parameters.

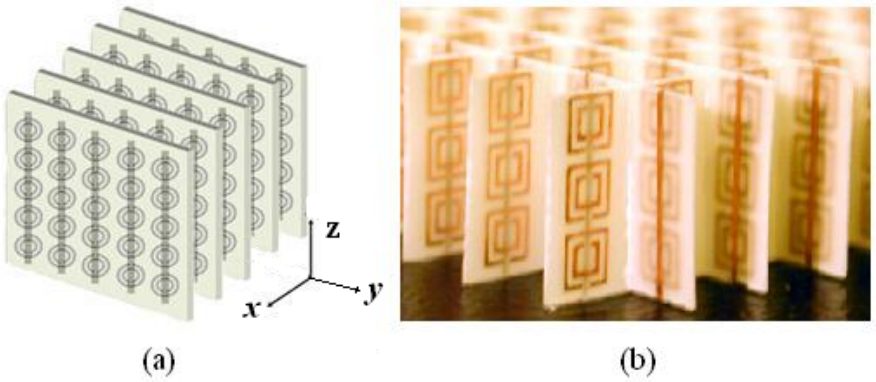

Figure 2.4: First LH structures combining TWs and SRRs, introduced by Smith's group (UCSD). (a) LH unidimensional structure [31]. (b) LH bidimensional structure [34].

The arguments proposed in that paper were questionable because the coupling between both types of structures were ignored. This could have made that the proposed structure would not have the superposition of their independent features. However, the same group demonstrated the LH behaviour of their structure in [34]. Two years later, the group at Massachusetts Institute of Technology (MIT) formed by A. A. Houck, J. B. Brock and I. L. Chuang repeated the same experiment, confirming the previous results [35].

2.2 Implementation of Bulk Metamaterials

2.2.1 ENG Media: the Thin Wire Structure

As introduced in Section 2.1, the Thin Wire structure (Fig. 2.3.a) has an ENG behaviour. If the excitation field $\mathbf{E}$ is parallel to the axis of the wires ($\mathbf{E} \| z$), so as to induce a current along them and generate equivalent electric dipole moments, this structure exhibits a plasmonic-type permittivity frequency function given by

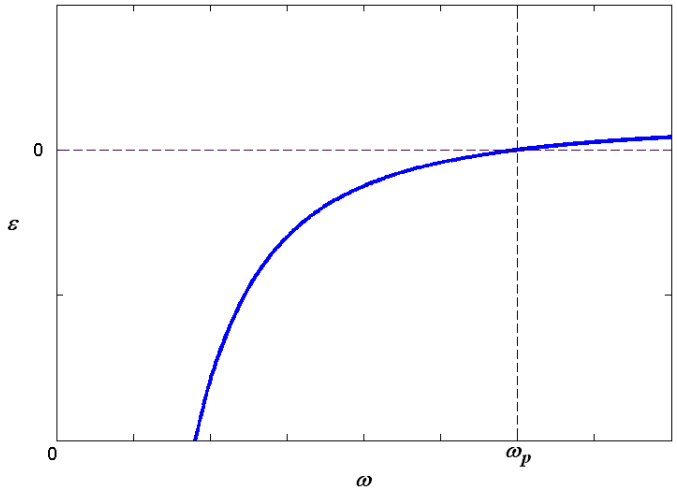

Figure 2.5: Permittivity of a TW structure as a function of frequency.

$$\varepsilon_r(\omega) = 1 - \frac{\omega_p^2}{\omega^2} \tag{2.1}$$

where ω_p is the *plasma frequency*, computed as

$$\omega_p = \sqrt{\frac{2\pi c^2}{p^2 \ln\left(\frac{p}{r}\right)}} \tag{2.2}$$

being c the speed of light in vacuum, p the period and r the radius of the wires. Losses have not been considered in this model. This function if depicted in Fig. 2.5. It is clear that the permittivity of this structure is negative ($\varepsilon_r < 0$) below the plasma frequency (ω_p). On the other hand, permeability is simply $\mu = \mu_0$, since no magnetic material is present and no magnetic dipole is generated. It should be noted that the wires are assumed to be much longer than the wavelength (theoretically infinite), which means that the wire are excited at frequencies situated far below their first resonance.

2.2.2 MNG Media: the SRR and other Magnetic Particles

The SRR consists of two concentric metallic split rings (Fig. 2.6.a). If the excitation magnetic field **H** is perpendicular to the plane of the rings ($\mathbf{H} \| z$),

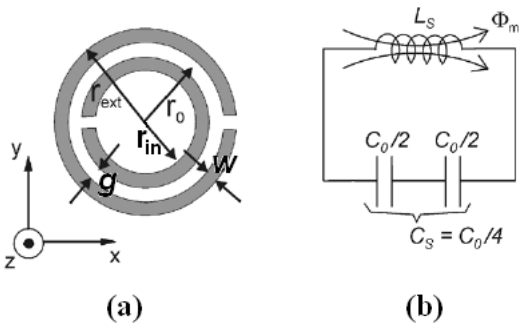

Figure 2.6: Topology of the SRR (a) and its equivalent circuit model (b).

this structure exhibits a plasmonic-type permeability frequency function of the form

$$\mu_r(\omega) = 1 - \frac{F\omega^2}{\omega^2 - \omega_0^2} \tag{2.3}$$

where $F = \pi(r_{in}/p)^2$ (r_{in}: inner radius of the smaller ring and p: period in Fig. 2.3.b) and ω_0 is the *quasi-static resonance frequency*, computed as

$$\omega_0 = c\sqrt{\frac{3p}{\pi \ln\left(\frac{2w}{g} r_{in}^3\right)}} \tag{2.4}$$

with w the width of the rings and g the gap between the rings. Losses have not been considered in this model. This expression shows (Fig. 2.7) the presence of a MNG region ($\mu_r < 0$) over the resonance frequency up to the *magnetic plasma frequency* (ω_{pm}). Thus, $\mu_r < 0$ for $\omega_0 < \omega < \omega_{pm}$ with

$$\omega_{pm} = \frac{\omega_0}{\sqrt{1-F}} \tag{2.5}$$

The equivalent circuit model of the SRR is a LC parallel tank [36] which is shown in Fig. 2.6.b. In this figure, C_0 is the total capacitance between the rings, computed as $C_0 = 2\pi r_0 C_{pul}$, where C_{pul} is the per-unit length capacitance between the rings and r_0 is the mean radius of the SRR ($r_0 = r_{ext} - w - g/2$). The value of C_{pul} can be obtained from classical approaches [37]. The inductance L_S can be approximated by that of a single ring with averaged radius r_0 and width w [38]. Hence, the resonance frequency of the SRR is given by

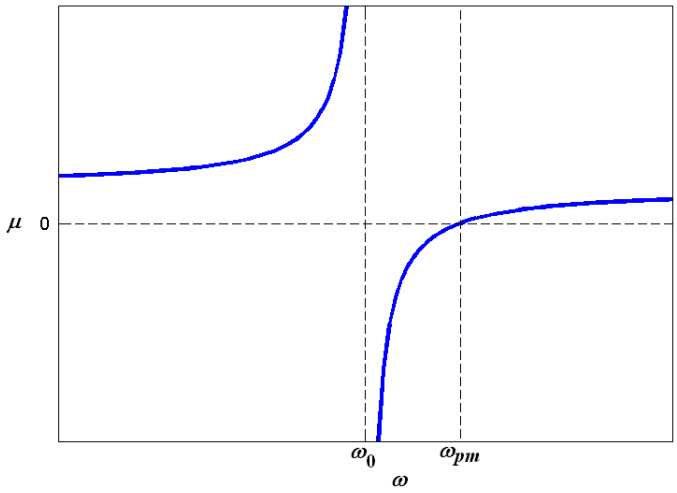

Figure 2.7: Permeability of the SRRs-based structure as a function of frequency.

$$f_0 = \frac{1}{2\pi\sqrt{C_S L_S}} \tag{2.6}$$

where C_S is the series capacitance of the upper and lower halves of the SRR, computed as $C_S = C_0/4$.

During the last years, several MNG particles alternative to the SRR have been proposed. For example, the Broadside-Coupled SRR particle is a modification of the SRR in which each ring is printed on a different side of a dielectric board. Other particles, such as the Double-Split SRR or the Spirals, have been proposed in [36]. These particles and their equivalent circuit models are shown in Fig. 2.8. Some of these particles can be use to miniaturize the SRR. For example, the resonance frequency of the Spiral resonator with two turns is half the resonance frequency of the SRR with the same radius.

2.2.3 Implementation of LH Media

As commented in Section 2.1, LH metamaterials can be obtained by using a ENG and another MNG media simultaneously. The classical implementation proposed by Smith and co-workers [31] consists of an array of TWs and SRRs as shown in Fig. 2.4.a. In order to achieve a DNG media, and thus LH propagation, the plasma frequency of the TW structure must be greater

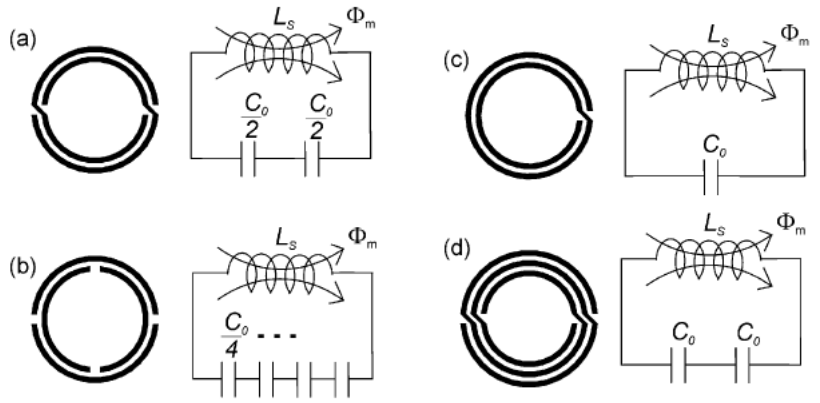

Figure 2.8: Topologies of the MNG particles proposed in [36] and their equivalent circuit models: (a) Nonbiasotropic SRR, (b) Double SRR, (c) Spiral Resonator, (d) Double Spiral Resonator.

than the magnetic plasma frequency of the SRRs ($\omega_p > \omega_{pm}$). In that case, the composed structure exhibits a LH passband in the frequency margin where the TW structure has a ENG behaviour and the SRRs present a MNG performance simultaneously. This structure behaves as a LH metamaterial in only 1-D, because the excitation electric field must be parallel to the TWs and the excitation magnetic field must be perpendicular to the plane of the SRRs. Hence, the metamaterials obtained are anisotropic and characterized by uniaxial permittivity and permeability tensors

$$[\varepsilon] = \begin{bmatrix} \varepsilon_{xx} & 0 & 0 \\ 0 & \varepsilon_{yy} & 0 \\ 0 & 0 & \varepsilon_{zz} \end{bmatrix} \tag{2.7a}$$

$$[\mu] = \begin{bmatrix} \mu_{xx} & 0 & 0 \\ 0 & \mu_{yy} & 0 \\ 0 & 0 & \mu_{zz} \end{bmatrix} \tag{2.7b}$$

with $\varepsilon_{zz} < 0$ and $\varepsilon_{xx}, \varepsilon_{yy} > 0$ for $\omega < \omega_p$ and $\mu_{xx} < 0$ and $\mu_{yy}, \mu_{zz} > 0$ for $\omega_0 < \omega < \omega_{pm}$.

In order to obtain a 2-D LH structure, an arrangement of orthogonal dielectric boards with printed SRRs on one side and metallic strips on the other can be used. This structure was proposed in [34] to show the effect of negative refraction at the interface between ordinary and LH media. A picture of this structure can be seen in Fig. 2.4.b and the sketch of its unit cell is

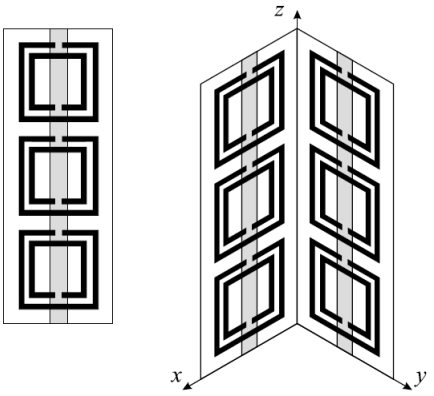

Figure 2.9: Unit cell of the 2-D LH metamaterial structure pictured in Fig. 2.4.b [34]. The metallic strips (gray) and the SRRs (black) are printed on opposite sides of the dielectric substrate. Figure extracted from [27].

shown in Fig. 2.9. This structure is a bidimensional LH metamaterial because although the excitation electric field **E** has to be directed along the axis of the wires, two directions are possible for the excitation magnetic field **H**. Hence, the composite metamaterial is characterized by the tensors (2.7) with $[\varepsilon]$ equals to the 1-D case, but $\mu_{xx}, \mu_{yy} < 0$ and $\mu_{zz} > 0$ for $\omega_0 < \omega < \omega_{pm}$.

An alternative to implement a 1-D LH media consists of using a lattice which exhibits simultaneous MNG and ENG behaviours. These types of structures have been studied by the group of Kong (MIT)[39, 40]. One of these structures is constructed by two reversed Omega-like metallic patterns which are printed back to back on each side of a substrate board, as it is shown in Fig. 2.10.a. Another alternative is based on two reversed S-shaped metallic strips, also printed on each side of a substrate (Fig. 2.10.b). In both cases, several unit cells are connected in series. The MNG performance is given by the two opposite patterns printed on both sides of the substrate and the ENG behaviour is provided by each metallic strip. Note that each strip is similar to a wire but with an Omega-like or S-like shape instead of the straight wires of the TW structure.

2.3 Implementation of Planar Metamaterials

There are two main approaches two implement planar metamaterials. The first one is the dual transmission line approach, which is based on the development of a transmission line which allows the propagation of backward

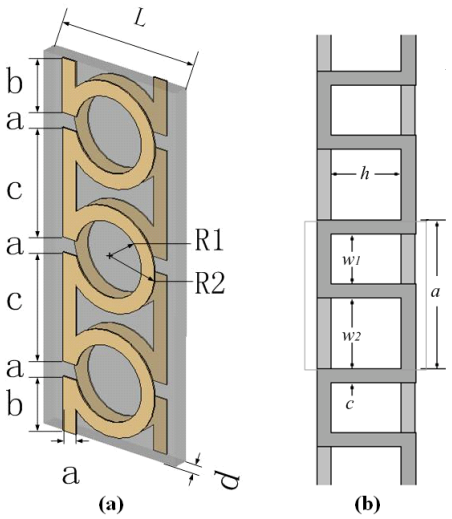

Figure 2.10: (a) Sketch of the Omega metamaterial structure [39]. (b) Diagram of the S-shape structure [40].

waves. This approach is studied in Subsection 2.3.1. The other approach consists of loading a host line with a printed version of metamaterial particles (e. g. printed SRRs). For this reason, this method is called the resonant-type approach due to the resonant behaviour of the loading particles. This approach is presented in Subsection 2.3.2. It will be shown throughout the present Section that both approaches are equivalent and both of them are proper for developing transmission lines with LH behaviour. Finally, this equivalence is explained in Subsection 2.3.3.

2.3.1 The Dual Transmission Line Approach

This approach was proposed by the group of Eleftheriades (University of Toronto) [41], Oliner (Polytechnic University, Brooklyn, NY) [42] and Caloz and Itoh (UCLA) [43] almost at the same time in June 2002. This approach has been used to develop novel applications in the field of microwave engineering (see for instance [24, 25]).

A lossless conventional RH TL can be modelled as a concatenation of unit cells formed by series inductances L_R and shunt capacitances C_R. The T-circuit model of one of these cells is shown in Fig. 2.11.a. Theoretically, the dual cell of the previous one allows the propagation of backward waves. Thus, the dual of the RH TL is an ideal LH TL formed by series capacitances

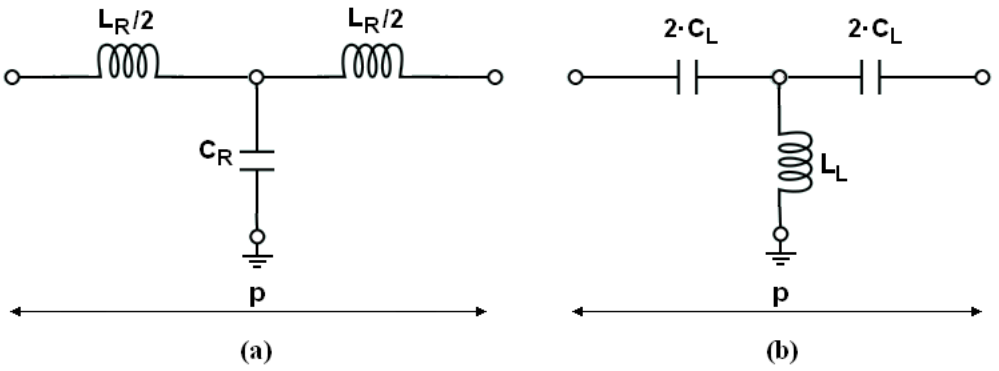

Figure 2.11: Unit cell of the conventional (RH) TL (a) and the dual (LH) TL (b).

C_L and shunt inductances L_L. Fig. 2.11.b shows the T-circuit model of a LH unit cell. The analysis of the propagation characteristics of these TLs can be made from the theory of periodic structures [44], where the structure is either infinite or matched at the ports. From this analysis, the phase constant, β, and the Bloch (or characteristic) impedance, Z_B, can be obtained as

$$\cos \beta p = 1 + \frac{Z_{se}(\omega)}{Z_{sh}(\omega)} \tag{2.8}$$

$$Z_B = \sqrt{Z_{se}(\omega)\left[Z_{se}(\omega) + 2Z_{sh}(\omega)\right]} \tag{2.9}$$

where Z_{se} and Z_{sh} are the series and shunt impedances of the unit cell described by its T-circuit model, and p is its period. Hence, these parameters for the RH and LH TLs are:

$$\beta_{RH} = \frac{1}{p}\cos^{-1}\left[1 - \frac{L_R C_R}{2}\omega^2\right] \tag{2.10}$$

$$Z_{BRH} = \sqrt{\frac{L_R}{C_R}\left(1 - \frac{\omega^2}{\omega_{cRH}^2}\right)} \tag{2.11}$$

$$\beta_{LH} = \frac{1}{p}\cos^{-1}\left[1 - \frac{1}{2L_L C_L \omega^2}\right] \tag{2.12}$$

$$Z_{BLH} = \sqrt{\frac{L_L}{C_L}\left(1 - \frac{\omega_{cLH}^2}{\omega^2}\right)} \tag{2.13}$$

where

$$\omega_{cRH} = \frac{2}{\sqrt{L_R C_R}} \tag{2.14}$$

and

$$\omega_{cLH} = \frac{1}{2\sqrt{L_L C_L}} \tag{2.15}$$

are the angular cutoff frequencies for the RH and LH TLs, respectively. Considering these expressions, the RH TL is a low-pass structure whose cutoff frequency is (2.14) and the LH TL is a high-pass structure with a cutoff frequency equal to (2.15). Transmission is limited to those frequency intervals in which the phase constant and the characteristic impedance are real numbers. As it is shown in the previous expressions, it seems that dispersion is present in both structures, even in the lossless RH line. However, this equivalent circuit is only valid for frequencies satisfying $\omega \ll \omega_{cRH}$, that is, in the long wavelength limit (in that case the unit cell period is much smaller than the guided wavelength $p \ll \lambda_g$). Thus, to model properly a TL working at higher frequencies, the period p must be reduced and the cutoff frequency will be higher. Under this condition, the expressions (2.10) and (2.11) can be approximated by the well-known non-dispersive expressions

$$\beta_{RH}(\omega) = \omega\sqrt{L'_R C'_R} \tag{2.16}$$

and

$$Z_{BRH} = \sqrt{\frac{L'_R}{C'_R}} \tag{2.17}$$

where L'_R and C'_R are the per-unit length inductance and capacitance of the transmission line. These can be obtained as $L'_R = L_R/p$ and $C'_R = C_R/p$.

As commented in the introduction (Section 2.1), in order to consider a effective homogeneous medium, the condition $p \ll \lambda_g$ is satisfied, and thus, the long wavelength limit approximation ($\omega \gg \omega_{cLH}$) can be applied to the LH case, obtaining:

$$\beta_{LH}(\omega) = \frac{-1}{\omega\sqrt{L'_L C'_L}} \tag{2.18}$$

and

$$Z_{BLH} = \sqrt{\frac{L'_L}{C'_L}} \tag{2.19}$$

where L'_L and C'_L are the per-unit length inductance and capacitance of the transmission line. These can be computed as $L'_L = L_L p$ and $C'_L = C_L p$.

The dispersion diagrams of both structures can be computed from the expressions of the propagation constants (2.16) and (2.18), resulting in Fig. 2.12. As it is shown, the phase constant of a RH TL is always positive ($\beta > 0$) and linear with frequency. On the other hand, the phase constant of a LH TL is always negative ($\beta < 0$) and proportional to $1/\omega$. The negative behaviour of the phase constant in the LH case indicates the backward propagation.

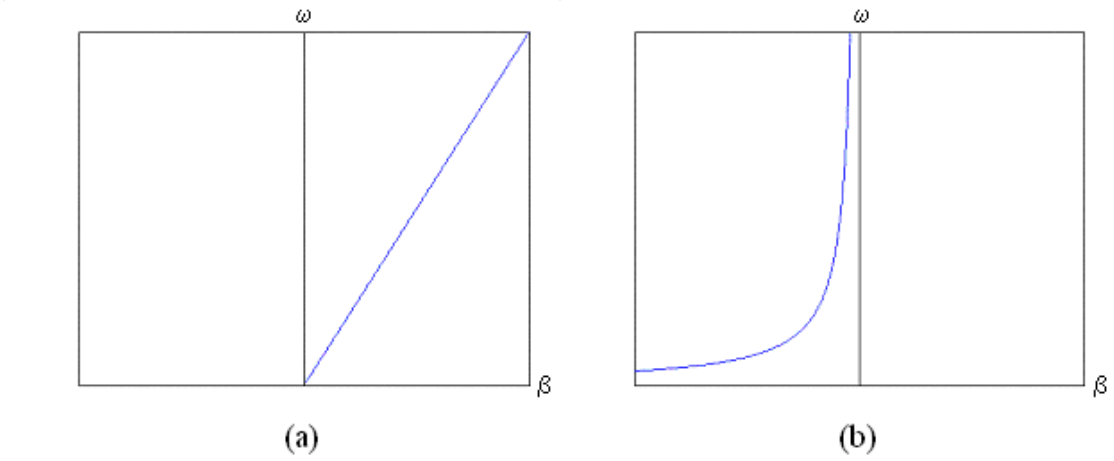

Figure 2.12: Dispersion diagrams of the ideal TLs. (a) RH. (b) LH.

The group and phase velocities of the TL can be obtained from the propagation constant as

$$v_p = \frac{\omega}{\beta} \tag{2.20}$$

and

$$v_g = \frac{\partial \omega}{\partial \beta} \tag{2.21}$$

In the case of the RH TLs, we obtain

$$v_{pRH} = \frac{1}{\sqrt{L'_R C'_R}} \tag{2.22a}$$

$$v_{gRH} = \frac{1}{\sqrt{L'_R C'_R}} = v_{pRH} \tag{2.22b}$$

whilst in the LH case these velocities are

$$v_{pLH} = -\omega^2 \sqrt{L'_L C'_L} \tag{2.23a}$$

$$v_{gLH} = \frac{1}{\omega^2 \sqrt{L'_L C'_L}}. \tag{2.23b}$$

As it can be seen in the equations (2.22)-(2.23) and in the dispersion diagrams (Fig. 2.12), the phase and group velocities are always positive in the RH TL ($v_{pRH}, v_{gRH} > 0$), whilst in the LH one the group velocity is positive ($v_{gLH} > 0$) and the phase velocity is negative ($v_{pLH} < 0$). Hence, these velocities are antiparallel in the LH TL ($v_{pLH} v_{gLH} < 0$), allowing the propagation of backward waves. This means that the energy is propagated from the source, but the wavefronts propagate towards the source. It is important to note the dispersive behaviour of the LH case, contrary to the conventional one.

The effective constitutive parameters can be computed as

$$\varepsilon = \frac{Y'_{sh}}{j\omega} \tag{2.24a}$$

$$\mu = \frac{Z'_{se}}{j\omega} \tag{2.24b}$$

where Y'_{sh} and Z'_{se} are the shunt admittance and series impedance per-unit length. For a RH TL, the effective constitutive parameters result

$$\varepsilon_{RH} = C'_R \tag{2.25a}$$

$$\mu_{RH} = L'_R \tag{2.25b}$$

and for the LH case

$$\varepsilon_{LH}(\omega) = \frac{-1}{\omega^2 L'_L} \tag{2.26a}$$

$$\mu_{LH}(\omega) = \frac{-1}{\omega^2 C'_L}. \tag{2.26b}$$

The expressions for the LH TL are always negative and thus, confirm the DNG behaviour of the LH TLs. Moreover, the effective constitutive parameters are a function of frequency, showing again the dispersive nature of these TLs.

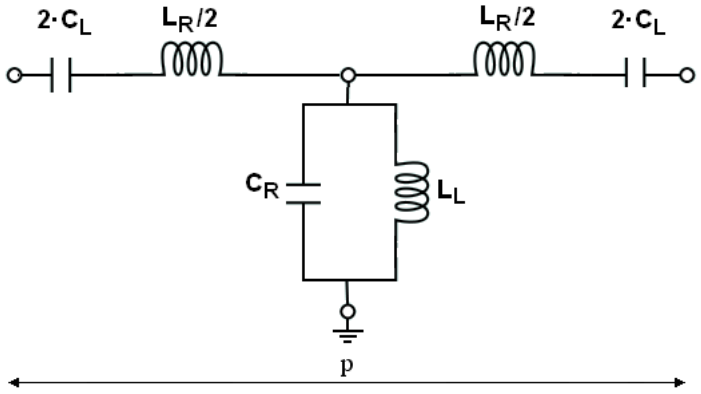

Figure 2.13: Equivalent circuit model of a CRLH TL unit cell.

In practical situations it is not possible to implement purely LH TLs. As it will be shown below, the simplest approach to achieve a TL with LH performance consists of periodically loading a conventional host line with the elements which compose a LH unit cell. In that case, the RH behaviour of the host line cannot be neglected and the complete model which represents this novel structure is termed as Composite Right/Left-Handed (CRLH) TL. This model was proposed by Caloz and Itoh [24]. The equivalent circuit model of one period of this CRLH TL is depicted in Fig. 2.13, where p is the period of the unit cell and L_R, C_L,C_L and L_L are its equivalent components. By using the expression (2.8), the dispersion relation is obtained as

$$\beta = \frac{1}{p}\cos^{-1}\left\{1 - \frac{1}{2}\left[\frac{\omega_L^2}{\omega^2} + \frac{\omega^2}{\omega_R^2} - \left(\frac{\omega_L^2}{\omega_{se}^2} + \frac{\omega_L^2}{\omega_{sh}^2}\right)\right]\right\} \tag{2.27}$$

where

$$\omega_R = \frac{1}{\sqrt{L_R C_R}} \tag{2.28a}$$

$$\omega_L = \frac{1}{\sqrt{L_L C_L}} \tag{2.28b}$$

are introduced for convenience and

$$\omega_{se} = \frac{1}{\sqrt{L_R C_L}} \tag{2.29a}$$

$$\omega_{sh} = \frac{1}{\sqrt{L_L C_R}} \tag{2.29b}$$

are the series and shunt resonance frequencies, respectively. This dispersion relation is depicted in Fig. 2.14. It must be noted an important difference with respect to the RH and LH TLs, because in this case there is a stopband in which the propagation is not allowed. Moreover, there are two propagation regions separated by this gap. The cutoff frequencies of this stopband are

$$\omega_{\Gamma 1} = \min(\omega_{se}, \omega_{sh}) \tag{2.30a}$$

$$\omega_{\Gamma 2} = \max(\omega_{se}, \omega_{sh}) \tag{2.30b}$$

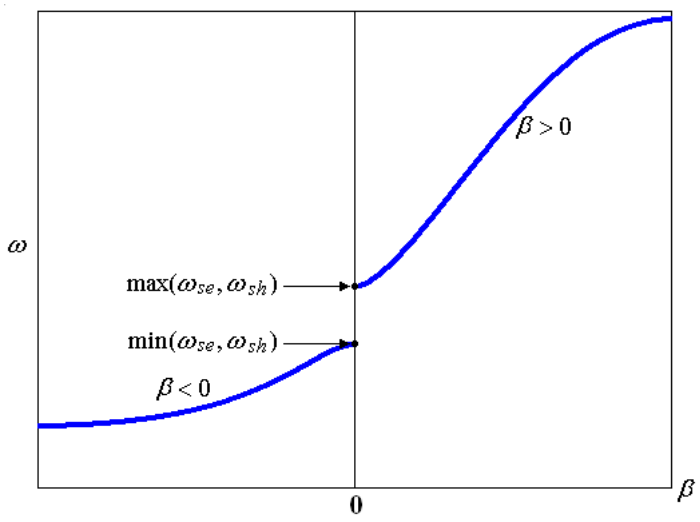

Figure 2.14: Dispersion diagram of the CRLH TL.

Thus, there are three different regions in the dispersion diagram, each of them with a different behaviour:

- In the lowest frequency region ($\omega < \omega_{\Gamma 1}$) the dominant behaviour is LH and the propagation is backward ($\beta < 0$).
- The stopband occurs between the cutoff frequencies ($\omega_{\Gamma 1} < \omega < \omega_{\Gamma 2}$).

- Above the stopband ($\omega > \omega_{\Gamma 2}$) the dominant behaviour is RH ($\beta > 0$).

The characteristic impedance of the CRLH TL can be computed from (2.9) as:

$$Z_{BCRLH} = Z_{BLH} \sqrt{\frac{\left(\frac{\omega}{\omega_{se}}\right)^2 - 1}{\left(\frac{\omega}{\omega_{sh}}\right)^2 - 1}}. \tag{2.31}$$

It must be noted that the characteristic impedance of a CRLH TL is a function of frequency. This is not the case of the RH and LH TLs (equations (2.17) and (2.19)). This makes that the CRLH TL can be matched only in a narrow bandwidth (ideally at only one frequency).

The effective constitutive parameters of the CRLH TL are also obtained from the expressions (2.24), obtaining

$$\varepsilon_{CRLH}(\omega) = \frac{C_R}{p} - \frac{1}{\omega^2 L_L p} = \varepsilon_{RH} + \varepsilon_{LH}(\omega) \tag{2.32a}$$

$$\mu_{CRLH}(\omega) = \frac{L_R}{p} - \frac{1}{\omega^2 C_L p} = \mu_{RH} + \mu_{LH}(\omega). \tag{2.32b}$$

Both parameters are negative (DNG characteristic) below the stopband (LH region) and they are positive (DPS behaviour) above the stopband (RH region).

A particular case of interest is the so-called balanced CRLH TL. This corresponds to the situation where the series and shunt resonances are identical, namely $\omega_{se} = \omega_{sh} = \omega_0$. This is obtained when the condition

$$L_R C_L = L_L C_R \tag{2.33}$$

is satisfied. In this case, there is not a forbidden gap between the LH and RH regions and the propagation changes from backward to forward at the transition frequency, ω_0, without any stopband, as shown in Fig. 2.15. Moreover, for the balanced CRLH TL, wave propagation with $\beta = 0$ ($\lambda_g = \infty$) at this frequency is possible. This is because the group velocity (given by the slope of the group velocity) is not null in this case ($v_g \neq 0$). On the other hand, the group velocity for the unbalanced CRLH TL (general case not satisfying the balanced condition) is zero at the edge frequencies of the gap and hence, the propagation is not allowed.

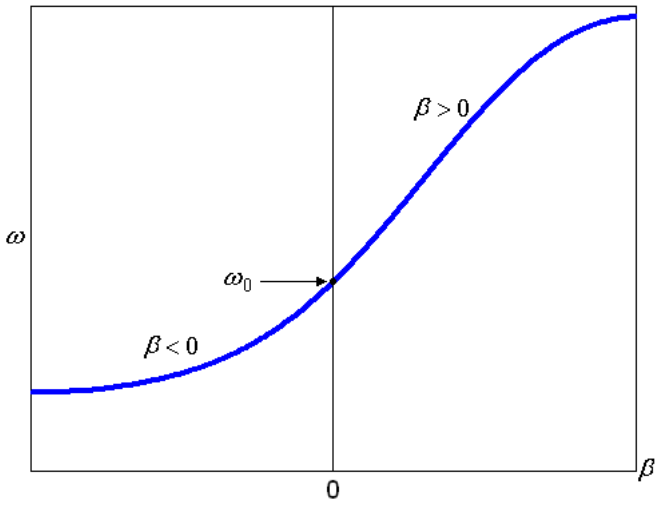

Figure 2.15: Dispersion diagram of the balanced CRLH TL.

The characteristic impedance of the balanced CRLH TL is

$$Z_{BLH} = Z_{BRH} \tag{2.34}$$

where Z_{BRH} and Z_{BLH} are those defined in equations (2.17) and (2.19), respectively. It is important to note that this magnitude does not depend on frequency. This means that the balanced CRLH TL can be matched over a broad bandwidth which is a considerably advantage over the unbalanced case.

Implementation of 1-D CRLH TLs

As it has been indicated previously, practical implementations of TLs with a LH behaviour require a host line, and hence, the obtained structures are CRLH. The host line can be any type of planar TL such as microstrip, stripline or CPW (Coplanar Waveguide) structures. This host line provides the series inductance (L_R) and shunt capacitance (C_R) in the CRLH model (Fig. 2.13). The LH components, namely L_L and C_L, are implemented by periodically loading the host line with lumped or distributed components. The first approach is usually implemented by using surface mount devices (SMD) whilst the distributed approach consists of implementing the series capacitances and shunt inductances via a printed technology.

The choice of one or another approach depends on several factors. In

terms of analysis and design, CRLH structures based on lumped elements are generally easier and quicker to implement. SMD chip components are readily available and do not need to be designed and fabricated, unlike their distributed counterparts. Moreover, the lumped elements are smaller than the distributed ones. On the other hand, SMD components are only available in discrete values and are limited to low frequencies (typically up to 6 GHz) because the parasitic effects can cause self-resonance at higher frequencies. As a result, specific phase responses and operational frequency ranges are limited for CRLH structures based on lumped elements. Finally, the use of lumped elements is more expensive because soldering is needed which produces additional losses.

CRLH TLs based on lumped elements have been used in numerous circuit applications [24, 25, 45]. On the other hand, different printed host lines have been considered for the synthesis of distributed CRLH TLs: the microstrip configuration, the CPW structure and the CPS (Coplanar Strip) line. The former was proposed by the group of Caloz and Itoh in 2002 [43, 46] and it has been used in several applications, see for example [47]. This structure is based on a periodic arrangement of interdigital capacitors and grounded (through metallic vias) stubs, which act as shunt-connected inductors (Fig. 2.16).

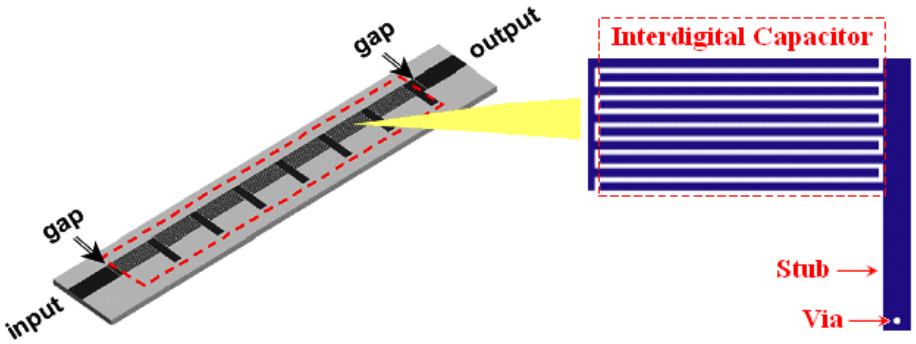

Figure 2.16: CRLH TL implemented in microstrip technology. Each unit cell is composed of an interdigital capacitor and a grounded stub [43].

The unit cell of this structure has the typical CRLH equivalent circuit (Fig. 2.13). The LH components, L_L and C_L, are provided by the short-circuited stub and the interdigital capacitor, respectively. The RH elements are due to the parasitic effects, which are more important at higher frequencies. The capacitance C_R is provided by the plane-parallel capacitor formed between the ground plane and the metallization strips, and the inductance

L_R is produced by the currents through the elements in the interdigital capacitor.

An interesting alternative to the previous structure was proposed by the same research group [48]. The unit cell of this second implementation is shown in Fig. 2.17. This configuration is via free, which simplifies the manufacturing process. In this case, meandered inductors are used instead of stubs to implement L_L and the direct connection to the ground plane is substituted by a capacitive coupling through the virtual ground C_g.

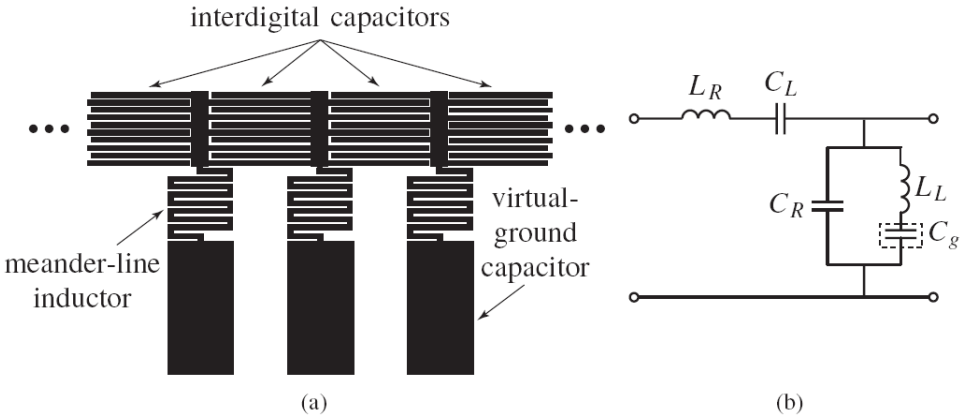

Figure 2.17: Via-free CRLH TL implemented in microstrip technology [48]. (a) Layout of the structure. (b) Equivalent circuit model of one unit cell.

In the CPW technology, the shunt inductors can be implemented by means of connecting strips between the central strip and ground planes. The series capacitors can be implemented through interdigital geometries, or by means of series gaps. The latter are more simple, but the achievable capacitance values are much smaller. The Eleftheriades' group at the University of Toronto presented a realization of a LH line fabricated in CPW technology by using series gaps and shunt strips (see Fig. 2.18) [49].

The same group has proposed an implementation based on CPS techonology [51]. In that case, the series capacitances are implemented with interdigital capacitors and the shunt inductances are based on meandered inductors which interconnect the metallic strips of the CPS host line, as depicted in Fig. 2.19. The proposed CRLH structures in CPW and CPS technologies have been successfully applied to the development of leaky-wave antennas with backward radiation [49, 50, 51] (Section 2.6.1).

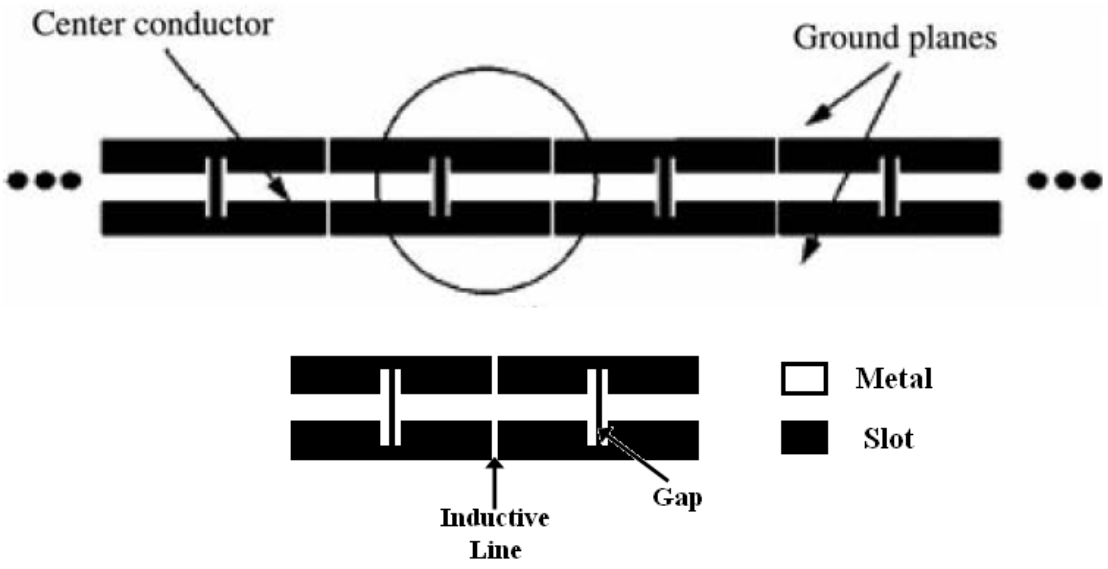

Figure 2.18: Distributed CPW CRLH TL proposed by Eleftheriades' group [49, 50].

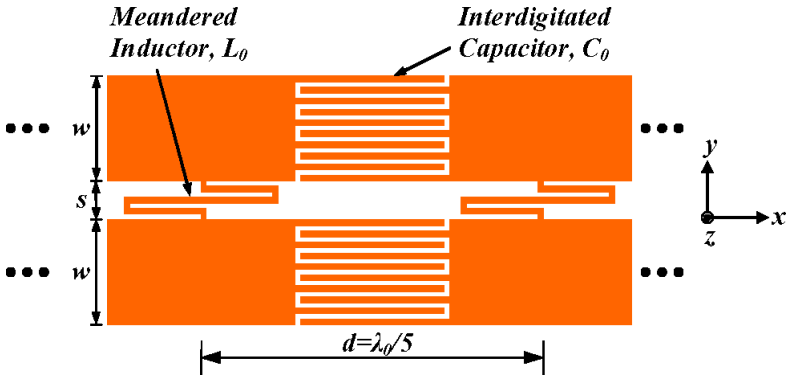

Figure 2.19: Unit cell of the distributed CPS CRLH TL proposed by Eleftheriades' group [51].

Implementation of 2-D CRLH TLs

The 2-D CRLH TL is obtained by considering the 1-D case along two orthogonal dimensions. The equivalent circuit model of a 2-D CRLH unit cell is shown in Fig. 2.20.

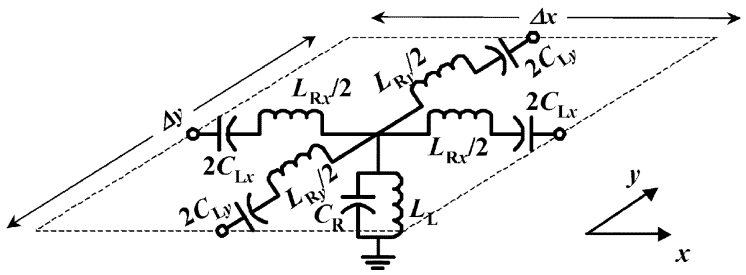

Figure 2.20: Equivalent circuit model of a 2-D CRLH unit-cell [52].

The main difference with respect to the 1-D CRLH structure is that in the 2-D case the propagation constant is a vector instead of a scalar. This can be represented by the next equation

$$\vec{\beta} = \beta_x \hat{x} + \beta_y \hat{y} \tag{2.35}$$

defined over the reciprocal lattice of a direct one with the unit cell periods p_x and p_y along the two main directions. The dispersion diagram is usually represented only with a segment which includes the most important symmetry points. These symmetry points are given by

$$\Gamma : \vec{\beta} = 0 \tag{2.36a}$$

$$X : \vec{\beta} = \frac{\pi}{p_x}\hat{x} \qquad \left[Y : \beta = \frac{\pi}{p_y}\hat{y}\right] \tag{2.36b}$$

$$M : \vec{\beta} = \pi\left(\frac{1}{p_x}\hat{x} + \frac{1}{p_y}\hat{y}\right) \tag{2.36c}$$

which define the segment $\Gamma - X - M - \Gamma$. In the case of anisotropy the point Y is also considered.

Fig. 2.21 shows the typical dispersion diagram for 2-D balanced and unbalanced CRLH TLs, obtained through the analysis of the equivalent circuit model of Fig. 2.20. The equivalent circuit parameters for the unbalanced case (Fig. 2.20.a) are: $L_{Rx} = L_{Ry} = L_R = 1$ nH, $C_R = 1$ pF, $L_L = 1$ nH, $C_{Lx} = C_{Ly} = C_L = 0.6$ pF. The only difference in the balanced case

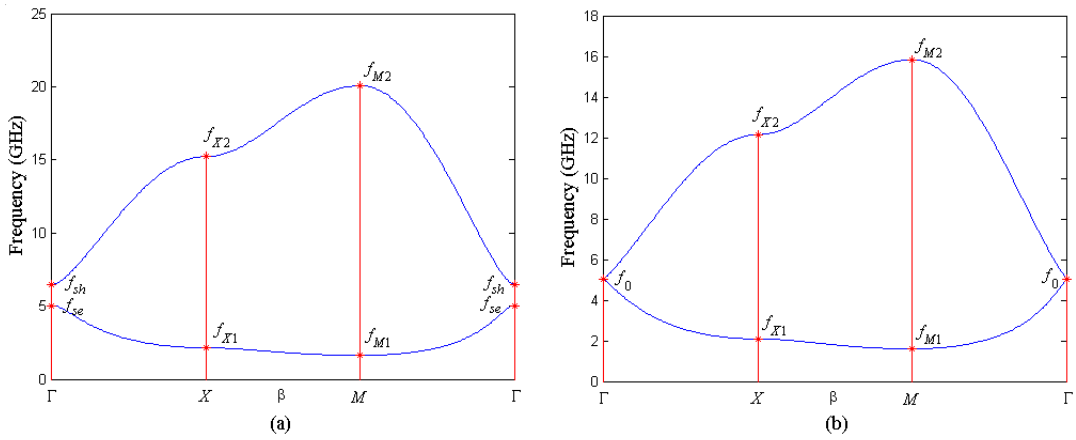

Figure 2.21: Dispersion diagrams of 2-D CRLH TLs. (a) Unbalanced case with $L_{Rx} = L_{Ry} = L_R = 1$ nH, $C_R = 1$ pF, $L_L = 1$ nH, $C_{Lx} = C_{Ly} = C_L = 0.6$ pF. (b) Balanced case with $L_{Rx} = L_{Ry} = L_R = 1$ nH, $C_R = 1$ pF, $L_L = 1$ nH, $C_{Lx} = C_{Ly} = C_L = 1$ pF.

(Fig. 2.20.b) is that the LH capacitances are $C_{Lx} = C_{Ly} = C_L = 1$ pF. The propagation performance is similar to the 1-D case, showing a LH mode at lower frequencies and a RH one at higher frequencies. In the unbalanced case, there is a stopband between both modes whilst there is a continuous transition under the balanced condition. It seems that the group velocity (slope of the dispersion diagram) changes its sign in the $M - \Gamma$ region. However, it must be noted that the propagation vector in that region is negative ($\vec{\beta} = -k_i(\hat{x} + \hat{y}), 0 < k_i < \pi/p$) and thus, the sign of the group velocity remains unchanged.

Similar approaches used to synthesize 1-D CRLH TLs are valid to implement the 2-D case. The first implementations of 2-D CRLH TLs were developed by loading a host 2-D TL with lumped elements. These structures were proposed by the group of Eleftheriades in 2002 [53]. Fig. 2.22 shows the sketch of a loaded 2-D unit cell and its dispersion diagram considering one principal direction. The structure has a CRLH behaviour with a LH propagation band at lower frequencies, a RH one at higher frequencies and a stopband between them. The LH performance is achieved thanks to the loading elements (C_0 and L_0 in Fig. 2.22) whilst the RH behaviour is due to the host line.

The same group proposed several distributed implementations. The first one is described in [54] and it is based on microstrip technology. Fig. 2.23 shows the sketch of a unit cell and its corresponding dispersion diagram. The

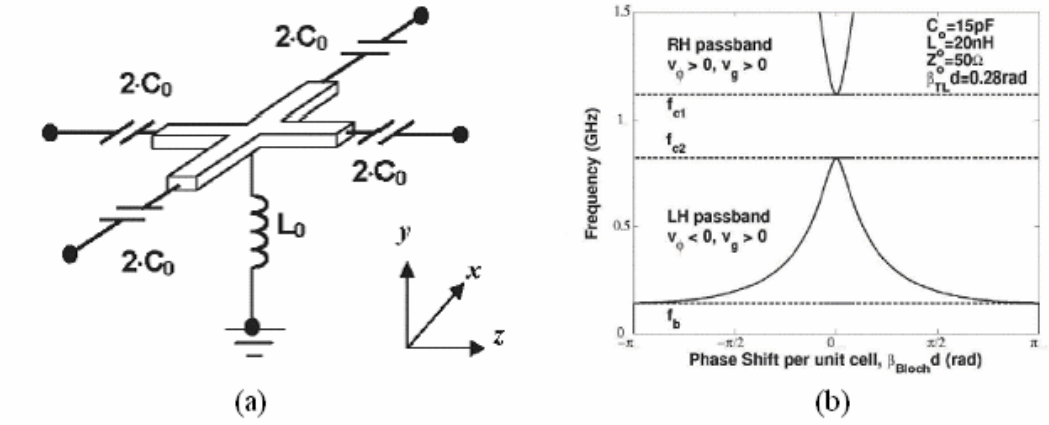

Figure 2.22: 2-D lumped-loaded CRLH TL proposed in [53]. (a) Sketch of the unit cell. (b) Dispersion diagram considering one of the principal directions.

LH elements are implemented with capacitive gaps between the adjacent cells (C_L) and coils connected between the metallization and the ground plane (L_L).

The second distributed implementation is based on a CPS structure [55]. Fig. 2.24 shows the equivalent circuit model and the layout of a unit cell. The series capacitances are implemented with interdigital capacitors in each of the strips which compose the host line and the shunt inductances are meandered inductors which interconnect both strips.

Alternatively, the research group led by Caloz and Itoh proposed several distributed 2-D CRLH TLs implementations [52, 24]. These implementations are based on the structure proposed by Sievenpiper to achieve high-impedance surfaces [56]. Sievenpiper's elements are also known as *mushroom structures*. These structures are based on microstrip patches with gaps between adjacent cells and shorting vias which connect the metallic patches to the ground plane. Initially, Sievenpiper used the stopband provided by these structures to eliminate the surface waves in planar antennas. Then, Caloz and Itoh observed that the structure presented a LH band below the stopband and proposed the mushroom structure as a distributed 2-D CRLH TL.

Fig.2.25 shows the microstrip implementation based on the mushroom structure and its unit cell. This structure has some similarities with the one proposed by the group of Eleftheriades (Fig. 2.23). The LH behaviour of the structure is provided by the capacitive gaps between the adjacent cells (C_L) and the vias which connects the metallic patches with the ground plane (L_L).

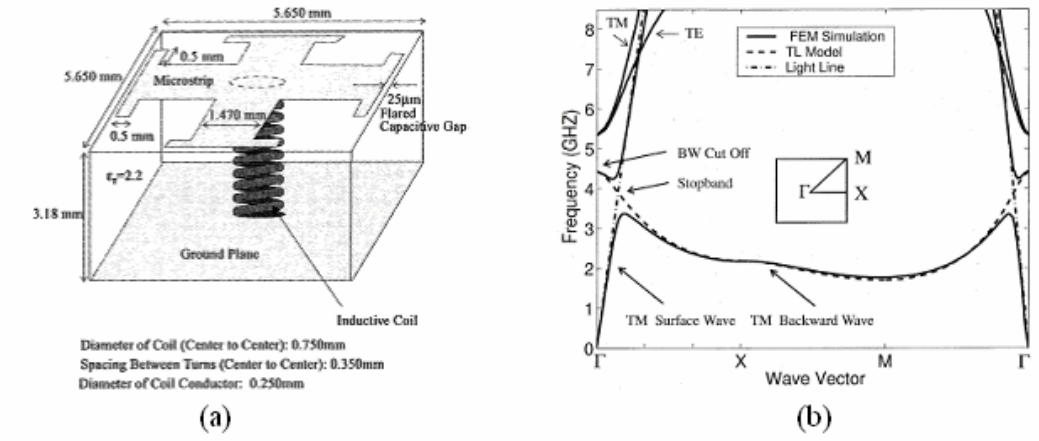

Figure 2.23: 2-D CRLH TL based on distributed elements in microstrip technology [54]. (a) Unit cell. (b) Dispersion diagram.

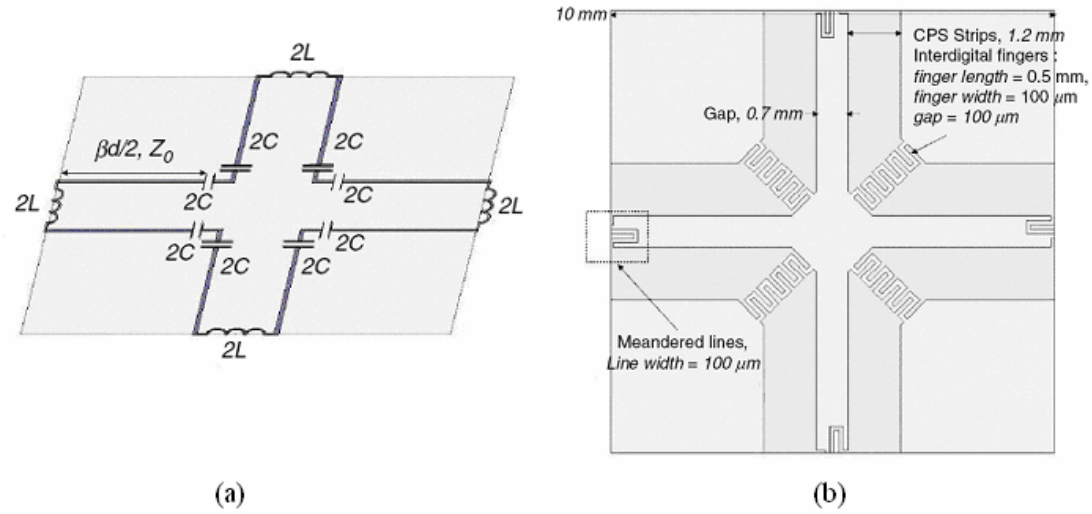

Figure 2.24: 2-D distributed CRLH TL in CPS technology [55]. (a) Equivalent circuit model of a unit cell. (b) Layout of a unit cell.

The RH parasitic elements are due to the current flux through the microstrip patches (C_R) and the parallel-plate capacitors formed between the metallic patches and the ground plane (C_R).

Caloz and Itoh also proposed some techniques to increase the value of the series capacitances (C_L) and thus, obtain the LH band at lower frequencies. The first proposal to enhance the series capacitances consisted of using interdigital capacitors between the unit cells [24]. Another approach is based on metal-insulator-metal (MIM) strucutres, *caps*, obtained by including metallizations between upper patches and the ground plane [52]. The use of these caps is shown in Fig. 2.25. These caps increase the series capacitance, providing lower frequencies for the LH band. On the other hand, the use of these elements makes more difficult and expensive the fabrication of the LH structures, which is not desirable.

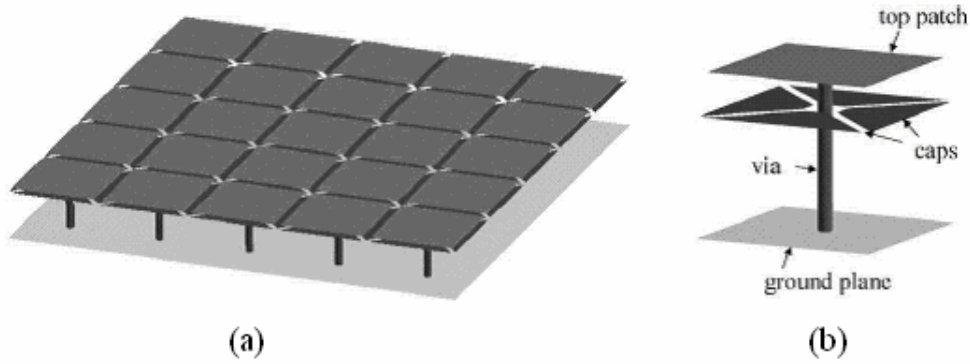

Figure 2.25: 2-D CRLH TL based on the mushroom structure [52]. (a) Overall structure. (b) Unit cell.

The authors of [52] also proposed the use of hexagonal geometries to improve the isotropy. However, the hexagonal structure has not been applied after its proposal due to the complexity to manufacture it. It is also possible to achieve an anisotropy structure by considering rectangular unit cells or changing the caps to achieve different series capacitances in each direction.

The same group proposed a modification to achieve a 2-D CRLH TL using stripline technology. This TL consisted of two mirrored mushroom structures, considering the metallic patches as the plane of symmetry (Fig. 2.26).

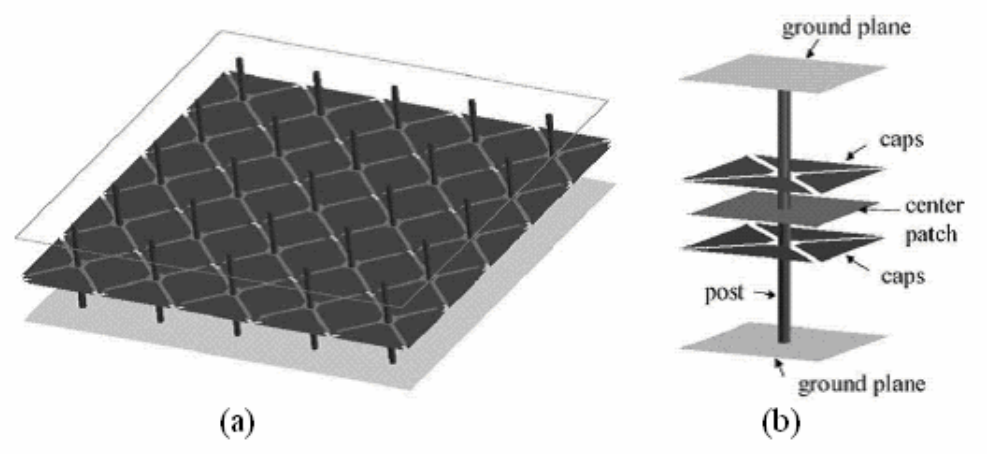

Figure 2.26: 2-D CRLH TL in stripline technology [52]. (a) Overall structure. (b) Unit cell.

2.3.2 The Resonant Type Approach

This second approach to develop metamaterial-based transmission lines was proposed by the groups of Marqués (Universidad de Sevilla),Martín (Universitat Autònoma de Barcelona) and Sorolla (Universidad Pública de Navarra, UPNA). This approach is called resonant-type because a host line is loaded with subwalenght resonators (e. g. SRRs). These research groups have proposed several implementation of metamaterial-loaded transmission lines using the CPW and the microstrip line as hosting lines [27].

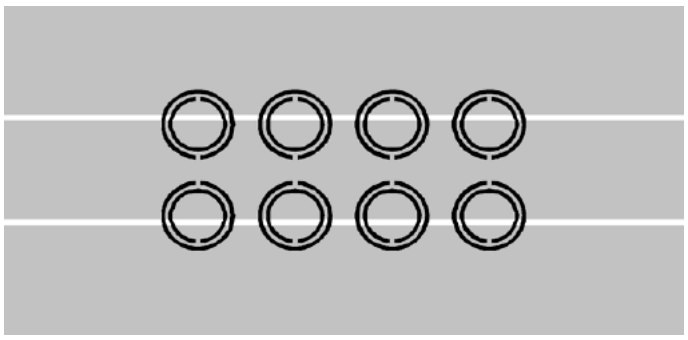

Figure 2.27: MNG CPW TL based on a conventional CPW line loaded with SRRs [36]. The SRRs are printed on the side of the substrate opposite to the host TL.

The first type of metamaterial-loaded transmission lines are those with effective negative permeability. In order to obtain transmission lines with negative effective permeability it is necessary to load a host printed line with printed MNG metamaterial particles (e. g. SRRs). These particles must be properly placed in order to excite them and achieve the desired behaviour. Hence, the magnetic field generated by the current flowing through the line has an important component perpendicular to the plane of the particles. In the case of CPW TL, the simplest implementation consists of loading the TL with SRRs etched in the slot region, either in the upper metal level or in the back substrate side (considering that there is no ground metallization at this side of the substrate). The first structure seems to be easier to manufacture, but the second one is preferred because it provides higher coupling between the line and the particles, lower insertion losses and easier matching [27]. An example of this MNG TL is shown in Fig 2.27. In microstrip technology, the particles must be etched as close as possible to the host line in order to achieve high magnetic coupling. In practical implementations, square or rectangular SRRs are used to enhance the coupling between the line and the metamaterial particles, as shown in Fig. 2.28.

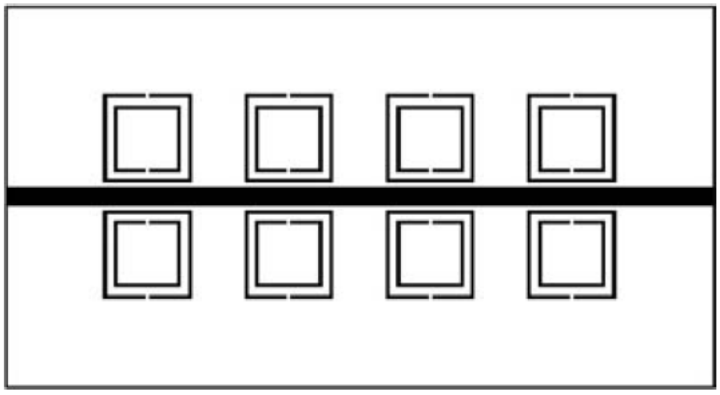

Figure 2.28: Sketch of a MNG microstrip line loaded with SRRs [27].

In this type of transmission lines a forbidden band appears in the vicinity of the resonance frequency of the metamaterial magnetic particles. Within this band, the power injected in the line is returned back to the source. Outside the forbidden band, the structure behaves as a conventional line and the energy propagates through the line without being altered by the metamaterial particles.

As explained in Section 2.2.2, MNG metamaterial particles can be modelled as a LC resonant tank. Following this approach, it is easy to develop

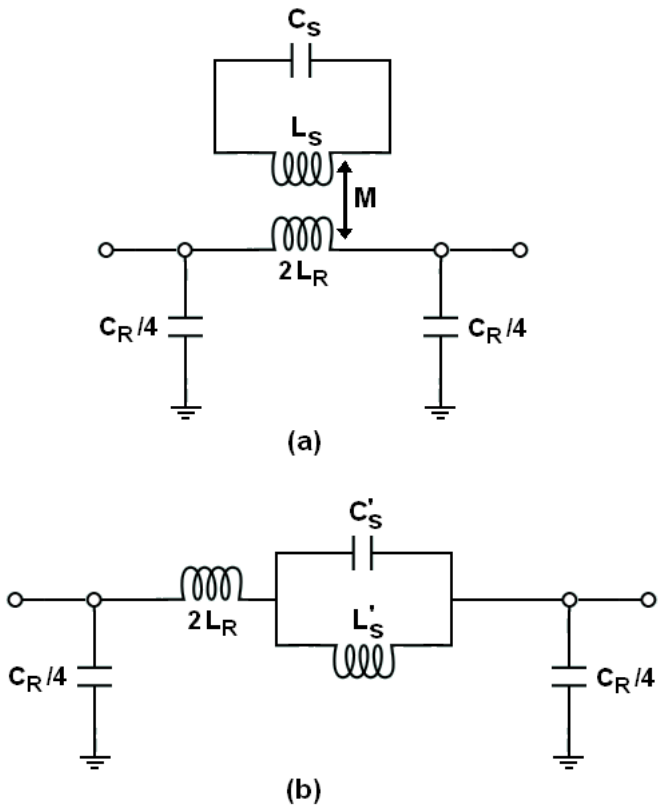

Figure 2.29: Equivalent circuit model of a TL loaded with MNG particles (e. g. Figs. 2.27-2.28). (a) $\pi-$model of the unit cell. (b) Model of the unit cell after the transformation of the series branch.

equivalent circuit models for the metamaterial-loaded transmission lines. These models take into account the transmission line, the resonant particles and their coupling. The proposed equivalent circuit model for the MNG metamaterial-loaded TL is shown in Fig. 2.29.a. As explained in Section 2.3.1, the host TL is can be modeled by a conventional RH line with inductances L_R and capacitances C_R. The MNG metamaterial particles are modeled as resonant tanks (with inductance L_S and capacitance C_S) magnetically coupled to the line through a mutual inductance M. The equivalent impedance of the series branch can be simplified to that shown in Fig. 2.29.b, considering the following conditions:

$$L'_S = \omega_0^2 M^2 C_S \tag{2.37a}$$

$$C'_S = \frac{L_S}{\omega_0^2} M^2 \tag{2.37b}$$

where $\omega_0 = 1/\sqrt{C_S L_S} = 1/\sqrt{C'_S L'_S}$ is the resonance frequency of the metamaterial particles.

The dispersion relation for this structure can be computed from equation (2.8), taking into account the equivalent circuit model (Fig. 2.29.b). Therefore, we obtain

$$\beta = \frac{1}{p} \cos^{-1} \left[1 - \frac{L_R C_R \omega^2}{2} + \frac{\frac{C_R}{C'_S}}{4\left(1 - \frac{\omega_0^2}{\omega^2}\right)} \right] \tag{2.38}$$

This expression has been evaluated with the following parameters: $L_R = 1.00$ nH, $C_R = 3.12$ pF, $L'_S = 1.58$ nH and $C'_S = 1.28$ pF. The resulting dispersion diagram is depicted in Fig. 2.30. A stopband is obtained in the vicinity of the resonance frequency of the particles $f_0 = \omega_0/(2\pi) = 3.54$ GHz, as expected. The propagation is inhibited up to the resonance frequency of the series branch, given by

$$\omega_{se} = \sqrt{\frac{1}{2C'_S L_R} + \frac{1}{C'_S L'_S}} = \sqrt{\frac{1}{2C'_S L_R} + \omega_0^2}, \tag{2.39}$$

which is $f_{se} = \omega_{se}/(2\pi) = 4.73$ GHz in this case.

It is possible to develop TLs with LH passbands using the resonant-type approach. In order to achieve these TLs is necessary to add a shunt inductance in the models of Fig. 2.29. This implies making the structure behave as an effective medium with negative dielectric permittivity up to the plasma

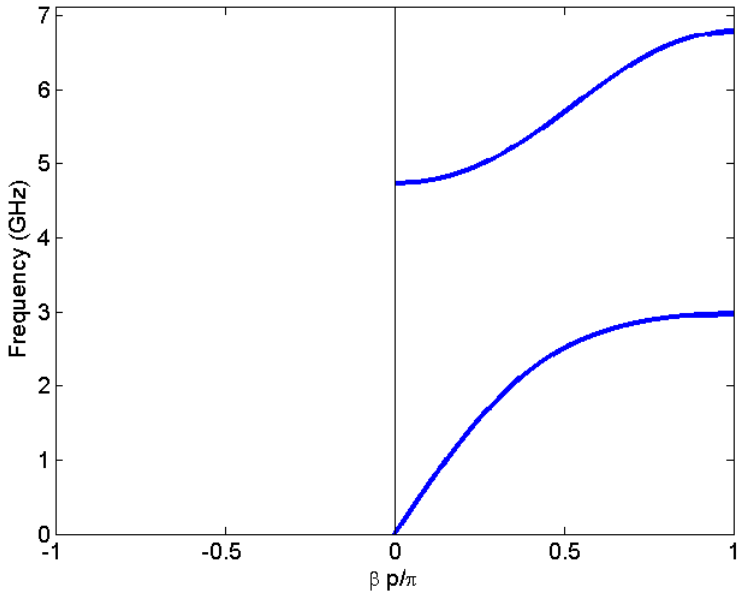

Figure 2.30: Dispersion diagram of a TL loaded with MNG particles. The parameters of the model are: $L_R = 1.00$ nH, $C_R = 3.12$ pF, $L'_S = 1.58$ nH and $C'_S = 1.28$ pF.

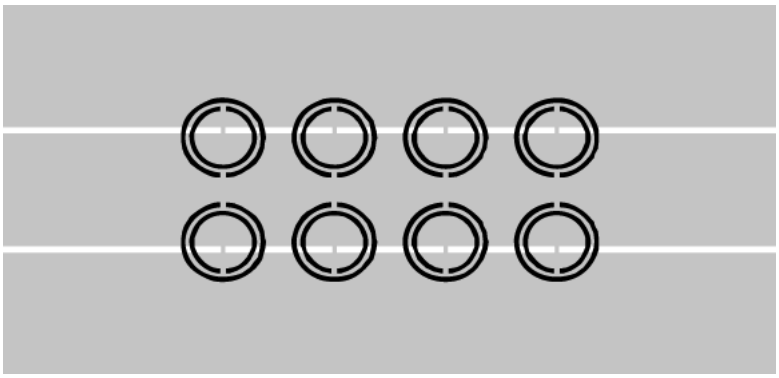

Figure 2.31: LH CPW TL based on a conventional CPW line loaded with SRRs and shunt metallic strips [36]. The SRRs are printed on the side of the substrate opposite to the host TL.

frequency ($f_p = \omega_p/(2\pi)$) defined by the period of the shunt inclusions. If f_p is set above the resonance frequency of the MNG metamaterial particles, both ε and μ are simultaneously negative in a frequency band above the resonance frequency of the MNG particles. The propagation is allowed in that band but with backward waves (LH transmission). This approach can be easily implemented in CPW technology by adding metallic connections (strips) to the previous MNG CPW TL (Fig. 2.27). These strips must be periodically located above the MNG particles, as shown in Fig. 2.31, acting as shunt inductances. In the case of microstrip TLs, shunt inductances are achieved with metallic vias to the ground plane, similar to the case of mushroom structures (Section 2.3.1). Hence, vias are added to the MNG-loaded TL to achieve a microstrip LH TL based on subwavelength resonators. The resulting structure is shown in Fig. 2.32.

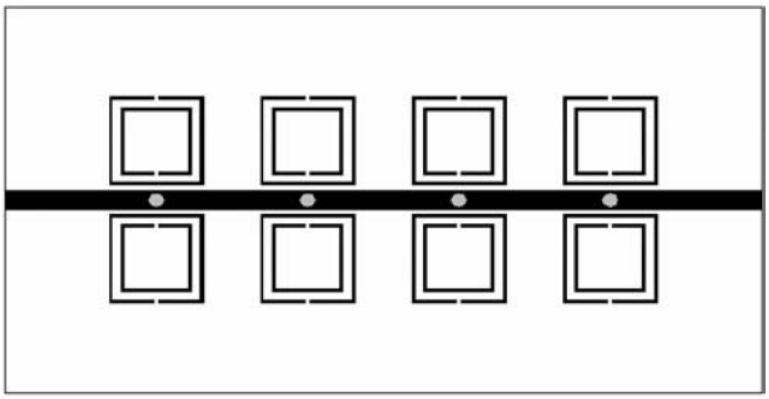

Figure 2.32: Sketch of a LH microstrip line loaded with SRRs and vias [27].

The equivalent circuit models of the LH resonant-type TLs is similar to the ones of Fig. 2.29, but with the addition of the shunt inductance. This circuit is sketched in Fig. 2.33.

It is important to note that these resonant-type TLs have a shunt and series resonant tanks equivalent to that of the CRLH TLs (Fig. 2.13). Thus, these resonant-type TLs also present a CRLH behaviour with a RH propagation band above the LH one and a gap between them. In this case, the series resonance frequency of the line is the same as the MNG TL (equation (2.39)) and the shunt resonance frequency is the same as the conventional CRLH TL (equation (2.29b)).

Equation (2.8) can be used to compute the dispersion relation of these CRLH structures, resulting

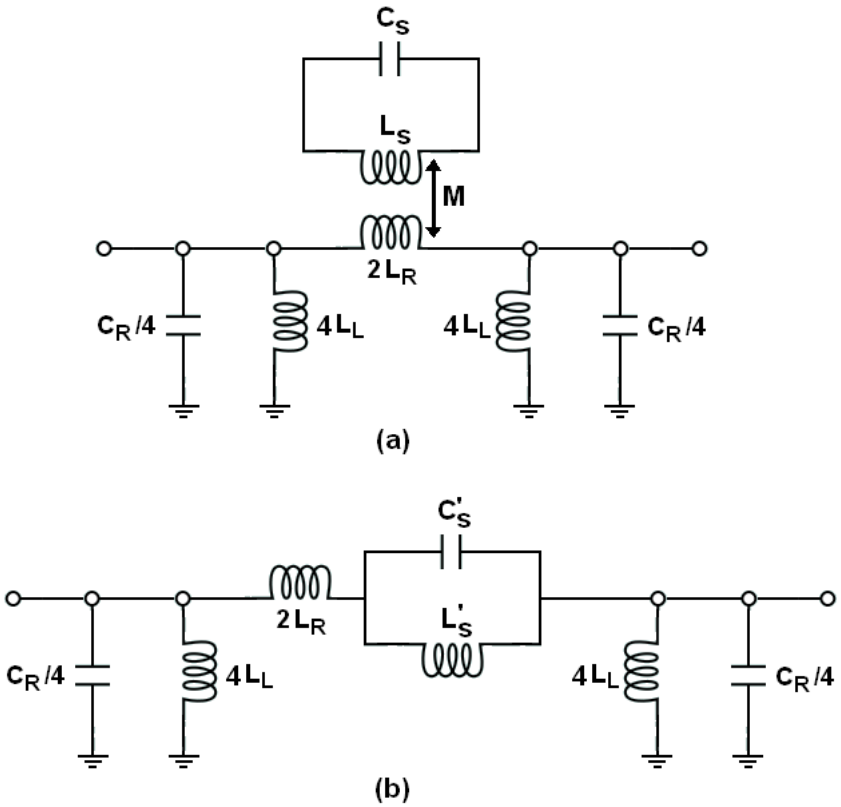

Figure 2.33: Equivalent circuit model of a CRLH TL loaded with MNG particles and shunt inductors (e. g. Figs. 2.31-2.32). (a) $\pi-$model of a unit cell. (b) Model of a unit cell after the transformation of the series branch.

$$\beta = \frac{1}{p}\cos^{-1}\left[1 - \frac{L_R C_R \omega^2}{2}\left(1 - \frac{\omega_{sh}^2}{\omega^2}\right)\left(1 - \frac{1}{2L_R C'_S \omega^2\left(1 - \frac{\omega_0^2}{\omega^2}\right)}\right)\right] \quad (2.40)$$

The developers of this approach also propose the concept of complementary particles [36, 27] as an alternative to the design of metamaterial based on resonant elements, providing an effective negative permittivity, rather than permeability. By considering duality and complementarity, the complementary particles can be obtained.

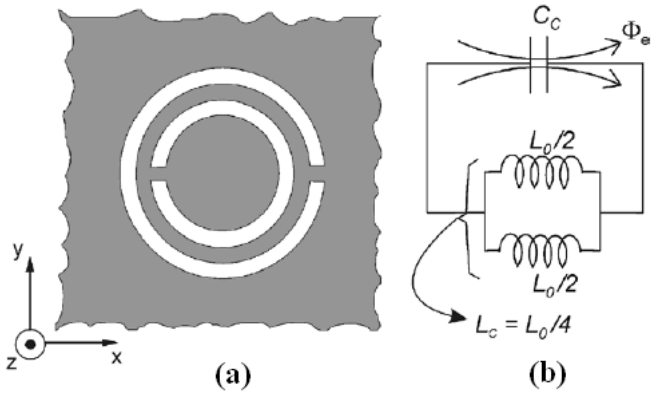

Figure 2.34: Topology of the CSRR (a) and its equivalent circuit model (b). Figure extracted from [36].

The complementary of a planar metallic structure is obtained by replacing the metal parts of the original structures with apertures, and the apertures with metal plates. If the thickness of the metal is zero and its conductivity infinity (perfect electric conductor), then the apertures behave as perfect magnetic conductors. In that case the original structure and its complementary are effectively dual, and if the field $F = (E, H)$ is a solution for the original structure, its dual F' defined by

$$F' = (E', H') = (-\sqrt{\mu/\varepsilon} \cdot H, \sqrt{\varepsilon/\mu} \cdot E) \quad (2.41)$$

is the solution for the complementary structure. Thus, under these ideal conditions, a perfectly dual behaviour is expected for the complementary screen of a MNG particle. In particular, the Complementary Split Ring Resonator (CSRR) is the dual of the SRR (Fig. 2.34). Considering these ideal

conditions, whereas the SRR can be considered as a resonant magnetic dipole excited by an axial magnetic field, the CSRR mainly behaves as an electric dipole (with the same frequency of resonance) that can be excited by an axial electric field. Moreover, the equivalent circuit model of the CSRR is the dual of the SRR. Hence, the inductance L_S of the SRR is substituted by the capacitance C_C which is the capacitance of a disk of radius $r_0 - w/2$ surrounded by a ground plane at a distance w of its edge. The series connection of the two capacitances $C_0/2$ in the SRR model are replaced by the parallel combination of the two inductances connecting the inner disk to the ground. Each inductance is given by $L_0/2$, where $L_0 = 2\pi r_0 L_{pul}$ and L_{pul} is the per-unit-length inductance of the CPWs connecting the inner disk to the ground. Considering the ideal conditions of zero thickness in the metallizations and the absence of dielectrics, the parameters of the SRR and the CSRR are related by

$$C_C = 4\frac{\varepsilon_0}{\mu_0} L_S \tag{2.42a}$$

$$C_0 = 4\frac{\varepsilon_0}{\mu_0} L_0 \tag{2.42b}$$

which gives the same resonance frequency for both particles, as expected. The factor of 4 in these relations comes from the different symmetry properties of the electric and magnetic fields of both elements [36]. In the presence of a dielectric substrate, the values of the capacitances C_S and C_0 are modified, producing a shift in the resonance frequencies of the particles.

The same concepts can be considered to obtain other ENG particles which are the dual of the MNG ones. These dual ENG particles are depicted in Fig. 2.35.

The simplest metamaterial transmission line based on complementary particles consists of etching these particles on the ground plane under the strip of a microstrip TL, as depicted in Fig. 2.36. Hence, an electric field in the axial direction is obtained, producing a proper excitation of the particles. This TL is ENG in the vicinity of the complementary particles' resonance which produces a notch in the passband of the TL. The equivalent circuit model of this TL is shown in Fig. 2.37, where L_R and C_R are the per-section inductance and capacitance of the host line and L_C and C_C model the complementary particle, as explained before.

The dispersion relation of this equivalent circuit model is computed from the expression (2.8), obtaining:

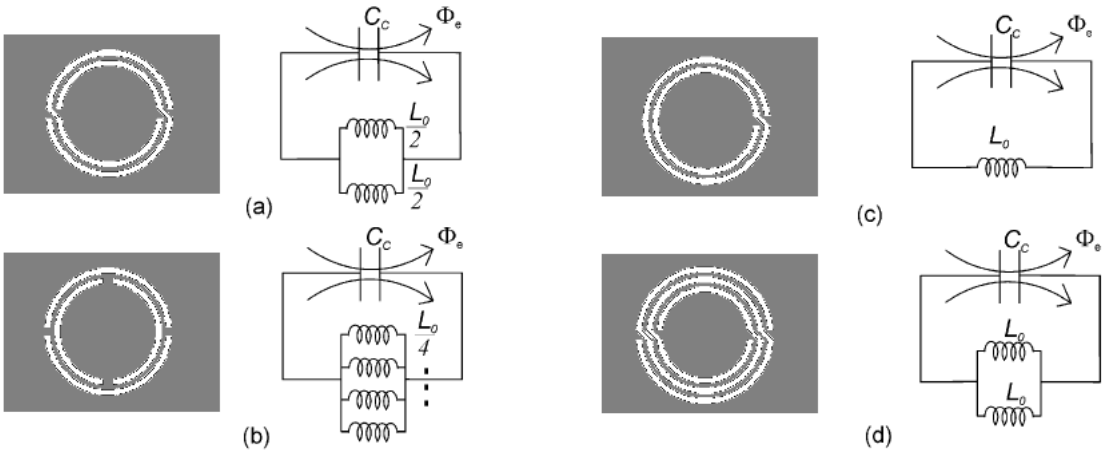

Figure 2.35: Topologies of the ENG complementary particles proposed in [36] and their equivalent circuit models: (a) Nonbiasotropic CSRR, (b) Double CSRR, (c) Complementary Spiral Resonator, (d) Complementary Double Spiral Resonator.

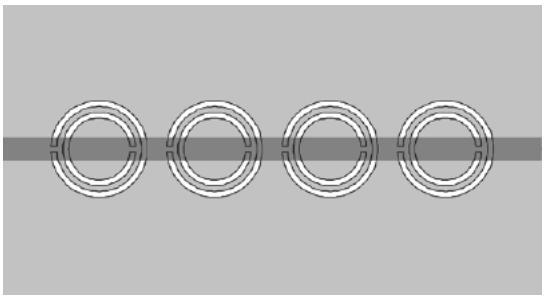

Figure 2.36: Sketch of a ENG microstrip line loaded with CSRRs [36]. The CSRRs are etched on the ground plane under strìp.

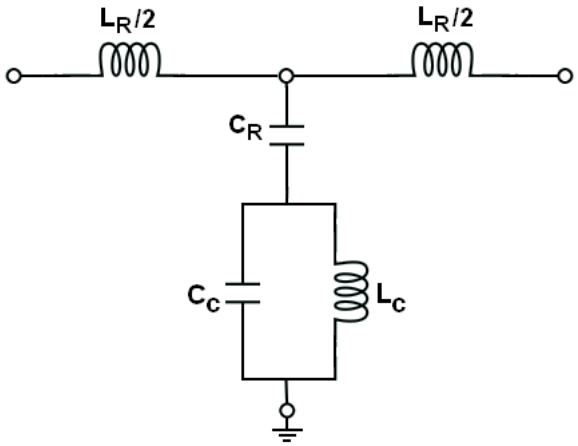

Figure 2.37: Equivalent circuit model of a TL loaded with ENG particles (e. g. a microstrip line loaded with CSRRs, as shown in Fig. 2.36).

$$\beta = \frac{1}{p}\cos^{-1}\left[1 + \frac{L_R}{2\left(\dfrac{L_C}{1-\dfrac{\omega^2}{\omega_0^2}} - \dfrac{1}{C_R\omega^2}\right)}\right]. \tag{2.43}$$

The limits of the stopband can be computed by examining the previous dispersion relation. The higher cutoff frequency is the the resonance frequency of the complementary particles ($\omega_0 = 1/\sqrt{L_C C_C}$) and the lower cutoff frequency is given by the resonance frequency of the shunt branch

$$\omega_{sh} = \frac{\omega_0}{\sqrt{1 + C_R L_C \omega_0^2}}. \tag{2.44}$$

The dispersion relation of this structure has been evaluated with the following equivalent parameters: $L_R = 1.00$ nH, $C_R = 3.12$ pF, $L_C = 0.93$ nH and $C_C = 2.81$ pF. The obtained dispersion diagram is plotted in Fig. 2.38. As explained before, there is a stopband between the shunt resonance frequency ($f_{sh} = \omega_{sh}/(2\pi) = 2.14$ GHz) and the resonance frequency of the particles ($f_0 = \omega_0/(2\pi) = 3.11$ GHz).

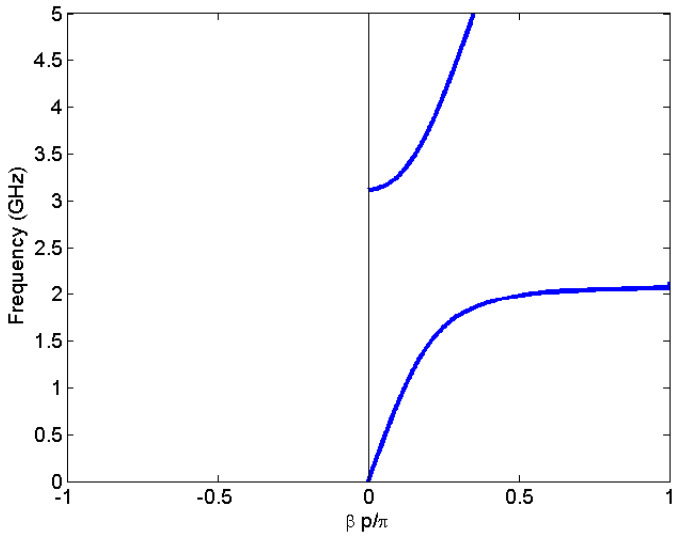

Figure 2.38: Dispersion diagram of a TL loaded with ENG complementary particles. The equivalent circuit parameters are: $L_R = 1.00$ nH, $C_R = 3.12$ pF, $L_C = 0.93$ nH and $C_C = 2.81$ pF.

In order to achieve a TL loaded with complementary particles and a LH band it is necessary to add elements which provide the required effective negative permeability. Equivalently, it is necessary to add series capacitances in the circuit model of Fig. 2.37. These elements make the structure have a MNG behaviour which must be extended beyond the resonance frequency of the complementary particles to achieve the desired LH band. In microstrip technology, gaps behave as series capacitances (Section 2.3.1). Thus, a microstrip TL loaded with dual particles in the ground plane (such as CSRRs) and gaps in the strip has a LH passband. Fig. 2.39 shows a sketch of this TL. Its equivalent circuit model, shown in Fig. 2.40, is the same as that of the ENG TL but with the addition of the series capacitance C_L provided by the gaps.

The dispersion relation of this TL is computed from the general expression (2.8), resulting:

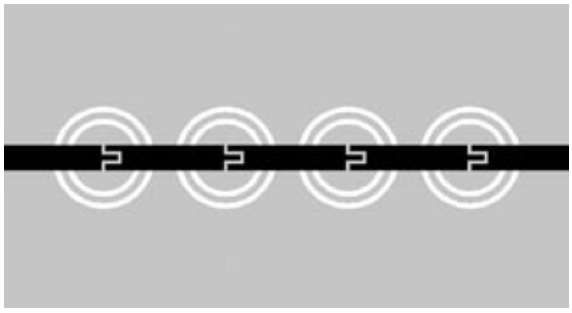

Figure 2.39: Sketch of a LH microstrip line loaded with CSRRs and series gaps [36].

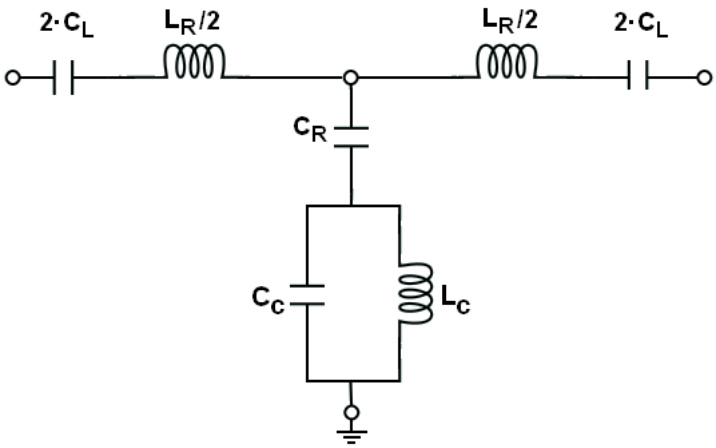

Figure 2.40: Equivalent circuit model of a CRLH TL loaded with ENG particles and series capacitors (e. g. Figs. 2.39).

$$\beta = \frac{1}{p}\cos^{-1}\left[1 + \frac{L_R\omega - \frac{1}{C_L\omega}}{2\left(\frac{L_C\omega}{1-\frac{\omega^2}{\omega_0^2}} - \frac{1}{C_R\omega}\right)}\right] \tag{2.45}$$

This TL has a CRLH behaviour with a RH propagation band above the LH one and a stopband between them. The limits of this stopband are given by the shunt and series resonance frequencies, as in the general CRLH TL (Section 2.3.1). In this case, the series resonance frequency is similar to the general case (equation (2.29a)) and the shunt resonance frequency equals the ENG TL case (equation (2.44)). In practical situations, the capacitance C_R is very high (for example if the substrate thickness is small or its permittivity is high) and can be neglected. For that situation, the shunt resonance frequency can be approximated by the resonance frequency of the complementary particles and the equivalent circuit model is the same as the general CRLH TL (Fig. 2.13) but with C_C and L_C instead of C_R and L_L.

2.3.3 Equivalence Between Both Approaches

As it was explained in the previous Subsection, the TLs developed with the resonant approach have a CRLH behaviour and they are equivalent to the CRLH TLs. This can be observed by comparing the equivalent circuit model of the CRLH structure developed with the TL approach (Fig. 2.13) and the ones obtained with the resonant approach (Figs. 2.33.b and 2.40). The only difference between both models is the existence of the inductance L'_S in Fig. 2.33.b and the coupling capacitance in Fig. 2.40 which are not present in the CRLH TL (Fig. 2.13). As explained at the end of the previous Subsection, the coupling capacitance can be neglected in practical implementations and thus, the equivalent circuit for both approaches are the same. The inductance L'_S cannot be neglected in most cases. Anyway, the structure of Fig. 2.33.b has a CRLH behaviour with a LH passband at lower frequencies, a RH propagation band at higher frequencies and a gap between them with cutoff frequencies equal to the resonance frequencies of the series and shunt branches.

Initially, there was a controversy about the possibility of developing balanced CRLH TLs with the resonant approach [24, 57]. However, this is possi-

ble by equalizing the shunt and series resonant frequencies ($\omega_{sh} = \omega_{se} = \omega_0$) independently of the approach considered. The developers of the resonant approach demonstrated this possibility in [57], designing a balanced TL based on CSRRs and interdigtal series gaps in microstrip technology.

2.4 CRLH Resonators

CRLH TLs support the propagation of travelling waves when they are matched to the elements that they are connected to. This is the case of most microwave circuits, but not the resonant-type devices such as resonant antennas. When CRLH TLs are open-ended or short-ended, standing waves are produced due to the boundary conditions and CRLH resonators are obtained. This is similar to conventional TLs, but in the case of CRLH resonators some extraordinary properties can be obtained [24].

The resonance frequencies of a resonator ω_n correspond to the frequencies where the physical length of the structure ℓ is a multiple of half a wavelength or, equivalently, the electrical length $\theta = \beta\ell$ is a multiple of π:

$$\ell = n\frac{\lambda}{2} \qquad \text{or} \qquad \theta_n = \beta_n \ell = \left(\frac{2\pi}{\lambda}\right) \cdot \left(\frac{n\lambda}{2}\right) = n\pi \tag{2.46a}$$

with

$$n = +1, +2, \ldots, +\infty. \tag{2.46b}$$

as illustrated in Fig. 2.41

These resonance frequencies can be obtained by sampling the dispersion diagram $\beta(\omega)$ with a sampling rate of π/ℓ. In the case of a conventional (RH) resonator (Fig. 2.41.a) all the resonances have a positive index and they are harmonics of the fundamental frequency ω_1, that is $\omega_n = n\omega_1$. This is due to the positive and linear behaviour of the RH dispersion diagram (Section 2.3.1).

On the other hand, CRLH structures have an exotic dispersion diagram, as explained in Section 2.3.1. In particular, a CRLH TL has $\beta < 0$ in the LH region, $\beta = 0$ and $\beta > 0$ in the RH passband. Therefore, the electrical length θ can be zero and negative, which means that the resonance index n becomes symmetrically defined around $n = 0$:

$$\ell = |n|\frac{\lambda}{2} \qquad \text{or} \qquad \theta_n = \beta_n \ell = \left(\frac{2\pi}{\lambda}\right) \cdot \left(\frac{n\lambda}{2}\right) = n\pi \tag{2.47}$$

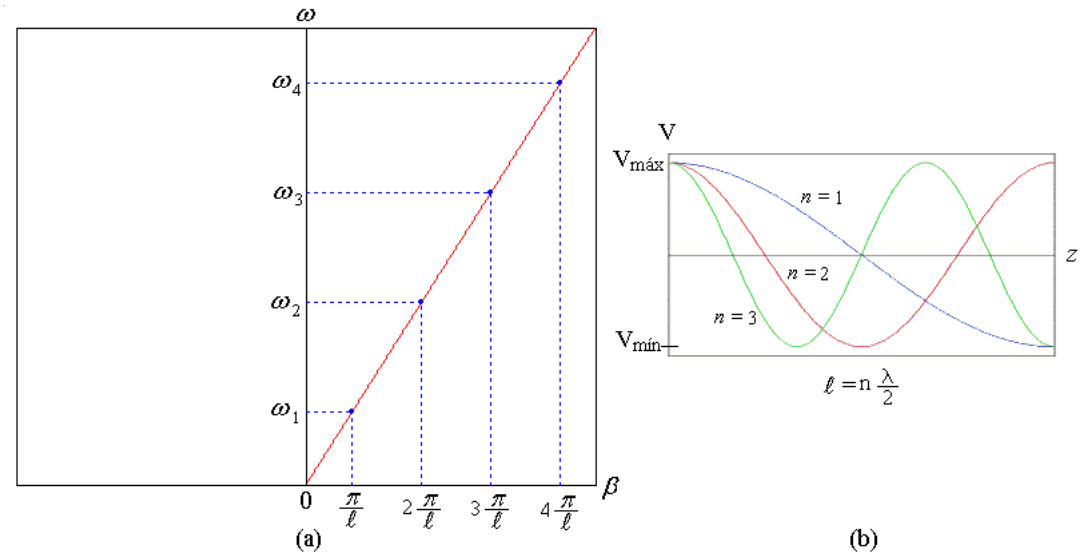

Figure 2.41: Conventional (RH) resonator. (a) Dispersion diagram and resonance frequencies ω_n. (b) Voltage distributions for the different modes of the open-ended RH resonator.

with $\beta(\omega)$ given by (2.27). Therefore, when this dispersion diagram is sampled at the rate π/ℓ to obtain the resonance frequencies it must be taken into account that the CRLH structure is composed of N unit cells with period p. Hence, the total length of the structure is $\ell = Np$ which divides the Brillouin zone into N regions of width π/ℓ on each side of axis $\beta = 0$ (Fig. 2.42). Thus, there are $N-1$ positive resonances and $N-1$ negative resonances plus the resonance with index $n = 0$, which represents a total of $2N-1$ resonances. It should be noted that the frequencies located at the edges of the Brillouin zone ($\beta p/\pi = 1$) are not additional resonance frequencies because they correspond to Bragg frequencies where the unit cell is resonating instead of the total structure. In summary, for a CRLH resonator composed of N unit cells the following resonance indices are obtained:

$$n = 0, \pm 1, \pm 2, \ldots, \pm(N-1) \tag{2.48}$$

It is important to identify what is the resonance frequency of the mode with $n = 0$. In the case of the open-ended resonator, the $n = 0$ resonance frequency is given by

$$\omega_{n=0}^{open} = \omega_{sh} = \frac{1}{\sqrt{L_L C_R}} \tag{2.49}$$

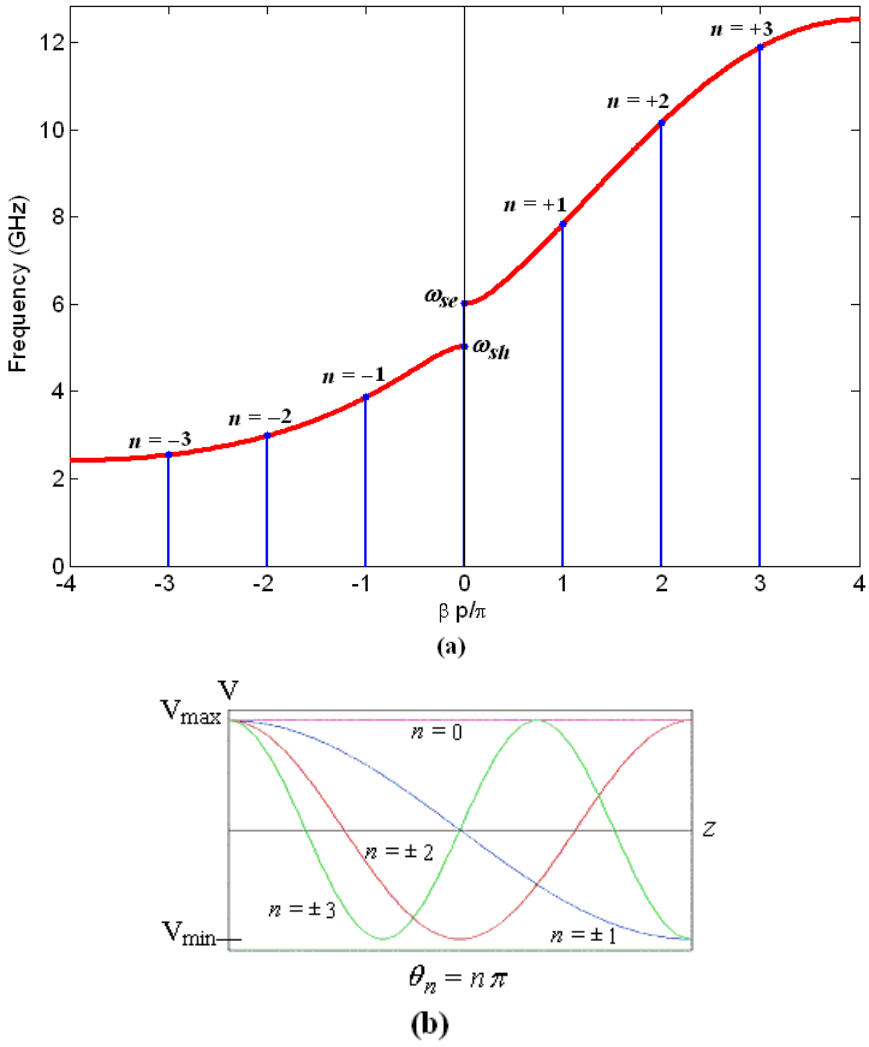

Figure 2.42: (a) Dispersion relation and resonance frequencies of a CRLH resonator composed of $N = 4$ unit cells. Parameters of the unit cell: $L_R = 1$ nH, $C_R = 1$ pF, $L_L = 1$ nH y $C_L = 0.7$ pF. (b) Voltage distributions of the resonance modes (open-ended resonator).

while at ω_{se} no resonance occurs. On the other hand, the resonance frequency of the $n = 0$ mode for the short-circuited resonator is

$$\omega_{n=0}^{short} = \omega_{se} = \frac{1}{\sqrt{L_R C_L}} \tag{2.50}$$

and no resonance occurs at ω_{sh}. For the particular case of balanced CRLH resonators, the resonance frequency for the $n = 0$ mode is independent of the open-ended or short-ended termination because $\omega_0 = \omega_{se} = \omega_{sh}$.

It is important to note that the resonance frequency of the $n = 0$ mode only depends on the equivalent circuit parameters of the unit cell and not on the physical dimensions of the resonator. This suggests that there is not limitation in size and the resonators can be made arbitrarily small. However, it must be taken into account the technological limitations to achieve arbitrary values of the LC elements which compose the unit cells.

In summary, CRLH resonators provide several additional features in comparison with conventional resonators:

- Additional resonances with negative ($n < 0$) and zero ($n = 0$) indices are obtained. Particularly, for a CRLH resonator composed of N unit cells, the following modes are obtained: $n = -N + 1, -N + 2, \ldots, 0, +1, +2, \ldots, N - 1$.
- Each positive mode ($+n$) has a corresponding mode with the opposite sign ($-n$). Both modes have similar field distributions.
- The resonant frequencies are not in harmonic ratios ($\omega_n \neq \omega_{-1}/n$ for $n < 0$ and $\omega_n \neq n\omega_{+1}$ for $n > 0$).
- The $n = 0$ has a uniform electric field distribution, which cannot be obtained with conventional resonators. Moreover, this mode is not related to the total physical length of the structure, but to the equivalent circuit elements of the unit cell, which suggests that it can be used to realize, theoretically, arbitrarily small resonators. In practice, this will be limited by the technology used to implement the resonator.

2.5 Low-Cost Approach Based on an Eigenfrequency Method to Obtain the Dispersion Diagram in CRLH Structures

The working frequencies of the applications based on CRLH resonators are computed by sampling the dispersion diagram of the CRLH cell. Moreover,

the equivalent circuit parameters of distributed CRLH cells are typically obtained from the dispersion diagram and the Bloch impedance. Thus, the dispersion diagram is a fundamental tool to analyse and design antennas and microwave circuits based on CRLH TLs and resonators.

The conventional approach to obtain the dispersion diagram of CRLH structures and extract their equivalent circuit parameters is the following [52]:

1. Develop the equivalent circuit model for the structure under study.
2. Apply the Bloch-Floquet periodic boundary condition and compute the dispersion relation by solving the eigenvalue problem.
3. Compute the dispersion diagram and Bloch impedance by full-wave analysis where a structure composed of an infinite number of cells or equivalently a cell with periodic boundary conditions is considered.
4. Extract the equivalent circuit parameters from the results obtained in the previous step.

As it is commented above, this dispersion diagram has traditionally been computed by full-wave analysis of the infinite CRLH structure, which consumes a great amount of time. Moreover, there is no possibility of computing the dispersion diagram from the simulation or measurement of a device based on CRLH cells. For that reason, a novel method based on the eigenfrequencies of a CRLH resonator composed of a finite number of cells is proposed [58]. The proposed method can be used to analyse or design CRLH structures. This approach drastically reduces the total computation time to obtain the CRLH unit cell dispersion diagram. In addition it makes easier the design of microwave circuits or antennas based on CRLH TLs and resonators.

The dispersion diagram of a CRLH structure, equation 2.27, is a function of four angular frequencies: ω_R, ω_L, ω_{sh}, ω_{se}. As explained in Section 2.4, an open-ended or short-circuited CRLH TL composed of a finite number of unit cells (N) is a resonant structure. All the eigenfrequencies satisfy the resonant condition:

$$\theta_n = \beta_n \ell = n\pi \tag{2.51}$$

where ℓ is the total length of the TL and n is the resonant index. If the CRLH TL is composed of N unit-cells ($\ell = Np$), the eigenfrequencies can be computed from (2.27) and (2.51) as

$$\frac{n\pi}{N} = \cos^{-1}\left\{1 - \frac{1}{2}\left[\frac{\omega_L^2}{\omega_n^2} + \frac{\omega_n^2}{\omega_R^2} - \left(\frac{\omega_L^2}{\omega_{se}^2} + \frac{\omega_L^2}{\omega_{sh}^2}\right)\right]\right\} \tag{2.52a}$$

$$n = 0, \pm 1, \pm 2, \ldots, \pm(N-1). \tag{2.52b}$$

Considering a pair of resonant frequencies $\omega_{\pm n}$, the resonant condition (2.52) for both frequencies is

$$\begin{cases} \dfrac{n\pi}{N} = \cos^{-1}\left[1 - \dfrac{1}{2}\left(\dfrac{\omega_L^2}{\omega_{+n}^2} + \dfrac{\omega_{+n}^2}{\omega_R^2} - \dfrac{\omega_L^2}{\omega_{se}^2} - \dfrac{\omega_L^2}{\omega_{sh}^2}\right)\right] \\ \dfrac{-n\pi}{N} = \cos^{-1}\left[1 - \dfrac{1}{2}\left(\dfrac{\omega_L^2}{\omega_{-n}^2} + \dfrac{\omega_{-n}^2}{\omega_R^2} - \dfrac{\omega_L^2}{\omega_{se}^2} - \dfrac{\omega_L^2}{\omega_{sh}^2}\right)\right] \end{cases} \tag{2.53}$$

where the positive sign in the index is used for the mode in the RH region ($+n$) and the negative index ($-n$) is the corresponding one in the LH region, and n is any possible index. The relation (2.53) can be rewritten as

$$\begin{cases} \dfrac{\omega_L^2}{\omega_{+n}^2} + \dfrac{\omega_{+n}^2}{\omega_R^2} - \dfrac{\omega_L^2}{\omega_{se}^2} - \dfrac{\omega_L^2}{\omega_{sh}^2} = 2\left[1 - \cos\left(\dfrac{n\pi}{N}\right)\right] \\ \dfrac{\omega_L^2}{\omega_{-n}^2} + \dfrac{\omega_{-n}^2}{\omega_R^2} - \dfrac{\omega_L^2}{\omega_{se}^2} - \dfrac{\omega_L^2}{\omega_{sh}^2} = 2\left[1 - \cos\left(\dfrac{-n\pi}{N}\right)\right]. \end{cases} \tag{2.54}$$

As the cosine function is an even function [$\cos(x) = \cos(-x)$], it can be obtained that

$$\frac{\omega_L^2}{\omega_{+n}^2} + \frac{\omega_{+n}^2}{\omega_R^2} = \frac{\omega_L^2}{\omega_{-n}^2} + \frac{\omega_{-n}^2}{\omega_R^2}. \tag{2.55}$$

Therefore, all the eigenfrequencies of the structure are related by

$$\omega_L \omega_R = \omega_{+n}\omega_{-n} = \omega_{se}\omega_{sh}. \tag{2.56}$$

As commented before, the expression of the dispersion diagram (2.27) depends on four unknowns: ω_L, ω_R, ω_{se} and ω_{sh}. Actually, it only depends on three of them, because one of these eigenfrequencies can be obtained from the rest (2.56). The proposed method consists of computing these unknowns from three known eigenfrequencies: ω_0 and $\omega_{\pm n}$. Thus, by solving (2.52) and (2.56) simultaneously, the unknowns ω_R and ω_L can be computed as

$$\omega_R^2 = \frac{\left(\omega_{-n}^2 + \omega_{+n}^2 - \omega_{se}^2 - \omega_{sh}^2\right)}{2\left[1 - \cos\left(\dfrac{n\pi}{N}\right)\right]} \tag{2.57a}$$

$$\omega_L^2 = \frac{2\left[1-\cos\left(\frac{n\pi}{N}\right)\right]}{\frac{1}{\omega_{-n}^2}+\frac{1}{\omega_{+n}^2}-\frac{1}{\omega_{se}^2}-\frac{1}{\omega_{sh}^2}} \tag{2.57b}$$

The previous equations still depend on the unknowns ω_{se} and ω_{sh}. These eigenfrequencies denote the resonance frequency of the $n = 0$ mode for the short-ended and open-ended boundary conditions, respectively (Section 2.4). If we solve (2.52) for the $n = 0$ mode, it results the following bi-quadratic equation in ω_0^2:

$$\frac{\omega_L^2}{\omega_0^2}+\frac{\omega_0^2}{\omega_R^2}=\frac{\omega_{sh}^2}{\omega_R^2}+\frac{\omega_{se}^2}{\omega_R^2} \tag{2.58}$$

This equation has two solutions for ω_0^2, one for the open-ended boundary condition:

$$\omega_0^2 = \omega_{sh}^2 \tag{2.59}$$

and the other one for the short-ended boundary condition:

$$\omega_0^2 = \omega_{se}^2 \tag{2.60}$$

Considering these solutions and the relation (2.56), the unknowns ω_{se} and ω_{sh} can be directly computed from the three known eigenfrequencies as:

$$\omega_{sh} = \omega_0 \quad \text{and} \quad \omega_{se} = \frac{\omega_{+n}\omega_{-n}}{\omega_0} \qquad \text{(Open-ended resonator)} \tag{2.61a}$$

$$\omega_{se} = \omega_0 \quad \text{and} \quad \omega_{sh} = \frac{\omega_{+n}\omega_{-n}}{\omega_0} \qquad \text{(Short-ended resonator)} \tag{2.61b}$$

Finally, ω_R and ω_L can be computed as a function of the three known eigenfrequencies ($\omega_{\pm n}$ and ω_0) using the following expressions

$$\omega_R^2 = \frac{\left(\omega_{-n}^2+\omega_{+n}^2-\omega_0^2-\frac{\omega_{+n}^2\omega_{-n}^2}{\omega_0^2}\right)}{2\left[1-\cos\left(\frac{n\pi}{N}\right)\right]} \tag{2.62a}$$

$$\omega_L = \frac{\omega_{+n}\omega_{-n}}{\omega_R}. \tag{2.62b}$$

Thus, the proposed approach can be summarized as follows:

1. Consider a CRLH resonator composed of a finite number of unit cells N. Obtain the following resonance frequencies: ω_0 and $\omega_{\pm n}$, where n is any possible index: $n = 1, 2, \ldots, N-1$. These frequencies can be obtained from different ways: $[S]$ parameters extraction of the resonator or modal analysis of the structure. Both methods can be applied when the resonator is simulated. The first one is used when we want to characterized a manufactured device.

2. Use the formulas (2.61) to compute the unknowns ω_{se} and ω_{sh}, considering the boundary conditions.

3. Compute ω_R and ω_L from (2.62).

4. The dispersion diagram can now be computed using the expression (2.27). This tool can be used to analyse the proposed CRLH structure. If the objective is the design of new applications based on the same CRLH cells they can be easily designed from the obtained diagram, even a different number of unit cells are needed. This is because the dispersion diagram is inherent to the unit cell and not to the number of cells which compose the CRLH resonator.

Once the unknowns of the dispersion diagram (ω_{se}, ω_{sh}, ω_R and ω_L) are computed, the circuit parameters can be easily extracted. In order to extract the four equivalent circuit parameters (L_R, C_L, L_L and C_R) it is also necessary to know one of them or the Bloch impedance [52]. For any given distributed CRLH structure, it is easy to estimate, at least, one of the parameters and then compute the other ones from the unknowns of the dispersion diagram. For example, in the mushroom structure presented in Section 2.3.1, the LH inductance L_L can be easily estimated from the closed expression of the inductance provided by a metallic via [59]. Then, the other parameters are estimated as follows:

$$C_L = \frac{1}{\omega_L^2 L_L} \tag{2.63a}$$

$$C_R = \frac{1}{\omega_{sh}^2 L_L} \tag{2.63b}$$

$$L_R = \frac{1}{\omega_{se}^2 C_L} \tag{2.63c}$$

To show the validity of the proposed approach the dispersion diagram of a CRLH structure is computed. The CRLH structure under study has a

mushroom-type cell with parameters $a = 7.00$ mm, $b = 15.00$ mm, $gap = 0.20$ mm and vias radius = 0.35 mm, according to Fig. 2.43. The substrate is FR-4 ($\varepsilon_r = 4.5$ and $\tan\delta = 0.01$) with height $h = 1.50$ mm.

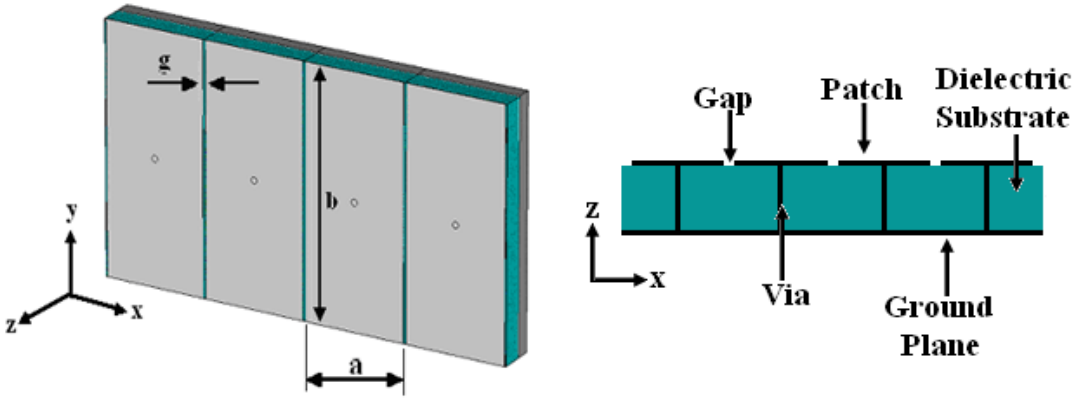

Figure 2.43: Open-ended CRLH resonator composed of $N = 4$ mushroom cells.

The first step consists of considering a resonator composed of a finite number of unit cells. Fig. 2.43 shows the final configuration, which is based on $N = 4$ unit cells placed along the x direction. The modal solver of CST Microwave Studio ® with the proper boundary conditions (open-ended in this case) is used to obtain a modal analysis of the resonator. Fig. 2.44 shows the transversal electric field (E_z) distributions computed for each of the $2N - 1 = 7$ eigenmodes of the resonator. The computed eigenfrequencies of the structure are shown in Table 2.1. The separation between the resonance frequencies in the LH region is smaller than in the RH one. This is because the slope in the LH region of the dispersion diagram is much smaller than in the RH one. This is the usual behaviour of CRLH TLs and resonators, as it was explained in Sections 2.3.1 and 2.4.

In order to compute the dispersion diagram with the proposed approach, the following values are used: $f_{-2} = \omega_{-2}/2\pi = 2.55$ GHz, $f_0 = 3.13$ GHz and $f_{+2} = 7.59$ GHz. The unknowns f_{se}, f_{sh}, f_R and f_L are computed using the the equations (2.61)-(2.62), resulting $f_{sh} = 3.13$ GHz, $f_{se} = 6.18$ GHz, $f_R = 2.84$ GHz and $f_L = 6.83$ GHz. Finally, the dispersion diagram is computed by using these values in the dispersion relation (2.27). The resulting dispersion diagram is plotted in Fig. 2.45 (blue line).

The accuracy of the obtained dispersion diagram is checked by comparing with the dispersion diagram computed by full-wave simulation of the CRLH

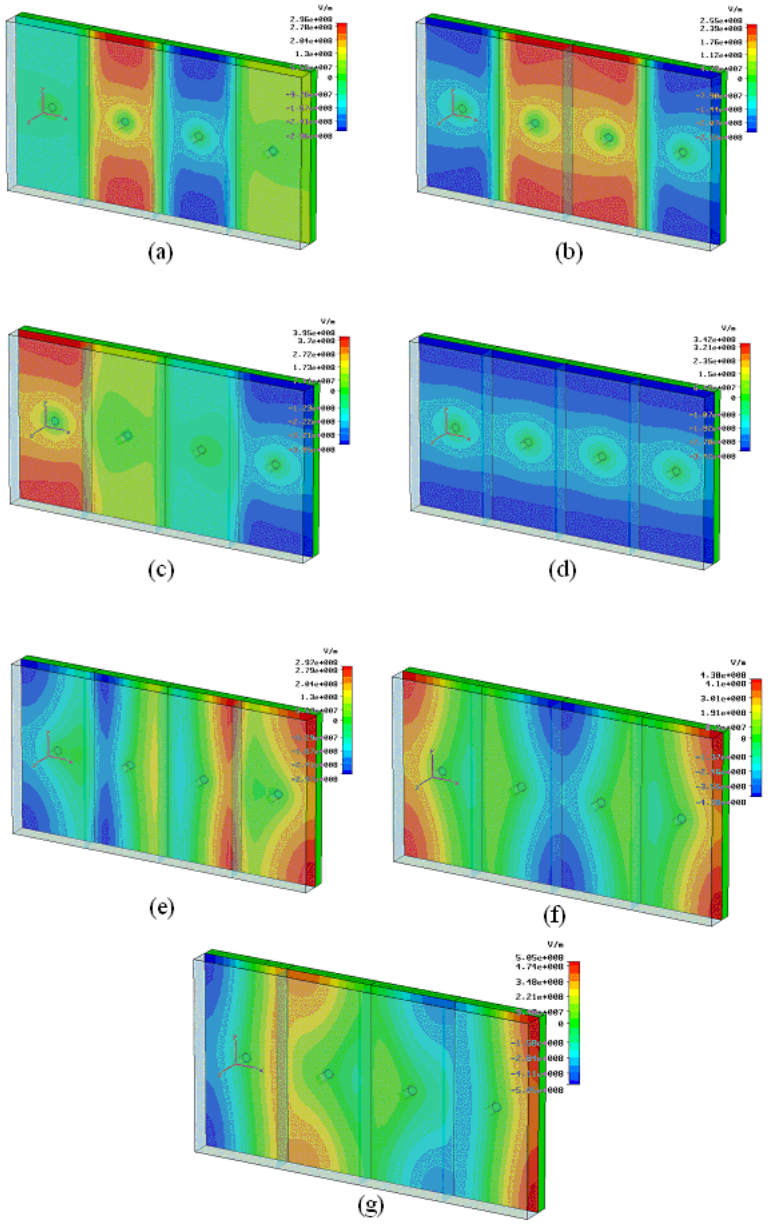

Figure 2.44: E_z field distributions for each of the modes of the four-cell CRLH resonator. (a) $n = -3$. (b) $n = -2$. (c) $n = -1$. (d) $n = 0$. (e) $n = +1$. (f) $n = +2$. (g) $n = +3$.

n	f_n
-3	2.33 GHz
-2	2.50 GHz
-1	2.90 GHz
0	3.13 GHz
$+1$	6.25 GHz
$+2$	7.59 GHz
$+3$	9.13 GHz

Table 2.1: Eigenfrequencies of the resonator computed by the modal solver.

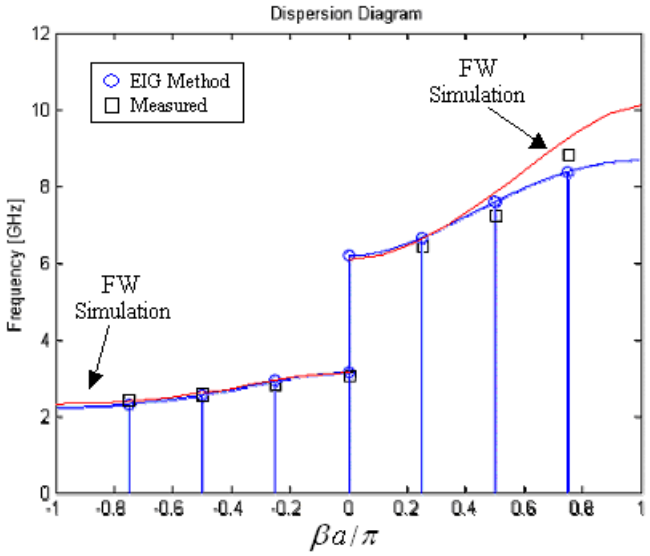

Figure 2.45: Dispersion diagram of the CRLH unit cell computed using the eigenfrequencies method (blue line). The dispersion diagram obtained by the conventional approach is also plotted (red line). The resonance frequencies obtained with each method are plotted with dots (conventional approach) and circles (EIGs). The measured resonance frequencies are plotted with squares.

unit cell considering periodic boundary conditions. The obtained dispersion diagram is plotted in Fig. 2.45 (red line). There is an excellent agreement between the two different approaches in the LH region. The resulting dispersion diagrams are also very close in the RH region, except for very high frequencies. The most important difference between both approaches is the computation time. The total computation time to extract the eigenfrequencies of a finite resonator with the modal solver is only a few minutes while the time to compute the dispersion diagram considering the periodic structure is several hours. It has been estimated that more than 90% computation time is saved by the proposed approach with respect to the conventional approach.

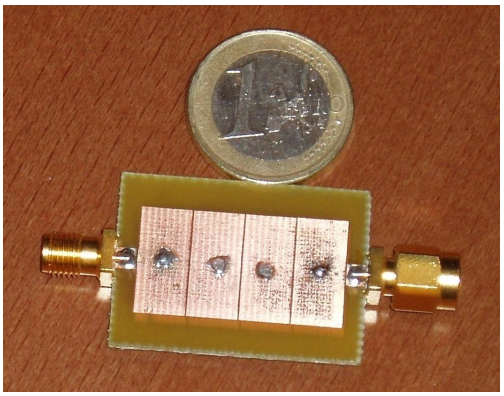

Figure 2.46: Picture of the manufactured CRLH resonator prototype.

A prototype has been manufactured and measured in order to show the accuracy of the approach for designing new devices. The geometry is maintained (a four-cell CRLH open-ended resonator) as it is shown in Fig. 2.46. The structure is ended by two microstrip ports coupled to the resonator by 0.20-mm gaps in order to measure the resonance frequencies. The results are summarized in Table 2.2. The resonance frequencies given by the proposed and conventional methods (first and second columns) are computed by sampling the dispersion diagram obtained with each method. According to (2.51), the sampling rate for the normalized dispersion diagram ($\beta_n p/\pi$) is $1/N = 1/4$. The computed resonance frequencies are plotted in Fig. 2.45 with dots for the conventional approach and circles for the proposed method. The measured resonance frequencies of the prototype are plotted with squares. The third column of Table 2.2 shows the measured resonance frequencies of the prototype and the fourth and fifth columns give the relative error committed by both methods with respect to the measured results. There is a good agreement between the resonance frequencies of the prototype and the val-

ues obtained by the proposed method. Measurements show that the relative error made by eigenfrequencies method is comparable to the one obtained with the conventional approach and it is smaller than 5% and thus, provides a good accuracy.

n	f_n(EIGs)	f_n(Conv.)	f_n(Measured)	E_r(EIGs)	E_r(Conv.)
-3	2.31 GHz	2.33 GHz	2.45 GHz	5.7%	4.9%
-2	2.55 GHz	2.55 GHz	2.59 GHz	1.5%	1.5%
-1	2.91 GHz	2.90 GHz	2.83 GHz	2.8%	2.5%
0	3.13 GHz	3.13 GHz	3.07 GHz	1.9%	1.9%
$+1$	6.25 GHz	6.25 GHz	6.44 GHz	2.9%	2.9%
$+2$	7.59 GHz	7.82 GHz	7.24 GHz	4.8%	8.0%
$+3$	8.38 GHz	9.23 GHz	8.81 GHz	4.9%	4.8%

Table 2.2: Resonance frequencies obtained with the eigenfrequencies method (EIGs), the conventional method (Conv.) and the measured prototype. The last two columns show the relative error of each method with respect to the measured resonance frequencies.

2.6 State of the Art of the Application of Metamaterial Structures to Antenna Engineering

2.6.1 Enhanced Leaky-Wave Antennas

A leaky wave is a travelling wave progressively leaking out power as it propagates along a waveguiding structure. Leaky-wave (LW) structures support one or several leaky waves. They are typically used as antennas, where the leakage phenomenon is generally associated with high directivity. LW antennas are fundamentally different from resonating antennas, in the sense that they are based on a travelling-wave as opposed to a resonating-wave mechanism. Therefore, their size is not related to the operation frequency, but to directivity. Leaky waves are fast-wave modes which means that the phase velocity is faster than the velocity of light ($v_p > c$) or equivalently $\beta < k_0$ where β is the propagation constant along the LW structure and $k_0 = \omega/c$ is the

free space wavenumber. Thus, LW antennas are structures whose dispersion diagram $\omega(\beta)$ penetrates into the radiation region or radiation cone where the condition $\beta < k_0$ (or $\omega > \beta c$) is satisfied. Moreover, the propagation constant determines the angle of radiation of the main beam (θ_{MB}) following the simple relation

$$\theta_{MB} = \sin^{-1}\left[\frac{\beta}{k_0}\right]. \tag{2.64}$$

Conventional LW antennas are uniform or periodic structures. In the first case, only the dominant mode of the structure propagates and thus this mode is a fast wave to achieve radiation. As the propagation constant is positive in these structures ($\beta > 0$) only forward angles can be obtained according to equation (2.64). In addition, broadside radiation cannot be achieved since it requires the condition $\beta = 0$. In the second case, which is periodic LW structures, the wave can be expanded as the superposition of an infinite number of space harmonics. In contrast to uniform LW antennas, periodic LW structures have a slow-wave/guided dominant mode and their radiation can therefore be obtained only from the contribution of one or several fast-wave space harmonics to the total field. In this case, backward radiation ($\theta_{MB} < 0$) can be achieved by using a negative space harmonic in addition to forward radiation using a positive space harmonic. However, broadside radiation cannot be achieved with this type of LW antennas because of the presence of a gap at $\beta = 0$. Moreover, these periodic LW antennas require complex and low efficient feeding schemes to operate at higher order modes. On the other hand, CRLH structures can be used to achieve LW antennas with continuous backward, broadside and forward radiations. Furthermore, CRLH LW antennas work at its fundamental mode and thus, they can be fed by a very simple and efficient mechanism, such as a simple TL. This application of metamaterial structure was developed almost at the same time by the groups of the University of Toronto (Eleftheriades' group) [49] and UCLA (Caloz and Itoh's group) [60].

UCLA group developed a LW antenna with continuous backfire-to-endfire frequency-scanning capability based on a balanced CRLH TL optimally matched to the air impedance [60]. This CRLH structure was the microstrip implementation presented in Section 2.3.1 (Fig. 2.16) terminated with a matched load to eliminate reflections which would otherwise produce spurious beams. For this antenna working at its fundamental mode, the main beam θ_{MB} was able to take values from -90 (backfire) to $+90$ (endfire), since $|\beta| < k_0$ for a continuous frequency range, as seen in Fig. 2.47.a. Fig. 2.47.b depicts the scanning operation of the CRLH LW antenna. By operating the CRLH LW

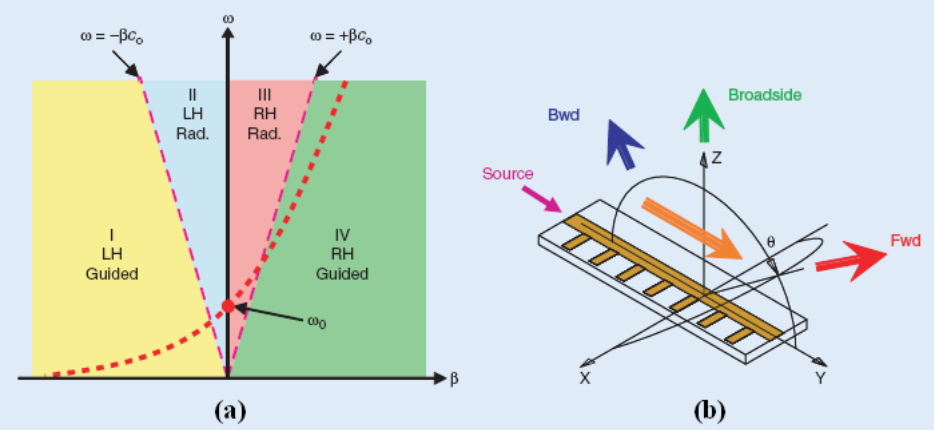

Figure 2.47: CRLH LW Antenna. (a) Typical dispersion diagram showing guided and radiation regions. (b) Scanning operation. Figure extracted from [61].

antenna below or above its transition frequency ω_0, forward and backward scanning was achieved. Referring to Fig. 2.47, the antenna radiated backward in Region II (LH), and the antenna radiated forward in Region III (RH). At ω_0, the antenna was able to radiate broadside because $v_g \neq 0$ at $\beta = 0$ for the balanced CRLH TL. Continuous backfire-to-endfire scanning was achieved from 3.1 to 6.0 GHz with this implementation. The scanning angle of the CRLH LW antennas, as well as the conventional ones, depend on the operation frequency. In [62] the same group proposed the use of varactor diodes instead of series and shunt capacitors to implement each CRLH unit cell. In this case, the dispersion diagram was controlled by the voltages applied to the unit cells. Thus, the scanning angle was then controlled by the biasing voltages. The antenna was implemented with 30 unit cells and worked at 3.3 GHz. A scanning range of $[+50°, -50°]$ was obtained experimentally with a maximum gain of 18 dB at broadside. Moreover, the cells were biased independently achieving a beamwidth-controllable LW antenna. Experimental results showed that the Half Power Beamwidth was increased from 43% to 200% compared to the uniformed biased case.

The same research group proposed the use of the previous LW antennas to develop novel reflecto-directive systems. In [63] a reflecto-directive system was proposed by combining a frequency-scanned CRLH LW antenna and heterodyne mixing. This system was able to receive an incident signal at any angle and reflect it at any arbitrary angle by tuning the local oscillator frequency. Fixed-frequency scanning was achieved by using the electronically

controlled CRLH LW antenna in place of the frequency-scanned CRLH LW antenna [24].

The University of Toronto group developed a LW antenna with backward radiation in CPW technology [49, 50]. The structure used was reviewed in Section 2.3.1. This antenna also radiated in its fundamental spatial harmonic. Recently, this group has proposed an implementation based on CPS technology [51]. The sketch of this structure was presented in Section 2.3.1 and its unit cell is depicted in Fig. 2.19. As commented before, LW structures present a different radiation angle at different frequencies, which is not desirable in communication applications. This CRLH CPS LW antenna was developed to achieve a reduced *beam squinting* (the angular variation of the main radiated beam with frequency) over a broad bandwidth which cannot be achieved with other low-profile antennas. In [51] it was shown that by operating the LW antenna in the upper right-handed band where the phase and group velocities are closest to the speed of light, the beam squinting that the antenna experiences can be minimized. This 20−element CRLH CPS LW antenna produced a radiated beam at an angle of $\theta_{MB} = +45$ at 5 GHz and exhibits a measured return-loss bandwidth below −10 dB of 0.91 GHz (18.2%), and an average beam squint of 0.031°/MHz.

An approach similar to the one used in printed technologies was proposed by S. Hrabar and G. Jankovic (University of Zagreb) in waveguide technology [64]. In this work, a waveguide was filled with an uniaxial ENG TW structure, achieving three different modes of propagation: the backward-wave mode, the mode with zero propagation constant (but with non-zero group velocity) and the forward-wave mode. An slot was realized in the waveguide to operate as a LW antenna with backward-to-forward scanning capability. The developed antenna worked in the 10 GHz band with a scanning angle of ±60° from broadside for the slotted waveguide with six unit cells.

Finally, the group of Universidad de Málaga and C. Caloz collaborated in [65] to develop an active CRLH LW antenna. This antenna was designed to operate at broadside and was constituted by passive CRLH microstrip LW sections (similar to the ones described above) interconnected by amplifiers, which regenerated the power progressively leaked out of the structure in the radiation process in order to increase the effective aperture of the antenna and thereby its gain. The gain was further enhanced by a matching regeneration effect induced by the quasi-unilateral nature of the amplifiers. The quasi-uniform and binomial field distribution cases, corresponding to maximum directivity and minimum side-lobe level, respectively, were described. An active LWA prototype was demonstrated in transmission mode with a gain enhancement of 8.9 dB compared to its passive counterpart.

2.6.2 Superstrates for Antenna Applications

As commented in the Introduction (Chapter 1), printed antennas are very interesting due to their characteristics, but they present relatively low gains (usually $G < 8$ dB) when used as single radiators. The use of cover layers over the printed antennas, *superstrates*, was proposed during the eighties to improve the gain of these antennas [66, 67, 68]. Nevertheless, these configurations require fairly thick layers leading to an overall thickness which could be incompatible with integrated circuit antenna applications in most cases. Besides, the BW varies inversely with gain and the efficiency of these structures is typically less than 60%.

More recently, several authors proposed the application of partially reflective surfaces (PRS), such as EBGs or Frequency Selective Surfaces (FSS), as superstrates in order to improve the antenna performance [69]. The EBG behaves as an aperture antenna and its effective aperture size becomes larger than that of the original feeding antenna, achieving aperture efficiencies close to 80%. Several proposals were developed following this approach, see for instance [70, 71, 72]. FSS based on the Fabry-Perot effect have also been proposed, e. g. [73, 74]. The drawback of thickness remains as distance between the ground plane of the printed antenna and the PRS is close to $\lambda/2$. More recent results proposed the use of either Artificial Magnetic Conductor (AMC) surfaces or metamaterial ground planes in combination with PRS to design low-profile high-gain planar antennas [75, 76]. The overall thickness of the configuration was reduced to $\lambda/6$ and the aperture efficiency rounded to 60%.

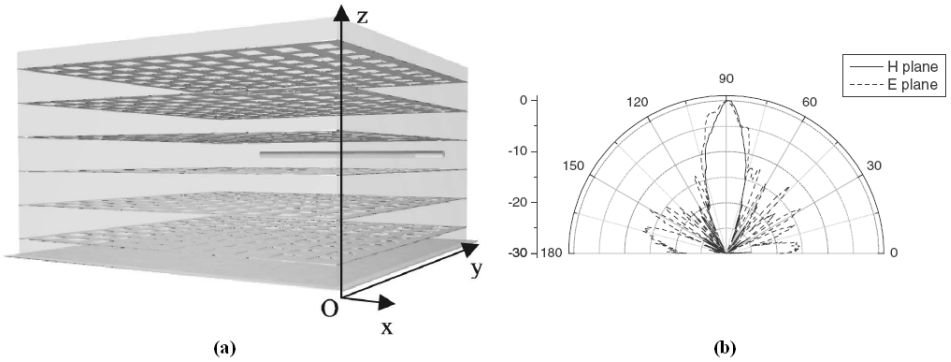

Figure 2.48: Monopole embedded in six layers of a Zero-n grid structure [77]. (a) Sketch of the structure. (b) Radiation pattern.

A pioneering study of Gupta [78] demonstrated that a metamaterial slab

made of TWs excited by a single source could produce a high directivity. A similar idea was proposed in [77]. In that work, the metamaterial structure was composed of metallic grids in a square lattice. Hence, this periodic grid was considered a 2-D TW structure. The operation principle takes into account that the permittivity of ENG metamaterials just above the plasma frequency (ω_p) is positive and less than one which makes that the refraction index is less than one, eventually very close to zero. For this reason, these structures working under this condition are known as *Zero-index* (Zero-n) metamaterials. In this case, all the rays emanating from a point source within such a slab of Zero-n material would refract, by Snell's law, almost parallel to the normal of every radiating aperture. This can be used to achieve antennas with very high directivity. In [77], six layers of this structure were excited by a monopole antenna situated in the middle of the layers (Fig. 2.48.a). This radiating device operated at 14.5 GHz and the measured directivity was over 25 dB with a cross-polarization level lower thant -20 dB with respect to the co-polar component. The directive radiation pattern is shown in Fig. 2.48.b.

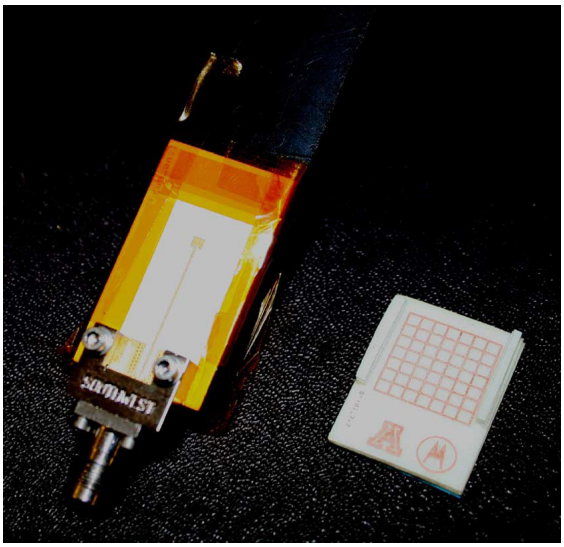

Figure 2.49: Picture of the manufactured microstrip patch antenna and a layer of the foam-based Zero-n grid structure for millimeter-wave frequencies [79].

Recently, Franson and Ziolkowski (University of Arizona) have employed these Zero-n grid structures as a superstrate of a microstrip patch antenna working at millimeter-wave frequencies (60 GHz band) [80, 79]. They have printed the grid structure on foam dielectric layers and they have studied dif-

ferent configurations (one to four layers over the microstrip patch antenna). Experimental results have showed an increase of the antenna gain from 5 dB to 11 dB. Moreover, they have demonstrated the usefulness of the proposed approach for real wireless data transfer in the millimeter-wave regime, verifying a proper 1.25-Gb/s data transfer over a 60-GHz wireless link between two computers [79]. A picture of the manufactured prototypes is shown in Fig. 2.49.

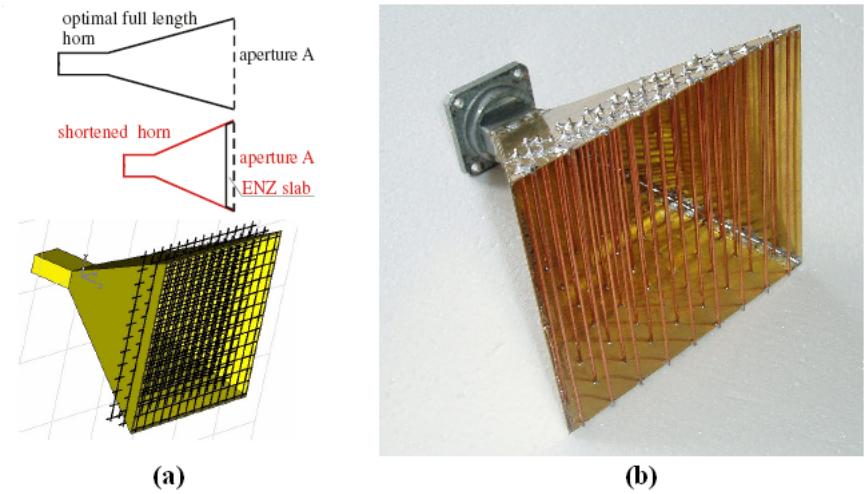

Figure 2.50: Miniaturized horn antennas with a TW structure in the aperture [81, 82, 83]. (a) Sketch and comparison with the conventional optimal horn. (b) Picture on a manufactured prototype.

These Zero-n structures can be applied to more applications, such as the miniaturization of horn antennas [81, 82, 83]. The group of Hrabar (University of Zagreb, Croatia) has embedded TW structures with Zero-n in the aperture of horn antennas, demonstrating that an important degree of miniaturization can be achieved. This approach is depicted in Fig. 2.50.a. For example, in [83] they presented two horn antennas with lengths of 52% and 33% of the length of the optimal horn. Measured gain was found to be very similar to the gain of the full length optimal horn (within 0.1 dB), but in a narrow band ($5\% - 12\%$). A picture of one of these horns is shown in Fig. 2.50.b.

The Antenna Group of Universidad Pública de Navarra (UPNA) developed, in collaboration with other research groups, bulk and planar *metasurfaces* for antenna applications [84, 85, 86, 87]. These metasurfaces are metamaterial resonant structures placed above (superstrates) or below (sub-

strates) a radiator to enhance its characteristics. The first implementation consisted of a bulk periodic structure whose unit cell was constituted by a dielectric slab in which four capacitively loaded strips (CLSs) and one SRR were embedded. This structure was used as a superstrate of a dipole antenna [84]. A sketch of this configuration is shown in Fig. 2.51.a. The key idea behind this configuration was to allow radiation from a primary source to spread over a larger radiating aperture. By tuning the dipole antenna to the pass-band frequency of the superstrate, an in-phase resonance of the unit cells yielded to a more uniform illumination of the superstrate. Hence, the radiating effective area was enlarged. The measured gain of the proposed configuration was approximately 4.5 dB with a measured radiation efficiency over 80%. The main drawback of the structure was that its thickness was approximately $\lambda_0/4$. This structure was also applied to a multifrequency configuration of a radiating element between other two working at another frequency. A high isolation between the elements (20 dB for a distance of $\lambda_0/4$) and low back radiation were achieved.

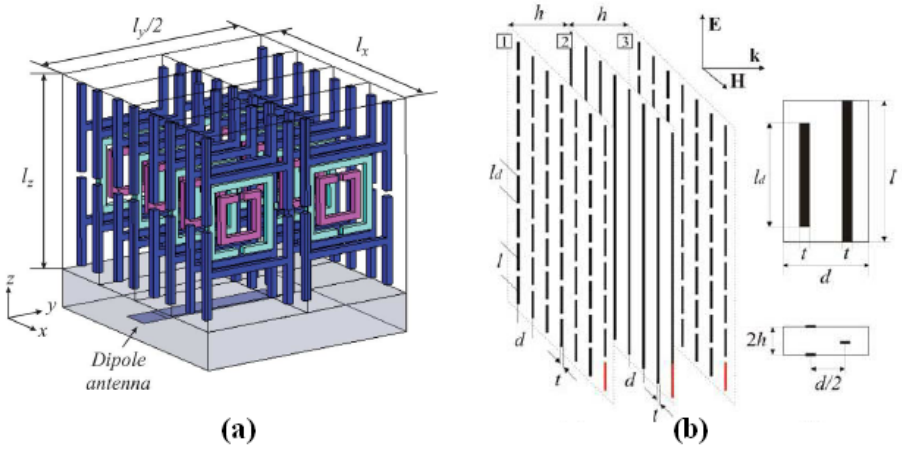

Figure 2.51: Metasurfaces proposed by the Antenna Group of UPNA [84, 85, 86, 87]. (a) Volumetric implementation based on SRRs and CLSs. Configuration of a dipole antenna with a 4×4 uniform superstrate. (b) Planar superstrate and its unit cell.

Then, they proposed the use of planar metasurfaces based on three layers of wires [85, 86]. The first and third layers consisted of parallel short dipoles, while the second grid consisted of continuous thin wires (Fig. 2.51.b). Under normally incident plane-wave excitation, at the resonant frequency, out-of-phase currents were induced in the pairing dipoles printed on the first and third layers. Because of the proximity of the dipoles, a closed loop was formed

which creates a strong magnetic dipole moment that produces radiation and a transmission window appeared. To widen the pass-band, a lattice of solid wires was placed in between the dipole lattices. Thanks to the in-phase oscillation of the metasurface inclusions a uniform illumination was obtained. A finite version of this planar metasurface was used as a superstrate of a printed dipole [86], achieving a measured gain of 6.8 dB, 82% aperture efficiency and low back radiation. The total thickness of this configuration was only $0.14\lambda_0$ achieving a very low profile. In [87], they proposed the use of this structure as the superstrate of an array of printed dipoles to reduce the mutual coupling between them. A reduction between 3 and 14 dB in the mutual coupling was achieved when using the superstrate over the array.

2.6.3 Small and/or Multifunction Resonant Antennas based on Metamaterials

Electrically small antennas are one of the most interesting topics in antenna engineering. Nevertheless, it is well known that an electrically small antenna, e. g. an small electric dipole, is an inefficient radiator because it has a very small radiation resistance while simultaneously having a very large reactance; hence, a large impedance mismatch to any realistic power source exists. Therefore, an external matching network that produces an impedance that is conjugately matched to the small antenna's impedance is used to increase the efficiency of the radiator [88]. Because of the very large reactance values involved, these matched resonant systems generally have very narrow bandwidths and high tolerance requirements for their fabrication. Moreover, the total size of the system is considerably enlarged and thus, it cannot be considered as electrically small. During the last years, the research group of Ziolkowski has proposed the use of metamaterial structures to achieve efficient electrically small antennas [89, 90, 91, 92].

Initially, they studied analytically and numerically the effect of surrounding an electrically small dipole antenna with a shell of DNG metamaterial [89]. In that case, the reactance of the antenna was considerably decreased and the shell acted as a natural matching network. They concluded that a properly designed dipole-DNG shell combination increases the real power radiated by more than an order of magnitude over the corresponding free space case. This study was extended in [90], where the so-called *metamaterial-based electrically small antennas* were proposed. In that work, they demonstrated that it is only necessary a negative permittivity shell to match a highly capacitive antennas (e. g. small dipoles). Three different systems were studied: an infinitesimal electric dipole, a very short center-fed cylindrical electric dipole

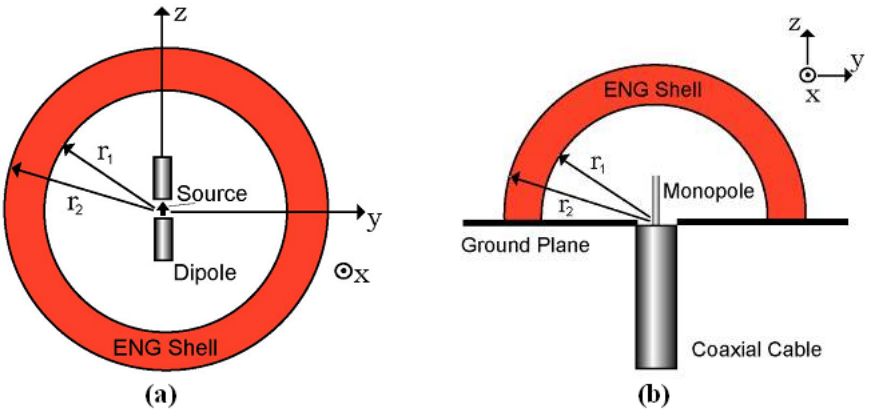

Figure 2.52: Metamaterial-based ellectrically small antennas [90]. (a) A very short center-fed cylindrical electric dipole with an ENG shell. (b) A very short coaxially-fed electric monopole over an infinite ground plane with an ENG shell.

(Fig. 2.52.a), and a very short coaxially-fed electric monopole over an infinite ground plane (Fig. 2.52.b). Analytical and numerical models demonstrated that a properly designed ENG shell provides a distributed inductive element resonantly matched to these highly capacitive electrically small antennas, and hence, an ENG shell can be designed to produce an electrically small system with a zero input reactance and an input resistance that is matched to a specified source resistance, leading to overall efficiencies approaching unity. Moreover, they also concluded that the dispersion and losses reduce significantly the bandwidth of the proposed antennas.

Recently, they have proposed some practical realizations called *metamaterial-inspired efficient electrically small antennas* or EZ antenna systems [91]. In these metamaterial-inspired antennas the conjugate matching is not achieved with a metamaterial shell but rather with a unit cell of a ENG, MNG, or DNG metamaterial structure. Planar 2-D and volumetric three-dimensional (3-D) versions of the electric and magnetic versions of these antennas were proposed, manufactured and measured in that work, showing a proper matching to a $50-\Omega$ impedance. The magnetic realizations were based on half loops surrounded by capacitive elements (an extruded 3-D capacitively-loaded loop in the three-dimensional system, and planar interdigitated or lumped-element capacitively-loaded loop elements in the planar versions) and coaxially-fed through a finite ground plane. The electric versions were composed of a electrically-small electric monopole antenna over a finite ground plane integrated with a 3-D cylindrical helix wire strip in the

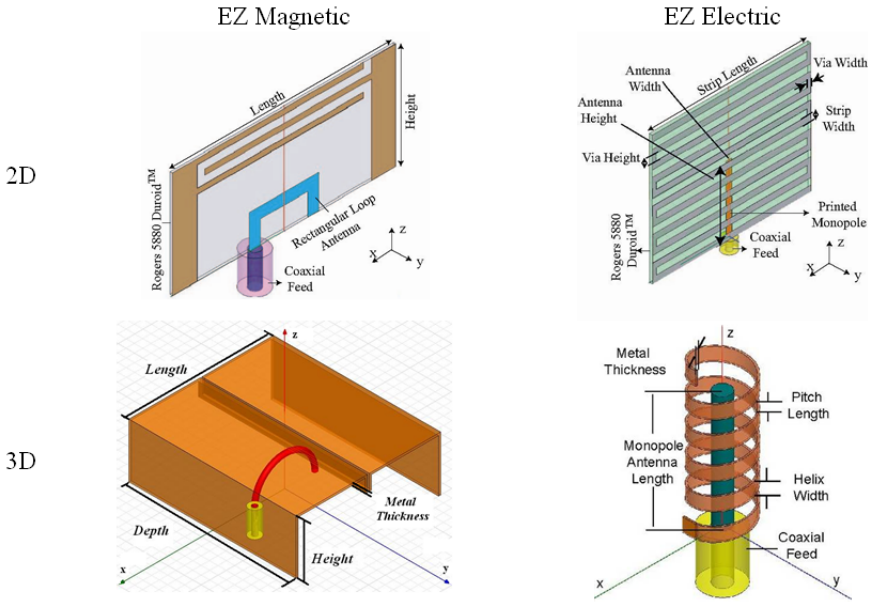

Figure 2.53: Metamaterial-inspired efficient electrically small antennas (EZ antenna systems) proposed in [91].

volumetric system and a 2-D meander-line in the planar structure. These EZ antennas are depicted in Fig. 2.53. Very high measured efficiency values were reported in that work ($> 90\%$). The main drawback of these antennas is their low bandwidth due to their high Q factor. Currently, they are working on developing efficient electrically small antennas with increased bandwidth by using near-field parasitic elements as an approach to reduce the Q factor [92]. The small Z, stub and canopy antennas are proposed in that work. Moreover, they explain their current research lines to achieve broader bandwidths. The first one consists of a metamaterial filling inside the canopy antenna. The other one, which seems promising, is based on active internal matching elements, probably implemented with Negative Impedance Converters.

Another interesting type of antennas are based on CRLH resonators. As explained in Section 2.4, the indices of the resonances present in these resonators can be negative ($n < 0$), zero ($n = 0$) and positive ($n > 0$). Moreover, the resonance frequencies depend on the unit cell elements and the number of cells, rather than the physical dimensions of the whole resonator. It is important to note the special case of the $n = 0$ mode whose resonance frequency only depends on the unit cell elements and not on the number of them. Initially, the group of Caloz and Itoh (UCLA) proposed the use of resonators

based on CRLH TLs in microstrip technology (Section 2.3.1, Figs. 2.16 and 2.17) to develop resonant antennas working at the $n = 0$ mode [93, 24]. They demonstrated that the resonance frequency only depends on the unit cell and showed that it is independent on the number of cells. This was used to obtain small resonant antennas in which about 75% footprint reduction was achieved in comparison with that of conventional $\lambda/2$ resonant antennas [93]. These antennas had a broadside radiation pattern which was more directive when more cells were used. This is clear since the frequency was unchanged while the physical length was enlarged. Hence, a higher miniaturization degree leaded to a less directive pattern. Moreover, a high degree of miniaturization meant a low efficiency and narrow bandwidth, as in all the electrically small antennas.

More recently, Caloz in collaboration with the group of the University of Duisburg-Essen have considered the same approach the other way around. As the resonance frequencies can be controlled by engineering the unit cells, they can be made electronically larger than conventional resonant antennas and thus high directivity values can be achieved [94, 95, 96]. For example, in [95, 96] zeroth-order CRLH resonant antennas with electrical length larger than $0.8\lambda_0$ were presented. A picture of one prototype is shown in Fig. 2.54.a. Furthermore, these authors also proposed the use of the half-wavelength modes ($n = \pm 1$) to achieve multifrequency and/or multifunction CRLH antennas [94, 96]. It is important to note that the efficiency of these modes was lower than in the case of the $n = 0$ mode because the field distributions were less uniform along the structure. Nevertheless, they had a broadside radiation pattern with a narrow beam in the longitudinal plane of the CRLH TL. An example of a dual-frequency CRLH resonant antenna working at the two half-wavelength modes ($n = \pm 1$) was presented in [96]. This antenna was composed of $N = 7$ CRLH unit cells based on interdigital capacitors and symmetric short-ended stubs in microstrip technology. The antenna operated at $f_{-1} = 2.23$ GHz and $f_{+1} = 3.19$ GHz with gains of 4.2 dB and 4.5 dB for f_{-1} and f_{+1}, respectively, and cross-polarization lower than -20 dB. The electrical length of the antenna was $0.56\lambda_0$ at f_{-1} and $0.80\lambda_0$ at f_{+1}. Multifunctionality was achieved with these structures by simultaneously using the $n = 0$ mode which is transversally-polarized and the half-wavelength modes $n = \pm 1$ which are longitudinally-polarized. For example, in [97] a tri-band and dual-polarized antenna based on this principle was presented. The antenna operated at $f_{-1} = 5.18$ GHz, $f_0 = 5.43$ GHz and $f_{+1} = 5.69$ GHz with a electrical length of $2.97\lambda_0$ at f_{-1}, $3.13\lambda_0$ at f_0 and $3.29\lambda_0$ at f_{+1}. The directivity of the antenna ws larger than 10.5 dBi at the three working frequencies.

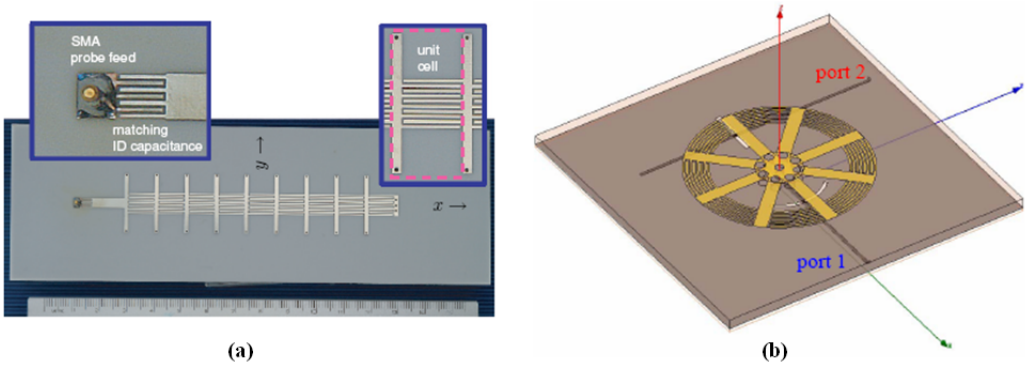

Figure 2.54: (a) Series mode zeroth-order resonantor antenna prototype fed via a matching network (interdigital capacitor connected to a 50 line) in order to transform the low input impedance of the antenna [95]. (b) Sketch of a CRLH loop antenna [98]. A radial slot and another azimuthal one are used to excite both modes corresponding to the $n = 0$ condition.

These groups have also proposed CRLH resonant antennas in loop configurations [99, 94, 96]. A CRLH loop structure is obtained by folding a rectilinear CRLH structure so as to form a closed circular loop. Then, the stubs are compactly placed in a radial manner within the loop area, with a unique shorting via at the center of the structure, as shown in Fig. 2.54.b. Due to the additional (compared to the rectilinear case) azimuthal boundary condition, such a CRLH structure supports only modes of even order, i.e., corresponding to loop circumferences that are multiples of the guided wavelength. Initially, these structures were proposed to work as multifunction antennas by using the $n = \pm 2$ modes simultaneously [99]. It was also possible to excite both modes with two orthogonal ports in quadrature obtaining circular polarization at the two bands [100]. Currently, they are using the structure to develop a dual-monopole antenna. This is possible because the CRLH resonator is not short-ended or open-ended in this case and thus, both resonance frequencies corresponding to the $n = 0$ condition, namely ω_{se} and ω_{sh} can be excited by using a radial and an azimuthal slot, respectively. This configuration was initially proposed in [98], where a balanced CRLH structure was used and thus both monopolar modes worked at the same frequency, each of them excited through a different port. The simulated isolation between both ports was 15 dB approximately.

Another type of CRLH resonant antennas are the miniaturized microstrip patch antennas. These antennas were firstly proposed by the group of the Technische Universität Darmstadt in 2004 [101]. The unit cell of these an-

tennas was the mushroom structure (Section 2.3.1). The miniaturized patch antennas were composed of a finite number of mushroom cells placed along one direction (1-D CRLH resonator). The metallizations of adjacent cells were overlapped to create a MIM capacitor and increase the series capacitance (C_L). The authors also proposed a cavity antenna based on two mushroom cells, which were short-ended at their opposite edges, and a radiating slot between them. These antennas worked at the $n = -1$ resonance mode in the LH region. In this region, the propagation constant increases as the frequency decreases, therefore, a small guided wavelength can be obtained at a lower frequency to provide the small $\lambda_g/2$ resonant length used to realize a compact antenna design. Furthermore, the physical size and the operational frequency of the antenna depend on the unit cell size and its equivalent circuit elements and thus, a miniaturized antenna can be achieved by designing the unit cell properly. The group of Darmstadt mainly studied the Q factor of these antennas [102].

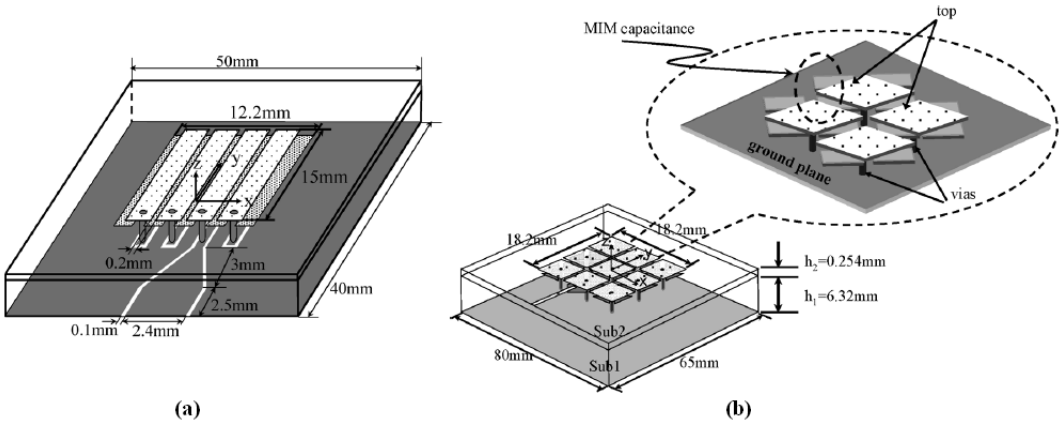

Figure 2.55: Miniaturized patch antennas based on CRLH structures proposed by Itoh's group [103, 104]. (a) 4×1 array of rectangular mushroom structures fed by a CPW line. (b) 3×4 arrangement of square mushrooms fed by a coupled microstrip line.

This approach was also proposed almost at the same time by the research group of Itoh (UCLA) [103, 104]. Their initial designs were also based on the mushroom structure with MIM capacitances between the adjacent cells, but using a rectangular technology and CPW stubs made in the ground plane which are connected in series with the shorting vias to increase the shunt inductance (L_L). This type of antenna is depicted in Fig. 2.55.a. A great degree of miniaturization was achieved by using this technology. For instance,

in [103] a four-cell antenna working at $f_{-1} = 1.06$ GHz was proposed. The length, width and height of the proposed antenna were $1/19\lambda_0$, $1/23\lambda_0$ and $1/83\lambda_0$, respectively. However, the efficiency of this antenna was very low which leads to a very poor gain (-13 dB). In order to improve these results, another configuration based on a 2-D array of square mushrooms with MIMs, such as the 2-D structure in Fig. 2.25, was proposed. In this case the feeding scheme was a microstrip line coupled to the patch with a small gap. An example of this implementation was presented in [104] and shown in Fig. 2.55.b. This prototype was based on a 3×3 mushroom array. The operation frequency was $f_{-1} = 1.17$ GHz and the electrical length of each side of the patch antenna was $1/14\lambda_0$ at this frequency. In this case the gain of the antenna was 0.6 dB. In that paper, the same design was applied for the development of a circularly polarized antenna operating at 2.46 GHz by using two orthogonal ports fed by a hybrid coupler. A 116° beamwidth with axial ratio better than 3 dB was observed. The electrical length of the patch side was $1/10\lambda_0$ at this frequency and the gain was increased up to 2.16 dB. In both cases, a patch-like radiation pattern (maximum radiation at broadside) was achieved, although the back radiation was close to -10 dB probably because of the small dimensions of the ground planes or the antenna themselves.

Related to the previous works, Itoh's group has also proposed an interesting idea which consists of using the $n = 0$ mode present in the previous structure thanks to its CRLH resonant behaviour [105]. This mode has a uniform electric field distribution in amplitude and phase which is typical in short-circuited patch antennas but not present in conventional ones. The interesting feature of this mode is that it has a monopolar equivalent magnetic current (Fig. 2.56) leading to a monopolar radiation pattern (null at broadside). Several designs of CRLH patch antennas working at $f_0 = 3.5$ GHz were presented in [105]. These patch antennas were based on a simple square or rectangular implementation of the mushroom unit cell without MIMs (similar to the one presented in Fig. 2.43). The electrical dimensions of the proposed antennas varied between $\lambda_0/6 \times \lambda_0/6$ and $\lambda_0/6 \times \lambda_0/2$, achieving measured efficiencies between 70% and 90%. Finally, it is important to note that this group proposed in [106] this implementation as a dual-frequency and dual-mode antenna by simultaneously using the $n = -1$ and $n = 0$ modes. One of this antennas is depicted in Fig. 2.56.

The group of Eleftheriades has also developed several small antennas working at the $n = 0$ mode [107, 109, 110, 108, 111]. Their initial designs consisted of two microstrip CRLH unit cells arranged in a ring configuration [107, 109, 110]. The LH elements were implemented with two series capac-

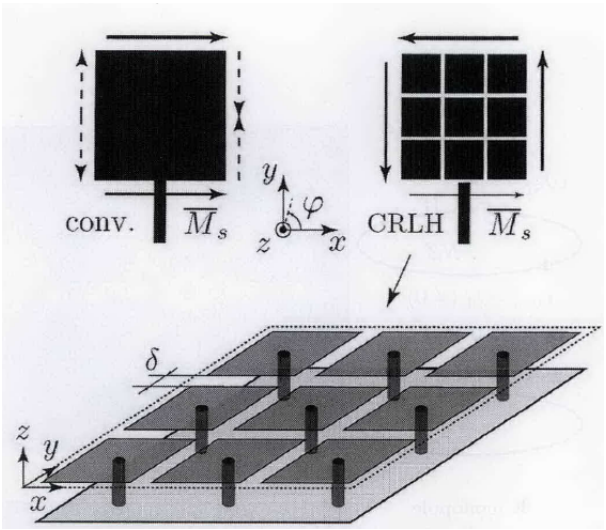

Figure 2.56: Miniaturized patch antennas based on mushrooms with a monopolar radiation pattern [105]. The operation principle is also depicted: the equivalent magnetic current distribution is monopolar in the CRLH structure working at the $n = 0$ mode. On the other hand, this distribution is dipolar in the conventional patch antenna.

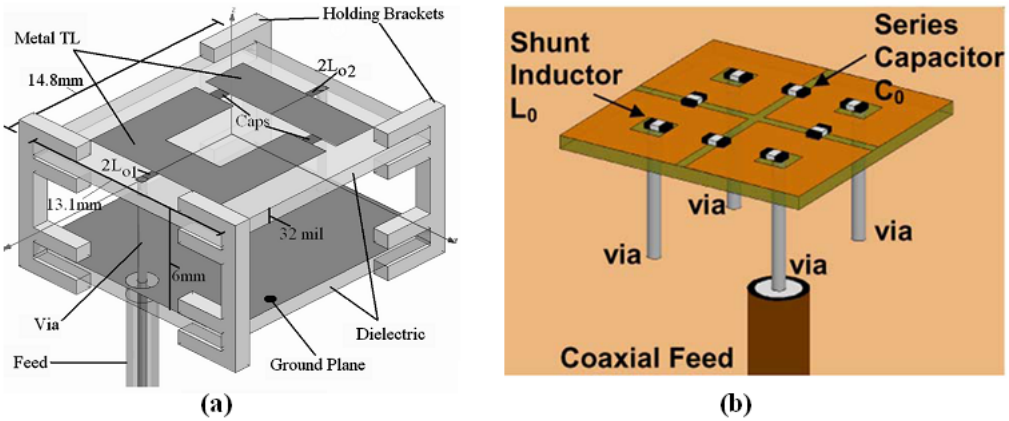

Figure 2.57: Small ring antennas working at the $n = 0$ mode proposed by the group of Eleftheriades. (a) Implementation based on two cells [107]. (b) Four-cell implementation [108].

itors and two inductors, one of them connected to a grounded via and the other one to a coaxial feed, as shown in Fig. 2.57.a. Both implementations of the LH elements (with lumped-chips [107] and microstrip distributed components [109, 110]) were developed. The vias acted as the main radiating elements and since the currents in them were equal in magnitude and phase, thanks to the $n = 0$ mode, the radiation pattern was monopolar (null at broadside and omnidirectional in the plane of the ring) with vertical polarization. The CRLH cells acted as a feeding network for the vias and provided internal matching. More recent designs were based on four unit cells but maintaining the ring geometry [108], as depicted in Fig. 2.57.b. This configuration provided a deeper null at broadside. In all of the cases, they had a low profile ($\lambda_0/20 - \lambda_0/30$) and small dimensions ($\lambda_0/10 - \lambda_0/12$ side). The first prototype was manufactured at 30 GHz with distributed elements [110], but after that they have also proposed several designs at 1.75 GHz (loaded with lumped chips [107] and also with distributed components [109]) and another one at 3.1 GHz with lumped chips [108]. The measured efficiencies of the first prototypes were between 30% and 50% [107, 109] but they have improved these results up to 70% [108]. The main drawback of these antennas is their narrow bandwidth ($< 2\%$). For that reason, now they are trying to join the resonances of two different arms working at the $n = 0$ mode, achieving a 3% bandwidth [111].

Another technique to miniaturize a patch antenna is based on the idea of a subwalength resonator. In [112] Engheta showed that by combining a slab of a conventional material and another one of a metamaterial structure is possible to obtain a resonator independent on their effective physical size. This idea was used by the group of University of Roma Tre to develop a miniaturized patch antenna. Firstly, they studied the effect of mounting a patch antenna over a dielectric composed of different combinations of conventional dielectrics and metamaterials [113]. They concluded this work explaining that it was possible to obtain such miniaturized patch by using a filled ring geometry in which the core was a metamaterial structure and the outer ring was a conventional dielectric. In [114] they proposed the use of a MNG structure in the core (Fig. 2.58.a) and they studied the best type of elements to implement such core. As it was not possible to develop a 3-D isotropic MNG structure, they proposed to use MNG particles properly oriented as inclusions in the dielectric substrate of the patch to achieve a MNG core. They explained that these inclusions (SRRs or Spirals) should be aligned vertically to excite them properly. Finally, they proposed a prototype with vertical SRRs as inclusions inside a dielectric substrate, shown in Fig. 2.58.b. They simulated this patch, obtaining a mode with broadside

radiation at a frequency much lower than the fundamental one of the conventional patch. The obtained resonance frequencies were 470 MHz and 2.44 GHz, with 0.67 and 0.92 simulated radiation efficiencies, respectively. These results seem promising. However, from the author's point of view, it is not easy to manufacture a substrate with SRR inclusions which can make the fabrication costs extremely expensive.

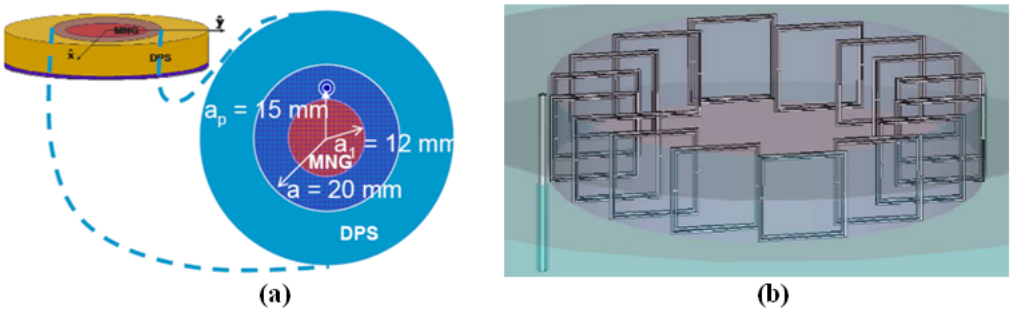

Figure 2.58: Miniaturized patch antenna based on a MNG core [114]. (a) Proposed model. (b) Implementation based on vertical SRR inclusions.

Finally, it is important to mention the works of the group of Peter Hall (The University of Birmingham, United Kingdom) concerning wire antennas loaded with LH structures. The state of the art of these antennas is reviewed in Section 3.3.1.

2.7 Conclusion

The concepts of metamaterials and their implementations have been reviewed in this Chapter. Moreover, the application of CRLH metamaterial TLs to resonant structures has been studied. It can be deduced that the dispersion diagram is a powerful tool to compute the working frequencies of CRLH resonant applications. For this reason, a novel approach based on an eigenfrequency method to compute the dispersion diagram of CRLH structures has been proposed in Section 2.5. This method drastically reduces the computation time needed to compute the dispersion diagram of CRLH structures with respect to the conventional approach. This approach has been validated by comparison with the conventional approach and experimental results.

Finally, the state of the art of the application of metamaterial structures to antenna engineering has been reviewed. It can be concluded that the use of metamaterial structures in antenna engineering has been focused

on three applications: the development of enhanced leaky-wave antennas, the use of metamaterial structures as superstrates and the development of small resonant antennas based on metamaterial particles. However, from the author's point of view, the use of metamaterial particles as loading elements of printed antennas to achieve multifrequency and/or multifunction and miniaturization performance has not been exploited previously. This approach will be presented throughout this Thesis.

CHAPTER 3

Metamaterial-Loaded Printed Wire Antennas

3.1 Introduction

Wire antennas such as dipoles, monopoles and loops are probably the most popular radiators. The printed versions of these antennas provide additional characteristics such as light weight, low profile, easy fabrication and low cost. On the other hand, the features required for modern antennas, such as multifrequency with arbitrary ratios and miniaturization, cannot be obtained with conventional approaches.

In this Chapter, printed wire antennas are loaded with metamaterial particles to achieve additional features. This technique has been previously applied to planar TLs and circuits, as it was reviewed in Sections 2.3.1 and 2.3.2. In those works, MNG (or ENG) particles were coupled to a host TL achieving a miniaturized stop-band filter. On the other hand, the use of LH cells allowed a passband with backward propagation. In the present Chapter, MNG particles are coupled to printed dipole antennas to achieve interesting characteristics such as multifrequency or miniaturization. Furthermore, LH loading is applied to the monopole and loop antennas to obtain miniaturization with internal matching and other interesting features such a radiation pattern orthogonal to the one obtained with conventional wire antennas.

Loaded wire antennas have been used for a long time. For example in [115] a monopole antenna was loaded with an inductor to improve the gain and the antenna matching. This technique has been traditionally used with electri-

cally small antennas working at low frequencies (up to VHF) to compensate the high reactive component of the input impedance [116]. For example, electrically small monopoles are loaded with inductors to compensate their high capacitive behaviour. Nevertheless, up to the author's knowledge, MNG or ENG metamaterial loading has not been applied to wire antennas till now.

The chapter is divided in two Sections. The first one (Section 3.2) deals with the dipoles loaded with metamaterial particles. A conventional printed dipole is presented in Subsection 3.2.1, showing its fundamental characteristics and demonstrating that it cannot be used as a multifrequency antenna. After that, a first approximation to the metamaterial loaded dipoles is exposed in Subsection 3.2.2, where the dipoles are loaded with the equivalent circuit of MNG particles achieving a dual-frequency performance. Then, in Subsection 3.2.3 it is demonstrated that dual-frequency printed dipoles can be achieved by using metamaterial loading. This approach is extended in Subsections 3.2.4 and 3.2.5 to achieve additional features such as miniaturization and multifrequency performance. Finally, an equivalent circuit model of the metamaterial-loaded dipole antennas is also proposed in Subsection 3.2.6.

The last Section presents the LH wire antennas over a finite ground plane. The state of the art of LH loaded wire antennas is reviewed in Subsection 3.3.1. After that, the LH monopole antenna and the LH half-loop antenna over ground plane are explained in Subsections 3.3.2 and 3.3.3, respectively. These antennas have been developed in collaboration with the group of Prof. Peter S. Hall (University of Birmingham).

3.2 Multifrequency Printed Dipoles Loaded with Metamaterial Particles

3.2.1 Reference Dipole

The reference antenna is an antipodal printed dipole. Each half of the antipodal dipole is implemented by printing a metallic strip on one side of a dielectric substrate with height h (Fig. 3.1). The parameters of each strip of the dipole are the length L and the width W. This configuration has been chosen because it avoids the use of a balun to feed the antenna. This is possible because the antipodal printed dipole is fed through a paired strips transmission line [59] with a SMA connector soldered to the end of the line. The dimensions of the feeding line are the length L_f and the width W_f.

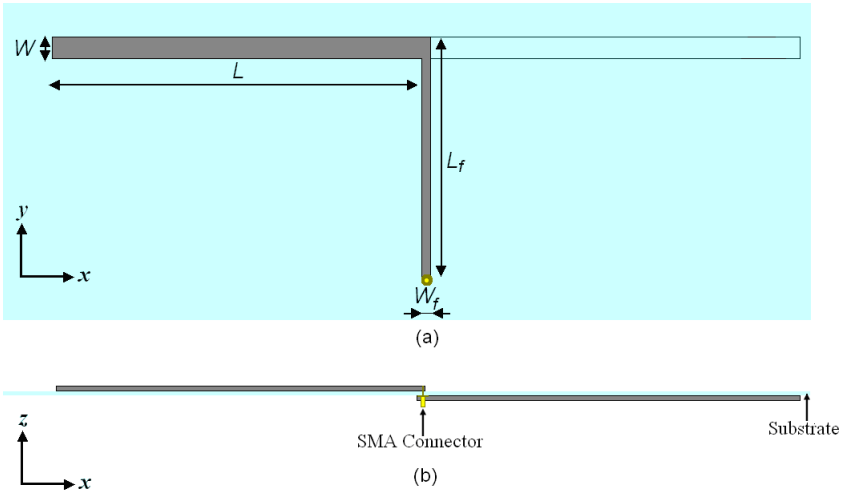

Figure 3.1: Sketch of an antipodal printed dipole. (a) Top view. (b) Side view.

In general, a dipole antenna is a resonant structure in which each mode corresponds to a standing wave on the dipole which satisfies the following relation

$$L_d = n\frac{\lambda_d}{2} \tag{3.1}$$

where L_d is the total length of the dipole, λ_d is the wavelength of the standing wave on the dipole antenna and n is the mode index. For the particular case of the antipodal printed dipole antenna L_d is computed as

$$L_d = 2L + W_f. \tag{3.2}$$

The relation between the wavelength of the standing wave and the wavelength in free space (λ_0) is given by

$$\lambda_d = c_\varepsilon \lambda_0 \tag{3.3}$$

where c_ε is a constant which depends on the value of the dielectric constant of the substrate (ε_r).

The geometry of the antipodal printed dipole antenna imposes an open-circuit boundary condition at the edges of each strip. This implies a minimum in the current distribution on the antenna at these points. On the other hand, a maximum in the current distribution must occur at the centre of the antenna because it is directly connected to the feed. These boundary conditions

impose that only odd modes can be excited in the antipodal printed dipole antenna. Thus, n takes values $n = +1, +3, +5, \ldots$

Taking into account the relation

$$c = \lambda_0 f \tag{3.4}$$

where c is the speed of ligth in free space, the resonant frequencies of the printed antipodal dipole antenna can be computed as

$$f_n = n\frac{c}{2L_d}c_\varepsilon \tag{3.5}$$

which imposes that all the resonant frequencies are harmonics of the fundamental one ($f_n = nf_{+1}$) and depends on the physical dimensions of the dipole antenna (in particular the total length L_d).

Let us consider a dipole with $L = 42.05$ mm, $W = 2.50$ mm, $L_f = 27.50$ mm and $W_f = 1.00$ mm. The substrate is the low-cost FR-4 ($\varepsilon_r = 4.5$ and $\tan\delta = 0.015$) with $h = 0.50$ mm. It has been determined experimentally that c_ε can be approximated by 0.85 for this substrate. Thus, according to (3.5) the theoretical resonant frequency of the fundamental mode ($n = +1$) of this antenna is $f_{+1} = 1.5$ GHz. The second mode ($n = +3$) resonates at $f_{+3} = 4.5$ GHz theoretically. The resonant frequency of any other higher order mode can be computed from (3.5).

This antenna has been simulated with CST Microwave Studio ®. The simulated resonant frequencies agrees with the ones computed theoretically, as it can be seen in the simulated reflection coefficient (Fig. 3.2, blue dashed line). Fig. 3.3.a shows the current distribution on the antipodal dipole at the fundamental resonant frequency (mode $n = +1$). The obtained currents present the expected $\lambda_d/2$ sinusoidal distribution, with minima at the edges of the dipole halves (open-circuit conditions) and maxima at the centre of the dipole. This current distribution provides the conventional dipolar-like radiation pattern, showed in Fig. 3.4.a. The current distribution on the dipole for the $n = +3$ mode has three half-wavelengths, shown in Fig. 3.3.b, which produces a radiation pattern with three lobes (Fig. 3.4.b). Subsequent higher order modes ($n = +5, +7, \ldots$) have n lobes in their radiation patterns.

A prototype of the antipodal dipole has been manufactured (Fig. 3.5) and measured. This antenna will be used as reference in the next Subsections. The measured reflection coefficient of this reference antipodal dipole is shown in Fig. 3.2 (dark solid line) where good agreement with respect to the simulations can be seen. Fig. 3.6 shows the measured radiation pattern of the reference antipodal printed dipole at $f_{+1} = 1.5$ GHz. A dipolar radiation

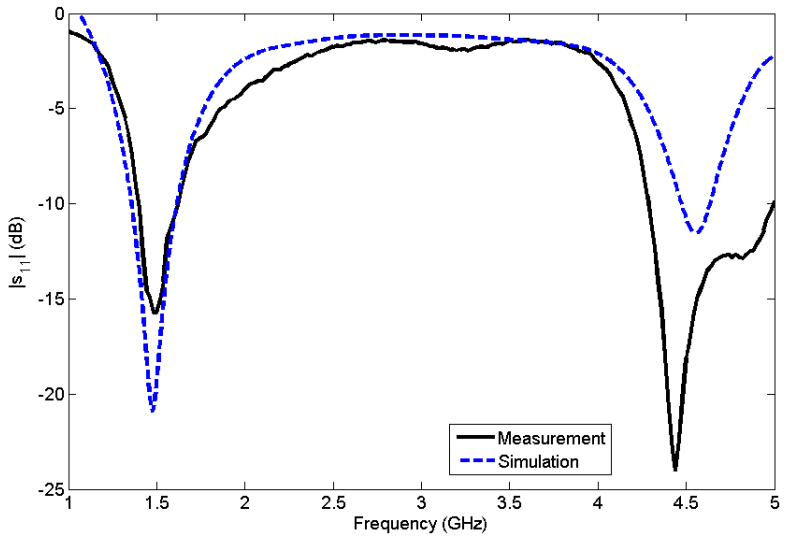

Figure 3.2: Measured and simulated reflection coefficient of the reference antipodal printed dipole.

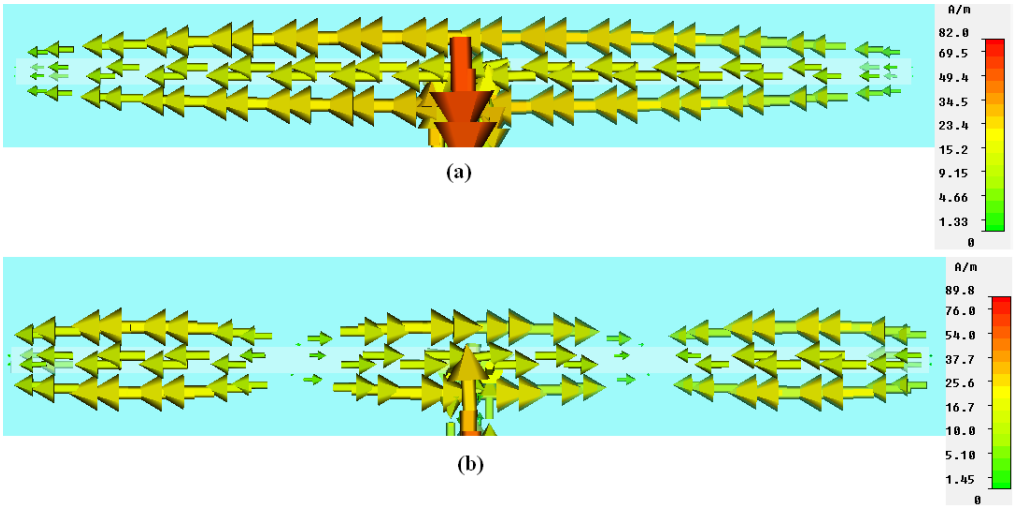

Figure 3.3: Current distributions of an antipodal printed dipole. (a) Fundamental mode ($n = +1$). (b) $n = -3$ mode.

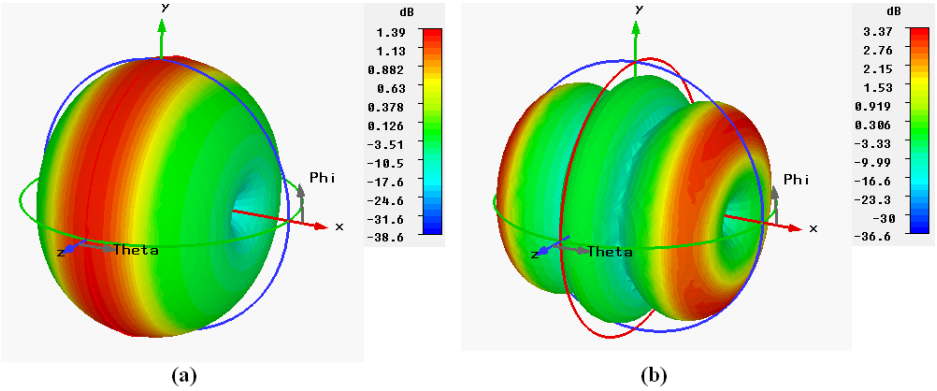

Figure 3.4: Radiation patterns of an antipodal printed dipole. (a) Fundamental mode ($n = +1$). (b) $n = -3$ mode.

pattern is obtained, as expected. A ripple can be appreciated, specially in the $x - z$ plane, due to the presence of unavoidable metallic elements in the measurement setup. The cross-polarization (XPOL) normalized with respect to the co-polarization (COPOL) is below -18 dB in the $x - y$ plane and -14 dB in the $y - z$ plane. The measured gain of the antenna is 1.99 dB. Furthermore, the radiation efficiency of this prototype has been also measured with the Wheeler Cap method [14, 117, 118, 119, 120], resulting in 94%.

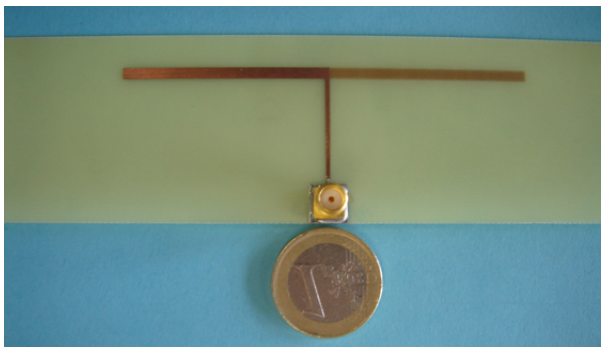

Figure 3.5: Picture of the manufactured reference antipodal printed dipole.

It can be concluded that conventional antipodal printed dipoles cannot be used as multifrequency antennas because all the resonant frequencies are multiples of the fundamental one and depend on the physical length of the dipole. Thus, there is only one degree of freedom in the design: once the fundamental frequency is fixed by the length, all the other working frequencies

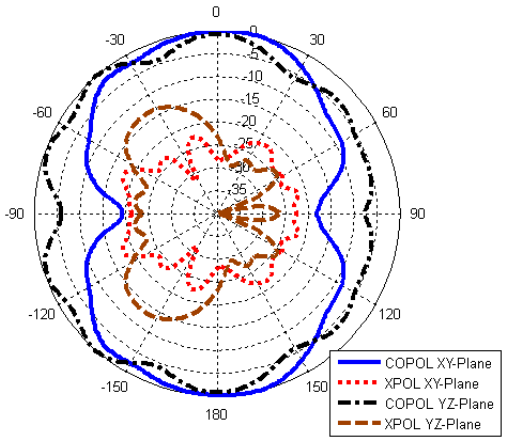

Figure 3.6: Measured radiation pattern of the reference antipodal printed dipole working at its fundamental mode ($n = +1$).

cannot be arbitrarily chosen. Moreover, the radiation patterns of higher order modes have multiple lobes which are not interesting for most of applications.

3.2.2 Dual-Frequency LC-Loaded Printed Dipoles

The first approach to develop dual-frequency printed antennas consists of loading a simple printed wire antenna with LC parallel tanks. These cells have been chosen because most of the elemental metamaterial magnetic cells, such us SRRs or spiral resonators, can be modelled as LC parallel tanks, as it was proposed in [36] and reviewed in Subsection 2.2.2. Thus, the reference printed dipole (Section 3.2.1) has been loaded with one LC parallel tank per strip, as it is shown in Fig. 3.7. In order to implement this approach a gap is made in each strip of the dipole and a LC parallel tank is connected between the edges of each gap. The gaps are made at a distance d from the centre of the dipole. The other parameters of the antenna are the same to those of the reference dipole of Section 3.2.1.

The self-resonant frequency of the LC parallel tanks is computed as

$$f_{LC} = \frac{1}{2\pi\sqrt{L_{LC}C_{LC}}} \tag{3.6}$$

Let us consider the reference dipole loaded with LC parallel tanks placed at a distance $d = 35.00$ mm from the centre. The values of the components are $L_{LC} = 10.00$ nH and $C_{LC} = 0.47$ pF. According to the expression (3.6) the

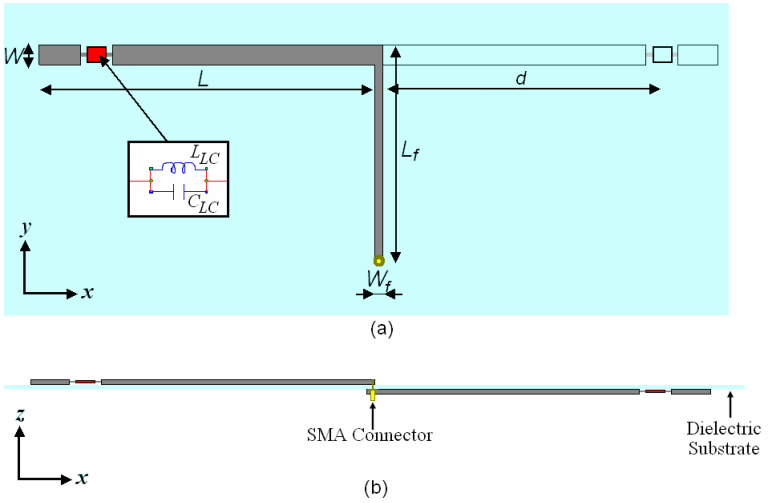

Figure 3.7: Sketch of a LC-loaded antipodal printed dipole. (a) Top view. (b) Side view.

self-resonant frequency of these LC parallel tanks is 2.30 GHz. The proposed LC-loaded printed dipole antenna has been simulated with CST Microwave Studio ®. Fig. 3.8 shows the simulated reflection coefficient of the proposed antenna (in blue dashed line). This dipole presents an unusual dual-frequency performance and two resonances are achieved. The resonance frequencies are 1.40 GHz and 2.00 GHz. The first resonance is very close to the fundamental one of the conventional dipole. On the other hand, the second resonance is due to the LC parallel tanks loading, but it has been shifted down towards lower frequencies. This frequency shift is 13% approximately. This value depends on the position of the LC parallel tanks as it will be shown below.

The currents on the dipole have a half-wavelength sinusoidal distribution (Fig. 3.9). At the first frequency they are similar to the unloaded dipole (Fig. 3.3.a). On the other hand, the LC tanks impose a hard boundary condition (open circuit) at the second frequency. This produces that there is almost no current between the tanks and the dipole edges. In this case, the minima are located at the tank edges and the maximum is maintained at the feeding point. Both half-wavelength sinusoidal currents provide a dipolar-like radiation pattern (Fig. 3.10).

In the previous example the ratio between the working frequencies is 1.43 which is inharmonic. Moreover, the proposed antenna has a dipolar-like radiation pattern at both working frequencies. Thus, it seems that this approach is valid to develop dual-frequency printed dipoles with arbitrary working

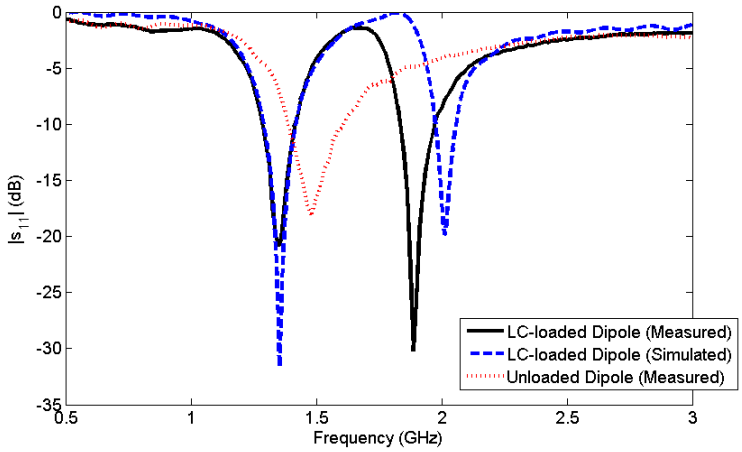

Figure 3.8: Measured and simulated reflection coefficient of the LC-loaded printed dipole. The measured reflection coefficient of the refference dipole is also plotted.

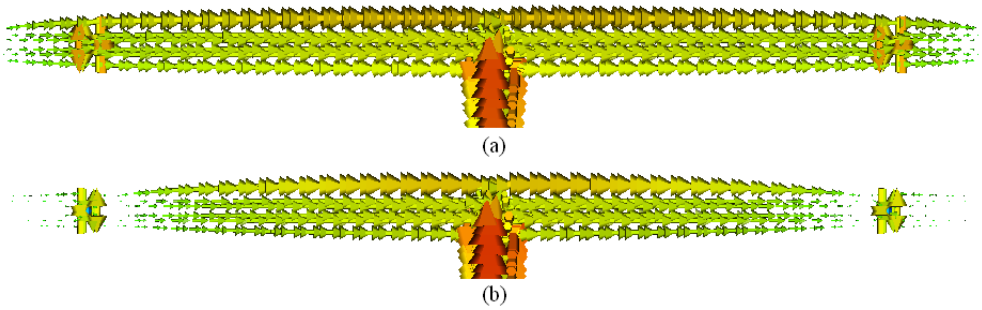

Figure 3.9: Simulated currents on the LC-loaded printed dipole. (a) 1.40 GHz. (b) 2.00 GHz.

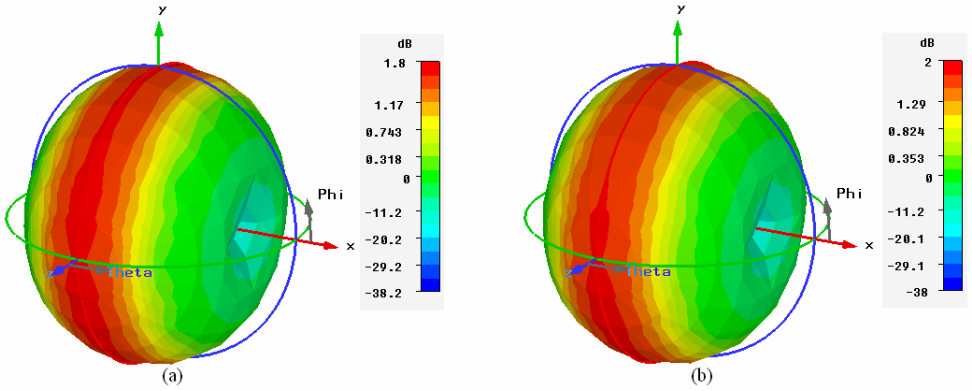

Figure 3.10: Simulated radiation patterns of the LC-loaded printed dipole. (a) 1.40 GHz. (b) 2.00 GHz.

bands. In order to show its validity, the proposed LC-loaded dipole has been simulated for different values of C_{LC} and L_{LC}. Fig. 3.11 shows the simulations of the LC-loaded dipole for different values of C_{LC} while the other parameters of the antenna are unchanged with respect to the previous example. It can be seen that the first working frequency remains almost fixed but the second frequency depends on the value of C_{LC}. In this parametric analysis, the ratio between the maximum and minimum additional frequencies that can be achieved is 2.38 GHz/1.83 GHz = 1.30 for a ratio between the values of C_{LC} equals 0.68 pF/0.22 pF = 3.09. A similar behaviour can be seen in Fig. 3.12 in which the value of L_{LC} is varied while the other parameters are the same as in the original LC-loaded dipole. In this case, the ratio between the additional frequencies that can be achieved is 2.52 GHz/1.86 GHz = 1.35 for a variation in the L_{LC} component equals 13.00 nH/5.60 nH = 2.32. These two parametric studies show that dual-frequency dipoles with arbitrary bands can be developed. One of the frequencies is set by the dipole length and the other one can be chosen by a proper selection of the LC components of the loading parallel tanks.

The effect of the position of the LC parallel tanks has also been studied (Fig. 3.13). In this plot the distance d between the LC parallel tanks and the center of the dipole is varied while the other parameters are unchanged. The value of d has influence on the matching and frequency shift of both working resonances. For values of d smaller than 25.00 mm the resonance produced by the dipole has a large frequency shift ($> 15\%$) and the resonance due to the LC tanks is poorly matched. This frequency shift is considerably reduced when the distance is increased. Moreover, the matching of the additional res-

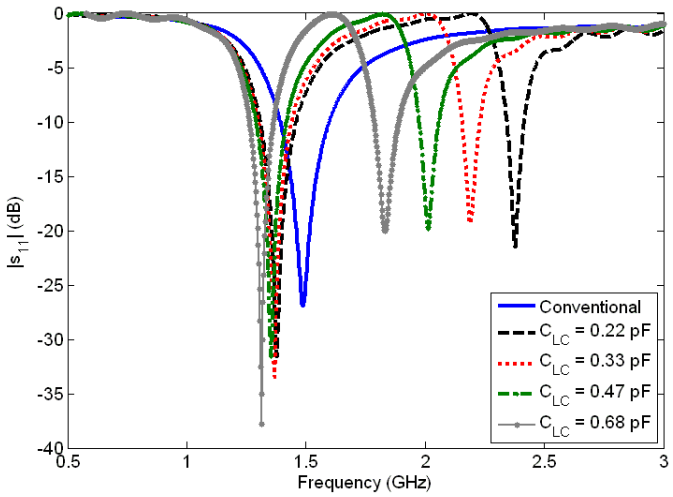

Figure 3.11: Simulated reflection coefficient of the LC-loaded dipole for different values of C_{LC}.

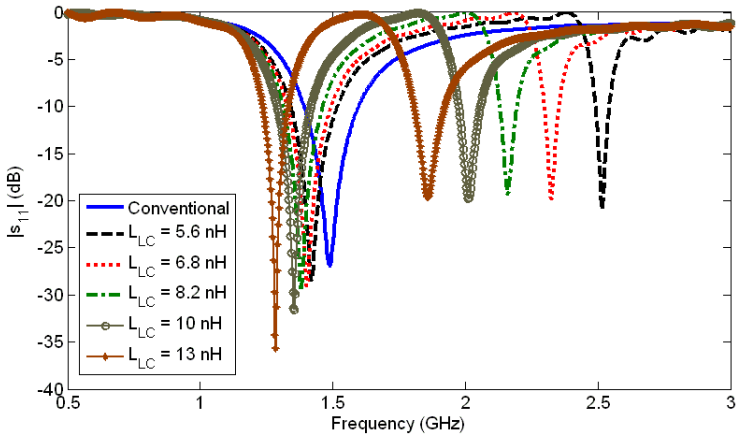

Figure 3.12: Simulated reflection coefficient of the LC-loaded dipole for different values of L_{LC}.

onance is considerably better for values higher than 25.00 mm. On the other hand, the resonance produced by the dipole is well matched independently of the parameter d. It can be also seen that the frequency shift of the second resonance depends on d. The frequency of the second resonance is equal to the self-resonant frequency of the LC parallel tanks for $d = 25.00$ mm. For values smaller than 25.00 mm the resonance is shifted towards higher frequencies while it is shifted towards lower frequencies for values larger than 25.00 mm. Anyway, in all of the cases the frequency shift of the additional resonance is smaller than 17%. In the proposed example, the parameter d has been set to 30.00 mm because the antenna is properly matched at both working bands without large shifts in the operation frequencies. In conclusion, it can be said that the design procedure for a dual-frequency LC-loaded antipodal dipole is as follows:

1. As a first approximation, design a printed dipole working at one of the desired frequencies and load it with LC parallel tanks which resonate at the other working frequency.

2. Study the effect of the parameter d. Set this parameter to a value in which both resonances are properly matched.

3. An optimization process over the variables L, L_{CL} and C_{LC} can be performed in order to achieve a fine adjustment of the desired frequencies.

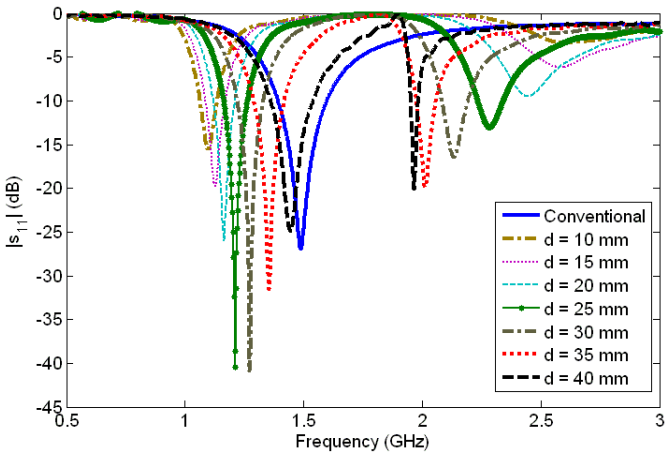

Figure 3.13: Simulated reflection coefficient of the LC-loaded dipole for different values of the parameter d.

A prototype of the proposed example ($d = 30.00$ mm, $L_{LC} = 10.00$ nH, $C_{LC} = 0.47$ pF and the rest of parameters as in the reference antipodal printed dipole antenna) has been manufactured and measured. The LC parallel tanks have been implemented with commercial SMD components. The measured reflection coefficient is shown in Fig. 3.8 (black bold line) and is compared with the simulated results (blue dashed line) and the measured reflection coefficient of the unloaded dipole (red dotted line). It is demonstrated that the unloaded dipole has only one working band within the range of interest, while the proposed LC-loaded dipole have two resonances. There is a great agreement between the simulated and experimental results. A small frequency shift can be seen in the second resonance. This is mainly produced by the tolerances of the components and the manufacturing process. The working frequencies of the manufactured prototype are 1.40 GHz and 1.90 GHz. The $|s_{11}|$ parameter is -21 dB at the first frequency and -31 dB at the second frequency. The ratio between the working frequencies is only 1.36. These experimental results show that this approach is valid for developing dual-frequency printed dipoles.

3.2.3 Printed Dipoles Loaded with Metamaterial Particles: Fundamentals and Dual-Frequency Performance

As it was described in the Subsection 2.2.2, elemental metamaterial MNG cells, such us SRRs, square SRRs or spiral resonators can be modelled as LC parallel resonators. For this reason, one can think about substituting the series LC parallel tanks in the previous dipole antennas for electromagnetically coupled planar MNG metamaterial particles. This is possible if the planar MNG metamaterial particles are located in a way such the magnetic field generated by the currents on the dipole antennas has an important component in the direction normal to the plane of the particles [27]. In order to study this possibility, Fig. 3.14 shows the full-wave simulation of the magnetic field generated by the reference antipodal printed dipole (Section 3.2.1). As it can be seen, the currents on the dipole strips generate magnetic fields which form loops around the strips, leading to field lines which are normal to the interface between the dielectric and the air. Thus, the models proposed in Fig. 3.15 can be used to develop printed dipoles loaded with meatamaterial particles. In both cases the blue boxes represent a set of planar MNG metamaterial particles printed on the dielectric substrate. In the first case (Fig. 3.15.a) each set of particles is printed close to the dipole strips on the same side of the substrate. In the other case (Fig. 3.15.b) each set of particles is

printed on the side of the substrate opposite to each dipole strip. In either of the cases, the sets of particles are printed on a dielectric substrate so they are located in the interface between the dielectric and the air and are excited by the normal magnetic field generated by the currents on the dipole. In order to implement this approach, the blue boxes in Fig. 3.15 must be substituted for particular set of MNG metamaterial particles.

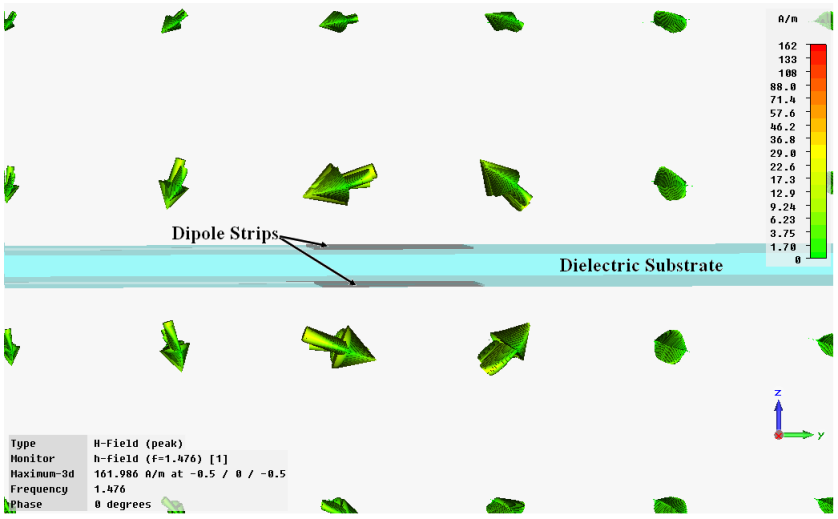

Figure 3.14: Simulation of the magnetic field generated by the antipodal printed dipole.

The first proposal is shown in Fig. 3.16. A set of four SRRs is printed on the opposite side of each dipole half. This configuration has been chosen because it provides a proper matching within a wide range of ratios between the working frequencies. The SRRs parameters, according to Fig. 3.16.b, are the external radius R, the width of the strips W_{SRR} and the gap between strips g. The SRRs are placed at a distance c from the dipole centre. The separation between the centres of the SRRs is s.

The proposed configuration provides the desired dual-frequency performance. The first frequency (f_{+1}) is close to the fundamental frequency of the dipole ($n = +1$ mode) while the additional frequency (f_{SRR}) occurs in the vicinity of the SRRs self-resonant frequency. Fig. 3.17 (obtained with CST Microwave Studio ®) shows the current distributions on the proposed dipole at the two working frequencies. At f_{+1} (Fig. 3.17.a) the current distribution is similar to the one obtained in the conventional half-wavelength dipole (Fig. 3.3.a). It can be appreciated that the effect of the SRRs at this frequency is negligible and nearly no current passes along them. This implies that the

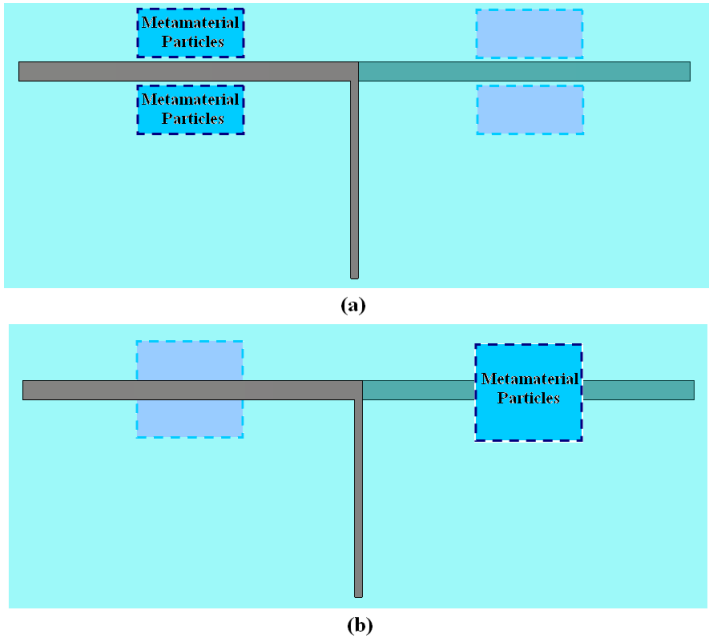

Figure 3.15: Sketch of the different implementations of metamaterial-loaded printed dipoles. (a) Metamaterial particles printed close to the dipole strips. (b) Metamaterial particles printed on the side of the substrate opposite to the dipole strips.

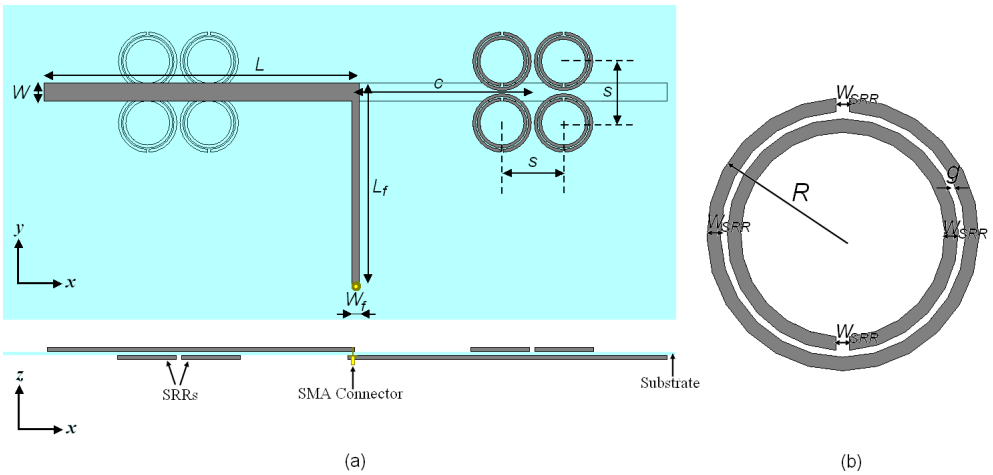

Figure 3.16: (a) Top and side views of the SRRs-loaded dipole antenna. (b) Split Ring Resonator parameters.

expected radiation pattern at this frequency is also similar to the reference dipole. In fact, the only modification in the antenna performance is a very slight frequency shift in the resonant frequency towards lower frequencies due to the capacitive parasitic effect of the SRRs. On the other hand, the working principle at f_{SRR} is somewhat different since the resonant frequency is imposed by the SRRs. At this frequency the SRRs are resonating, as can be seen in Fig. 3.17.b, where the currents on them are maximum. In this case, the SRRs are imposing a hard boundary condition (an open circuit) where they are placed. In this way, the currents on the dipole are nearly zero from this position to the end of the overall dipole. Thus, the effect of the SRRs is similar to the one obtained with the LC parallel tanks in the Section 3.2.2. This means that the radiating element is formed by the current distribution on the dipole between the SRRs arrangements. It should be noted that this radiating element is a dipole with a length shorter than $\lambda/2$ sustaining a current between the edges where the SRRs are placed. Thus, it is expected that the proposed structure gives a dipolar-like radiation pattern at f_{SRR}. This is an important feature because the proposed dipoles not only present the desired dual-frequency performance but they keep the dipolar-like radiation pattern at both working frequencies.

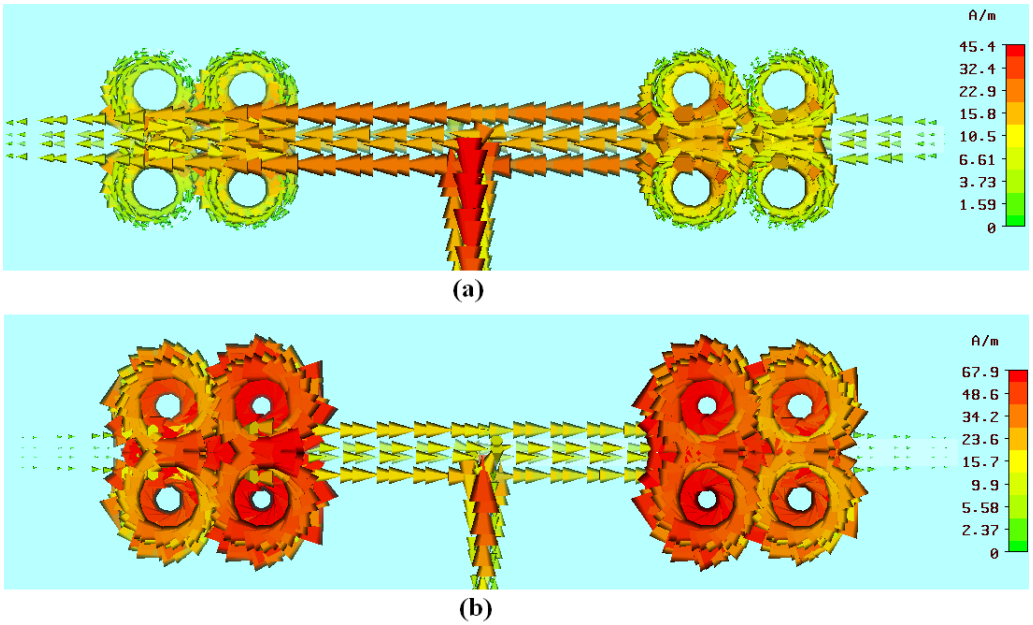

Figure 3.17: Currents on the SRRs-loaded dipole: (a) f_{+1}. (b) f_{SRR}.

It is clear from the previous currents study that the resonance frequency

f_{+1} is close to the fundamental frequency of the reference dipole and thus, it depends mainly on the dipole dimensions. On the other hand, the additional resonance frequency (f_{SRR}) mainly depends on the SRRs parameters. A study has been realized with CST Microwave Studio ® to illustrate this dependency. Fig. 3.18 shows the obtained results for a variation of the parameter R between 4.00 mm and 5.00 mm (22% variation). The other parameters of the SRRs are $W_{SRR} = 0.40$ mm and $g = 0.20$ mm, according to Fig. 3.16. The dimensions of the dipole are similar to the reference one (Section 3.2.1). The variation of the additional frequency is close to 24% while the dependency of the first frequency is smaller (less than 9%).

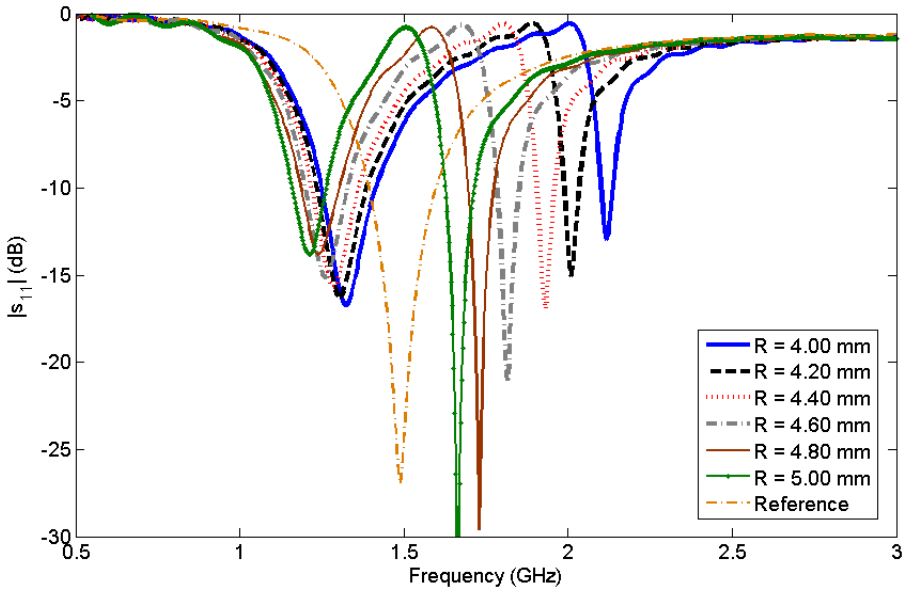

Figure 3.18: Dependency of the simulated reflection coefficient of the SRRs-loaded dipole on the SRRs external radius R.

It has been demonstrated that the resonance frequencies mainly depend on the dimensions of the dipole and the SRRs. However, it is important to know the role of the position of the SRRs. For this reason, a parametric study has been developed. The proposed SRRs-loaded dipole (Fig. 3.16) has been simulated for different values of the parameter c (spacing between the sets of SRRs). The dimensions of the dipole are the same as the reference dipole (Section 3.2.1) and the SRRs have the following parameters: $R = 4.00$ mm, $W_{SRR} = 0.40$ mm and $g = 0.20$ mm. The obtained results are shown in Fig. 3.19. It is clear that both working frequencies are shifted towards lower frequencies when the SRRs are located far away from the feeding line (higher

values of c). Regarding the matching of the working resonances, the first one is almost independent of the parameter c. On the other hand, the parameter under study has a strong influence on the matching of the second resonance. It can be concluded that the best matching is achieved when the SRRs are located close to the half of each dipole strip ($c = 20$ mm).

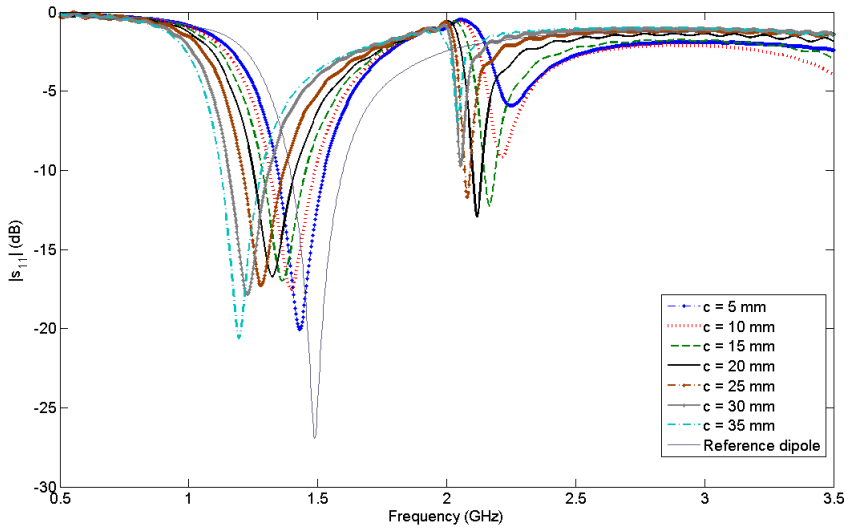

Figure 3.19: Simulated reflection coefficient of the SRRs-loaded dipole for different values of the parameter c, keeping the other parameters of the antenna fixed.

Two prototypes of the proposed SRR-loaded dipole antenna have been designed, each of them with a different ratio between the two working frequencies. The first one has a frequency ratio larger than 2, while the second one presents a frequency ratio smaller than 2. It is important to note that it is necessary to achieve dual-frequency antennas with ratios smaller than 2 for nowadays systems (e.g. GPS/Galileo receivers), but they are very difficult to obtain with the conventional approaches. Some conventional approaches to obtain a single dipole with two resonances consist of making two U-slotted arms inside the dipole [121] or incorporating two compact resonant cells [122]. In both cases, the ratio between the working frequencies is always larger than 2. It seems that smaller ratios cannot be achieved with these approaches. The main reason for that is that the additional resonance is fixed by the structure introduced inside the dipole (U-slots or compact resonant cells). For this reason, a decrease in the frequency ratio involves an increase in the inner resonators size. This fact can cause the resonators not to fit inside the dipole. This implies that achieving a working ratio smaller than 2 is an important

advantage over the conventional approaches.

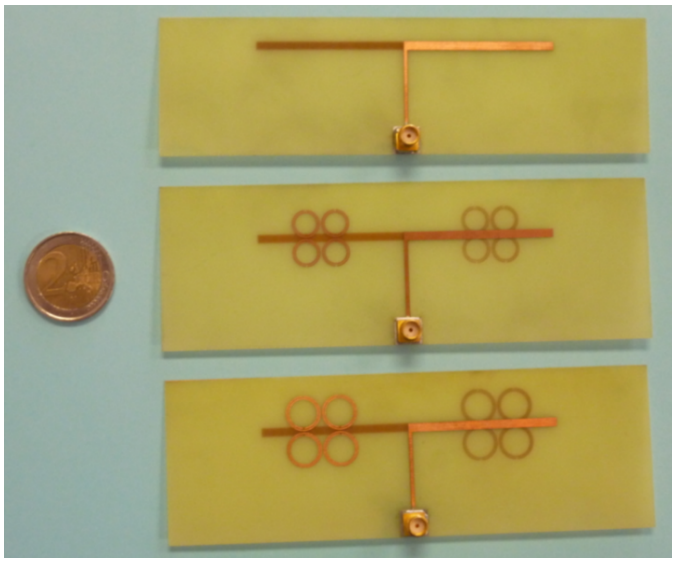

Figure 3.20: Picture of the manufactured antipodal dipole prototypes. Top: conventional dipole. Centre and bottom: SRRs-loaded dipoles.

In both prototypes the dimensions of the dipole are the same as the reference antenna of Section 3.2.1($L = 42.05$ mm, $W = 2.50$ mm, $L_f = 27.5$ mm and $W_f = 1.00$ mm). The same substrate (FR-4 with $h = 0.50$ mm) has been used. Both prototypes are loaded with a set of four SRRs per branch, placed at a distance c that is varied depending on the SRRs size: for the two designed dipoles this distance has been set to 24.20 and 25.20 mm, respectively. The separation s is 8.40 and 10.40 mm, respectively. The parameters of the SRRs sets are the external radius ($R = 4.00$ for the first prototype and $R = 5.00$ mm for the second one), the width $W_{SRR} = 0.40$ mm and the gap between rings $g = 0.20$ mm. According to [36] the resonant frequency of the SRRs is 2.55 GHz for the first prototype and 1.92 GHz for the second one.

The proposed SRRs-loaded dipoles have been manufactured (Fig. 3.20). The measured reflection coefficients of the proposed antennas and the reference dipole are shown in Fig. 3.21. The reference dipole frequency is $f_{+1} = 1.48$ GHz, while the proposed SRRs-loaded dipoles present the desired dual-frequency performance. The first resonance appears at $f_{+1} = 1.32$ GHz and $f_{+1} = 1.20$ GHz for the dipole loaded with 4 mm-radius and 5 mm-radius SRRs, respectively. At these frequencies the current along the SRRs is negligible and the only effect of the SRRs is to slightly shift down the frequency of

the conventional dipole. The second working frequency (f_{SRRs}) is 2.83 GHz for the first prototype and 2.05 GHz for the second one, which are close to the SRRs self-resonance frequencies. This frequency is shifted towards higher frequencies due to the mutual couplings between the different elements which compose the antenna. This effect is similar to the one studied in the LC-loaded dipoles (Section 3.2.2) in which the additional frequency provided by the LC tanks was shifted. The frequency shift also depends on the value of the parameters c and s, as commented before. Finally the tolerances of the substrate and the manufacturing process cannot be neglected because the resonant frequency of the metamaterial particles is very sensible to small changes.

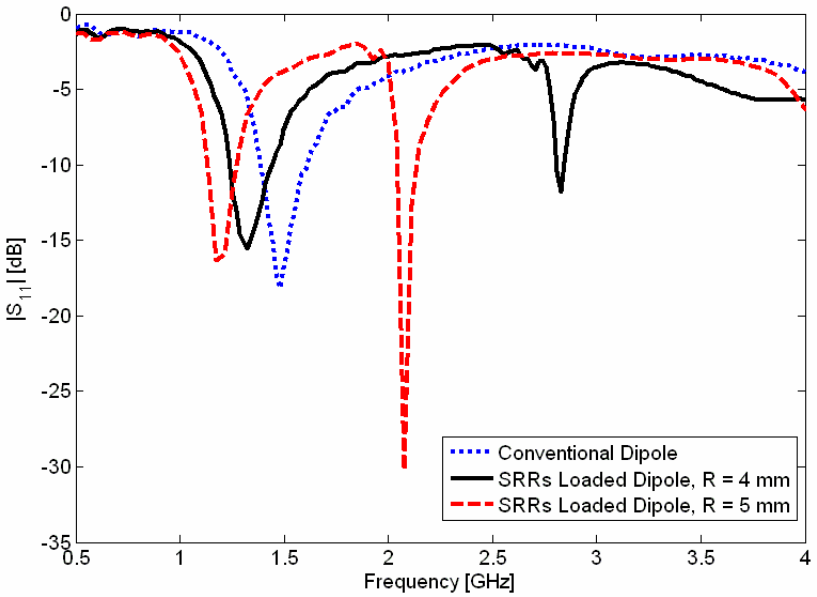

Figure 3.21: Measured reflection coefficient of the proposed SRRs-loaded and conventional dipoles.

The bandwidth at the lower band is around 15% considering $|s_{11}| < -10$ dB for the three dipoles. On the other hand, the bandwidth at the additional band (considering $|s_{11}| < -10$ dB) for the proposed dipoles is much lower (1.27% and 3.5% for the first and second prototypes, respectively). This is due to the high Q factor of the SRRs what implies a much smaller bandwidth in the additional band.

The measured radiation patterns of the dual-frequency dipole loaded with 4 mm-radius SRRs at both working frequencies (1.32 GHz and 2.83 GHz) are shown in Fig. 3.22. In both cases, the radiation patterns are dipolar-like and

similar to the ones presented by the reference dipole (Section 3.2.1). A ripple can be appreciated, specially at the H plane ($y-z$ plane). This is due to the measurement procedure where the metallic plane of the positioner behind the antenna could not be avoided. At the first working frequency the maximum cross-polarization level (XPOL) in the E ($x-y$) plane (defined with respect to the normalized 0 dB co-polarization level, COPOL) is -17 dB and occurs at $-25°$ with respect to the 0 dB direction. For the H plane the maximum cross-polarization level is -14 dB and occurs at $-32°$ respect to the 0 dB direction. At the other frequency the effect is similar to the ones described before: a ripple appears due to the metallic plane of the positioner behind the dipole. The maximum XPOL is -15 dB for the E plane and occurs at 20° with respect to the 0 dB direction. For the H plane the cross-polar component is -16 dB and occurs at $-32°$.

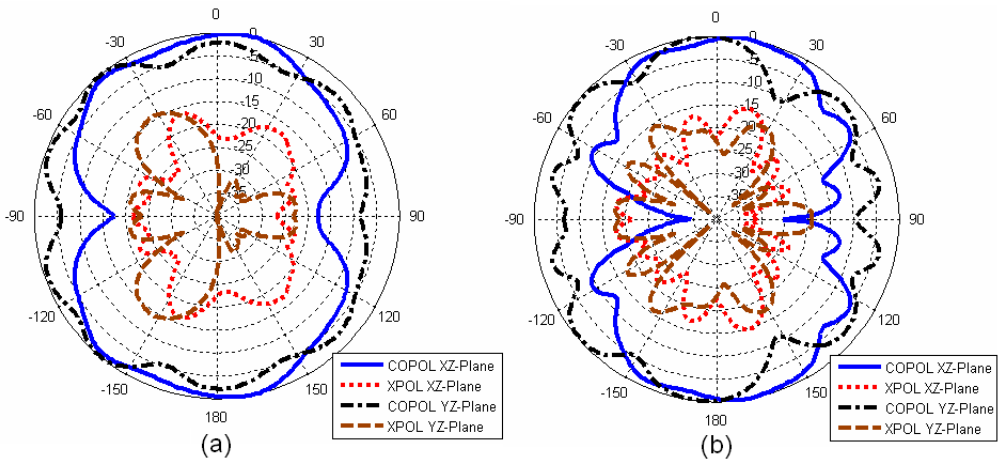

Figure 3.22: Measured radiation patterns of the dipole loaded with 4 mm-radius SRRs. (a) 1.32 GHz. (b) 2.83 GHz.

The measured gain of the reference dipole is 1.99 dB (Section 3.2.1). For the first dual-frequency dipole (1.32 GHz and 2.83 GHz) this magnitude is 1.81 dB at the first working frequency and 0.67 dB at the second one. For the second dual-frequency dipole (1.20 GHz and 2.05 GHz) the gain is 1.89 dB and 1.10 dB at the first and second frequencies, respectively. The efficiencies have been measured through the Wheeler cap method [14, 117, 118, 119, 120]. The efficiency of the 4 mm-radius-SRRs-loaded dipole is 91% at the frequency associated with the dipole itself while decreasing to 62% at the frequency associated with the SRRs. For the other SRRs-loaded prototype the efficiency is 92% at the first working frequency and 70% at the second one. In both

Antenna	Frequency (GHz)	G (dB)	Efficiency	$BW_{-10\,\mathrm{dB}}$
Conventional dipole	1.48	1.99	0.94	14.89%
$R = 4$-loaded dipole	1.32	1.81	0.91	15.07%
	2.83	0.67	0.62	1.27%
$R = 5$-loaded dipole	1.20	1.89	0.92	11.70%
	2.05	1.10	0.70	3.50%

Table 3.1: Measured characteristics of the manufactured prototypes.

cases this is due to the large amount of energy stored in the SRRs that is not radiated. The effect of the high losses in the SRRs can also be appreciated in [27, 36] for a filter application. The measured results of the manufactured prototypes are summarized in Table 3.1.

These experimental results show the validity of printed dipoles loaded with metamaterial particles to develop printed dipoles with two working frequencies. One is close to the fundamental frequency of the dipole, while the other is close to the self-resonant frequency of the particles. In both cases, a dipolar-like radiation pattern is obtained. This novel approach can be used to design dual-band fully printed dipoles with an arbitrary ratio and it is useful for small ratios (smaller than 2) that are necessary for nowadays communications.

3.2.4 Miniaturization Performance of Metamaterial-Loaded Printed Dipoles

In the previous cases, the additional frequency is placed above the resonant frequency of the unloaded dipole, but the proposed approach allows exciting the additional frequency below the resonant frequency of the unloaded dipole. This implies achieving miniaturization and multifrequency at the same time. An example is shown below.

The second multifrequency dipole implementation is based on loading the antipodal printed dipole with a modified version of the Omega structure. The original Omega structure was presented in Section 2.2.3 (Fig. 2.10.a) and it was composed of two reversed Omega-like metallic strips printed on each side of a dielectric substrate [39]. In that case, several unit cells were connected in series achieving a simultaneous ENG and MNG behaviour. In the present case, the unit cells are not connected in series, achieving only

MNG performance. Hence, the Omega particles can be used to develop dual-frequendy printed dipoles in a similar way that has been done with the SRRs. It is important to note that Omega particles with rectangular shape are used instead of the classical ones because the computation time is reduced when straight shapes are simulated.

According to Fig.3.1, a dipole with $L = 28.50$ mm, $W = 3.00$ mm, $L_f = 36.50$ mm and $W_f = 1.00$ mm is considered. The substrate is the low-cost FR-4 ($\varepsilon_r = 4.50$ and $\tan\delta = 0.015$) with $h = 0.50$ mm. The resonant frequency of the fundamental mode of this dipole is 2.12 GHz. The previous dipole is loaded with an Omega particle per dipole strip (Fig. 3.23). The dimensions of each omega particle are: $L_p = 4.60$ mm, $W_p = 3L_p = 13.80$ mm and $W_s = 0.40$ mm. These particles are coupled at the centre of the dipole strips. The separation gap between the particles and the dipole is 0.20 mm.

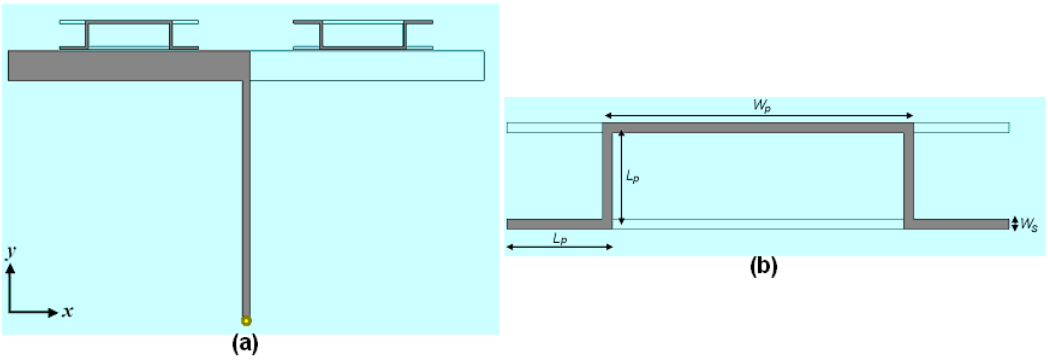

Figure 3.23: Sketch of the Omega-loaded antipodal printed dipole. (a) Top view. (b) Design parameters of the Omega particles.

Fig. 3.24 shows the reflection coefficient of the loaded and unloaded dipoles. The unloaded dipole has its fundamental resonance at 2.12 GHz, as expected. On the other hand, the loaded dipole has two resonances: the first one at 1.70 GHz, while the second one at 2.21 GHz. This second resonance is the resonance of the dipole which has been slightly shifted towards higher frequencies due to mutual couplings. The first one is the additional resonance produced by the Omega particles loading. It is important to note that this resonance is obtained below the resonant frequency of the fundamental dipole mode. This is opposite to the previous examples because in that case the additional resonances were placed above the fundamental resonance of the conventional dipole. This demonstrates that the additional resonances can be completely controlled by choosing the adequate particles. The electrical length of the dipole at the first resonant frequency is $0.32\lambda_0$,

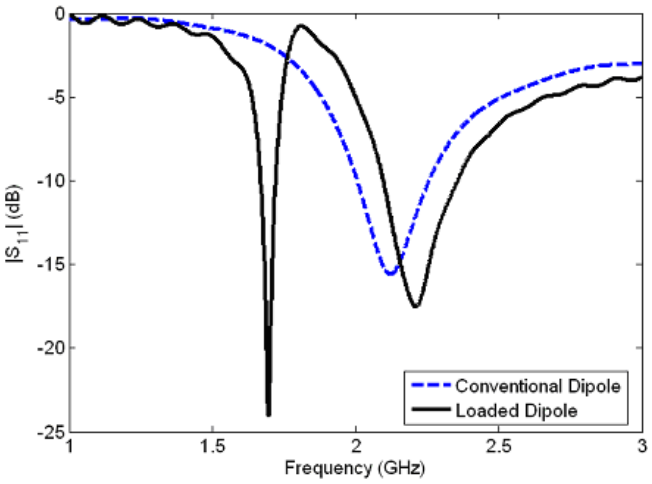

Figure 3.24: Reflection coefficient of the Omega-loaded and unloaded dipoles.

while it is $0.42\lambda_0$ at the second frequency. This means that miniaturization is achieved for the first frequency. The ratio between the working frequencies is smaller than 1.25, which cannot be achieved with conventional approaches.

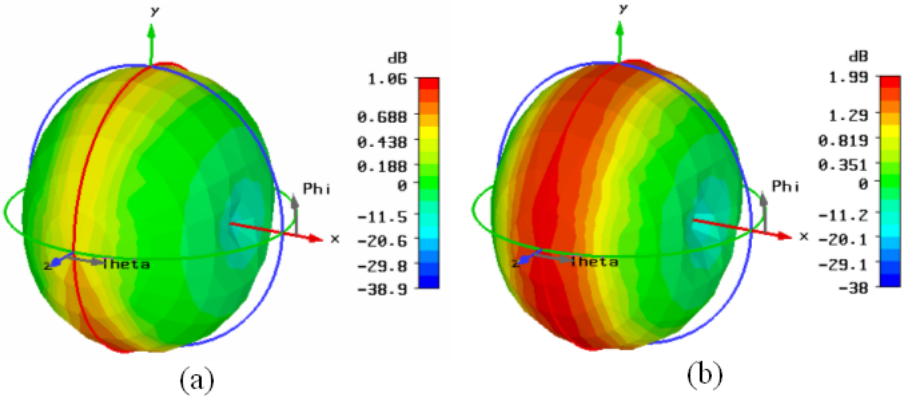

Figure 3.25: Simulated radiation patterns of the proposed Omega-loaded dual-band antipodal dipole. (a) 1.70 GHz. (b) 2.21 GHz.

The radiation patterns at the two working frequencies are shown in Fig. 3.25. In both cases, the dipolar radiation pattern is obtained. The computed gain is 1.06 dB at the first frequency, while it is 1.99 dB at the second one. The gain is smaller at the first frequency because the electrical length of the antenna is also reduced.

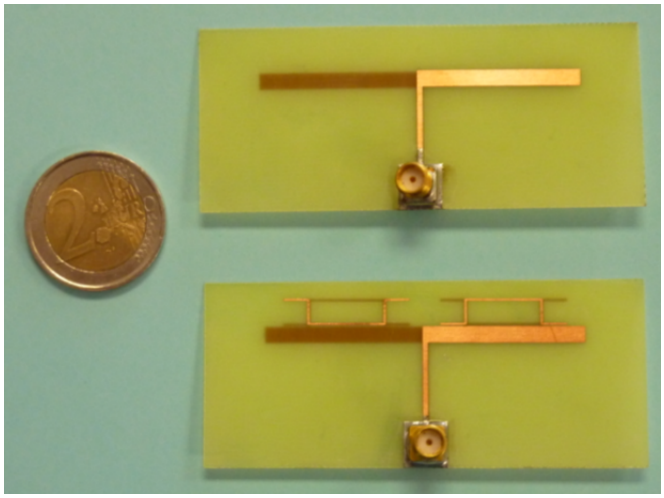

Figure 3.26: Picture of the manufactured Omega-loaded and unloaded dipoles.

A prototype of the previous miniaturized dual-frequency printed dipole has been manufactured. The unloaded dipole with the same dimensions has also been manufactured. The picture of both prototypes is shown in Fig. 3.26. The measured reflection coefficients of both antennas are plotted in Fig. 3.27. The results are very similar to the computed ones (Fig. 3.24). There is only a slight shift towards higher frequencies due to the tolerances of the manufacturing process. However, the ratio between the working frequencies is maintained and the first resonance frequency of the loaded dipole is below the fundamental frequency of the unloaded one, demonstrating the miniaturization capability of this approach.

3.2.5 Multifrequency Performance of Metamaterial-Loaded Printed Dipoles

The approach to obtain multifrequency printed dipoles (printed dipoles with three or more working frequencies) consists of exciting two or more additional resonances. These additional resonances are obtained by loading the dipole with different pairs of metamaterial particles. At least one metamaterial particle per dipole strip must resonate at each desired additional frequency. As an example, a triple-frequency printed dipole is proposed below.

According to Fig. 3.28, let us consider the case in which each dipole strip is loaded with two SSRs, each of them with different radius: $R_2 = R_1 + 0.40$

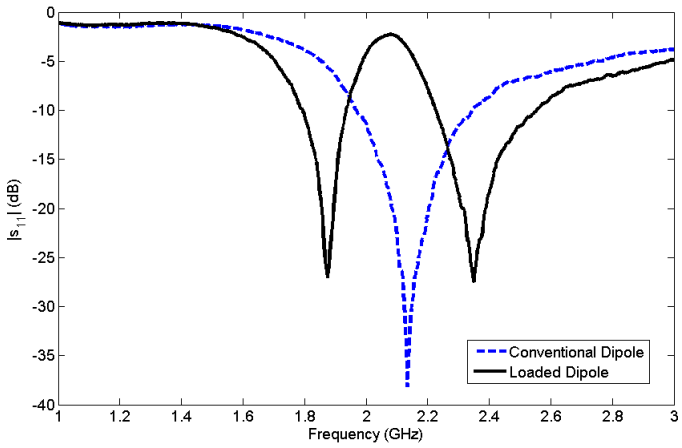

Figure 3.27: Measured reflection coefficient of the manufactured Omega-loaded and unloaded dipoles.

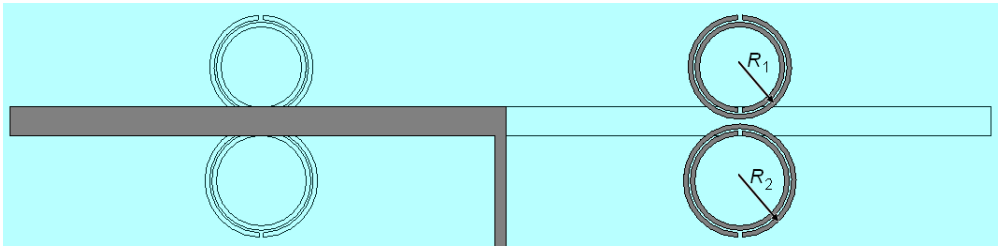

Figure 3.28: Sketch of the proposed triple-frequency printed dipole.

mm. In this case, the resonant frequencies of the SRRs above and below the dipole are separated 0.22 GHz and a triple-frequency antenna can be obtained.

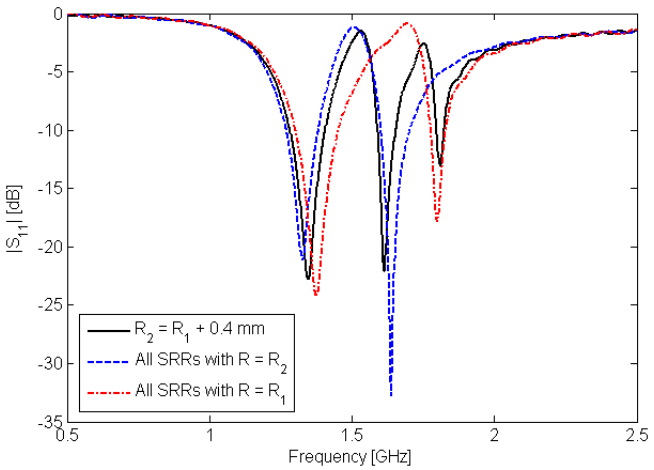

Figure 3.29: Reflection coefficient of the triple-frequency printed dipole antenna. The same information for the cases in which all the SRRs have the same dimensions is also plotted.

Fig. 3.29 shows the simulated (CST Microwave Studio ®) reflection coefficient for the proposed triple-frequency antenna. The three working frequencies can be easily identified. The $|s_{11}|$ parameter of the dipoles loaded with both SRRs with $R = R_1$ and $R = R_2$ are also plotted. These plots show that the three resonances of the triple-frequency antenna are due to the self-resonant frequencies of the dipole and the SRRs with different dimensions.

The simulated currents on the antenna at the three working frequencies are shown in Fig. 3.30. The distributions are similar to the one presented by the dual-frequency dipole (Fig. 3.17). The SRRs are not resonating at the first working frequency (f_1) and the currents on the dipole are similar to the unloaded dipole. The SRRs with R_2 are resonating at the second working frequency (f_2). The current on the dipole is mostly between the sets of SRRs and there is almost no current between the SRRs and the edges of the dipole. At the third working frequency (f_3) the distribution is similar to the previous one (f_2) but the SRRs with R_1 are resonating instead of the R_2 SRRs. The radiation pattern is dipolar at the three working frequencies.

A prototype of the triple-frequency printed dipole has been manufactured. This prototype is based on the reference dipole (Section 3.2) which has been loaded with two SRRs per dipole strip. The difference between the radius of

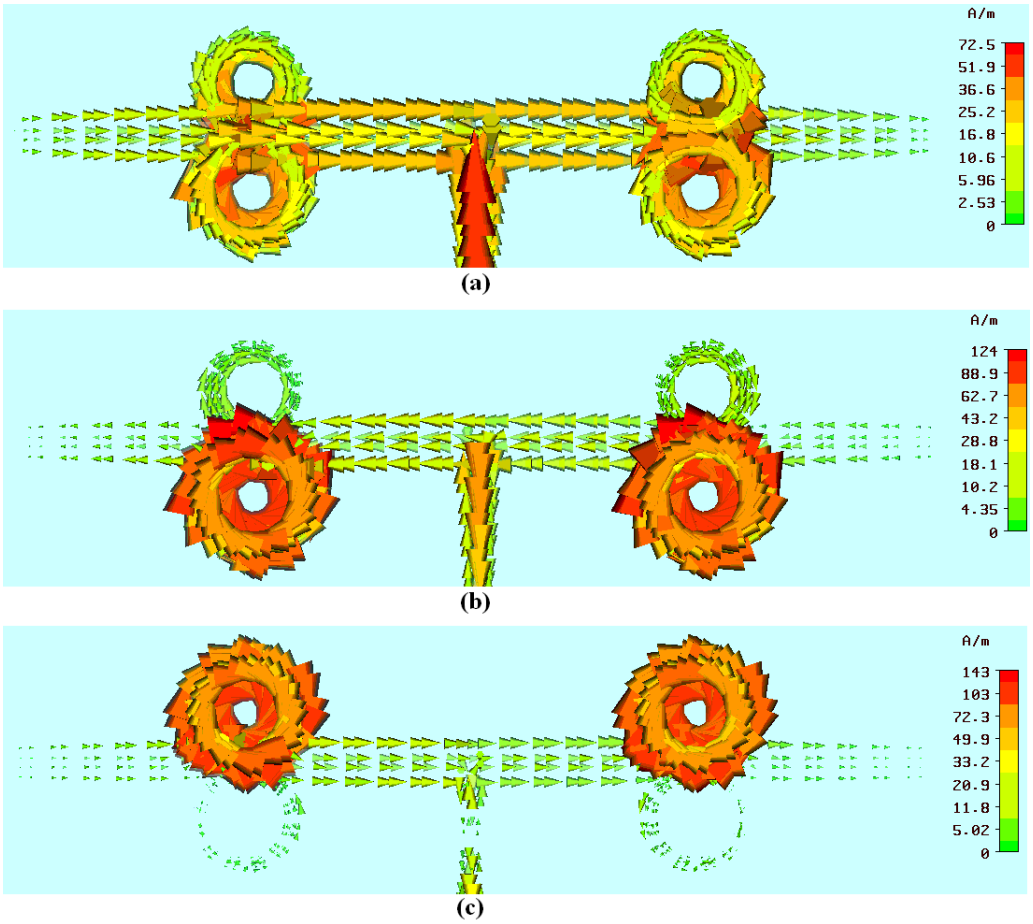

Figure 3.30: Currents on the triple-frequency printed dipole loaded with SRRs. (a) f_1 (fundamental frequency of the unloaded dipole). (b) f_2 (resonant frequency of the SRRs with R_2). (c) f_3 (resonant frequency of the SRRs with R_1).

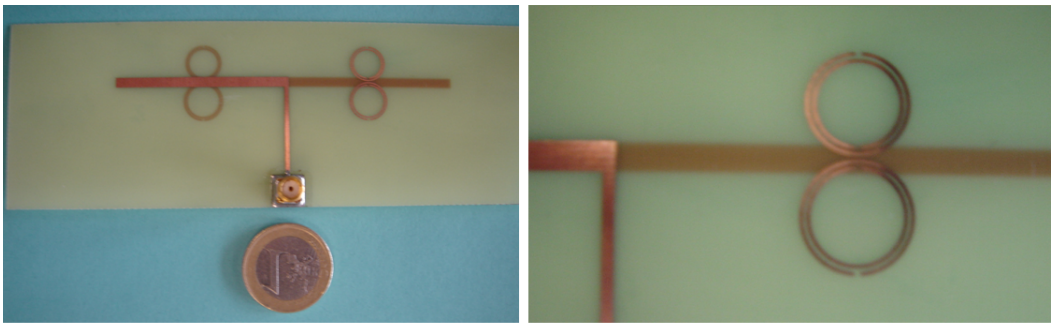

Figure 3.31: Pictures of the manufactured triple-frequency printed dipole loaded with SRRs. (a) View of the antenna. (b) Zoom on the SRRs with different external radius.

the pair of SRRs in each strip is 0.40 mm. Fig. 3.31 shows the pictures of this antenna, where the difference between the radius of the SRRs can be appreciated. The measured reflection coefficient of this manufactured prototype and the reference dipole are shown in Fig. 3.32. Three different working frequencies can be seen in the loaded dipole: 1.38 GHz, 2.07 GHz and 2.30 GHz. The first one is in the vicinity of the fundamental frequency of the unloaded dipole, while the other two resonance frequencies are due to the SRRs with different radius. The ratio between the additional frequencies and the fundamental one are 1.50 and 1.67 for the first and second additional frequencies, respectively. The ratio between both additional frequencies is only 1.11. These results show the validity of the proposed approach to develop multifrequency printed dipoles with arbitrary ratios.

3.2.6 Equivalent Circuit Model of Metamaterial-Loaded Printed Dipoles

In the present Section multifrequency metamaterial-loaded printed dipoles have been successfully developed. Although it seems difficult to achieve a complete analytic model to design this kind of antennas, any attempt to reduce the computational effort associated with the design of these antennas is welcome. In this sense it may be good to develop an equivalent circuit approach that simplifies the design of this kind of antennas. Moreover, equivalent circuit models explain how and why the structure works and what its design parameters are.

Any metamaterial-loaded dipole antenna input impedance can be mod-

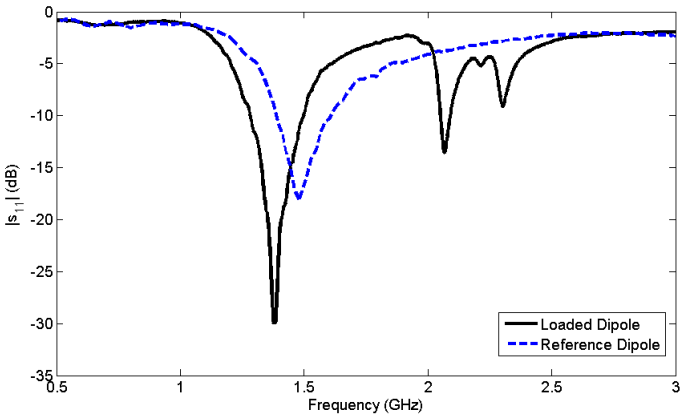

Figure 3.32: Measured reflection coefficient of the triple-frequency printed dipole antenna. The same information for the reference dipole is also plotted.

elled as a pair-resonant circuit. One of the resonance frequencies is related to the unloaded dipole length, as demonstrated in previous Subsections. The other is associated to the magnetic coupling between the antenna and the metamaterial particles at the particles self-resonant frequency. In addition, the equivalent circuit parameters of the dipole resonant circuit can be isolated from the resonant frequency associated with the metamaterial particles. Then, for the general case of a dipole loaded with MNG metamaterial particles, the equivalent network is shown in Fig. 3.33. A coupled resonator representing the particles is connected in series to each strip of the dipole. The coupled resonator is modelled by the following parameters: the unloaded quality factor Q, the coupling factor β (ratio between the unloaded quality factor and the external quality factor), the resonance frequency f_0 and a small capacitance c_a. This last capacitance comes from the common area between the particles and the dipole strips. The effect of this capacitor is to shift the resonant frequencies. This effect has been observed in all the implementations presented in the previous Subsections.

This circuit model can be used for any configuration of the metamaterial-loaded dipoles (one, two or four SRRs per dipole strip, spiral resonators, Omega particles, etc.) by only adequately choosing the parameters of the equivalent circuit. Moreover, it can be also used when two or more additional resonances are obtained. In that case, for each additional resonance another coupled resonator per dipole strip must be added to the model.

Thanks to the proposed equivalent circuit model, the operation principle of this kind of antennas can be explained in a simple way. In the initial ex-

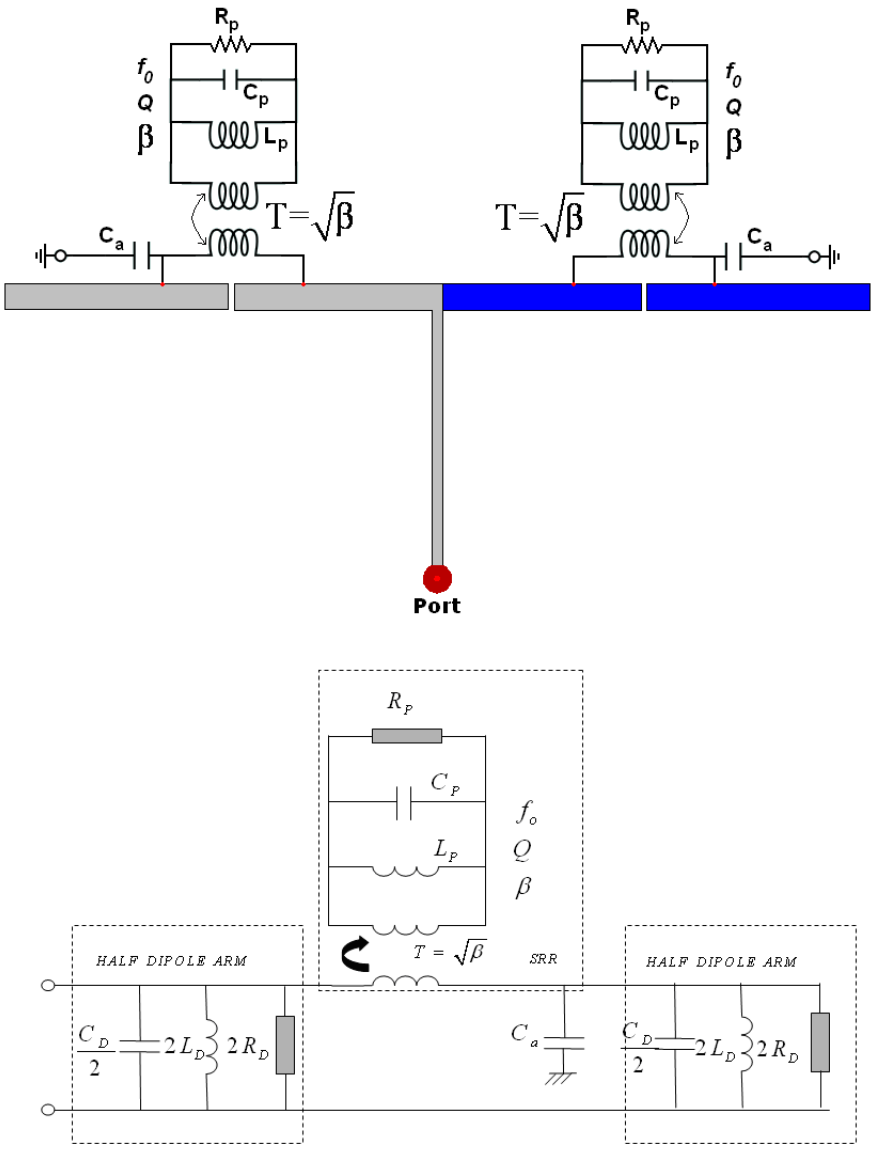

Figure 3.33: Equivalent circuit model of the antipodal printed dipoles loaded with magnetic metamaterial particles.

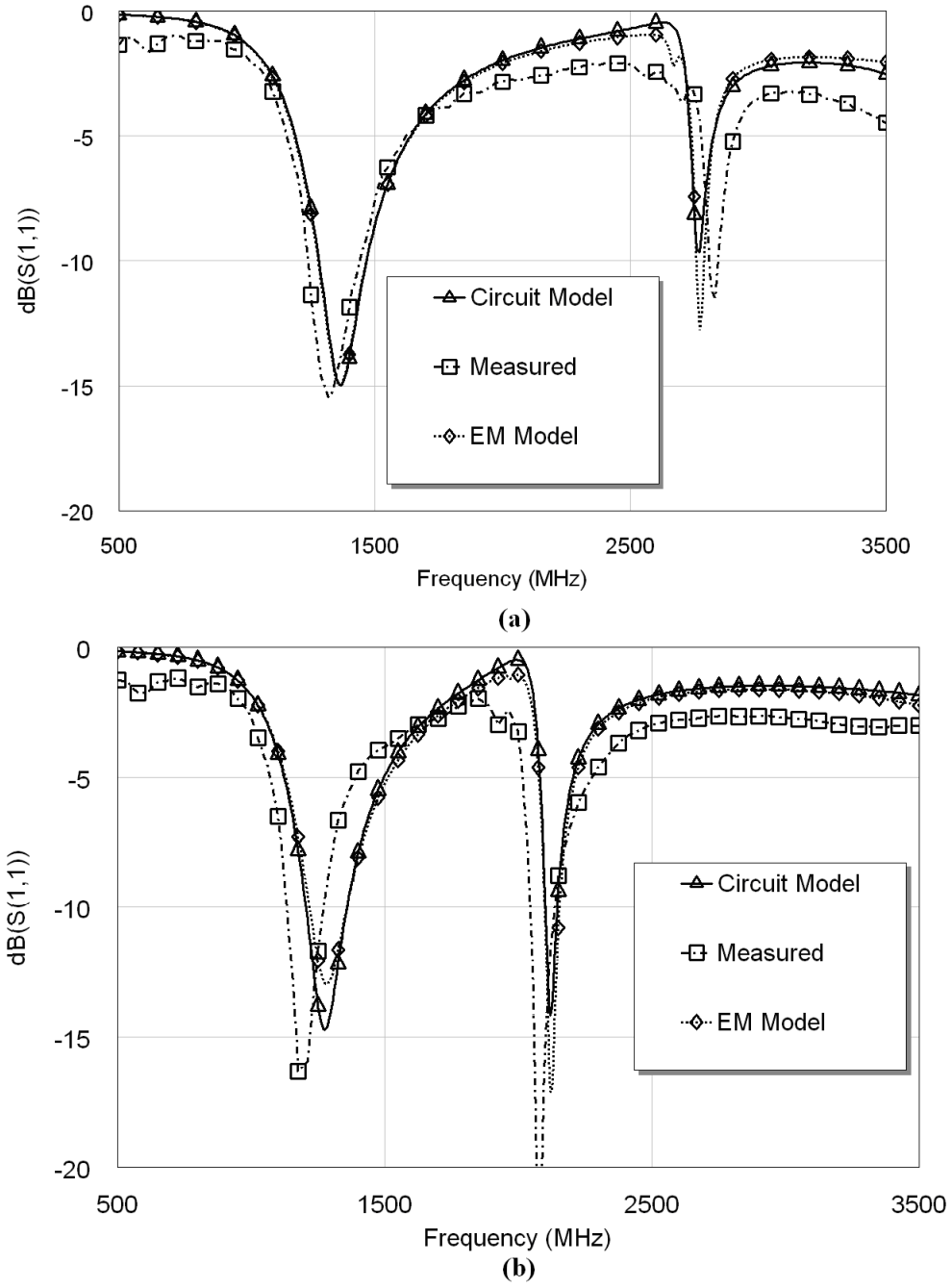

Figure 3.34: Reflection coefficient of the dual-band SRR-loaded dipoles computed with the equivalent circuit model and the FW simulator. The measured reflection coefficients are also plotted. (a) Dipole loaded with 4-mm-radius-SRRs. (b) Dipole loaded with 5-mm-radius-SRRs.

amples (dual-frequency dipoles loaded with SRRs, Subsection 3.2.3) at the first working frequency, the magnetic metamaterial particles are not excited, so the resonance frequency is determined by the length of the whole dipole ($\lambda_1/2$). On the other hand, the antenna second working frequency is determined by the resonant frequency of the particles. At this second frequency, the metamaterial particles are excited causing a magnetic wall (open circuit) at the position where they are placed. In this way, the current only flows on the dipole between the positions of the MNG metamaterial particles. The particles can be placed at any position along the dipole strip. However, in order to achieve a good matching condition, the particles should be placed at a particular distance c as shown in previous Subsections. Other way, the obtained input impedance will present a high inductance or capacitance behaviour leading to a poor matching. The effect of coupling more particles per dipole half (e. g. four particles instead of one per dipole half) is that the open-circuit condition is strengthened. This means that, in the equivalent circuit, the coupling and quality factors are increased. Thus, the Q factor increases as the electromagnetic coupling gets higher what causes that more energy is stored. As the equivalent circuit is the same even though the number of resonators increases, the quality and the coupling factors have to rise up because of the stored electromagnetic energy enlargement. Therefore, the assumption of a magnetic wall is better when the number of particles increases.

In order to show the validity of the proposed model, the two dual-frequency SRRs-loaded printed dipoles presented in Subsection 3.2.3 have been simulated with the proposed model and a full-wave electromagnetic simulator (Momentum ®). The adequate parameters for the dipole loaded with 4-mm-radius SRRs are: $Q = 327$, $f_0 = 2.71$ GHz, $\beta = 95$ and $c_a = 0.11$ pF. The values for the dipole loaded with 5-mm-radius SRRs are: $Q = 344$, $f_0 = 2.10$ GHz, $\beta = 87$ and $c_a = 0.16$ pF. An excellent agreement between the measurements, the full-wave simulator and the proposed model results can be seen in Fig. 3.34.

Furthermore, the equivalent circuit model of the triple-frequency loaded-dipole presented in Subsection 3.2.5 has also been simulated. As commented above, the use of metamaterial loading particles with different self-resonant frequencies is represented in the model with different coupled parallel tanks. For the case of the triple-frequency dipole, there are SRRs with two different sizes which leads to two additional resonance frequencies. Hence, two additional resonators are coupled to the equivalent circuit model of the dipole, as shown in Fig. 3.35. As the dipole is unchanged with respect to the previous examples, the parameters of the dipole (C_D, L_D, R_D) are the same.

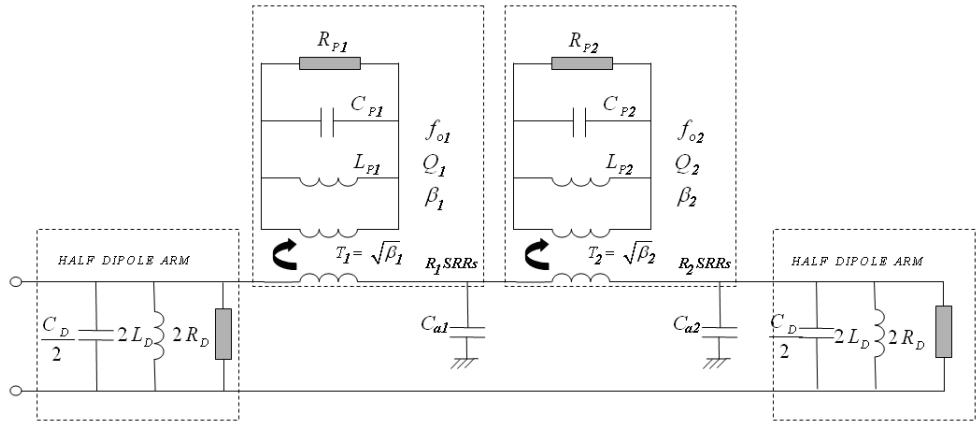

Figure 3.35: Equivalent circuit model of the triple-frequency dipole loaded with metamaterial particles (Subsection 3.2.5).

The parameters of the coupled resonators are $Q_1 = 200$, $f_{01} = 2.07$ GHz, $R_{p1} = 120\ \Omega$, $\beta_1 = 18.80$ and $c_{a1} = 0.08$ pF for the first tank and $Q_2 = 150$, $f_{02} = 2.30$ GHz, $R_{p2} = 90\ \Omega$, $\beta_2 = 18.80$ and $c_{a2} = 0.08$ pF for the second one. Fig. 3.36 shows the reflection coefficient computed with the proposed equivalent circuit model and the measured results. A great agreement between both results can bee seen. In this way, the proposed circuit approach serves as a powerful tool for the design of this kind of antennas.

3.3 LH Wire Antennas over Ground Plane

3.3.1 State of the Art of LH-Loaded Wire Antennas

As it was commented in the Introduction of this Chapter (Section 3.1), electrically small antennas (or miniaturization) is one of the hot topics in antenna engineering. However, electrically small antennas are difficult to match to any realistic source because of their very large reactance. Thus, considerable effort must be taken in the design of a matching network that conjugate matches the small antenna impedance [88]. Furthermore, the matching network increases the total size of the system which is contrary to the final goal. Recently, the group of Prof. Peter S. Hall (University of Birmingham) has successfully developed wire antennas (dipole and loop antennas) with LH loading [123, 124, 125]. These antennas are electrically small with internal matching. Moreover, the use of LH loading elements provides new features

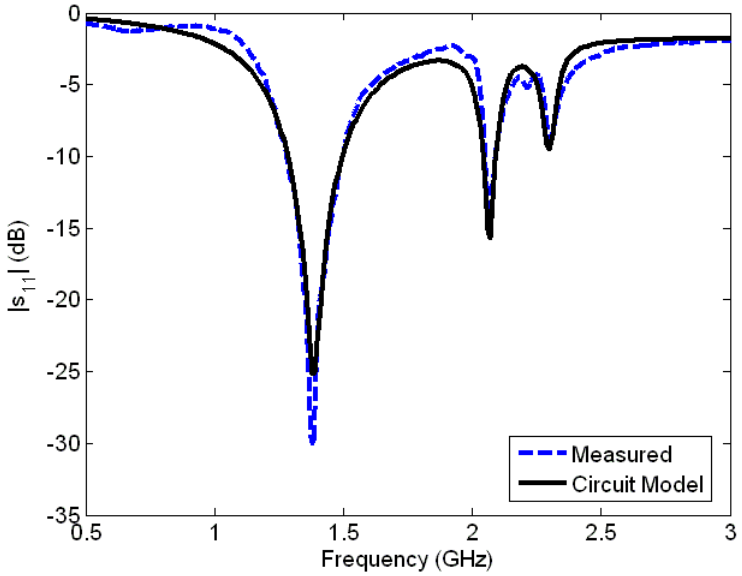

Figure 3.36: Reflection coefficient of the triple-frequency dipole loaded with metamaterial particles computed with the equivalent circuit model. The experimental results are also plotted.

which are described below.

Dipoles based on the metamaterial transmission line approach are a LH ladder network [123, 124]. This ladder network is a periodic structure whose unit element is the typical LH unit cell, formed by series capacitors (C_L) and a shunt inductor (L_L). This kind of dipole antenna is implemented by using two wires (as shown in Fig. 3.37). The capacitors are put on the wire connected to the feed and the inductors are placed in the interconnections between the two wires. The antenna is fed through a balun. The currents through the two wires are out-of-phase, but their amplitudes are different which produces radiation. The resonant frequencies and the impedance depends on the elements of the unit cell, as in all the LH resonators. Thus, small antennas with internal matching can be achieved.

A LH dipole can be modelled as a LH resonator with open ends. In particular, if we take into account the residual effect of the host wires, a CRLH resonator with open ends is a more accurate model. This means that the LH dipoles have the extraordinary features of a CRLH resonator:

- These dipoles have resonant modes with negative indices. Moreover, the number of modes depends on the number of unit cells used. The order in the frequency spectrum of the negative-index modes are the opposite

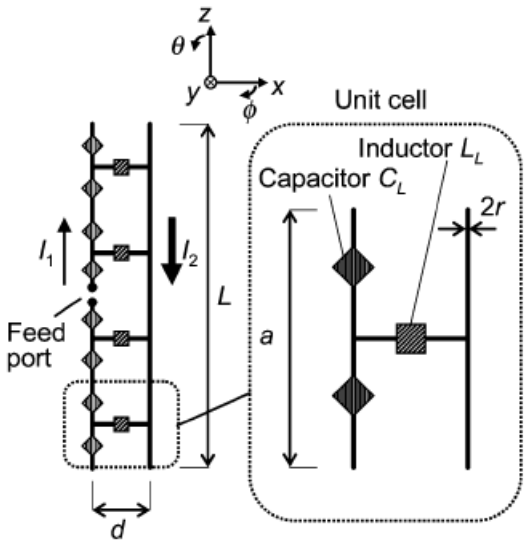

Figure 3.37: Sketch of a dipole loaded by LH network [123, 124].

to the conventional (or RH) modes. This means that a LH antenna with N cells has the following potential modes in the LH region: $n = -N+1, -N+2, \ldots, 0$

- In the LH operation region ($n < 0$), a decrease in the frequency results in decreasing the wavelength of the current on the antenna, which is contrary to the conventional behaviour and the operation in the RH region ($n > 0$).
- The resonant frequencies do not follow a linear ratio between them. The ratio between the frequencies can be controlled by the values of the components (C_L and L_L).
- As it is shown in [124], the resonant frequencies of the dipoles can be computed, with a very small error, by sampling the dispersion diagram of the infinite transmission line. This approach was demonstrated for any CRLH resonator in [58]. This means that the Eigenfrequency method presented in Section 2.5 can be applied to this kind of antennas.

Different implementations have been presented till now. The simplest implementation consists of loading the two wires with chip inductors and capacitors, but other implementations based on distributed elements have also been studied. In [124] two prototypes based on interdigital capacitors and meandered inductors have been manufactured and measured. The first

prototype is a short dipole with $N = 4$ cells, working at the $n = -1$ mode. Its resonant frequency is 547 MHz and its size is only 0.18 wavelengths in free space. The gain of the antenna is -3.9 dB with cross-polarization lower than -13 dB and the bandwidth is 1.7% for $|s_{11}| < -10$ dB. The other LH antenna presented in the paper is a meandered dipole antenna based on $N = 18$ cells working at the $n = -9$ mode. This antenna has orthogonal polarization with respect to the conventional dipoles. The size of the antenna is 0.77 wavelengths in free space at 643 MHz. The gain of the antenna is -11.7 dB, with cross-polarization lower than -6.8 dB.

The other implementation based on distributed elements is composed of parallel plate capacitors and spiral inductors [126]. In that paper a dipole with $N = 4$ LH cells working at $n = -1$ mode is presented. The working frequency is 487 MHz and the gain is -1.94 dB with a cross-polarization lower than -12 dB. The size of the antenna is only 0.16 wavelengths in free space. The efficiency of the different implementations is also studied in this paper. It is concluded that the implementation based on parallel plate capacitors and spiral inductors achieves the highest value of efficiency. A further study of the efficiency of these antennas has recently been presented in [127].

Only the odd modes are excited in the LH dipoles, while the even modes are not excited because they are anti-resonant in the dipolar geometry. It is interesting to obtain a geometry with even modes because the $n = 0$ mode has exceptional characteristics: it presents a uniform current distribution in amplitude and phase, which gives a radiation pattern orthogonal to the one given by conventional antennas. For this reason, LH loops are proposed [125] as a solution to excite the even modes.

The geometry of the LH loop is shown in Fig. 3.38. It is based on the typical LH ladder network with series capacitors and shunt inductors. The disposition is similar to the one proposed for the dipoles, which means that the capacitors are put on the fed wire and the inductors are placed between the interconnections of the two wires. In this case, the two wires forme close loops. A balun is used to feed the antenna. For a loop composed of N cells, the excited modes are $n = -N, -N + 2, \ldots, 0, +2, \ldots$. The implementation proposed in [125] is a LH loop made of $N = 4$ cells and the antenna has one wavelength circumference at 500 MHz. The proposed loop in this paper has been manufactured and measured. The prototype works at 500 Mhz ($n = 0$ mode) and the gain is 0.3 dB with a cross-polarization lower than -21.8 dB. As it can be deduced from the gain value, the efficiency of this mode is very high ($> 90\%$). The radiation pattern is omnidirectional in the plane of the loop, in contrast to the conventional figure of eight.

Recently, varactor diodes have been used instead of capacitors to obtain

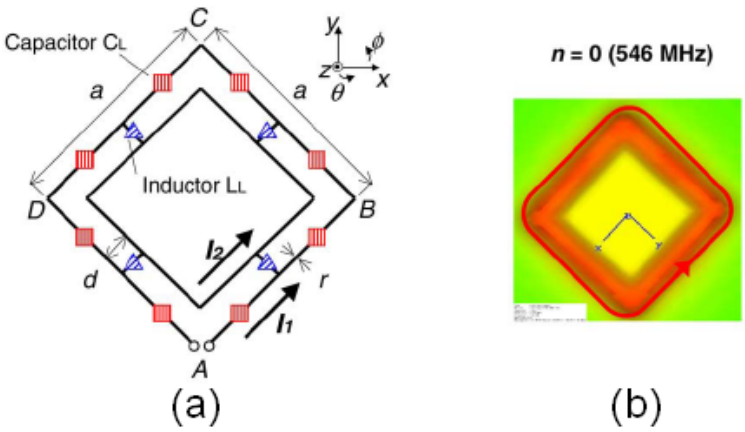

Figure 3.38: LH loop antenna [125]: (a) Configuration. (b) Simulated absolute near H-field distribution for the $n = 0$ mode.

a dual mode performance of the LH loop antenna [128]. This approach allows switching between the $n = 0$ and $n = +2$ modes at the same frequency (546 MHz) which gives two orthogonal radiation patterns.

The main drawback of these LH antennas is the need of a feeding balun. This implies several disadvantages: it makes more difficult the design of these antennas, it introduces losses reducing the efficiency of the overall antenna, it produces undesired resonances and has a limited bandwidth. The proposed approach to overcome these disadvantages is the use of a finite ground plane. Thus, a SMA connector can be directly soldered to the antenna avoiding the use of a balun. Moreover, the use of a ground plane has another important advantage because the length of the antenna can be reduced to the half. This is explained by image theory and it is well known that the length of a monopole over a ground plane is half the length of a dipole working at the same frequency [129]. This size reduction is very interesting; for example, in the case of the LH loop the total circumference of the proposed implementation is one wavelength. In the next Subsections, LH wire antennas over ground plane are presented. In particular, the LH monopole antenna is presented in Subsection 3.3.2 achieving a monopolar radiation pattern with size reduction and no need of a balun. In Subsection 3.3.3 the LH half-loop antenna over ground plane is developed. This antenna has a radiation pattern with maximum orthogonal to the ground plane which cannot be achieved with other wire antennas over ground plane. Moreover, it has a high efficiency and size reduction compared to the loop antennas.

3.3.2 LH Monopole Antenna

The proposed LH monopole antenna is a ladder network over a finite ground plane. The ladder network is a periodic structure whose unit element is the typical LH unit cell, formed by two series capacitors C_L and a shunt inductor L_L. This kind of monopole antenna is implemented by printing two parallel strips on a dielectric substrate (as shown in Fig. 3.39). An interconnection between both strips is also printed for each unit cell. One of the strips is connected to the feed while the other one is connected to the ground plane. The dielectric substrate is orthogonally mounted over the ground plane. The antenna is fed through a SMA connector. The outer conductor of the SMA connector is soldered to the ground plane while the inner conductor is soldered to the feeding strip. The capacitors are put on the strip connected to the feed and the inductors are placed in the interconnections between the two strips. The resonant frequencies and the input impedance depend on the elements of the unit cell, as in all the LH resonant structures [24]. Thus, the antenna operation frequency can be set by a proper choice of the unit cell elements (C_L and L_L). Internal matching can be obtained by a proper selection of these elements.

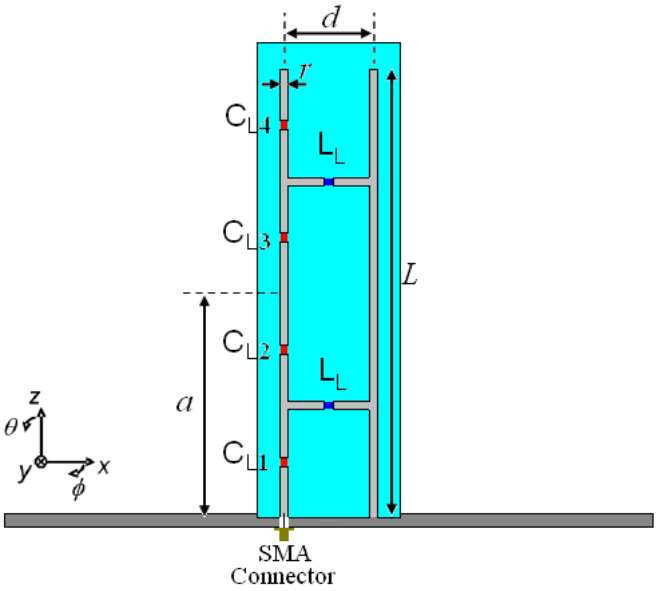

Figure 3.39: Sketch of the LH monopole antenna. In this example, the number of unit cells is set to $N = 2$.

In a practical implementation, the monopole antenna is limited to N unit cells. In addition to N, the other antenna parameters are the length of the

strips L, the separation between the strips d and the width of the strips r. These parameters result in a period a given by the ratio L/N.

The monopole antenna is a LH resonant structure in which each mode corresponds to a standing wave on the monopole which satisfies the following relation

$$L = |n|\frac{\lambda_a}{4} \tag{3.7}$$

where L is the length of the monopole, λ_a is the wavelength of the standing wave on the monopole antenna and n is the resonance number. In LH resonant antennas, n is a negative integer which decreases with decreasing frequency.

In general, for a LH resonant structure composed of N unit cells, the index n takes values from $-N+1$ to -1 (considering only the LH working region). For the particular case of the monopole antenna, image theory can be applied because of the presence of the ground plane. This makes that for a LH monopole antenna composed of N unit cells, n takes values: $n = -2N+1, -2N+2, -2N+3, \ldots, -1$ in the LH operation region.

The structure of the monopole antenna imposes an open circuit boundary condition at the open edges of the strips which implies a minimum in the current distribution at these points. On the other hand, a maximum in the current distribution must occur at the opposite edges because they are connected to the feed and the ground plane. These boundary conditions impose that only odd modes can be excited in the monopole antenna. For example, in the case of the LH monopole antenna composed of $N = 2$ unit cells, only the modes with $n = -3, -1$ are excited.

Considering the previous example, Fig. 3.40 shows the current distributions on the LH monopole antenna for both modes. In the case of the $n = -1$ mode the current distribution on each of the strips has a quarter-wavelength electrical length and is similar to the fundamental mode of the conventional monopole antenna. It is important to note that the currents on both strips have opposite directions, but their amplitudes have different values which produces radiation in the far field [124]. The current distribution of the mode with $n = -3$ has three quarter-wavelengths electrical length on each strip, as expected. Once again the currents have opposite directions on each strip, but the amplitudes are different. In both cases, a monopolar radiation pattern with maximum in the plane of the ground plane and null orthogonal to the ground plane is obtained, as shown in Fig. 3.41.

The resonance frequencies corresponding to the LH monopole antenna can be obtained by considering the relation between the phase constant β

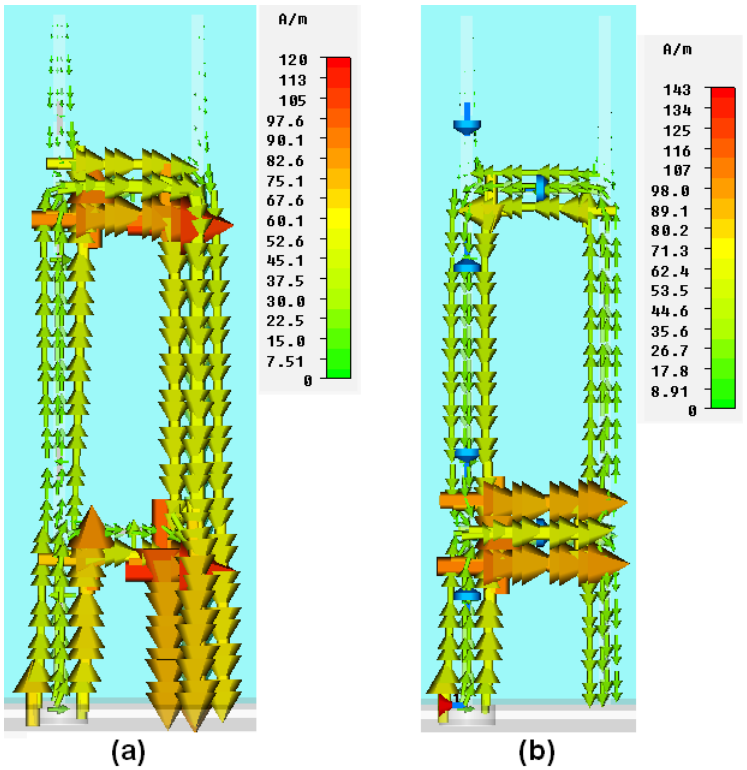

Figure 3.40: Currents on the LH monopole antenna. (a) $n = -1$ mode. (b) $n = -3$ mode.

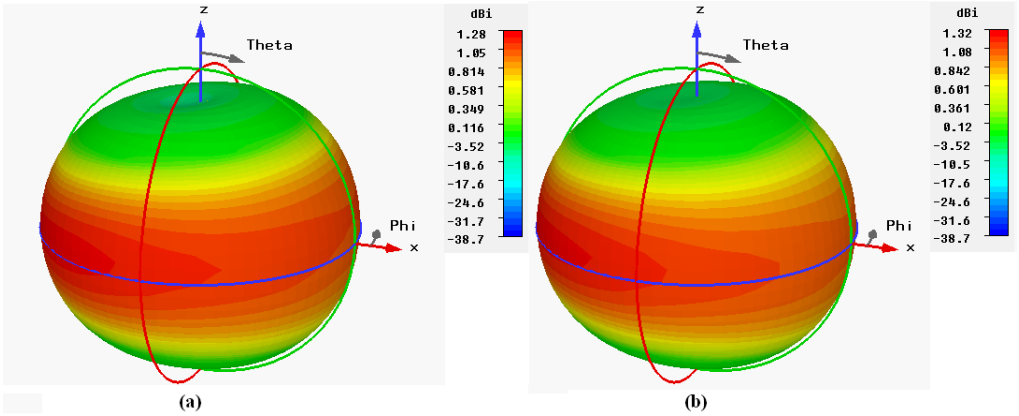

Figure 3.41: Simulated radiation patterns of the LH monopole antenna. (a) $n = -1$ mode. (b) $n = -3$ mode.

and the frequency. As a first approximation, the phase constant β can be obtained by considering an infinite transmission line composed of the LH unit cells and applying the Bloch-Floquet analysis, as shown in other LH resonant structures [24, 58, 124]. The resonance frequencies can be obtained by sampling the phase constant at the points

$$\frac{\beta a}{\pi} = \frac{|n|}{2N} \tag{3.8}$$

Fig. 3.42 shows the results for the monopole with $N = 2$ unit cells and the following parameters: $L = 50$ mm, $a = 25$ mm, $d = 10$ mm, $r = 0.90$ mm, $C_L = 0.5$ pF and $L_L = 20$ nH. The considered substrate is Duroid 5880 ($\varepsilon_r = 2.2$ and $\tan\delta = 0.0009$) with $h = 0.787$ mm. The computed resonant frequencies for this LH monopole are 782.5 MHz for the mode with $n = -3$ and 828 MHz for the mode with $n = -1$.

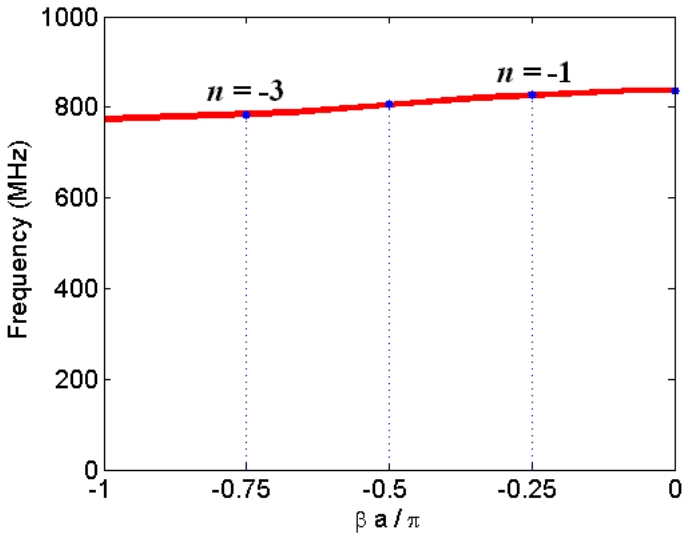

Figure 3.42: Dispersion diagram of the LH monopole antenna with $N = 2$ unit cells. The other parameters of the antenna are: $L = 50$ mm, $a = 25$ mm, $d = 10$ mm, $r = 0.90$ mm, $C_L = 0.5$ pF and $L_L = 20$ nH.

A prototype of the LH monopole with previous parameters have been manufactured and measured. SMD commercial components are used to implement the LH unit cell elements. The substrate is Duroid 5880 with $h = 0.787$ mm, $\varepsilon_r = 2.2$ and $\tan\delta = 0.0009$. The substrate is orthogonally mounted over a finite aluminium ground plane. A picture of the manufactured prototype is shown in Fig. 3.43. The simulated (CST Microwave Studio

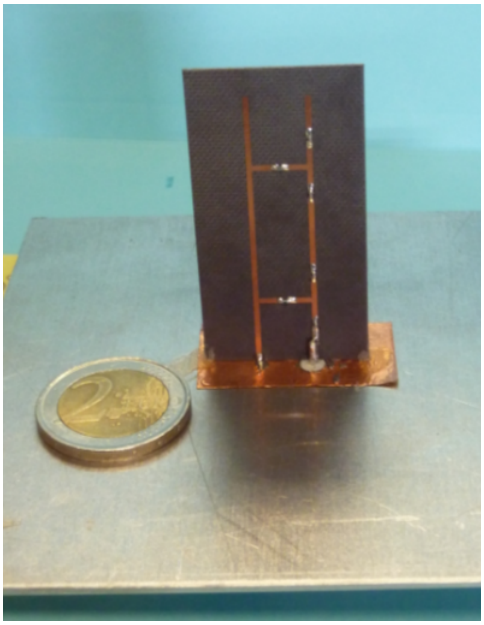

Figure 3.43: Picture of the manufactured LH monopole.

®) and measured reflection coefficient is shown in Fig. 3.44. The measured resonant frequencies are $f_{-3} = 751$ MHz and $f_{-1} = 828$ MHz. The value of the measured reflection coefficient is -17.7 dB at f_{-3} and -26.8 dB at f_{-1}. The efficiency of the antenna has been measured by using the Johnston-Geissler method based on the Wheeler Cap principle [14, 118, 119, 120]. This value is 57% at 828 MHz. The electrical length of the monopole is $0.14\lambda_0$ which is an important reduction compared to the conventional monopole.

Fig. 3.45 shows the measured radiation patterns of the manufactured prototype in the $x-z$ and $y-z$ planes at both resonant frequencies (f_{-3} and f_{-1}). The angular margin between $270° \pm 15°$ was not measured due to limitations in the anechoic chamber facility. A monopolar radiation pattern is obtained at both frequencies, as expected. In the case of the $n = -3$ mode, the null in the direction orthogonal to the ground plane is much deeper in the $y-z$ plane (-20 dB) than in the $x-z$ plane (-7.5 dB). This is not the case of the $n = -1$ mode, in which the radiation pattern has a null deeper than -14 dB in both planes. Cross-polarization is lower than -13 dB in the $x-z$ plane at f_{-3}. However, this magnitude is increased until -6 dB in the $y-z$ plane at that frequency. On the other hand, the cross-polar component is lower than -7.5 dB in both planes at f_{-1}.

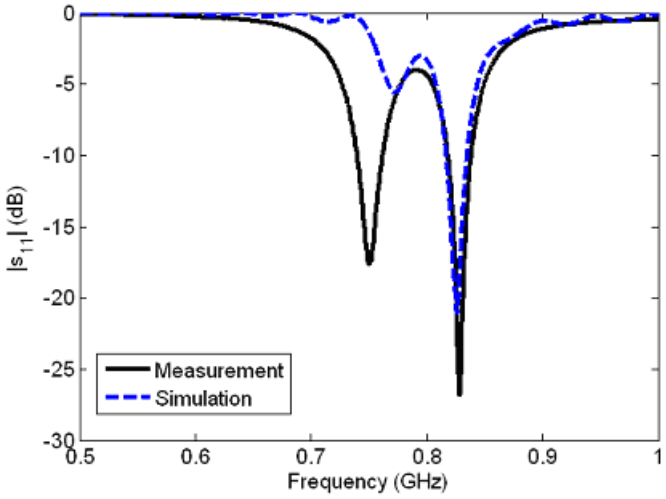

Figure 3.44: Simulated and measured reflection coefficient of the LH monopole antenna.

3.3.3 LH Half-Loop Antenna over Ground Plane

The LH half-loop antenna is also a ladder network over a ground plane whose periodic element is the typical LH unit cell. However, in this case the printed strips are folded and short-circuited to the ground plane forming a half-loop. This means that the outer strip has one end connected to the feed and the other one connected to the ground plane, whilst the inner strip has both ends connected to the ground plane. In this way the boundary conditions are changed from open circuits to short circuits. There are interconnections between the outer and inner strips. The capacitors C_L are connected to the outer strip, while the inductors L_L are put on the interconnections between the strips. The feeding scheme is the same as the one in the LH monopole antenna (a female SMA connector connected to the feed point with the outer conductor soldered to the ground plane).

This antenna is a LH resonant structure whose resonance frequencies depend on the elements of the unit cells. Each mode has a standing wave which satisfies the equation (3.7), being L the length of the half-loop, λ_a the wavelength of the standing wave on the half-loop antenna and n the resonance number. It is important to note that the boundary conditions imposed by this antenna are different than the ones in the monopole antenna. In this case, all the strip ends are connected to the feed or the ground plane, which implies maxima in the current distributions at all of these points. For this reason, only even modes are excited in this antenna, contrary to the monopole antenna

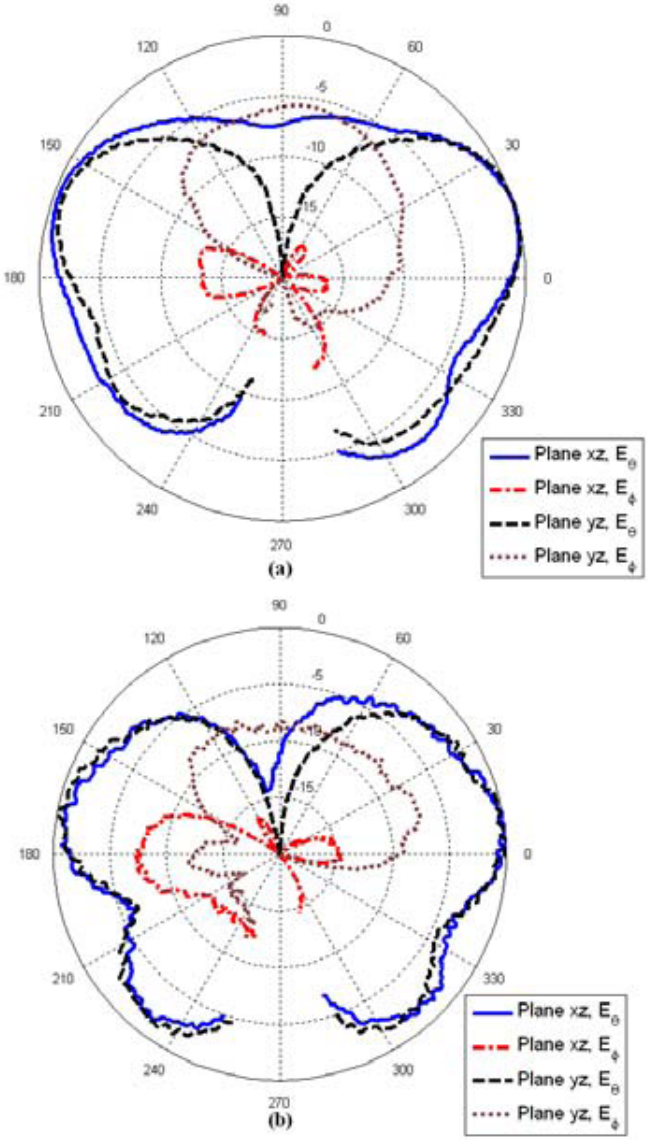

Figure 3.45: Measured radiation patterns of the manufactured LH monopole antenna. (a) $f_{-3} = 751$ MHz. (b) 828 MHz.

in which only odd modes were excited. Moreover, a mode satisfying equation (3.7) for $n = 0$ can be excited in this antenna. This provides interesting features as will be shown below. In conclusion, for a LH half-loop antenna composed of N unit cells, the modes with $n = -2N, -2N+2, -2N+4, \ldots, 0$ can be excited. For example, for a LH half-loop antenna with $N = 3$ unit cells, n takes value $-6, -4, -2, 0$ (considering the region with $n \leqslant 0$).

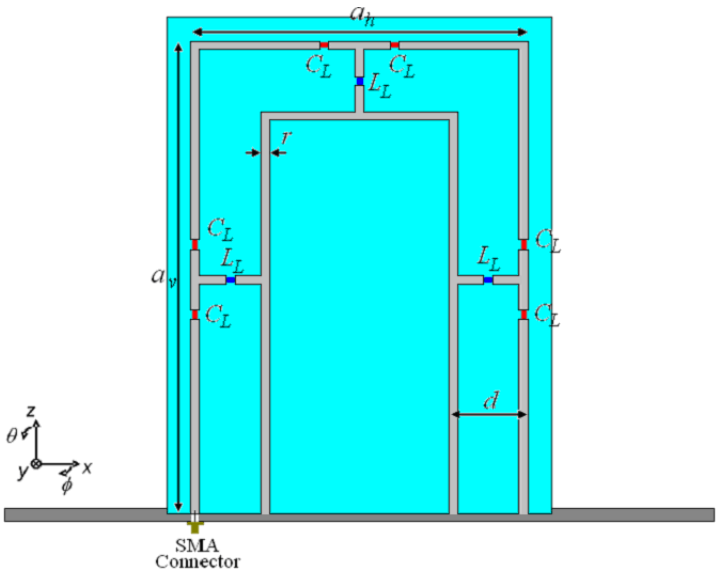

Figure 3.46: Sketch of the LH half-loop antenna over ground plane.

Fig. 3.46 shows the proposed implementation based on 3 unit cells. This antenna has been simulated (CST Microwave Studio ®) to compute the current distributions and radiation patterns of the different modes. The $n = 0$ mode is present in the antenna, as predicted by theory. This mode has the unique feature that the current on the strips is uniform in amplitude and phase (Fig. 3.47.a). This leads to a radiation pattern with maximum radiation orthogonal to the ground plane (Fig. 3.47.b) which cannot be achieved with other wire antennas mounted over a ground plane. Furthermore, E_ϕ is the main component in the $y-z$ plane, which is not the typical case of antennas mounted over a ground plane (see for instance the LH monopole antenna in the previous Subsection). Modes with negative indices ($n = -6, -4, -2$) are also present in the structure at frequencies lower than f_0. The $n = -6$ mode has a current distribution with six quarter-wavelengths electrical length on each strip (Fig. 3.48.a). The radiation pattern of this mode has the typical monopolar shape with a null at in the z axis and maximum radiation in the plane of the ground plane (Fig. 3.48.b). On the other hand, the $n = -4$

mode has also a radiation pattern with maximum radiation orthogonal to the ground plane (Fig. 3.48.d). However, it has been found by simulation that this mode has always very poor efficiency (< 15%). This mode has current distribution with four quarter-wavelengths electrical length on each strip (Fig. 3.48.c). Finally, the $n = -2$ mode has a current distribution with a null in the upper interconnection of the antenna which gives two in-phase quarter wavelengths on each strip (Fig. 3.48.e). This current distribution has the typical monopolar radiation pattern (Fig. 3.48.f).

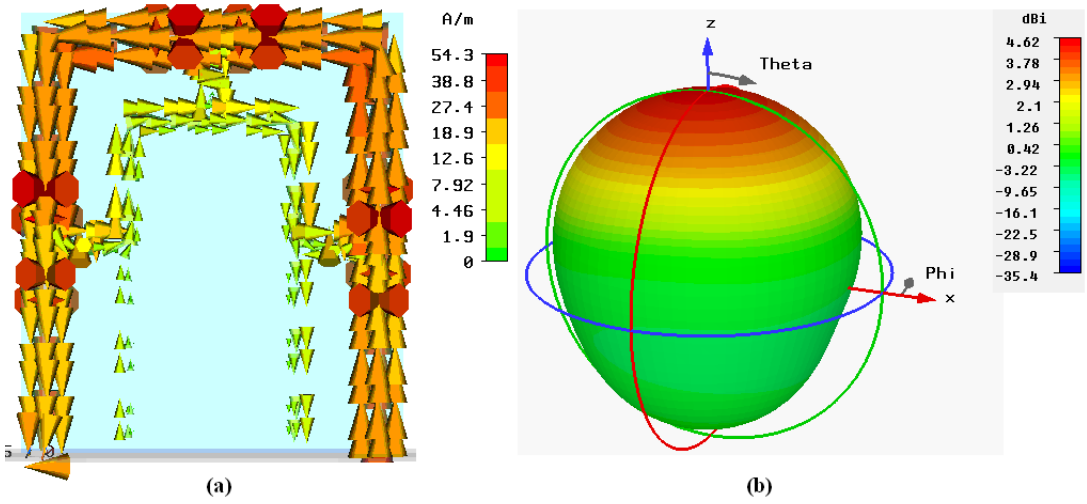

Figure 3.47: (a) Current distribution on the LH half-loop antenna over ground plane for the mode with $n = 0$. (b) Simulated radiation pattern of this mode.

A prototype of the LH half-loop antenna based on $N = 3$ unit cells has been designed, manufactured and measured (Fig. 3.49). The dimensions of the antenna, according to Fig. 3.46, are the following: length of the vertical cells $a_v = 50$ mm, width of the horizontal cell $a_h = 40$ mm, separation between the strips $d = 10$ mm, width of the printed strips $r = 0.90$ mm. The elements of the unit cells are $C_L = 0.5$ pF and $L_L = 10$ nH. SMD commercial components are used to manufacture the antenna. The substrate is Duroid 5880 with $h = 0.787$ mm, $\varepsilon_r = 2.2$ and $\tan\delta = 0.0009$. The substrate is orthogonally mounted over a finite aluminium ground plane. The length of the horizontal cell is different to the vertical ones in order to reduce the total size of the antenna. This modification respect to the periodic structure does not affect the performance of the antenna as it will be shown below. The simulated and measured reflection coefficients are shown in Fig. 3.50 where good agreement between both results can be seen.

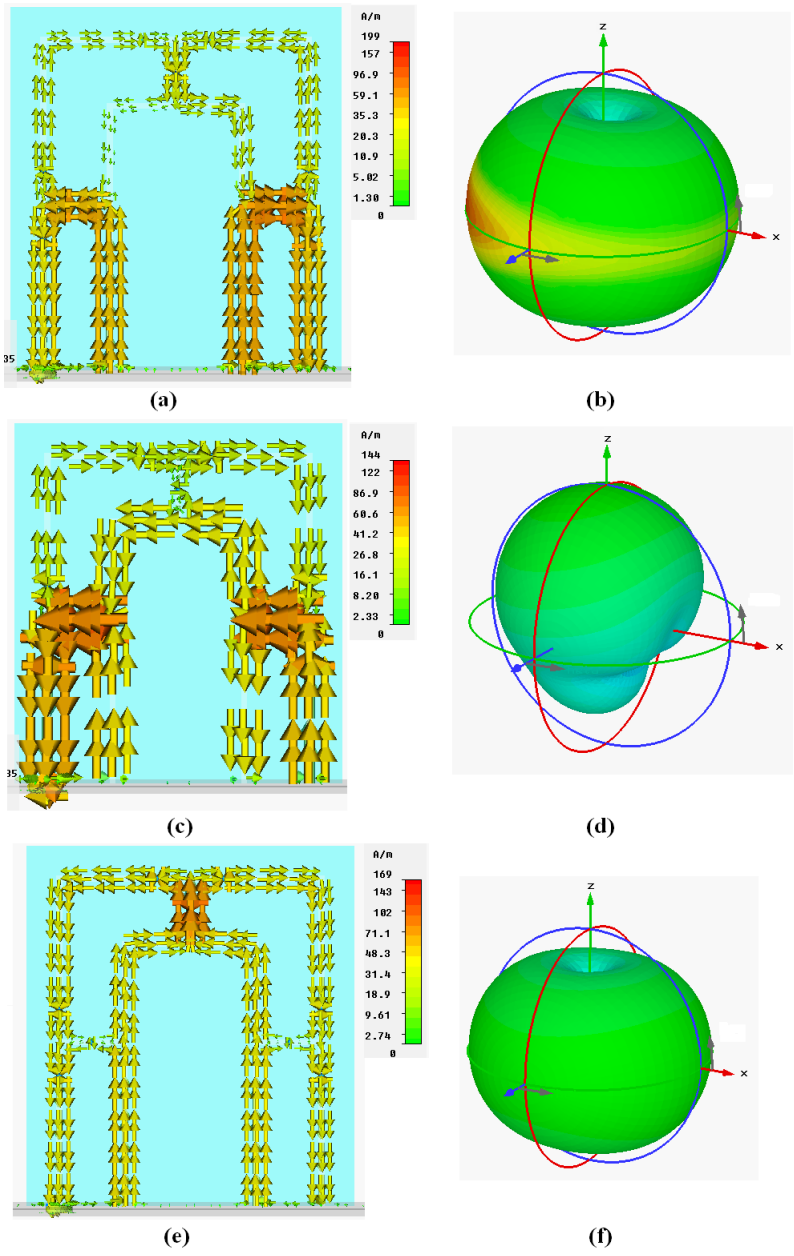

Figure 3.48: Current distributions on the LH half-loop antenna over ground plane of the modes: (a) $n = -6$, (c) $n = -4$ and (e) $n = -2$. Simulated radiation pattern of the modes: (b) $n = -6$, (d) $n = -4$ and (f) $n = -2$.

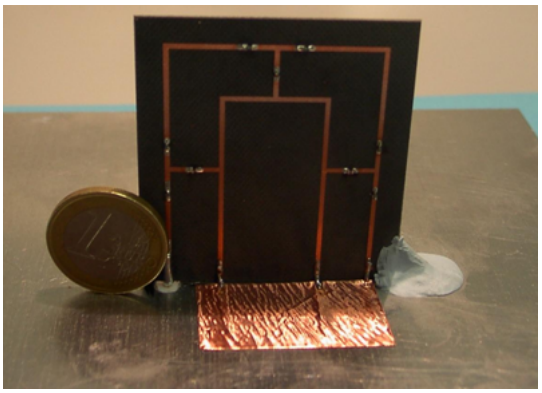

Figure 3.49: Manufactured prototype of the LH half-loop antenna over ground plane.

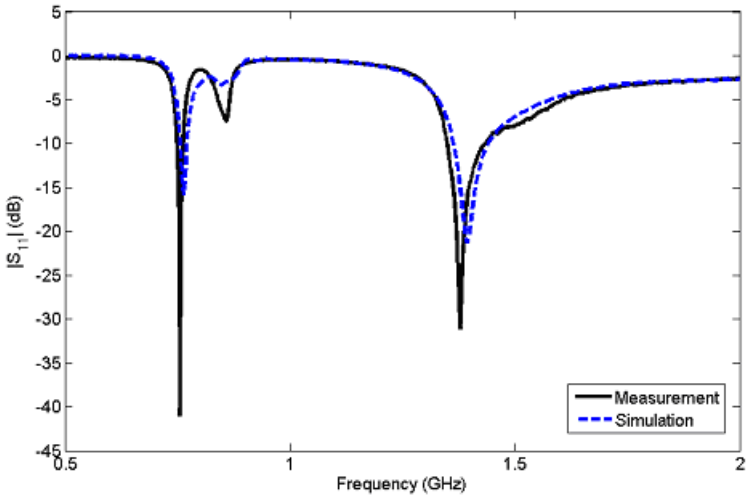

Figure 3.50: Simulated and measured reflection coefficient of the LH half-loop antenna.

The $n = 0$ mode resonates at $f_0 = 1.4$ GHz. The measured reflection coefficient of this resonance is -31.2 dB. Modes with negative indices are also excited in this implementation. In particular, the modes with $n = -6, -4$ can be identified in the simulated and measured reflection coefficient (Fig. 3.50), while the mode with $n = -2$ is not matched in this prototype. The frequency of the $n = -6$ mode is $f_{-6} = 755$ MHz and its measured reflection coefficient is -41.1 dB. The other mode with negative index ($n = -4$ mode) resonates at $f_{-4} = 858.5$ MHz and the measured $|s_{11}|$ at this frequency is -7.5 dB.

The radiation efficiency of this prototype has been measured by using the Johnston-Geissler method based on the Wheeler Cap principle [14, 118, 119, 120]. The measured radiation efficiency at $f_{-6} = 755$ MHz is 53%. On the other hand, it is only 7% at $f_{-4} = 858.5$ MHz, which confirms the very low efficiency of this mode. Finally, the measured radiation efficiency of the $n = 0$ mode is 87%, which proves that this mode has high radiation efficiency. The largest dimension of the antenna is only $0.13\lambda_0$ at 755 MHz and $0.23\lambda_0$ at 1.4 GHz.

The measured radiation patterns in the $x-z$ and $y-z$ planes at f_{-6} and f_0 are shown in Fig. 3.51. The angular margin between $270° \pm 15°$ was not measured due to limitations in the anechoic chamber facility. A monopolar radiation pattern is measured at f_{-6} with a cross-polarization below -14 dB in both planes. The expected radiation pattern with maximum orthogonal to the ground plane is measured at f_0, although an angular displacement is observed in the $x - z$ plane. This displacement has not been observed in other LH half-loops and it is not the generalized shape, as it will be shown in Section 5.3. In this particular example, this shift could be due to the coupling with higher order modes because the resonance frequency of the $n = 0$ mode is close to the highest that can be achieved because of the low value of the series capacitances $C_L = 0.5$ pF. The measured cross-polar component in this plane ($x - z$) is lower than -19 dB. On the other hand, the $y - z$ plane has the expected radiation pattern (maximum radiation orthogonal to the ground plane) with -20 dB of cross-polarization in the direction orthogonal to the ground plane. However, there is a higher cross-polar component in other directions. The reason could be the same as the one which causes the shift in the $x - z$ plane, because the level of the cross-polarization is much lower in this plane and this mode for other realizations of this antenna (see for instance Fig. 5.19 in Section 5.3.3). It is important to note that the main component in this plane is E_ϕ, as explained before, in contrast to the monopolar modes (e. g. $n = -6$) and other antennas mounted over a ground plane (see for instance the previous Subsection). Furthermore, the back radiation of the antenna at this mode is very low in both planes.

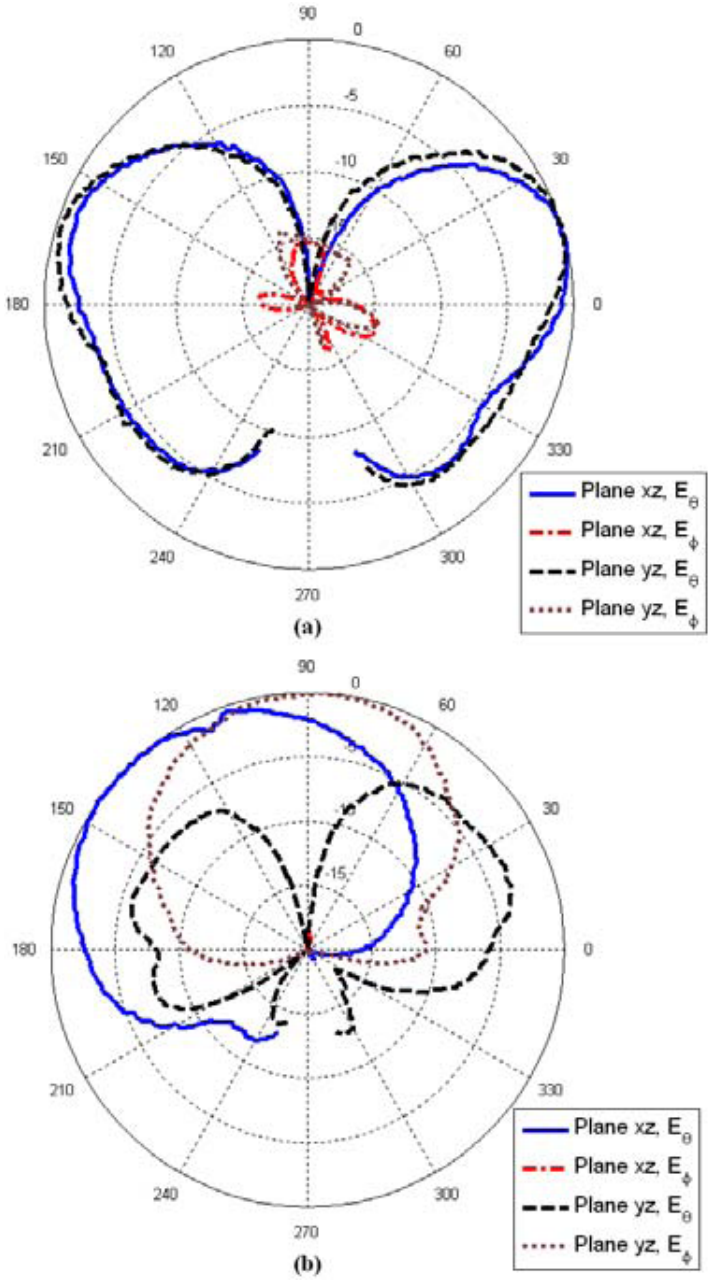

Figure 3.51: Measured radiation patterns of the manufactured LH half-loop antenna. (a) $f_{-6} = 755$ MHz. (b) $f_0 = 1.4$ GHz.

3.4 Conclusion

In the present Chapter metamaterial-loaded printed wire antennas have been presented. Two different kinds of wire antennas have been developed. The first one consists of printed dipole antennas loaded with metamaterial particles. It has been demonstrated the multifrequency performance of these antennas, achieving a dipolar-like radiation pattern at different frequencies. Moreover, the different working frequencies are close to the resonance frequencies of the unloaded dipole and the self-resonance frequencies of the loading metamaterial particles. It must be noted that mutual couplings cannot be neglected since they imply frequency shifts with respect to the unloaded elements for the case in which the resonance frequencies are very close. Nevertheless, the approach can be used to design multifrequency dipoles with an arbitrary ratio and is very useful when the ratio between the working frequencies is very small (< 2) which is required for nowadays user terminals. Two dual-frequency dipoles loaded with SRRs have been designed designed, manufactured and measured obtaining satisfactory results. The first dipole works at 1.32 and 2.83 GHz (2.14 ratio) whilst the second one works at 1.20 and 2.05 GHz (1.71 ratio). After that, a dual-frequency dipole with miniaturization has been achieved. This feature is obtained by achieving an additional resonance below the fundamental frequency of the unloaded dipole. Moreover, a prototype of a triple-frequency dipole antenna has been designed by loading the dipole with metamaterial particles with different resonance frequencies. Its measured working frequencies are 1.38 GHz, 2.07 GHz and 2.30 GHz, demonstrating that arbitrary ratios between the working frequencies can be obtained. Finally, an equivalent circuit model to reduce the computation time needed to simulate this type of antennas has been developed. This model has been validated by comparing the equivalent model results with the measured ones for the dual-frequency and triple-frequency manufactured prototypes. An excellent agreement between the simulated and experimental results has been achieved.

The other set of antennas presented in this Chapter are LH printed wire antennas over ground plane (Section 3.3). These antennas provide the interesting features of LH wire antennas (small antennas with internal matching and additional radiation characteristics) but a further size reduction is achieved thanks to image theory. Moreover, the problem of the feeding, which was an important disadvantage in previous LH antennas, is solved by directly soldering the inner conductor of a SMA connector to the antenna wire and the outer conductor to the ground plane. Two LH antennas over ground plane have been presented: the LH monopole antenna and the LH half-loop

antenna over ground plane. The LH monopole antenna provides the typical monopolar radiation pattern with onminidirectional shape parallel to the ground plane and minimum radiation in the axis of the monopole. A prototype working at 828 MHz has been manufactured and measured, achieving good results. The LH half-loop antenna over a ground plane provides a mode with $n = 0$ which has the unique feature that the currents on the antenna have a uniform distribution in amplitude and phase. This leads to a radiation pattern with maximum radiation orthogonal to the ground plane, which cannot be obtained with other linear antennas over a ground plane. Besides, it has an orthogonal polarization in one of the main planes with respect to the monopolar case. A prototype of the LH half-loop antenna has been manufactured and measured. Its working frequency for the $n = 0$ mode is 1.4 GHz and a radiation efficiency of 87% has been measured.

CHAPTER 4

Microstrip Patch Antennas Partially Filled with CRLH Structures

4.1 Introduction

Microstrip patch antennas are one of the most popular radiators due to their low profile, light weight, easiness of manufacturing and integrating with RF circuitry. However, conventional patch antennas do not provide miniaturization and mutifrequency and/or multifunction capabilities needed for nowadays communications. Conventional single patches cannot be used as multifrequency antennas due to the fact that the multifrequency performance comes from higher order modes with multiple lobes in their radiation patterns. The most common ways of obtaining multifrequency performance with patch antennas are the stacking of two or more patches with different resonance frequencies (leading to multilayer structures) and the addition of parasitic elements [28, 29]. Both of these techniques imply an increase of size instead of a reduction. Hence, they are not interesting for modern terminals and network elements. In addition, conventional microstrip patches are resonant antennas whose working frequency depends on their physical length and thus, there are not so many degrees of freedom to miniaturize them. For example, a usual technique to reduce the total size of a patch antenna consists of using a high-permittivity dielectric substrate, but this reduces the radiation efficiency of the patch antenna and thus it is not recommended. Due

to current demand, multifunction antennas have been developed to achieve different operation modes over several wireless services [11]. Thus, it would be desirable to have multimode patch antennas. For example, patch antennas with both patch-like (maximum at the broadside direction) and monopolar radiation patterns (null radiated at the broadside direction) and significant gains at either of the operation frequencies are required. Moreover, compactness and simplicity of manufacturing are also important to integrate these antennas into handheld devices.

The use of metamaterials has opened new ways for designing antennas with some of the characteristics required for modern wireless communications systems. Miniaturization, compactness, multifrequency or multifunction performance are some of the features which can be achieved by using metamaterial structures. Several LH-based resonant antennas were reviewed in Section 2.6.3. Some of these antennas clearly resembled a patch antenna formed by CRLH cells and these cells were the radiating elements. An important degree of miniaturization was achieved in some cases. This size reduction implied a gain reduction with respect to the gain of conventional patches.

Previous antennas based on CRLH structures mainly aim at miniaturization and make use of LH modes to obtain size reduction. However, previous designs have not fully exploited the possibility of achieving multifrequency and/or multifunction patch antennas. This multifrequency performance can be achieved by the joint use of RH and LH modes simultaneously. This feature is obtained in the patch antennas filled with CRLH structures described in the present Chapter. The main difference with previous CRLH antennas is that, in this case, CRLH structures have been included inside the microstrip patch to obtain the desired performance, but the radiating element is the microstrip patch. In this way the antenna behaves as a conventional patch but with enhanced characteristics. Thus, the proposed antennas have the benefits of a conventional patch, but with additional frequencies such as multifrequency and/or multifunction capabilities.

The outline of this Chapter is the following: first of all, conventional microstrip patch antennas are reviewed in Section 4.2. After that, resonators based on the combination of RH and CRLH structures are presented in Subsection 4.3.1. These resonators are used to explain the equivalent model of a patch filled with CRLH cells (Subsection 4.3.2). Once the basic theory is explained, two patch antennas filled with CRLH cells are presented. The first one is a triple-frequency and dual-mode patch antenna. The design, manufacturing and measurements of this antenna are shown in Section 4.4. A similar study is presented for a dual-frequency antenna in Section 4.5. Then, two different approaches for the analysis and design of the patch antennas

filled with CRLH cells are presented. The first one is an equivalent circuit model with low computational load (Section 4.6). The other one, Section 4.7, is a full-wave software based on the MPIE-MoM approach developed during a Short-Term Scientific Mission in the LEMA (Laboratory of Electromagnetics and Acoustics) at EPFL (École Polytechnique Fédérale de Lausanne). Finally, in Section 4.8 the approach of filling patch antennas with CRLH cells is extended to increase the multifunctionality of the patch antennas, obtaining dual-band circularly polarized patch antennas and patch antennas with frequency and/or polarization diversity.

4.2 Conventional Microstrip Patch Antennas

Microstrip patch antennas are composed of a metallization printed on a dielectric substrate mounted over a ground plane [28, 29]. Let us consider the case of a conventional square microstrip patch antenna fed through a probe placed along one principal direction. This antenna is a resonant structure in which the modes with propagation along the feeding direction are excited (TM_{0n}). Moreover, this antenna can be modelled as an open-ended TL. The equivalent circuit of an infinitesimal section of this TL is composed of a series inductance and a shunt capacitance. Thus, the propagation constant along this RH TL is positive and linear with frequency:

$$\beta^{RH} = \omega\sqrt{C'_{\mu S}L'_{\mu S}} \tag{4.1}$$

where $C'_{\mu S}$ and $L'_{\mu S}$ are the capacitance and inductance per unit length of the microstrip structure. As this propagation constant is always positive and linear with frequency, it can be expressed as:

$$\beta^{RH} = k_1 f \tag{4.2}$$

where k_1 is a positive constant.

The resonant frequencies (eigenfrequencies) of the TM_{0n} modes can be predicted by this model as

$$\beta d = \beta^{RH} d = n\pi \tag{4.3}$$

where d is the TL equivalent length. As the propagation constant is positive the resonant indices are

$$n = +1, +2, +3, \ldots \tag{4.4}$$

Moreover, all the eigenfrequencies are harmonics of the fundamental mode ($n = +1$) due to the linearity with frequency of the propagation constant:

$$f_n = n f_{+1} \tag{4.5}$$

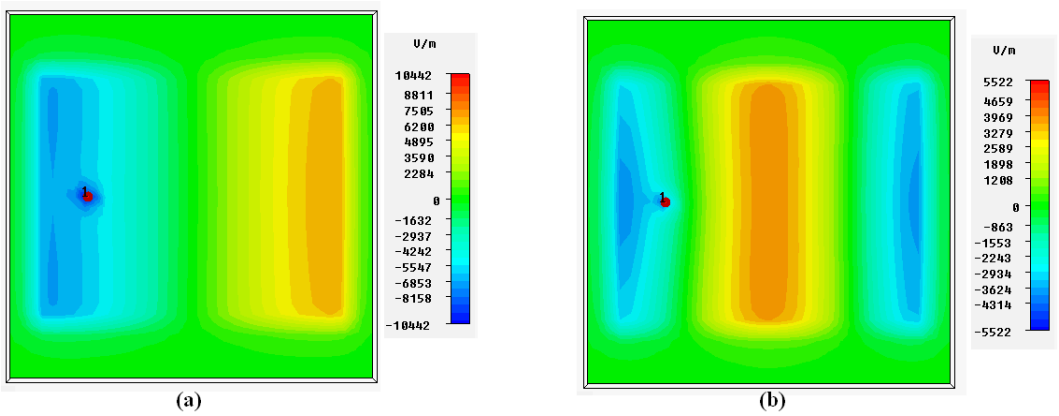

Figure 4.1: Electric field distributions of a conventional microstrip patch antenna. (a) $n = +1$ mode. (b) $n = +2$ mode.

The electric field distributions of these TM_{0n} modes have $n\lambda/2$ electric field distribution, as it can be seen in Fig. 4.1. The radiated fields for these modes can be deduced from the fringing fields along the propagation direction. The patch antenna can be modelled as an array of two radiating slots placed at the edges of the patch. The fundamental mode ($n = +1$) presents a half-wavelength electric field distribution. Thus, the radiating slots have opposite phases ($\beta_1 d = +\pi$) and the distance between them is $\lambda/2$ which leads to a broadside radiation pattern (maximum radiation in the direction opposite to the ground plane). This kind of radiation pattern is also known as patch-like (Fig. 4.2.a). All the modes different from the fundamental one have multiple lobes in the radiation pattern, as shown in Fig. 4.2.b for the $n = +2$ mode.

These characteristics make conventional patch antennas not suitable for multifrequency systems. The first reason is that arbitrary frequencies cannot be achieved because once the fundamental frequency is fixed, the other frequencies are always multiples of the fundamental one. The second reason is that the radiation patterns with multiple lobes are not interesting for most applications, since that implies a loss of directivity.

Patch antennas with an alternative radiation pattern can be developed by introducing shorting pins or using short-circuited geometries [10, 28, 29].

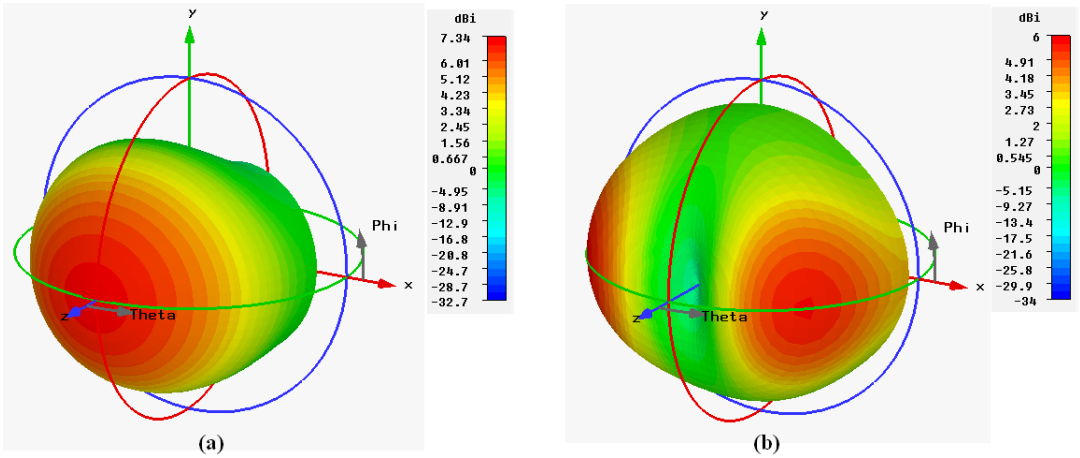

Figure 4.2: Radiation patterns of a conventional microstrip patch antenna. (a) $n = +1$ mode. (b) $n = +2$ mode.

The fundamental mode of these antennas ($n = 0$) has a constant electric field distribution (Fig.4.3.a) which satisfies the condition

$$n = 0 \Rightarrow \beta_0 d = 0 \tag{4.6}$$

Therefore, the radiating slots have the same amplitude and phase which leads to a monopolar radiation pattern (null at the broadside direction), as shown in Fig. 4.3.b. At frequencies higher than the operating frequency of the fundamental mode, these short-circuited patch antennas behave as conventional patch antennas. Thus, the second mode of these antennas corresponds to the $n = +1$ index, leading to the conventional patch-like radiation pattern.

4.3 Fundamentals of Microstrip Patch Antennas Partially Filled with CRLH Structures

4.3.1 RH+CRLH+RH Resonators

In Chapter 2 it was shown that the dispersion diagrams of CRLH resonators have the eigenfrequencies associated with LH modes ($n < 0$) at lower frequencies than those associated with RH modes (Section 2.4). In addition, the separation between the LH eigenfrequencies and the RH ones is quite large. For that reason, the effort on the applications of CRLH resonators (for

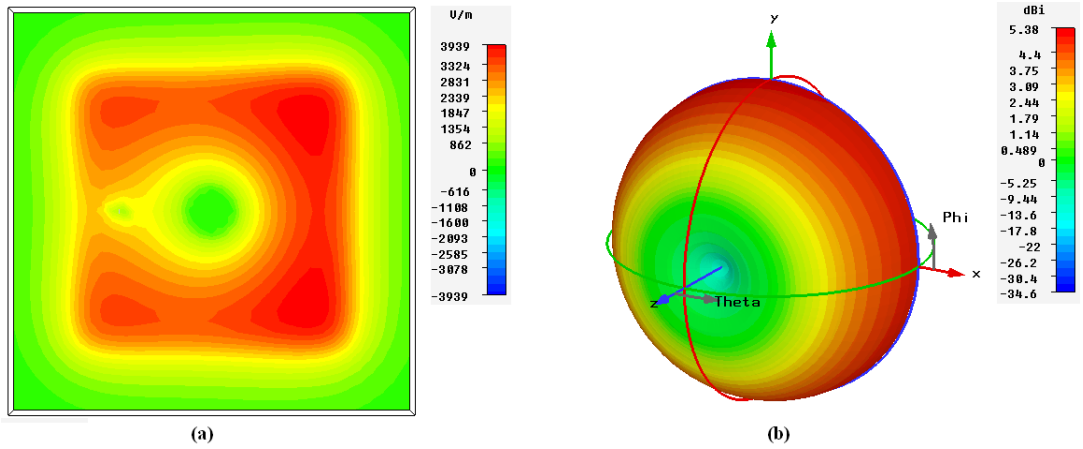

Figure 4.3: Short-circuited microstrip patch antenna. (a) Electric field distribution of the $n = 0$ mode. (b) Radiation pattern of the $n = 0$ mode.

example, resonant antennas) has been directed to miniaturization by making use of LH modes, as it was reviewed in Section 2.6.3. However, if the slope in the RH region were lowered so that the separation between the RH eigenfrequencies and the LH ones were reduced, multifrequency devices based on CRLH resonators (e. g. resonant antennas) could be designed by simultaneous using the modes with $\pm n$ indices. A structure combining a CRLH section between two conventional RH sections is proposed to obtain multifrequency resonators with non-integer frequency ratio between the modes and a resonance frequency spectrum with closer modes. As a first approach a 1-D model is proposed and showed in Fig. 4.4.

The proposed structure is composed of a CRLH TL with length ℓ between two $d/2$ conventional homogeneous RH TLs. The total length of the new TL is $L = \ell + d$. The RH sections can be implemented with conventional TLs (e. g. microstrip lines). The equivalent circuit elements of the microstrip RH TLs are $C'_{\mu S}$ and $L'_{\mu S}$. The CRLH section is composed of M unit cells. The CRLH unit cells with p length have equivalent circuit elements C_R, L_R, C_L and L_L (Section 2.3.1). Thus, the CRLH section length is given by $\ell = Mp$.

An open-ended RH+CRLH+RH structure, as the one proposed in Fig. 4.4, is a resonant structure. Under the impedance matching condition between all the sections [53], all the eigenfrequencies satisfy the resonant condition:

$$\beta_n L = \beta_n^{RH} d + \beta_n^{CRLH} \ell = \beta_n^{RH} d + \beta_n^{CRLH} pM = n\pi \tag{4.7}$$

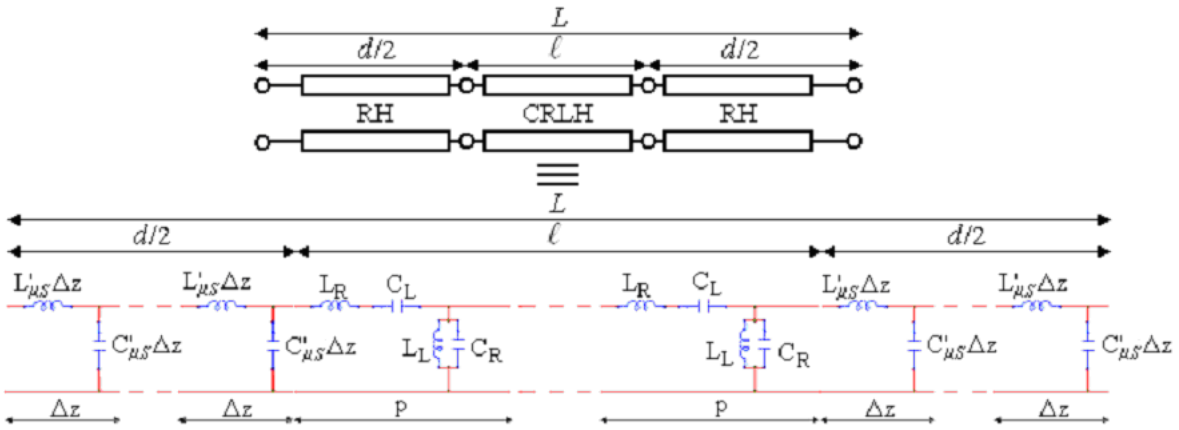

Figure 4.4: Sketch of the proposed RH+CRLH+RH resonator.

As the propagation constant of an ideal homogeneous microstrip line is given by (4.1) and, by using the dispersion relation of a CRLH unit cell [24], the analytical expression for the eigenfrequencies of the proposed structure is

$$\beta_n L = \omega_n \sqrt{C'_{\mu S} L'_{\mu S}}\, d + s(\omega) M \cos^{-1}\left\{1 - \frac{1}{2}\left[\frac{\omega_L^2}{\omega_n^2} + \frac{\omega_n^2}{\omega_R^2} - \left(\frac{\omega_L^2}{\omega_{se}^2} + \frac{\omega_L^2}{\omega_{sh}^2}\right)\right]\right\} = n\pi \tag{4.8}$$

where ω_R, ω_L, ω_{se} and ω_{sh} are the RH, LH, series and shunt resonant frequencies corresponding to the LC tanks of a CRLH unit cell. Moreover, the sign function $s(\omega)$ is -1 in the LH region $[\omega < \min(\omega_{se}, \omega_{sh})]$ and $+1$ in the RH region $[\omega > \max(\omega_{se}, \omega_{sh})]$.

The number of resonances of the new structure can be determined by studying its asymptotic behaviour. It must be noted that the phase constant is proportional to frequency in the RH sections while it is proportional to $1/f$ in the CRLH section at lower frequencies (when its dominant behaviour is LH); thus, the total structure mainly behaves as a CRLH TL at lower frequencies. On the other hand, as the CRLH section has a RH behaviour at higher frequencies, the overall structure works as a RH resonator at higher frequencies. Thus, there is a maximum length of the RH sections (d_{max}) to obtain the CRLH performance of the overall resonator at lower frequencies. Otherwise the CRLH effect would be masked.

The lowest CRLH resonant mode for a CRLH TL based resonator is given by $n = -M + 1$ [24, 58]. Therefore, the condition to obtain all the negative

index resonant modes in the overall resonator is given by

$$d_{max} = \frac{M\cos^{-1}\left\{1-\frac{1}{2}\left[\frac{\omega_L^2}{\omega_{-M+1}^2}+\frac{\omega_{-M+1}^2}{\omega_R^2}-\left(\frac{\omega_L^2}{\omega_{se}^2}+\frac{\omega_L^2}{\omega_{sh}^2}\right)\right]\right\}-(M-1)\pi}{\omega_{-M+1}\sqrt{C'_{\mu S}L'_{\mu S}}} \tag{4.9}$$

This condition has been obtained by substituting the lowest resonant mode in equation (4.8). Considering that the condition is satisfied ($d < d_{max}$) the proposed resonator presents the modes shown below:

$$n = -M+1, -M+2, \ldots, 0, +1, +2, \ldots \tag{4.10}$$

Fig. 4.5 shows the electrical length of a CRLH resonator vs. frequency (red dashed line) and the distribution of the different eigenfrequencies. This CRLH resonator has $M = 4$ cells and the equivalent parameters for each of them are $L_L = L_R = 1$ nH and $C_L = C_R = 1$ pF. In this case, the separation between the eigenfrequencies with the same absolute index ($\pm n$) is quite large, leading to a high ratio between them. For example, the eigenfrequencies for the $n = \pm 1$ modes are $f_{-1} = 3.46$ GHz and $f_{+1} = 7.33$ GHz. Hence, the ratio between them is 2.11.

Fig. 4.5 also shows the effect of adding two RH sections to the CRLH structure (black solid line). The RH sections have an electrical length of 90° at 2 GHz. The impedance of these RH sections is 31.62 Ω. These parameters of the RH sections can be obtained from the physical dimensions of the microstrip line [44, 59]. In this case, the ratio between the eigenfrequencies with the same absolute index ($\pm n$) is reduced. For example, for the $n = \pm 1$ modes the eigenfrequencies are $f_{-1} = 2.48$ GHz and $f_{+1} = 3.66$ GHz. Thus, the ratio between both frequencies has been reduced from 2.12 to 1.47. Moreover, it can be observed that the proposed RH+CRLH+RH resonator exhibits a behaviour that is similar to a CRLH resonator at low frequencies (non-integer ratios between the eigenfrequecies of the modes with $n < +2$) and similar to a RH resonator at higher frequencies (quasi-linear ratio between the eigenfrequencies in the region with $n > 2$). In addition, a large compression in the low frequency region of the eigenfrequencies chart can be noticed. These facts were predicted before by studying the asymptotic behaviour of equation (4.5).

The compression in the resonance chart strongly depends on the electrical length of the RH sections, which means that the larger this parameter is, the closer the eigenfrequencies are. This is because the slope of the electrical

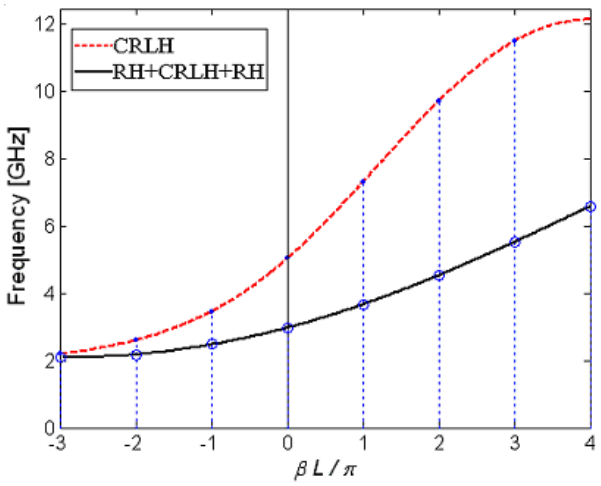

Figure 4.5: Electrical length of the CRLH (red dashed line) and the RH+CRLH+RH (black solid line) resonators. The resonant frequencies are marked with circles. The equivalent circuit parameters of the CRLH cells are: $L_R = L_L = 1$ nH, $C_R = C_L = 1$ pF and $M = 4$. The electrical length of the RH sections in the RH+CRLH+RH resonator is 90° at 2 GHz and their impedance is 31.62 Ω.

length of the resonator is lower when increasing the length of the RH sections. Fig. 4.6 shows the effect of increasing the length of the RH sections (d) in the proposed RH+CRLH+RH resonator. It can be seen that as the length of the RH sections is enlarged, the slope of the dispersion curve is reduced and the frequency separation between the eigenfrequencies is also decreased.

It seems that modes with frequencies as close as desired can be obtained. However, this is not true and two constraints must be taken into account. The first one is that the larger the lengths of the RH TLs are, the lower the number of modes in the non liner region of the dispersion diagram. The second drawback comes from the fact that using RH sections with large lengths can produce resonators with overlapped modes. This fact can be derived from equation (4.9).

The previous equations and examples were developed under the matching condition between the different sections which compose the proposed resonator. It is important to study what happens when the impedance of the RH sections is different from the impedance of the CRLH structure. Fig. 4.7 shows the effect on the electrical length of the proposed resonator for a RH sections impedance variation between 25 Ω and 70 Ω. As it can be seen, there is no important variation with the impedance of the RH sections. Thus,

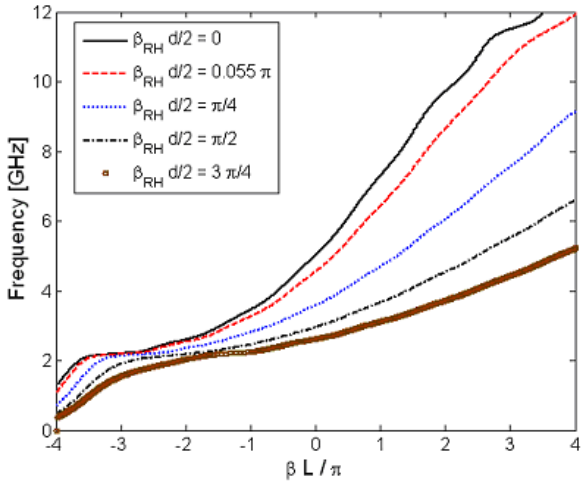

Figure 4.6: Variation of the electrical length of the RH+CRLH+RH resonator as a function of the RH lines electrical length. The equivalent circuit parameters of the CRLH section with $M = 4$ unit cells are: $L_R = L_L = 1$ nH and $C_R = C_L = 1$ pF. The impedance of the RH sections is 31.62 Ω.

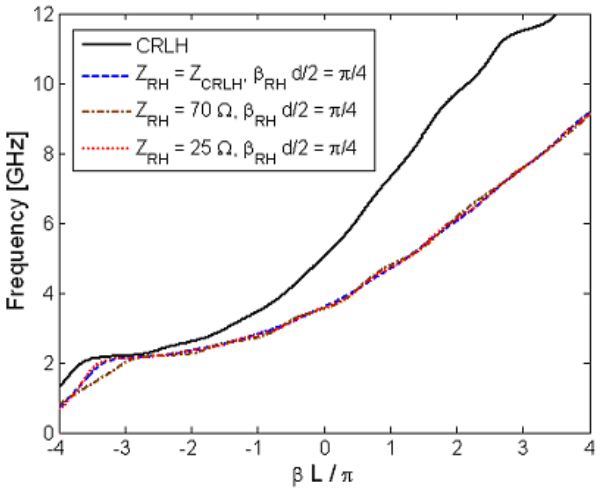

Figure 4.7: Dependence of the electrical length of the RH+CRLH+RH resonator on the RH lines impedance. The equivalent circuit parameters of the CRLH section with $M = 4$ unit cells are: $L_R = L_L = 1$ nH and $C_R = C_L = 1$ pF. The electrical length of the RH sections is 90°.

the previous results can be extended even when the different sections which compose the proposed resonator are not perfectly matched.

It has been demonstrated that the proposed RH+CRLH+RH structure allows developing multifrequency resonant structures with arbitrary ratios between the working frequencies even when the ratios are small (e. g. < 2).

4.3.2 Equivalent TL Model of Microstrip Patch Antennas Partially Filled with CRLH Structures

The multifrequency patch antennas are based on a microstrip patch partially filled with CRLH structures (Fig. 4.8.a). These CRLH structures can be implemented by using mushroom-type structures (Sections 2.3.1 and 2.5). Considering the case plotted in Fig. 4.8.a, the probe is located in the middle of one principal direction. Thus, only modes with propagation along this direction can be excited (TM_{0n} modes). It must be noted that the location of the probe is very important because if it were displaced along the orthogonal direction, other modes with propagation along both directions (TM_{nm}, with $m \neq 0$) could be excited. Hence, for the case proposed in this Fig. 4.8.a, the equivalent antenna TL model is composed of a CRLH section between two RH sections (Fig. 4.8.b). It must also be emphasized that the effect produced by the upper RH sections surrounding the cells is an increase in the series capacitances (C_L) which model the gap between the RH and CRLH sections (this will be shown in Section 4.6). This fact leads to lower resonant frequencies.

Considering the study of the Subsection 4.3.1, the dominant behaviour of the CLRH sections at low frequencies is mainly LH. Thus, the resonant condition (4.8) can be approximated by:

$$\beta_n L = \beta_n^{RH} d + \beta_n^{LH} \ell = k_1 f_n d - \frac{k_2}{f_n} \ell = n\pi \tag{4.11}$$

where k_1 and k_2 are positive constants; d and ℓ are the equivalent lengths of the RH and the CRLH sections, respectively. In this case, it is possible to obtain modes with negative, zero or positive index, contrary to the conventional patches in which n is always positive (Section 4.2). Specifically, for a LH section composed of M unit cells, n takes the values computed in (4.10).

In particular if $M \geq 2$, two interesting modes are achieved below the mode equivalent to the fundamental one of the conventional patch antenna:

- The first one is the $n = -1$ mode when the condition $\beta L = -\pi$ is satisfied. This mode has a half-wavelength electric field distribution

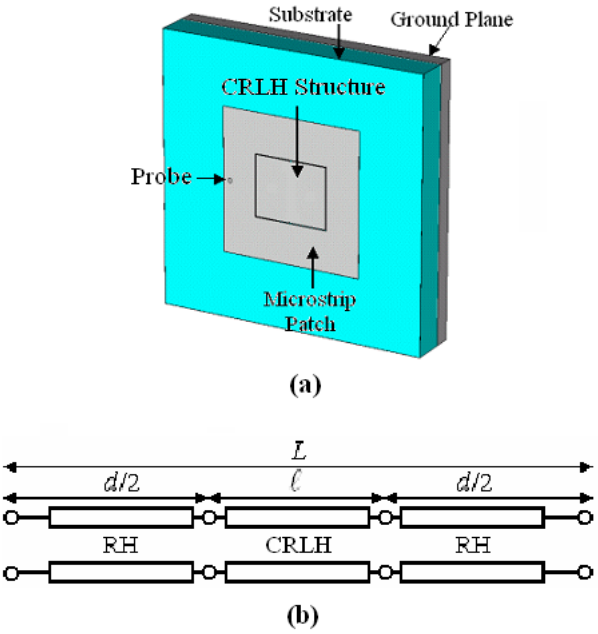

Figure 4.8: Microstrip patch filled with CRLH structures. (a) Representation of the antenna. (b) Equivalent TL model.

similar to the fundamental mode of a conventional patch antenna. Thus, a patch-like radiation pattern is achieved for this mode.

- The second one is the $n = 0$ mode when the condition $\beta L = 0$ is achieved. This mode has a uniform electric field distribution both in amplitude and phase inside the patch antenna, which gives a monopolar radiation pattern (null at broadside). This is the type of mode excited as the fundamental one in short-circuited patch antennas (Section 4.2).

Moreover, the conventional modes ($n \geq +1$) are also present in the proposed antennas. Thus, the $n = +1$ mode is also present in the structure, maintaining its patch-like radiation pattern. It is important to note that the resonance frequencies are not forced to follow a harmonic ratio in the proposed antennas. This is possible thanks to the non-linear behaviour introduced by the CRLH cells. Moreover, small ratios between the frequencies can be achieved with the proposed approach.

In conclusion, two interesting kinds of multifrequency patch antennas can be developed with this approach:

- A triple-frequency and dual-mode patch antenna when the modes $n =$

± 1 and $n = 0$ are excited simultaneously. The $n = \pm 1$ modes provide a patch-like radiation pattern, while the $n = 0$ mode has a monopolar one. The possibility of using this mode provides a degree of multifunctionality due to the fact that radiation pattern diversity is achieved.

- A dual-frequency antenna is achieved when only the $n = \pm 1$ modes are used. In this case, the radiation pattern is patch-like at both working frequencies.

Examples of both antennas are presented below.

4.4 Triple-Frequency and Dual-Mode Patch Antenna

4.4.1 Design

The proposed antenna is shown in Fig. 4.9.a where the patch dimensions $L \times W$ are 42.00 mm $\times$ 42.00 mm. The substrate is polypropylene (PP) with $\varepsilon_r = 2.2$ and $h = 10$ mm. The mushroom structure is based on a 2×1 cell array configuration and the dimensions of the mushrooms $L_m \times W_m$ are 10.60 mm $\times$ 17.80 mm. The diameter of the vias d is 0.70 mm, the gap between the two mushrooms g_1 is 0.40 mm and the separation gap between the microstrip patch and the CRLH structure g_2 is 0.20 mm. The antenna is fed through a coaxial probe placed at 14.00 mm from the centre. The dimensions of the ground plane are 80.00 mm $\times$ 80.00 mm. These dimensions have been chosen to obtain the resonant frequencies at 1.00 GHz (GSM) for the $n = -1$ mode, 1.50 GHz (navigation systems) for the $n = 0$ mode and 2.20 GHz (UMTS) for the $n = +1$ mode.

Fig. 4.9.b shows the electrical length of the proposed antenna versus frequency and the eigenfrequencies of the modes obtained through full-wave simulation. The same information for the conventional square patch antenna is also plotted. The electrical lengths have been computed by interpolating the discrete values of the eigenfrequencies. The linear ratio between the electrical length and the frequency for the conventional patch antenna can be appreciated. On the other hand, the patch partially filled with the mushroom structures presents the same relation for the modes with positive indices, but it has CRLH behaviour at lower frequencies. This CRLH relation has been computed with the Eigenfrequency method (Section 2.5). The chart shows that for the index $n = +1$, the working frequency is very close to the fundamental frequency of the conventional patch (but not equal due to the

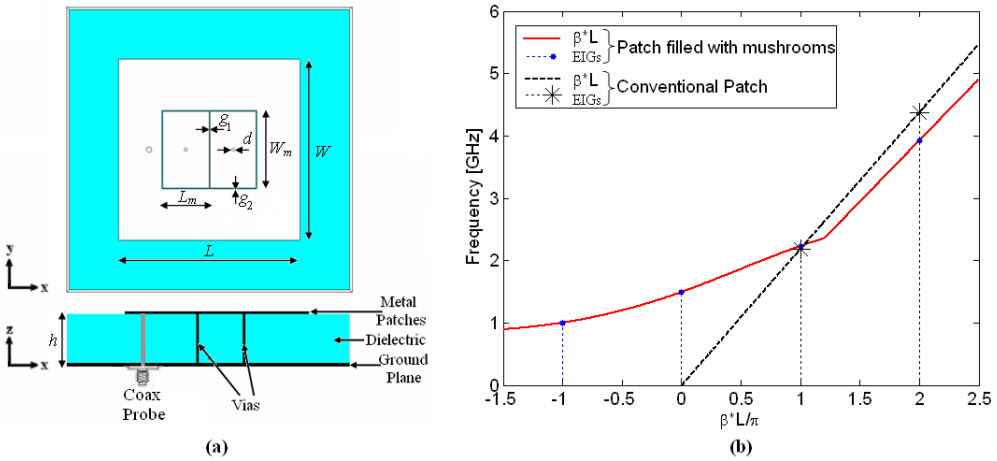

Figure 4.9: Triple-frequency and dual-mode antenna based on a microstrip patch filled with CRLH cells. (a) Sketch of the antenna. (b) Electrical length (βL) and eigenfrequencies (EIGs) of the resonant modes of the proposed antenna (solid line). The same information for the conventional patch antenna is also plotted (dashed line).

residual effect of the metamaterial structure). As a first approximation for general design, the patch length is chosen to obtain the $n = +1$ frequency as the fundamental mode of the patch without mushrooms. On the other hand, the frequencies of the lower modes ($n \leq 0$) strongly depend on the mushroom structure selection. Large mushrooms lead to higher separation between the working frequencies and thus, higher slope in the CRLH region, while smaller mushrooms provide closer resonances and smaller slopes in the CRLH region of the electrical length graph.

The resonance frequencies basically depend on the patch and cells dimensions (L, W, L_m, W_m). The width of the gaps (g_1, g_2) also makes influence on the resonant frequencies. The dependence of the eigen-frequencies with respect to the vias diameter (d) is negligible. As it has been said previously, the resonance of the $n = +1$ mode is mainly associated with the patch itself. Then, the higher frequency mainly depends on the patch length (L). A parametric study considering the dependence of the different resonant frequencies on the cells and gaps dimensions is shown in Figs. 4.10-4.12. This study has been carried out by using CST Microwave Studio ®. For each simulation, the parameter under study is varied while the other dimensions of the antenna are kept fixed. All the dimensions are normalized with respect to the patch length (L). The resonant frequencies are normalized with respect

to the fundamental frequency of the conventional patch antenna (a 42-mm square patch antenna without CRLH filling).

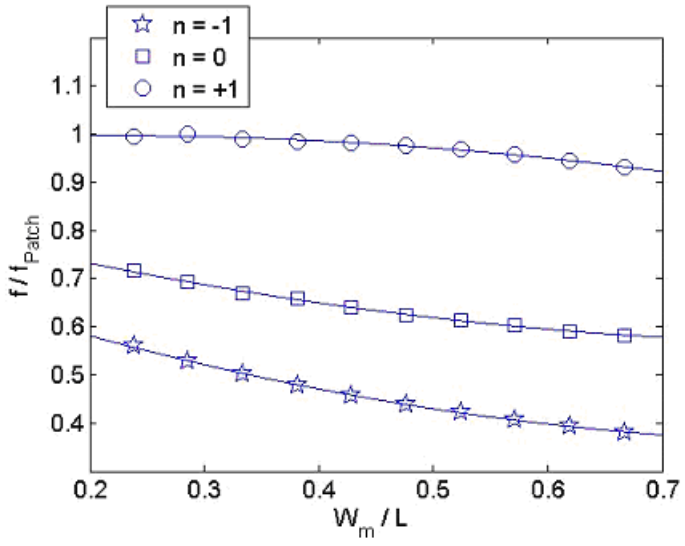

Figure 4.10: Ratio of the proposed antenna frequencies over conventional patch antenna frequency (f_{Patch}) against the ratio of the mushroom width (W_m) over the patch length (L).

Figs. 4.10-4.11 shows the dependence of the proposed antenna frequencies on the ratio between the width of the (W_m) or the length (L_m) CRLH cells over the overall patch length (L). An increase in the width or length cell (W_m or L_m) have an effect on the LH capacitance, C_L, increasing its value. Thus, the frequency of the $n = -1$ decreases. However, for the $n = +1$ mode the frequency variation follows different slopes depending on which dimension is changed (W_m or L_m). Then, the frequency of the proposed antenna practically agrees with the frequency of the corresponding conventional patch antenna for low values of W_m/L; this is coherent with the fact that at the higher frequency the LH effect is negligible. On the other hand, as W_m gets larger and larger, the frequency curve of the proposed antenna is bent towards lower frequency values. The dependence of this frequency on the ratio between the lengths L_m/L shows a different behaviour. An increase in L_m causes a reduction in the distance d (associated with the RH part in the proposed antenna). This shifts the frequency of the $n = +1$ towards higher frequencies.

Fig. 4.12 shows the variation of the antenna frequencies with respect to the width of the outer gap between the mushroom cells and the patch (g_2). As

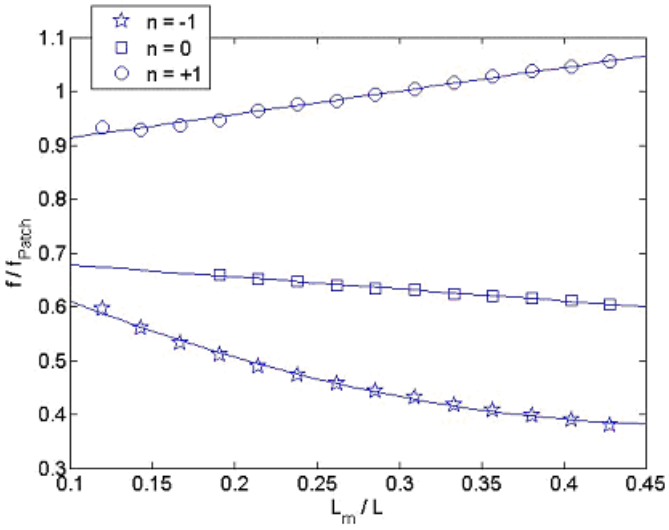

Figure 4.11: Ratio of the proposed antenna frequencies over conventional patch antenna frequency (f_{Patch}) against the ratio of the mushroom length (L_m) over the patch length (L).

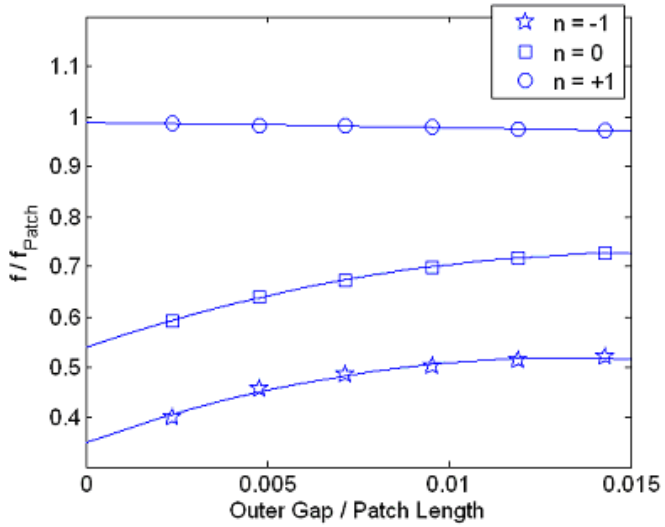

Figure 4.12: Ratio of the proposed antenna frequencies over conventional patch antenna frequency (f_{Patch}) against the ratio of the outer gap (g_2) over the patch length (L).

the width of the gap increases the LH capacitance decreases what causes the antenna additional frequencies (modes $n = -1$ and $n = 0$) to increase. This happens until the C_L reaches an asymptotic value from which the variation is negligible. At higher frequencies the contribution of the CRLH cells is negligible. Thus, the frequency of the $n = +1$ mode is a little lower than the frequency of the corresponding square patch antenna and remains almost constant. This agrees with the fact that ring antennas (patch formed by the metallization which surrounds the CRLH section over the dielectric and the ground plane) present lower resonant frequencies than their corresponding full counterparts.

Finally, a short design guide for the proposed patch antennas is given:

1. Start with a patch length similar to the conventional patch length for the upper frequency (f_{+1}).
2. The dimensions of the CRLH structure are chosen depending on the desired ratio. For a specific ratio and f_{+1}, the cell dimensions can be obtained from the Figs. 4.10-4.12.
3. Fine optimization of the antenna parameters to obtain an accurate design.

The electric field distributions (CST Microwave Studio ®) for the eigenfrequencies at $n = -1$, $n = 0$ and $n = +1$ indices are shown in Fig. 4.13. The LH performance is seen by a local 180° phase shift in the mushroom structure at f_{-1}. It must be highlighted that this singularity does not affect the radiation behaviour, as it will be shown in the experimental results. On the other hand, the RH performance can also be seen in the field distribution since it is the same as the fundamental mode of a conventional patch antenna at f_{+1} and does not present any local phase shift. Lastly, the electric field is uniform in amplitude and phase at f_0, as it was predicted.

4.4.2 Experimental Results

A prototype of the proposed patch antenna has been manufactured and is shown in Fig. 4.14.a. Fig. 4.14.b shows the simulated and measured reflection coefficient. There is a good agreement between both of them. In both cases, the three working resonances can be clearly seen. The return losses are −12.62 dB at $f_{-1} = 1.06$ GHz, −12.01 dB at $f_0 = 1.45$ GHz and −29.59 dB at $f_{+1} = 2.16$ GHz. The ratio between the frequencies of the first and second modes is 1.37 and the ratio between the two dipolar modes is 2.04. The ratio

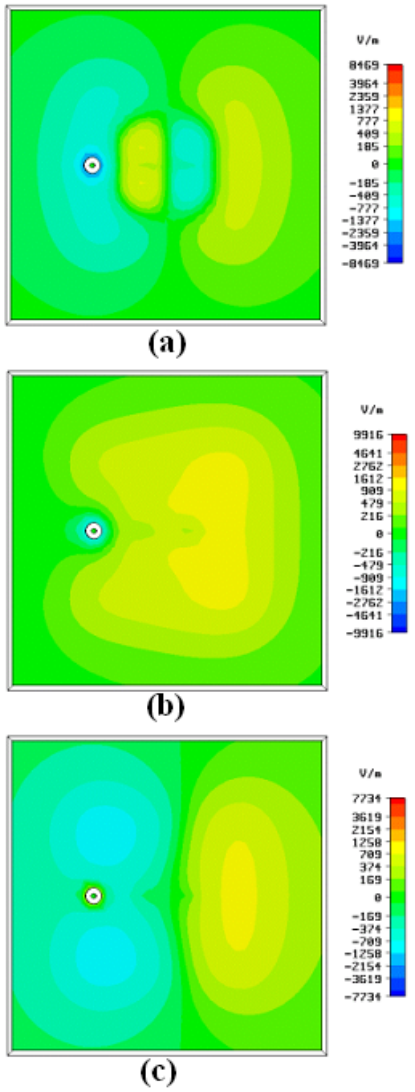

Figure 4.13: Electric field distributions for the proposed triple-frequency and dual-mode antenna: (a) $n = -1$ mode ($f_{-1} = 1.06$ GHz), (b) $n = 0$ mode ($f_0 = 1.45$ GHz), (c) $n = +1$ mode ($f_{+1} = 2.16$ GHz)

between these modes can be arbitrarily chosen and depends on the patch and mushrooms dimensions, as explained before. The patch length is $\lambda_0/6.74$ at f_{-1}, $\lambda_0/4.92$ at f_0 and $\lambda_0/3.31$ at f_{+1}. Moreover, the length is strongly reduced with respect to the conventional $\lambda/2$ patch antennas at the lower frequency.

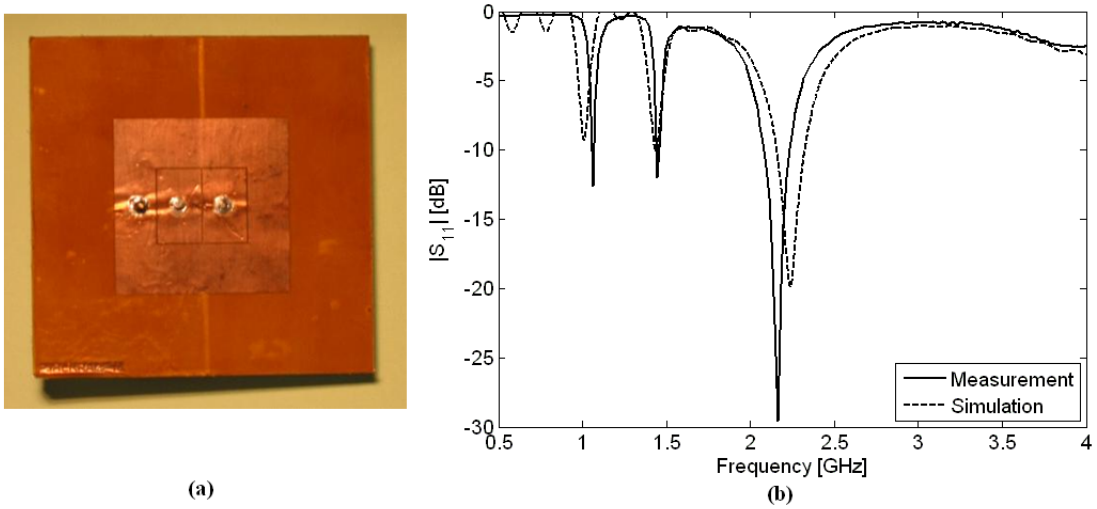

Figure 4.14: (a) Picture of the triple-frequency and dual-mode patch antenna. (b) Simulated and measured reflection coefficient of the proposed antenna.

Finally, Fig. 4.15 present the radiation patterns for the E-plane ($x-z$ plane) and the H-plane ($y-z$ plane) and their corresponding cross-polar components (XPOL). For the $n=-1$ mode (1.06 GHz) a dipolar pattern can be seen in Fig. 4.15.a. For the $n=-1$ mode in the E-plane, the maximum XPOL level (with respect to the normalized 0 dB co-polarization level), is -11 dB and occurs at around $-25°$. For the H-plane the maximum XPOL occurs at around $+55°$ and is -13 dB. For the $n=0$ mode (1.45 GHz) a monopolar pattern can be seen in Fig. 4.15.b. A null at the broadside direction is appreciated. The depth of this null is 16 dB for the E-plane radiation pattern and 15 dB for the H-plane pattern. Two comments must be made concerning the $n=0$ mode. First, the maximum of the radiation pattern that would be in the endfire direction is somewhat reduced due to the effect of the finite ground plane. Secondly, the $n=0$ mode is excited in a weaker way than the $n=0$ mode in a short-circuited patch antenna [10]. This can be seen because of the higher level of the XPOL. For the $n=+1$ mode (2.16 GHz) in the E-plane, the maximum XPOL level (with respect to the normalized 0 dB co-polarization level), is -12 dB and occurs at around

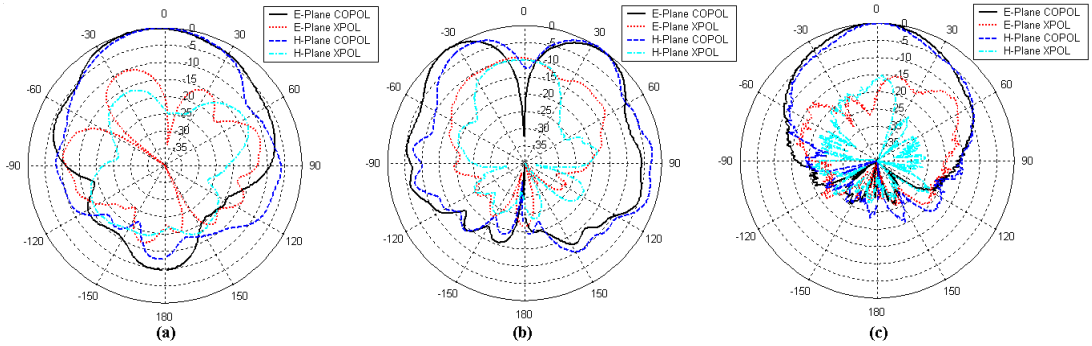

Figure 4.15: Measured radiation patterns of the triple-frequency and dual-mode patch antenna. (a) $n = -1$ mode (1.06 GHz). (b) $n = 0$ mode (1.45 GHz). (c) $n = +1$ mode (2.16 GHz).

Mode	Radiation Pattern	D (dBi)	G (dB)	L in terms of λ_0	$BW_{-6\,\mathrm{dB}}$
$n = -1$	Patch-like	4.5	-3	$\lambda_0/6.74$	3%
$n = 0$	Monopolar	5.1	1	$\lambda_0/4.92$	3%
$n = +1$	Patch-like	7.4	6.5	$\lambda_0/3.31$	13%

Table 4.1: Measured characteristics of the dual-mode antenna.

$+50°$. For the H-plane the maximum XPOL occurs at around $+10°$ and is -16 dB. The measured gain of the antenna is -3 dB at f_{-1}, 1 dB at f_0 and 6.5 dB at f_{+1}. The measured characteristics of the proposed antenna are summarized in Table 4.1.

4.5 Dual-Frequency Patch Antenna

4.5.1 Design

The proposed antenna is designed to work with similar radiation characteristics at 1.80 GHz (DCS) and 2.20 GHz (UMTS). Then, the first working frequency is obtained for the $n = -1$ mode while the second one is obtained for the $n = +1$ mode. Therefore, the same patch-like radiation pattern is achieved at the two frequencies. It must be noted that in this case the desired ratio between the working frequencies is extremely small (1.22). The monopolar mode ($n = 0$) is not excited in this case. It has been seen that when the vias are aligned with respect to the probe, the ratio between the different modes is higher and the mode $n = 0$ is excited. On the other hand,

when the vias are not located in line with the probe, the frequency ratio between the half-wavelength modes ($n = \pm 1$) is reduced and the monopolar mode ($n = 0$) is weakly excited. For that reason, the number of cells in the y-direction has been doubled (resulting in a 2×2 CRLH structure instead of a 2×1) so the vias are not aligned with the corresponding feeding.

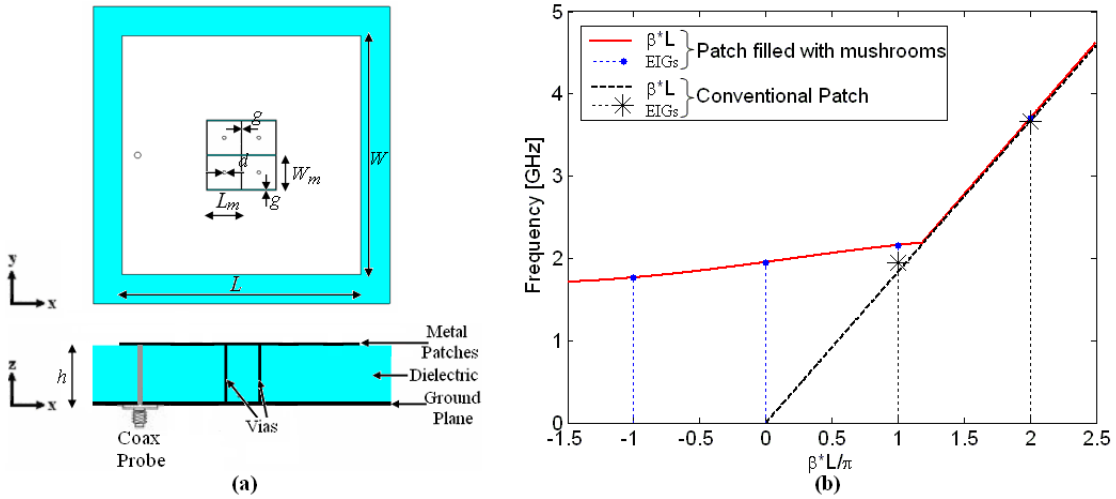

Figure 4.16: Dual-frequency antenna based on a microstrip patch filled with CRLH cells. (a) Sketch of the antenna. (b) Electrical length (βL) and eigenfrequencies (EIGs) of the resonant modes of the proposed antenna (solid line). The same information for the conventional patch antenna is also plotted (dashed line).

Thus, the proposed design is shown in Fig. 4.16.a. It consists of a 48.20 mm square patch ($L = W = 48.20$ mm) partially filled with a 2×2 mushroom arrangement. The substrate is Polypropylene (PP) with $\varepsilon_r = 2.2$ and $h = 8$ mm. The mushrooms are squares of $W_m = 6.80$ mm, the vias diameter d is 0.70mm and the separation gaps g are 0.20 mm. The patch is fed through a coaxial probe placed at 21.00 mm from the centre of the patch.

The resonant frequencies of the proposed patch and its electrical length, computed as in the previous case (Section 4.4), are plotted in Fig. 4.16.b. Again, the CRLH behaviour at low frequencies and the conventional effect at higher frequencies are observed. In this case, the slope in the CRLH region is lower than in the previous antenna (Fig. 4.9.b) to produce the desired reduction in the frequency ratio.

Fig. 4.17 shows the electric field distributions (CST Microwave Studio ®) for the two working modes ($n = \pm 1$). Similar half-wavelength electric fields

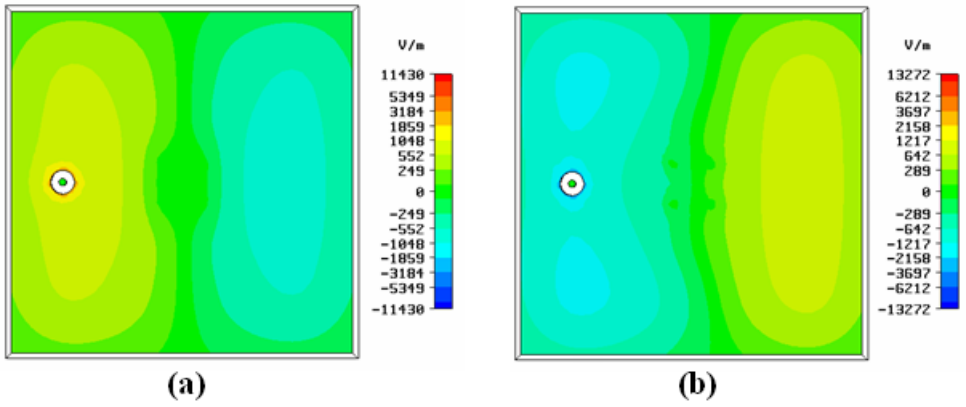

Figure 4.17: Electric field distributions of the proposed dual-frequency antenna: (a) $n = -1$ mode ($f_{-1} = 1.81$ GHz), (b) $n = +1$ mode ($f_{+1} = 2.20$ GHz)

distributions are obtained at the two modes. A local 180° phase shift is seen in the mushroom structure at f_{-1}, but this fact does not affect the radiation behaviour as it will be seen in the experimental results.

4.5.2 Experimental Results

Fig. 4.18.a shows a photograph of the dual-frequency antenna. The simulated and measured return losses are shown in Fig. 4.18.b. A great agreement is achieved between both results. The measured return losses are −9.83 dB at $f_{-1} = 1.81$ GHz and −22.03 dB at $f_{+1} = 2.20$ GHz. The ratio between these two frequencies is 1.21, which is considerably reduced with respect to the previous case. In this case the patch length is $\lambda_0/3.44$ at f_{-1} and $\lambda_0/2.83$ at f_{+1}. It can be seen that electrical length of the patch at $f_{\pm 1}$ is not as reduced as in the previous case because in this case both modes have been located very close to the fundamental mode of the equivalent conventional patch. In addition, the two patch-like modes are placed at frequencies with a relative separation between them of 0.19%, which cannot be obtained with another approach based on a single-layer patch.

The measured radiation patterns are shown in Fig. 4.19. The desired patch-like radiation pattern is obtained at both working frequencies. For the $n = -1$ mode in the E-plane, the maximum XPOL level (with respect to the normalized 0 dB co-polarization level), is −19 dB and occurs at around −10°. For the H-plane the maximum XPOL occurs at around −45° and is

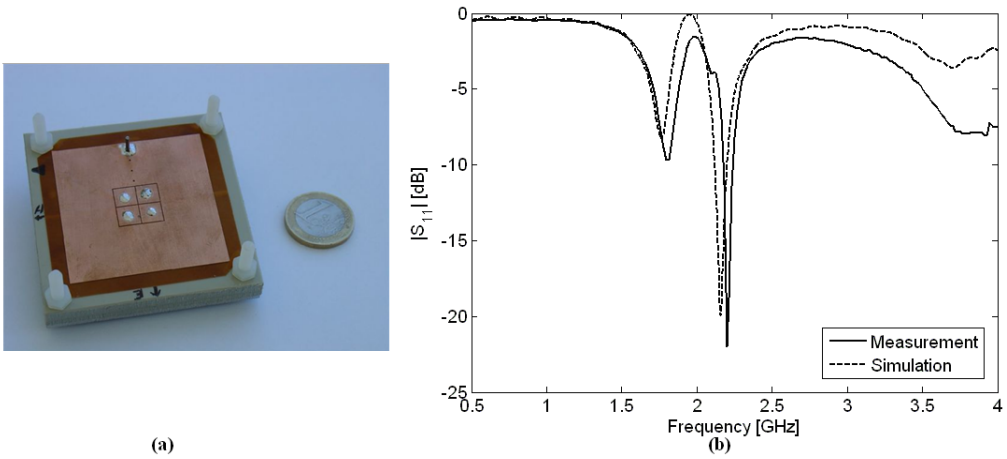

Figure 4.18: (a) Picture of the dual-frequency patch antenna. (b) Simulated and measured reflection coefficient of the proposed dual-frequency antenna.

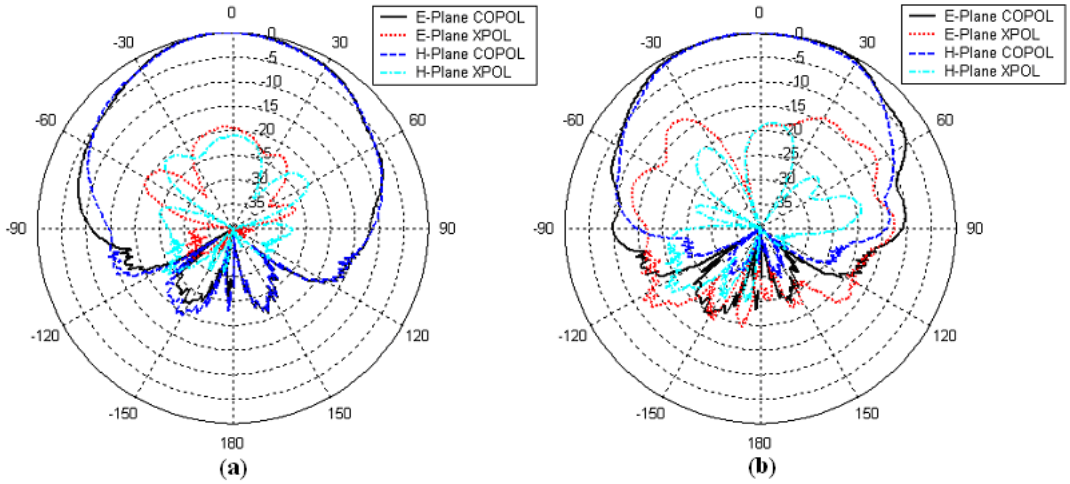

Figure 4.19: Measured radiation patterns of the dual-frequency patch antenna. (a) $n = -1$ mode (1.81 GHz). (b) $n = +1$ mode (2.20 GHz).

Mode	Radiation Pattern	D (dBi)	G (dB)	L in terms of λ_0	$BW_{-6\,\mathrm{dB}}$
$n=-1$	Patch-like	6.7	4.5	$\lambda_0/3.44$	7%
$n=+1$	Patch-like	7.6	6.8	$\lambda_0/2.83$	5%

Table 4.2: Measured characteristics of the dual-frequency antenna

-20.5 dB. In the case of the $n=+1$ mode, the maximum XPOL level in the E-plane (with respect to the normalized 0 dB co-polarization level), is -12.5 dB and occurs at around $-35°$ and $55°$. For the H-plane the maximum XPOL occurs at $+10°$ approximately and is -18 dB.

The measured gain of the antenna is 4.5 dB at the first working frequency and 6.8 dB at the second one. The measured characteristics of the proposed antenna are summarized in Table 4.2.

4.6 Equivalent Circuit Model of Microstrip Patch Antennas filled with CRLH Structures

The aim of this Section is to develop an equivalent circuit model for the proposed microstrip patch antennas filled with CRLH cells. In this way, these antennas can be analysed with a circuit simulator. This fact allows computing the different resonance frequencies and the reflection coefficient of these antennas with a low computation time. Thus, the effort on designing the proposed antennas is considerably reduced in terms of time and computational load.

The proposed equivalent circuit model is based on the transmission line model presented in Section 4.3.2. Hence, the proposed antennas are modelled as a CRLH section between two open-ended transmission lines. In order to implement this model in a circuit simulator, the CRLH section is substituted by its equivalent circuit composed of N unit cells with parameters L_R, C_L, C_R, L_L (Section 2.3.1). The values of these parameters are computed by analysing the CRLH structure with the Eigenfrequencies method proposed in Section 2.5. The RH sections are modelled by conventional transmission lines. The RH sections are ended with a parallel admittance (with a conductance G_S and susceptance B_S). These G_S and B_S elements are used to model the radiated and the stored fields in the proximity of the patch, respectively [28, 129]. Finally, the feeding is also modelled by a LC circuit connected to a port [28, 129]. In the case of the coaxial probe, an inductance (L_P) is used to model the feeding. A sketch of the proposed equivalent circuit model is

shown in Fig. 4.21.

This equivalent circuit model has been applied to the microstrip patch antennas filled with CRLH cells presented in Sections 4.4-4.5.

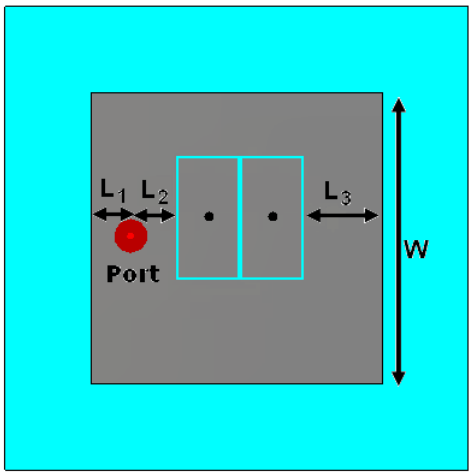

Figure 4.20: Sketch of the different transmission line sections which compose the equivalent circuit of the triple-frequency and dual-mode patch antenna (Section 4.9).

According to Fig. 4.20, the triple-frequency and dual-mode patch antenna presented in Section 4.9 is divided in four sections. The first and second ones are conventional RH sections. The feeding is placed between both sections. The third part is the CRLH section composed by $N = 2$ unit cells and the last one is a conventional RH section. This division results in the equivalent circuit model of Fig. 4.21, in which the CRLH cells are replaced by their equivalent circuit model. The dimensions of the different sections are: $L_1 = 7.00$ mm, $L_2 = 3.00$, $L_3 = 10.00$ and $W = 42.00$ mm. The computed value of the remaining patch parameters are: $G_S = 1/332\ \Omega^{-1}$, $B_S = 5.80\ \Omega^{-1}$ and $L_P = 5.50$ nH. The value of each unit cell elements are computed by the Eigenfrequencies method (Section 2.5). The obtained values are: $L_R = 8.25$ nH, $C_L = 0.41$ pF, $L_L = 6.09$ nH and $C_R = 0.32$ pF. As it was commented in Section 4.3.2, the value of the series capacitors (C_L) has to be increased to take into account the effect of the upper RH sections which surround the CRLH cells, resulting in $C_L = 1.38$ pF.

The simulated reflection coefficient obtained with the equivalent circuit model is shown in Fig. 4.24. The measured reflection coefficient of the manufactured prototype (Fig. 4.14.a) is also plotted. There is a good agreement

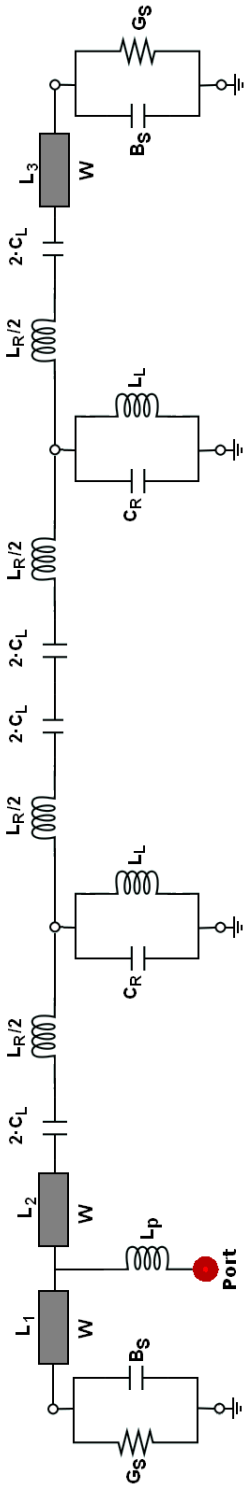

Figure 4.21: Equivalent circuit model of the triple-frequency and dual-mode patch antenna (Section 4.9).

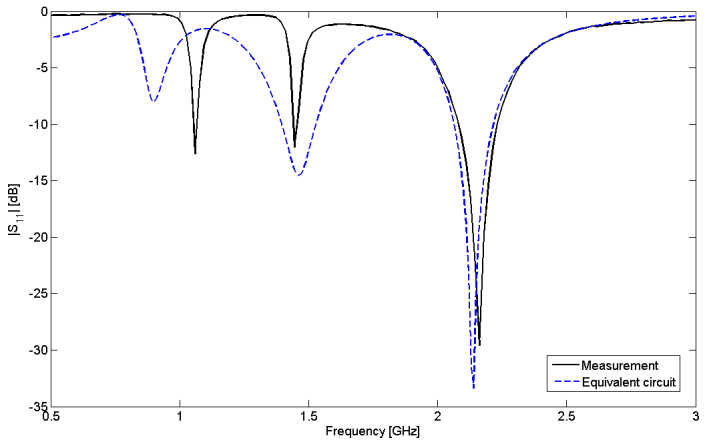

Figure 4.22: Simulated reflection coefficient of the triple-frequency and dual-mode patch antenna (Section 4.9) obtained with the equivalent circuit model. The measured reflection coefficient is also plotted.

between the simulated and the measured results, although there is a frequency shift in the resonance corresponding to the $n = -1$ mode. On the other hand, the other two resonances are well predicted. The value of the reflection coefficient is also well predicted by the model.

A similar model has been developed for the dual-frequency patch antenna presented in Section 4.5. The sketch of the different sections considered in this antenna is shown in Fig. 4.23. The antenna is divided into the same number of sections as the previous one. However, for this antenna, the CRLH section is composed of a 2×2 array of unit cells, resulting in the equivalent circuit model shown in Fig. 4.24. In this case, the upper RH section has been included in the model to take into account the interconnections along the non-propagating direction (y direction) between the CRLH cells. The dimensions of the different sections are: $L_1 = 3.10$ mm, $L_2 = 13.90$ mm, $L_3 = 14.20$ mm, $L_4 = 17.00$ mm, $W_1 = 48.20$ mm and $W_2 = 17.00$ mm. The computed value of the remaining patch parameters are: $G_S = 1/150.5\ \Omega^{-1}$, $B_S = 10.04\ \Omega^{-1}$ and $L_P = 4.99$ nH. The elements of the CRLH cells are computed by using the Eigenfrequencies method, obtaining: $L_R = 16.42$ nH, $C_L = 0.15$ pF, $L_L = 4.51$ nH and $C_R = 0.11$ pF.

The obtained results are shown in Fig. 4.25. The measured reflection coefficient of the manufactured prototype (Fig. 4.18.a) is also plotted. There is a good agreement between both reflection coefficients. The frequency and depth of the working resonances are well predicted by the proposed model. Moreover, the dip between both resonances is also predicted although the

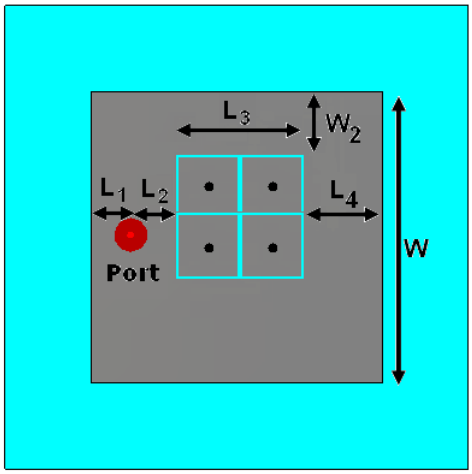

Figure 4.23: Sketch of the different transmission line sections which compose the equivalent circuit of the dual-frequency patch antenna (Section 4.5).

level is deeper than in the measured prototype. It is important to note that this detail in the reflection coefficient is not obtained by the commercial full-wave simulator (Fig. 4.18.b).

4.7 Modelling of Microstrip Patch Antennas Filled with CRLH Structures Using the MPIE-MoM Approach

The equivalent circuit model presented in the previous Section explains the multifrequency behaviour of the microstrip patch antennas filled with CRLH cells. Moreover, it can be used to compute the $[S]$ parameters of these antennas without a high computational load. On the other hand, that numerical approach does not provide information about the electromagnetic fields and the radiation performance of the proposed antennas. For this reason, commercial solvers have been used to analyse these antennas, but they present several problems:

- The computation time is very high. This is due to the higher number of mesh cells used because of the presence of CRLH distributed elements (namely gaps an vias) with dimensions much smaller than the patch.
- The computed reflection coefficients present frequency shifts and are

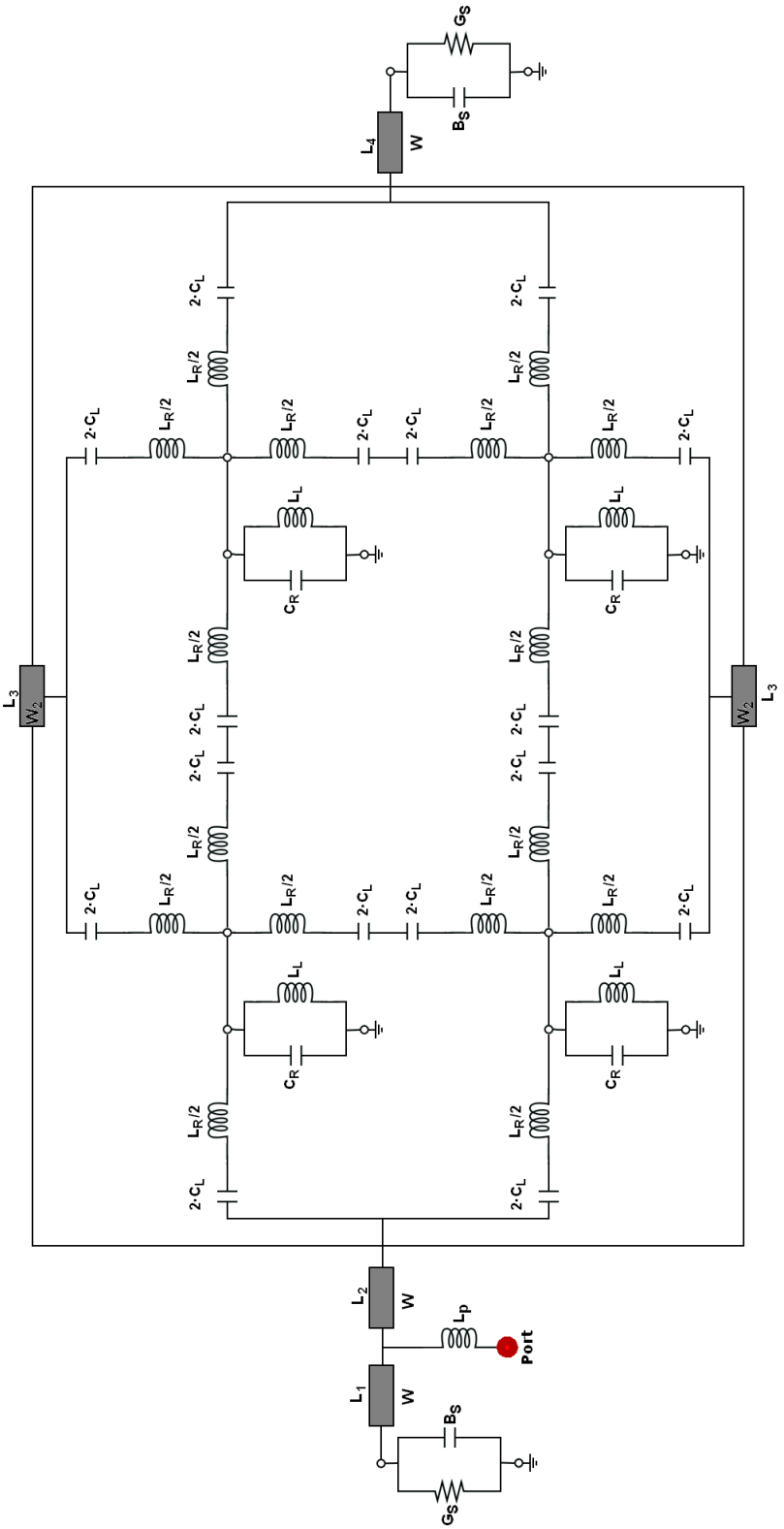

Figure 4.24: Equivalent circuit model of the dual-frequency patch antenna (Section 4.5).

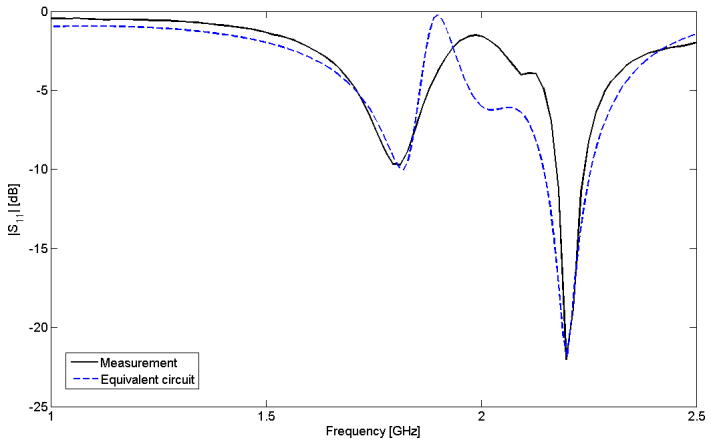

Figure 4.25: Simulated reflection coefficient of the dual-frequency patch antenna (Section 4.5) obtained with the equivalent circuit model. The measured reflection coefficient is also plotted.

not accurate.

- The convergence is not always guaranteed and there are some oscillations around the additional modes (see Fig. 4.14.b for instance).

For these reason, a home-made computational tool based on the MPIE-MoM approach [130, 131] was developed during a Short-Term Scientific Mission in the LEMA-EPFL directed by Prof. Juan R. Mosig. The purpose of this tool is double:

- Development of a full-wave simulator capable to overcome the problems presented by the commercial solvers.
- Analyse the results provided by this tool in order to explain the multifrequency performance of the patch antennas partially filled with CRLH cells.

The outline of the present Section is the following. Firstly, a short revision of the MPIE-MoM approach is presented. Then, the different decisions taken to implement the MPIE-MoM software tool for patch antennas filled with CRLH structures are described. Finally, the software is applied analyse some conventional and multifrequency patch antennas.

4.7.1 Review of the MPIE-MoM Approach

Let us consider the general problem shown in Fig. 4.26. In that model, there is a set of metallic bodies with an arbitrary form embedded in a dielectric multilayered media. The metallic bodies are illuminated by an incident electric field $\mathbf{E}_i$ and they scatter the electric field $\mathbf{E}_s$.

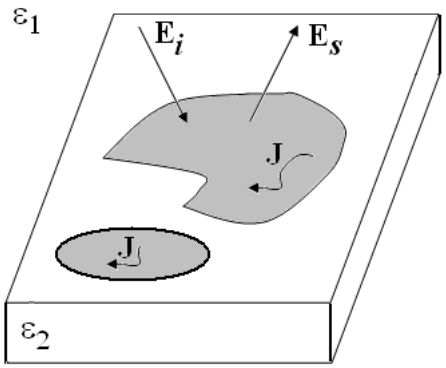

Figure 4.26: General representation of metallic shapes embedded in a dielectric multilayered media.

The total electric field $\mathbf{E}_t$ is the summation of the incident electric field and the scattered electric field:

$$\mathbf{E}_t = \mathbf{E}_i + \mathbf{E}_s. \tag{4.12}$$

Applying the boundary conditions on the surfaces of the electric bodies:

$$\hat{n} \times \mathbf{E}_t = 0 \tag{4.13}$$

which results in

$$\hat{n} \times (\mathbf{E}_i + \mathbf{E}_s) = 0 \tag{4.14}$$

Applying the linearity and superposition theorems, the scattered electric field can be obtained from the electric current $\mathbf{J}$ as

$$\mathbf{E}_s = \overleftrightarrow{\mathbf{G}}_{\mathbf{EJ}} \otimes \mathbf{J} \tag{4.15}$$

where $\overleftrightarrow{\mathbf{G}}_{\mathbf{EJ}}$ is the Green's function dyadic created by the electric current and the operator $\otimes$ is the integral convolution:

$$\overleftrightarrow{\mathbf{G}}_{\mathbf{EJ}} \otimes \mathbf{J} = \int_{S'} \overleftrightarrow{\mathbf{G}}_{\mathbf{EJ}}(\mathbf{r}|\mathbf{r}') \cdot \mathbf{J}(\mathbf{r}')\mathrm{d}S' \tag{4.16}$$

Substituting (4.15) into (4.14)

$$\hat{n} \times (\mathbf{E}_i + \overleftrightarrow{\mathbf{G}}_{\mathbf{EJ}} \otimes \mathbf{J}) = 0 \tag{4.17}$$

The electric field can be also derived from potentials as

$$\mathbf{E}_s = -j\omega\mathbf{A} - \nabla V \tag{4.18}$$

resulting the following Green's function for the potentials

$$\overleftrightarrow{\mathbf{G}}_{\mathbf{EJ}} \otimes \mathbf{J} = -j\omega \overleftrightarrow{\mathbf{G}}_{\mathbf{A}} \otimes \mathbf{J} - \nabla \left(G_V \otimes q_e\right) \tag{4.19}$$

where $\overleftrightarrow{\mathbf{G}}_{\mathbf{A}}$ and G_V are the Green's function dyadics related to the vector and scalar potentials and

$$q_e = -\frac{1}{j\omega}\nabla \cdot \mathbf{J}. \tag{4.20}$$

Finally, the Mixed Potential Integral Equation (MPIE) is obtained by using the Green's function for the potentials (4.19) in (4.17)

$$-\hat{n} \times \mathbf{E}_i = \hat{n} \times \left[-j\omega \overleftrightarrow{\mathbf{G}}_{\mathbf{A}} \otimes \mathbf{J} + \frac{1}{j\omega}(\nabla G_V) \otimes (\nabla' \cdot \mathbf{J})\right] \tag{4.21}$$

An important advantage of the method came from the fact that the Green's function for the potentials presents a singularity milder than those for the fields (R^{-1} instead of R^{-3}).

The MPIE equation (4.21) is solved by applying the Method of Moments (MoM) in the Galerkin form. The unknown current density $\mathbf{J}$ is expanded using a set of N basis functions $\mathbf{f}_k$ defined over a subdomain S_k of the surface S:

$$\mathbf{J} = \sum_{k=1}^{N} \alpha_{Ek}\mathbf{f}_k \tag{4.22}$$

where α_{Ek} are the unknown coefficients. By substituting (4.23) into the MPIE (4.21) and testing with the same basis functions, the following system of equations is obtained for each frequency ω:

$$\sum_{k=1}^{N}(a_{i,k}+v_{i,k})\alpha_{Ek}=e_k \tag{4.23}$$

where for $i,k=1,\ldots,N$

$$e_k=\int_S \mathbf{E}_i(\mathbf{r})\cdot\mathbf{f}_k(\mathbf{r})\mathrm{d}S=\langle\mathbf{E}_i,\mathbf{f}_k\rangle \tag{4.24a}$$

$$a_{i,k}=j\omega\left\langle\mathbf{f}_i,\overleftrightarrow{\mathbf{G}}_{\mathbf{A}}\otimes\mathbf{f}_k\right\rangle \tag{4.24b}$$

$$v_{i,k}=\frac{1}{j\omega}\left\langle\nabla\cdot\mathbf{f}_i,G_V\otimes(\nabla'\cdot\mathbf{f}_k)\right\rangle \tag{4.24c}$$

This numerical method must be implemented following a *numerical recipe*. The different steps to model and simulate an antenna by using the MPIE-MoM approach are summarized as follows:

1. Define the geometry and discretise the antenna:
   - Define the unit cell geometry and mesh the antenna.
   - Meshing depends on the basis functions chosen for the antenna.
2. Define the Green's functions.
3. Numeric part:
   (a) Compute the coupling integrals and fill the MoM matrix for each frequency.
   (b) Define the excitation.
   (c) Solve the matrix equation for each frequency.
   (d) Obtain the parameters of interest (current distributions).
   (e) Post-process of the computed results to obtain other interesting magnitudes ($[S]$ parameters, radiation patterns, etc.)

4.7.2 Implementation

The different implementation decisions which have been taken to develop the MPIE-MoM tool are detailed in this Subsection. A first general comment must be made regarding the programming language. The steps of the MPIE-MoM approach have been programmed in Matlab ®.

Geometry definition and discretisation

The antennas considered for simulation with the developed tool are patch antennas without dielectric (free space filling) and over an infinite ground plane. The feeding approach is a coaxial probe. Three different geometries are considered: rectangular patches, ring patches (rectangular patches with a rectangular slot inside them) and patch antennas filled with CRLH mushroom structures.

For all the cases, a 3-D problem is considered. The metallizations of the patches are placed on the $x-y$ plane. The vias to the ground plane and the coaxial feedings are implemented as prisms along the $\hat{z}$ direction.

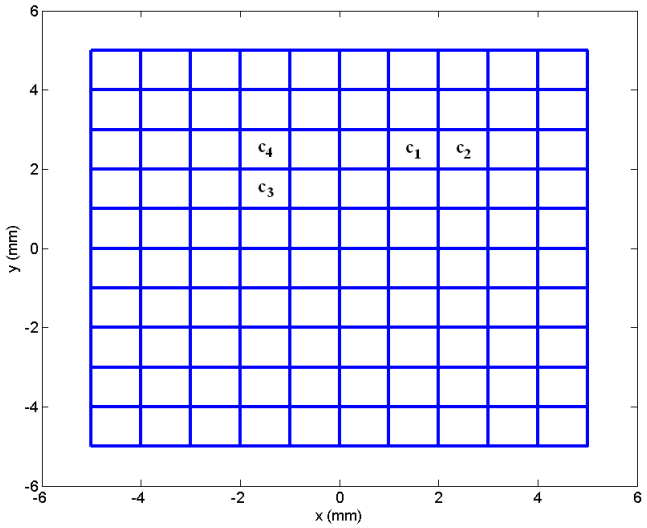

Figure 4.27: Metallic plate meshed with square mesh cells.

The initial step to simulate a concrete structure by the MoM consists of defining a unit cell geometry. Then, the metallic parts of the geometry are divided into mesh cells. For the proposed implementation, rectangular (or square) mesh cells are used. Fig. 4.27 shows an example of a square metallic plate with dimensions 5.00 mm $\times$ 5.00 mm which has been meshed with square mesh cells. In this case, the dimensions of each mesh cell are 1.00 mm $\times$ 1.00 mm.

Once the structure has been discretised into rectangular (or square) mesh cells, the base functions are defined between any pair of mesh cells. In this case, rooftop base functions along the three main directions $(\hat{x}, \hat{y}, \hat{z})$ are employed. Rooftop basis functions are normalized triangular functions defined between any pair of contiguous mesh cells. For example, Fig. 4.28 shows the

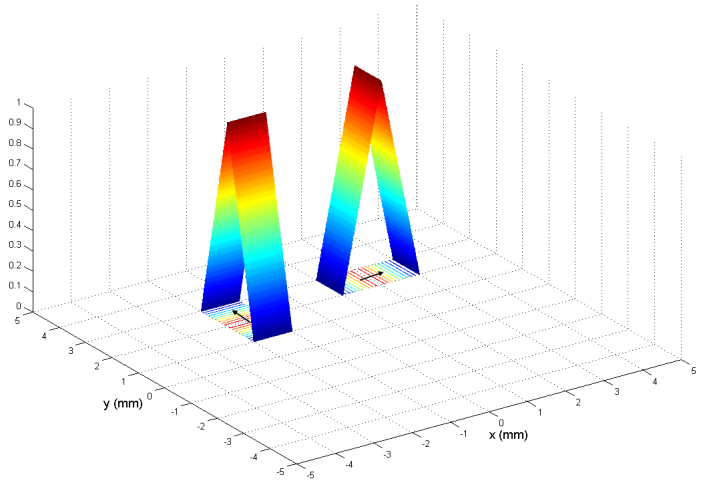

Figure 4.28: Rooftop functions defined by the mesh cells highlighted in Fig. 4.27.

rooftop function along the $\hat{x}$ direction defined by the mesh cells $\mathbf{c_1}$ and $\mathbf{c_2}$ in Fig. 4.27. The rooftop function along the $\hat{y}$ direction defined by the mesh cells $\mathbf{c_3}$ and $\mathbf{c_4}$ in Fig. 4.27 is also plotted.

The bends (i. e. connections between metallic parts placed along the $\hat{z}$ direction and other in the $x-y$ plane) and the interface between the ground plane and the vias or the coaxial probe are implemented by using half rooftop basis functions.

Definition of the Green's functions

Green's functions for the potentials in free space with one image have been used. Image theory has been used to take into account the effect of the infinite ground plane.

The Green's function for the potentials in free space are

$$\overleftrightarrow{\mathbf{G}}_{\mathbf{A}} = \mu_0 G(R) \begin{pmatrix} 1 & 0 & 0 \\ 0 & 1 & 0 \\ 0 & 0 & 1 \end{pmatrix} \tag{4.25a}$$

$$G_V = \frac{1}{\varepsilon_0} G(R) \tag{4.25b}$$

$$G(R) = \frac{\exp(-jkR)}{4\pi R} \tag{4.25c}$$

with $R = |\mathbf{r} - \mathbf{r}'|$, being $\mathbf{r}' = (x', y', z')$ the coordinates of the source.

As commented before, an image with coordinates $\mathbf{r}'' = (x', y', -z')$ is considered to take into account the effect of the infinite ground plane, resulting in the following Green's functions for the potentials:

$$\overleftrightarrow{\mathbf{G}}_{\mathbf{A}} = \mu_0 \begin{pmatrix} G^-(R, R^-) & 0 & 0 \\ 0 & G^-(R, R^-) & 0 \\ 0 & 0 & G^+(R, R^-) \end{pmatrix} \tag{4.26a}$$

$$G_V = \frac{1}{\varepsilon_0} G^-(R, R^-) \tag{4.26b}$$

$$G^-(R, R^-) = \frac{1}{4\pi} \left[\frac{\exp(-jkR)}{R} - \frac{\exp(-jkR^-)}{R^-} \right] \tag{4.26c}$$

$$G^+(R, R^-) = \frac{1}{4\pi} \left[\frac{\exp(-jkR)}{R} + \frac{\exp(-jkR^-)}{R^-} \right] \tag{4.26d}$$

with $R^- = |\mathbf{r} - \mathbf{r}''|$.

Numeric part

As the MoM matrix has to be computed for each frequency, a useful technique to reduce the computation time consists of expanding the Green's functions in the following way:

$$G^-(R, R^-) = G_0^-(R, R^-) + G_D^-(R, R^-) \tag{4.27a}$$

$$G^+(R, R^-) = G_0^+(R, R^-) + G_D^+(R, R^-) \tag{4.27b}$$

being $G_0^-(R, R^-)$ and $G_0^+(R, R^-)$ the static components of $G^-(R, R^-)$ and $G^+(R, R^-)$, respectively, and $G_D^-(R, R^-)$ and $G_D^+(R, R^-)$ the dynamic ones. The static components are independent of the frequency while the dynamic counterparts take into account the frequency dependence of the Green's functions. The resulting static components are:

$$G_0^-(R, R^-) = \frac{1}{4\pi} \left[\frac{1}{R} - \frac{1}{R^-} \right] \tag{4.28a}$$

$$G_0^+(R, R^-) = \frac{1}{4\pi} \left[\frac{1}{R} + \frac{1}{R^-} \right] \tag{4.28b}$$

and the dynamic ones are:

$$G_D^-(R,R^-) = G^-(R,R^-) - G_0^-(R,R^-) = \frac{1}{4\pi}\left[\frac{\exp(-jkR)-1}{R} - \frac{\exp(-jkR^-)-1}{R^-}\right] \tag{4.29a}$$

$$G_D^+(R,R^-) = G^+(R,R^-) - G_0^+(R,R^-) = \frac{1}{4\pi}\left[\frac{\exp(-jkR)-1}{R} + \frac{\exp(-jkR^-)-1}{R^-}\right] \tag{4.29b}$$

This expansion is a powerful method to alleviate the computational cost to compute the MoM matrix, because the static components can be computed once and stored in memory at the beginning of the numeric routine. Then, the coupling matrix is filled for each frequency by adding these pre-computed static components to the dynamic ones. The advantage of the method comes from the fact that the singularity in the Green's function for the potentials (R^{-1} singularity type) is extracted from the dynamic components remaining only a mild singularity. Hence, the R^{-1} singularity is removed from the frequency loop.

Considering the expansions (4.28)-(4.29), four types of coupling integrals are present in the computation of the MoM matrix:

$$I_{0+} = \int_S \int_{S'} \frac{1}{R} \mathrm{d}S'\mathrm{d}S \tag{4.30a}$$

$$I_{0-} = \int_S \int_{S'} \frac{1}{R^-} \mathrm{d}S'\mathrm{d}S \tag{4.30b}$$

$$I_{D+} = \int_S \int_{S'} \frac{\exp(-jkR)-1}{R} \mathrm{d}S'\mathrm{d}S \tag{4.30c}$$

$$I_{D-} = \int_S \int_{S'} \frac{\exp(-jkR^-)-1}{R^-} \mathrm{d}S'\mathrm{d}S \tag{4.30d}$$

After studying the behaviour of these integrals, some numeric rules have been applied in the proposed implementation to efficiently compute the previous coupling integrals with a minimum error. The integral (4.30a) is the only one which presents a R^{-1} singularity. As explained before, this integral is only needed for the computation of the static components. Considering, the sketch in Fig. 4.29, the computation of this integral has been implemented as follows:

- A Polar Transformation is used to remove the singularity when the source and the observation cells are the same.

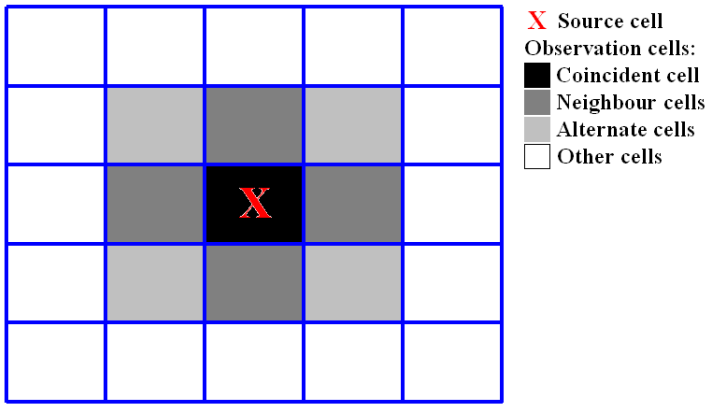

Figure 4.29: Classification of the observation cells depending on their distance to the source cell.

- A four-points Gaussian Quadrature is employed when the source and observation cells are neighbours.
- A two-points Gaussian Quadrature is used when the source and observation cells are alternate.
- The Midpoint Rule is employed for the rest of the interactions between cells.

The integral (4.30b) has no singularity in the integrand. For this reason, the following rules are applied to compute this integral:

- A four-points Gaussian Quadrature is used when the source and observation cells are coincident.
- A two-points Gaussian Quadrature is employed when the source and observation cells are close (neighbors or alternate cells).
- The Midpoint Rule is used for the rest of the interactions between cells.

The integral (4.30c) has a mild singularity in the integrand. Thus, the computation of this integral is as follows in the proposed implementation:

- A two-points Gaussian Quadrature is employed when the source and observation cells are coincident.
- The Midpoint Rule is used for the rest of the interactions between cells.

Finally, the integral (4.30d) has no singularity in the integrand. The Midpoint Rule is used for all the interactions between the cell because the error when this rule is used is very small in all of the cases.

After computing the MoM matrix, the excitation must be defined. The excitation of the antenna is defined by using the delta gap model. This model considers a constant voltage in the excitation and 0 elsewhere.

Once the MoM matrix is inverted, the current distribution on the metallic bodies is obtained for each frequency. Then, the reflection coefficient of the antenna is computed from the current results. The tool also offers the possibility of computing the radiation pattern. This functionality is implemented by considering each basis function as an infinitesimal dipole and integrating the radiated fields generated by all these infinitesimal dipoles.

Inputs and outputs of the software tool

The input parameters of the developed software tool are:

- The geometry of the antenna (rectangular, ring or CRLH-filled patch antenna), including the dimensions of all the elements.
- The frequency range and the step between each frequency for which the problem is solved.
- The maximum dimensions of the mesh cells.

The outputs of the program are:

- The reflection coefficient within the simulation range (the input impedance or admittance of the antenna under study can be also plotted).
- The current distributions at the frequencies of interest.
- The radiation patterns at the desired frequencies.

4.7.3 Examples and Analysis of the Results

In this Subsection, a microstrip patch antenna partially filled with CRLH cells is analysed with the developed software. The dimensions of the antenna, according to Fig. 4.9.a, are: $L = W = 42.00$ mm, $L_m = 12.00$ mm, $W_m = 18.00$ mm, $g_1 = g_2 = 0.2$ mm, $d = 0.70$ mm and $h = 10.00$ mm. The probe is placed at 4.00 mm from the edge of the patch.

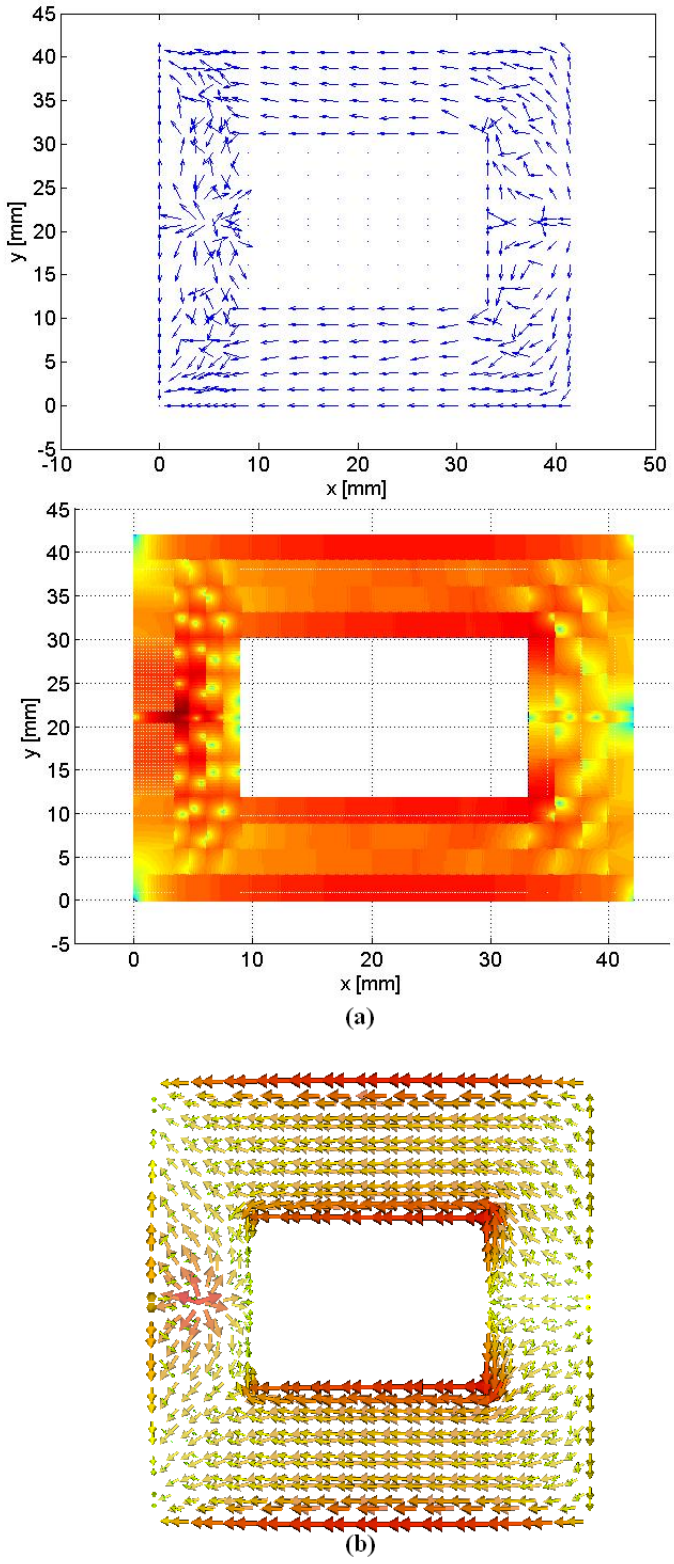

Figure 4.30: Currents on the ring patch antenna working at its fundamental mode ($n = +1$). (a) MPIE-MoM software. (b) CST Microwave Studio ®.

First of all, the equivalent ring patch antenna (the same patch antenna but without filling CRLH mushrooms) has been simulated with the home-made software and a commercial simulator (CST Microwave Studio ®) in order to show the validity of the developed tool. The resonance frequency of the fundamental fundamental mode of the ring patch antenna ($n = +1$) is $f_{+1} = 2.85$ GHz. The surface currents on the patch computed with both software programs are shown in Fig. 4.30. The typical half-wavelength current distribution is obtained in both cases. There is a great agreement between both results.

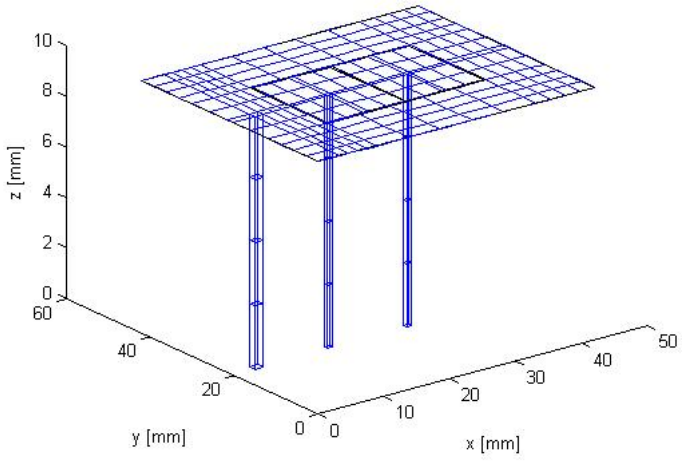

Figure 4.31: Meshing of a patch filled with CRLH cells computed by the proposed tool.

Once the home-made software has been validated, the proposed patch filled with CRLH structures has been simulated. Fig. 4.31 shows the meshing of the patch filled with CRLH cells computed with the proposed simulator.

Fig. 4.32 shows the current distributions of the three working modes ($n = -1, 0, +1$) computed with the home-made software. The resonance frequencies of these modes are: $f_{-1} = 1.60$ GHz, $f_0 = 2.20$ GHz and $f_{+1} = 2.95$ GHz. The analysis of the current distributions is useful to explain the triple-frequency and dual-mode behaviour of this antenna. The surface currents on the ring part at both half-wavelength modes ($n = \pm 1$) are similar to the fundamental mode of the conventional ring patch antenna (Fig. 4.30). For this reason, the patch antennas filled with CRLH cells present the patch-like radiation pattern at the $n = \pm 1$ modes. Moreover, in both $|n| = 1$ modes one of the mushroom vias is a current source while the other is a current sink. The difference between the RH mode ($n = +1$) and the LH mode ($n = -1$)

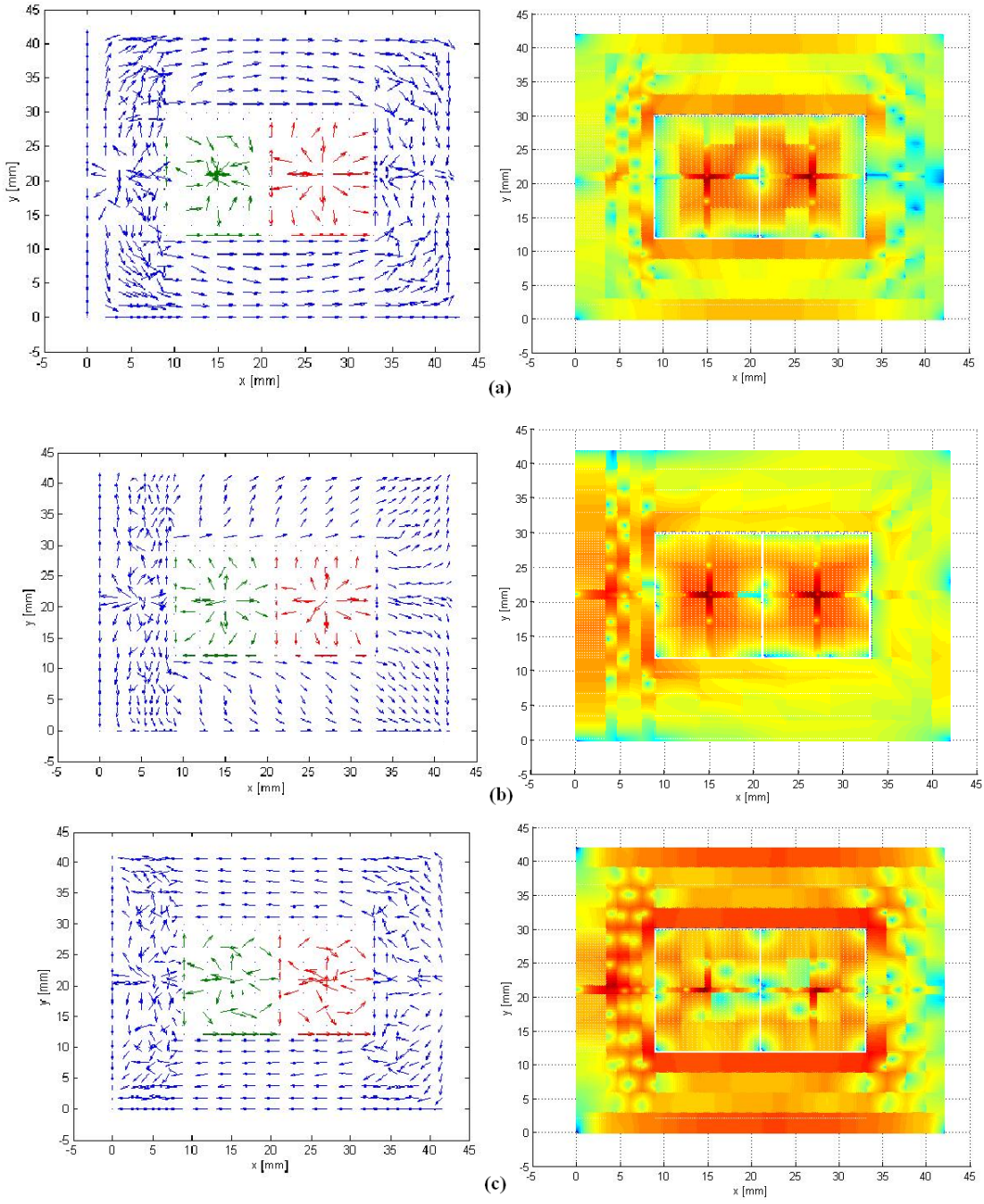

Figure 4.32: Current distributions computed with the home-made MPIE-MoM software. (a) $n = -1$ mode. (b) $n = 0$ mode. (c) $n = +1$ mode.

is that the source and sink vias are interchanged. A similar effect can be seen in the sense of the currents on the ring part of the patch, because in one case the currents flow from the left to the right whilst the other case is the other way around. On the other hand, the current distribution at the $n = 0$ mode is completely different. One important difference of the $n = 0$ monopolar mode with respect to the patch-like modes is that both mushroom vias act as sources or sinks at the same time. This different current distribution provides the multifunction performance of the microstrip patch antennas partially filled with CRLH cells.

4.8 Multifrequency Microstrip Patch Antennas with Multiple Polarizations

In the previous Sections, only modes with propagation along one main direction (TM_{n0} modes) have been used. Thus, all the patch-like modes were working with the same linear polarization (x axis, according to the Figs. 4.9.a-4.16.a). In this Section the possibility of exciting modes with orthogonal propagation with respect to the previous ones (TM_{0m} modes) is studied. This can be used to increase the multifunctionality of the patch antennas filled with CRLH cells because antennas with simultaneous multifrequency and polarization diversity can be obtained.

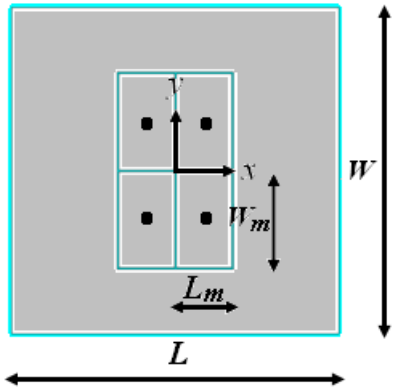

Figure 4.33: Sketch of the patch antenna partially filled with four CRLH cells, two in the x direction and two in the y direction.

The conventional technique to excite orthogonal modes in microstrip patch antennas consists of feeding the antenna through two orthogonal ports.

Moreover, the dimensions of the two propagation directions in the patch antenna must be different when the objective is to achieve different resonance frequencies. This is the case of a rectangular patch fed through two orthogonal ports in which the TM_{10} and TM_{01} are obtained at different frequencies. When microstrip patch antennas partially filled with CRLH cells (Fig. 4.33) are used, two different approaches can be proposed to excite modes with orthogonal polarizations and different frequencies:

1. Using square CRLH cells and a rectangular patch. In this way the dimensions L and W are different while L_m and W_m are equal. This is similar to the approach used for conventional patches, as commented before.

2. Keeping the patch square and the CRLH cells rectangular so the dimensions of the CRLH cells (L_m and W_m) are different. This idea comes from the fact that rectangular mushroom CRLH cells have a different propagation constant along the two main directions [52].

In order to study the suitability of both approaches to develop multifrequency antennas with polarization diversity two analysis have been made. The first one is a modal analysis of the structure to identify the modes which can be excited. The second analysis is a parametric study to compute the frequency ratio between the working modes which can be achieved by each approach.

The result of the modal analysis is similar for both approaches. For example, the results for the second approach are presented. In this case, the patch antenna of Fig. 4.33 has been simulated with the modal solver of CST Microwave Studio ®. The dimensions of the antenna are the following: $L = W = 40.00$ mm, $L_m = 7.00$, $W_m = 12.00$ mm, the gaps have 0.20 mm width and the vias radius is 0.35 mm. The substrate is Polypropylene ($\varepsilon_r = 2.20$) with $h = 4.00$ mm.

Fig. 4.34 shows the E_z field distributions for the first six modes obtained in the modal analysis. For simplicity, the conventional notation TM_{nm} is substituted by the pair $[n, m]$. It is important to note that four of the modes have half-wavelength electric field distribution ($[-1, 0]$, $[0, -1]$,$[+1, 0]$ and $[0, +1]$) and one pair has propagation along the x direction ($[-1, 0]$ and $[+1, 0]$) while the other pair has propagation along the orthogonal direction ($[0, -1]$ and $[0, +1]$). This can be used to develop novel patch antennas:

- Quad-frequency antennas with polarization diversity when the four dipolar modes are excited simultaneously at different frequencies.

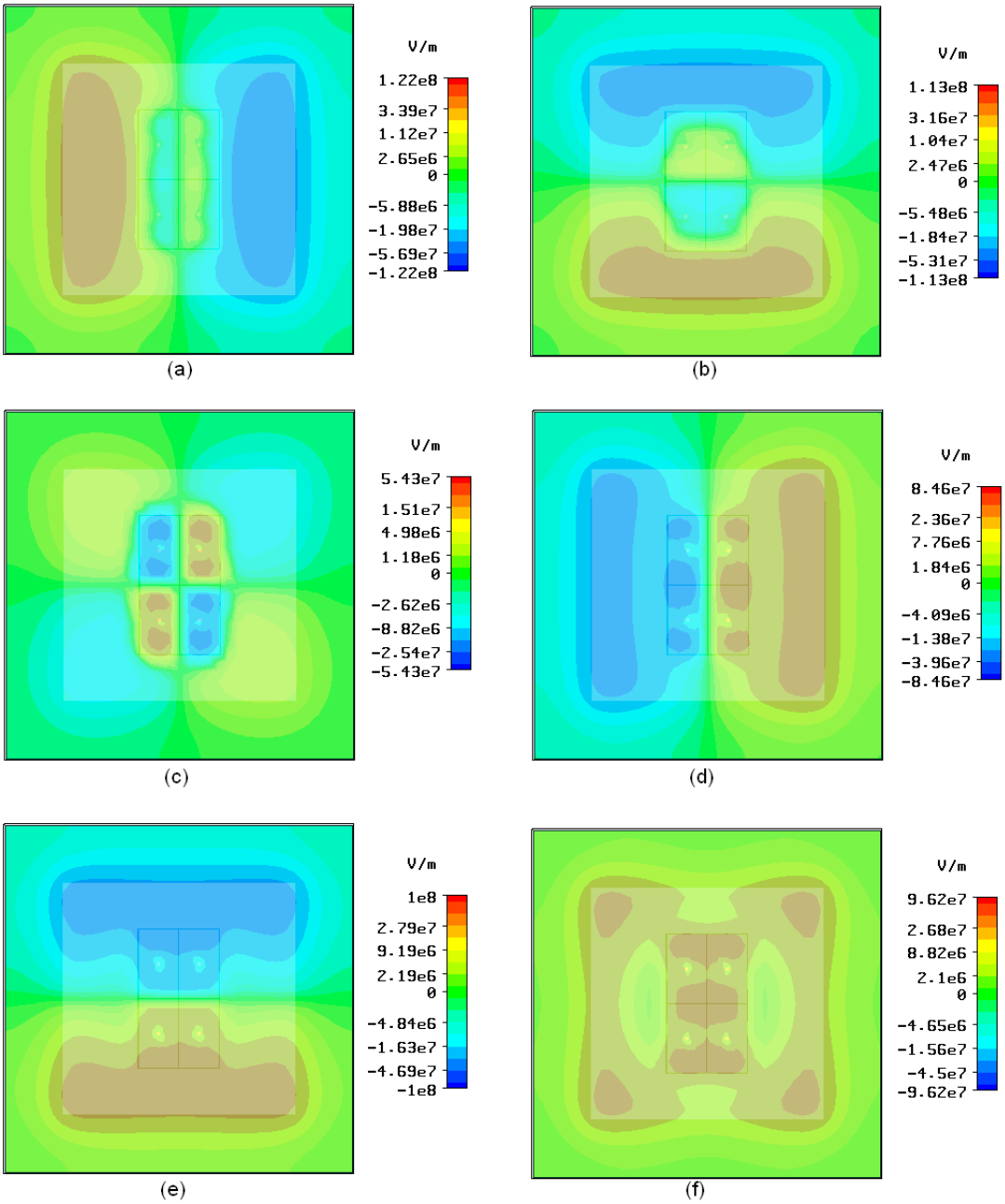

Figure 4.34: E_z field distributions for the different modes of the patch filled with a 2×2 array of CRLH cells. (a) $[-1, 0]$ at 1.78 GHz. (b) $[0, -1]$ at 1.89 GHz, (c) $[-1, -1]$ at 2.10 GHz, (d) $[+1, 0]$ at 2.56 GHz, (e) $[0, +1]$ at 2.73 GHz, (f) $[0, 0]$ at 2.97 GHz.

- Dual-frequency CP antennas when the pair of LH modes ($[-1,0]$ and $[0,-1]$) and the pair of RH modes ($[+1,0]$ and $[0,+1]$) are excited in quadrature.

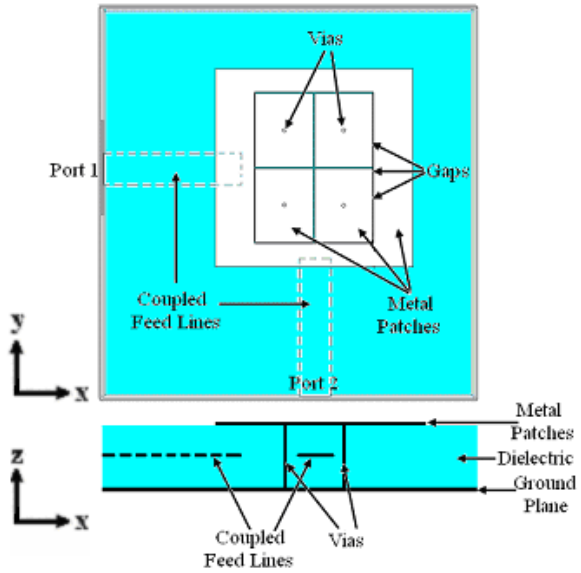

Figure 4.35: Quad-frequency patch antenna filled with CRLH cells and fed through two microstrip coupled lines.

In order to make the parametric study, the previous antenna structure has been used but in this case the antenna is fed through two orthogonal coupled lines placed at the center of each patch side to excite the modes with orthogonal polarizations (Fig. 4.35). The feeding lines are placed in the middle of the substrate height and they are shifted 15.00 mm away from the center of the patch. The port placed along the x direction is numbered as 1 while the orthogonal port is numbered as 2. Other feeding schemes are possible (microstrip line or coaxial probes) but feeding through coupled lines been chosen since it provides better isolation between the ports.

The frequency variation obtained with the two proposed approaches is studied. The first approach is implemented when the internal CRLH cells are kept square ($L_m = W_m = 7.00$ mm) while one of the patch dimension is varied. In this case, the vertical dimension of the patch, W, is varied while the horizontal one is maintained fixed,$L = 40.00$ mm, to obtain its parametric performance. Fig. 4.36 shows the antenna frequencies for the proposed situation. As the length of the patch is not varied, the resonant frequencies at

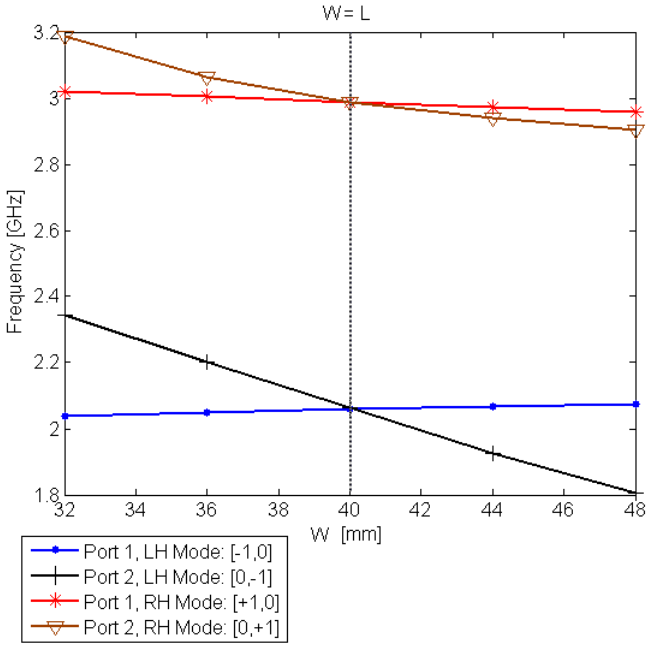

Figure 4.36: Resonant frequencies of the patch-like modes excited in the quad-frequency patch antenna when the CRLH cell dimensions (L_m, W_m) and the length of the patch (L) are set fixed while the width of the patch (W) is varied.

port 1 are nearly constant. The frequency variation is 1.78% for the LH mode $[-1, 0]$ and 1.98% for the RH mode $[+1, 0]$. This is logical since the only modification has been done along the orthogonal direction to port 1. On the other hand, as the vertical dimension is reduced, the resonant frequencies at port 2 are increased. It can also be seen that the slope for the RH mode ($[0, +1]$) is smaller than the one of the corresponding LH mode ($[0, -1]$) at this port. In particular, the frequency variation of the RH mode is 9.26% while it is 25.87% for the LH one. This makes that the resonant frequencies of the RH modes with orthogonal propagation constants ($[+1, 0]$ and ($[0, +1]$)) are very close independently of the patch dimensions (the maximum separation is only 5.41%).

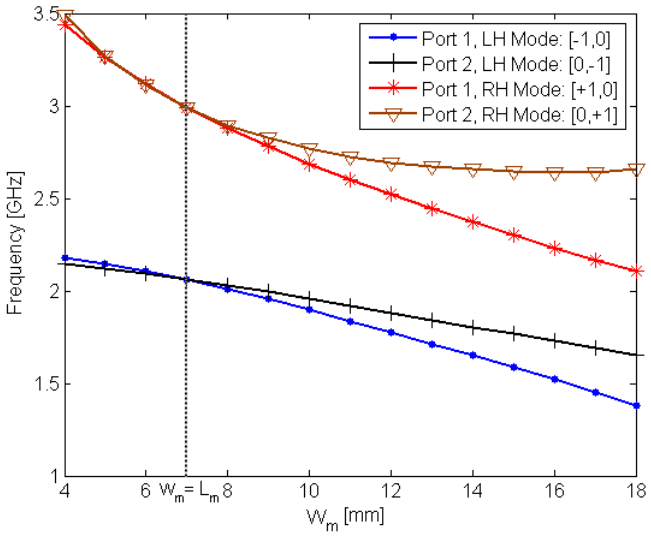

Figure 4.37: Resonant frequencies of the patch-like modes excited in the quad-frequency patch antenna when the dimensions of the patch (L, W) and the length of the CRLH cells (L_m) are set fixed while the width of the cells (W_m) is varied.

The effect of the second design procedure (variation of the vertical CRLH cell dimension W_m) can be seen in Fig. 4.37. In order to obtain its parametric performance, only this cell dimension is varied while the horizontal one is maintained to $L_m = 7.00$ mm. The patch dimensions are kept fixed ($L = W = 40.00$ mm). As it can be seen, the frequencies of the RH modes ($[+1, 0]$ and $[0, +1]$) and the LH ones ($[-1, 0]$ and ($[0, -1]$)) are almost the same for small CRLH cells ($W_m < 8$ mm) although the frequencies of both pairs decreases with increasing W_m. However, as the y dimension of the cell gets larger and larger, the spacing between each pair of modes also increases. The

maximum separation is 10.74% between the RH modes and 18.30% between the LH ones. It is important to note that the frequencies of the modes with propagation along x direction strongly depend on W_m, which is not the case of the previous approach. In summary, the frequency variation of the different modes is: 27.14% for the $[0, +1]$ mode, 48.12% for the $[+1, 0]$ mode, 25.81% for the $[0, -1]$ mode and 45.17% for the $[-1, 0]$ mode.

Thus, with the second design procedure it is easier to achieve four sufficiently spaced resonant frequencies. For that reason this design strategy is more suitable for the design of quad-frequency antennas. Moreover, as the patch is square instead of rectangular, the total area of the antenna is smaller.

Finally, it is clear that when both the patch and the CRLH cells are square (dashed lines in Fig. 4.36 and Fig. 4.37), the resonant frequencies of the LH and RH pairs agree. This situation can be used to develop CP antennas when the ports are fed in quadrature.

4.8.1 Quad-Frequency Microstrip Patch Antennas with Polarization Diversity

As it was concluded above, the best approach to design quad-frequency antennas with polarization diversity consists of a square microstrip patch partially filled with a 2×2 mushroom structure composed of rectangular cells. Two different feeding techniques can be used and each of them is suitable for a different application. The first one consists of feeding the antenna with two orthogonal ports centered at each side of the patch, as in the parametric study (Fig. 4.35). High isolation between both ports can be achieved. This approach can be used to develop antennas for transceivers working for two different wireless services. For most wireless services, the frequency bands for the uplink and the downlink are adjacent. Moreover, for some cases the polarization of both links are orthogonal in order to increase the isolation. Hence, each port of the proposed antennas can be directly connected to a dual-service transmitter and a dual-service receiver taking advantage of the high isolation between them.

The second approach consists of feeding the patch with only one port placed close to the edge of one patch side. Thus, a one-port multifunction patch antenna with four different patch-like modes is achieved. The antenna has both frequency and polarization diversity which can be used for systems in which diversity is required (e.g. MIMO systems).

Prototypes of both approaches are designed, manufactured and measured in the present Subsection.

Quad-Frequency Microstrip Patch Antenna with Polarization Diversity Fed Through Two Ports

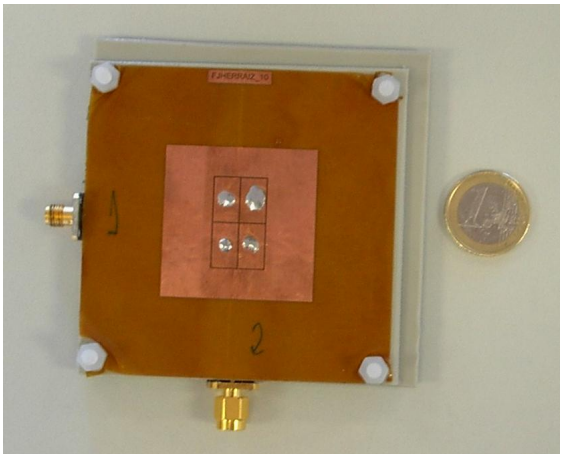

Figure 4.38: Picture of the manufactured quad-frequency microstrip patch antenna with polarization diversity fed through two ports.

As explained before, the first approach to achieve a quad-frequency microstrip patch antenna with polarization diversity consists of feeding a square microstrip patch filled with a 2×2 array of rectangular mushroom structures through two ports placed at the centre of each patch side, as shown in Fig 4.35. Proximity coupled lines have been used because they provide higher isolation than coaxial probes. A prototype of the two port quad-frequency patch antenna has been manufactured (Fig. 4.38). The dimensions of the antenna are unchanged with respect to the example used for the modal analysis: $L = W = 40.00$ mm, $L_m = 7.00$, $W_m = 12.00$ mm, the gaps have 0.20 mm width and the vias radius is 0.35 mm. The substrate is Polypropylene ($\varepsilon_r = 2.20$) with $h = 4.00$ mm (implemented with two 2-mm-heigth boards). The coupled lines are printed on the lower Polypropylene board and they are shifted 15.00 mm away from the center of the patch in each direction.

Fig. 4.39 shows the measured $[S]$ parameters. The return losses are -14 dB at $f_{[-1,0]} = 1.76$ GHz (port 1), -13 dB at $f_{[0,-1]} = 1.88$ GHz (port 2), -16 dB at $f_{[+1,0]} = 2.49$ GHz (port 1) and -38 dB at $f_{[0,1]} = 2.64$ GHz (port 2). The ratio between the working frequencies of the LH ($[-1, 0]$ and $[0, -1]$) and RH ($[+1, 0]$ and $[0, +1]$) modes is approximately 1.41. A little dip can also be appreciated at 2.10 GHz (port 1). According to the modal analysis in Fig. 4.34, this corresponds to a diagonal mode $[-1, -1]$. Lastly, the isolation between the antenna ports is larger than 30 dB for frequencies

up to 2.5 GHz. However, the isolation between port 2 and port 1 at the last working frequency is decreased down to 18 dB. This is due to the fact that a spurious resonance at port 1 appears at 2.63 GHz. The patch length is $\lambda_0/4.26$ and $\lambda_0/4.00$ at the LH frequencies and $\lambda_0/3.01$ and $\lambda/2.86$ at the RH ones, achieving an important degree of miniaturization at the LH frequencies.

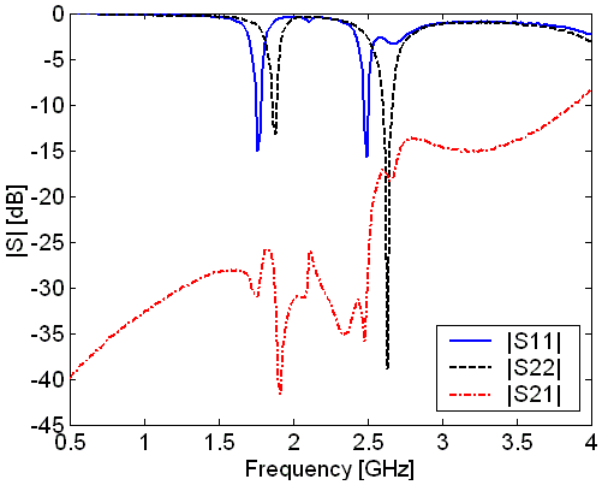

Figure 4.39: Measured $[S]$ parameters of the quad-frequency microstrip patch antenna with polarization diversity fed through two ports.

Fig. 4.40 present the radiation patterns in the $x-z$ and $y-z$ planes at the four working frequencies. The antenna has a patch-like radiation pattern at the four working frequencies, as desired. For the first three situations (modes $[-1,0]$, $[+1,0]$ and $[0,-1]$) the cross-polar component in both planes is lower than -20 dB (with respect to the normalized 0 dB co-polarization level) in most of the spacial directions. However the radiation pattern for the $[0,+1]$ mode at 2.64 GHz presents some distortion and higher cross-polarization due to the presence of the spurious mode seen at 2.63 GHz. It is important to note that the co-polar component is oriented along the x axis for the modes excited through the port 1 ($[-1,0]$ and $[+1,0]$), while it is oriented along the y axis for the modes excited through the port 2 ($[0,-1]$ and $[0,+1]$). Hence, polarization diversity is achieved. Measured gains at the four working frequencies are 5.4 dB at $f_{[-1,0]}$ and $f_{[0,-1]}$, 6.2 dB at $f_{[+1,0]}$ and 6.3 dB at $f_{[0,+1]}$.

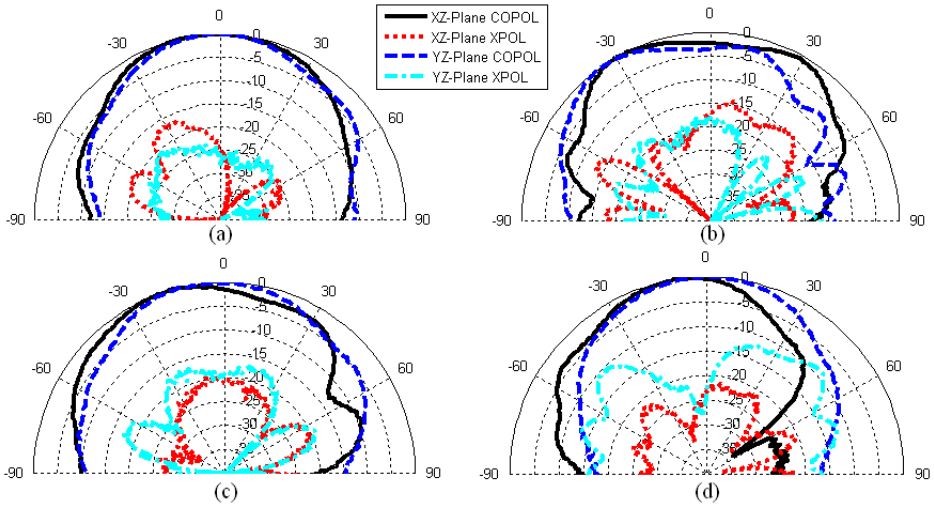

Figure 4.40: Measured radiation patterns of the quad-frequency microstrip patch antenna with polarization diversity fed through two ports. (a) $f_{[-1,0]} = 1.76$ GHz (port 1, COPOL = x). (b) $f_{[+1,0]} = 2.49$ GHz (port 1, COPOL = x). (c) $f_{[0,-1]} = 1.88$ GHz (port 2, COPOL = y). (d) $f_{[0,+1]} = 2.64$ GHz (port 2, COPOL = y).

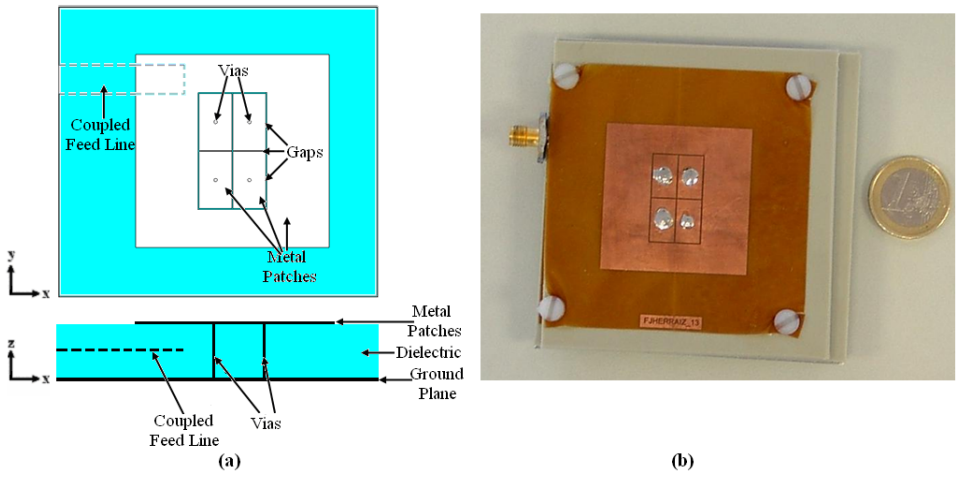

Figure 4.41: Single-port quad-frequency microstrip patch antenna with polarization diversity. (a) Sketch of the antenna. (b) Picture of the manufactured prototype.

Quad-Frequency Microstrip Patch Antenna with Polarization Diversity Fed Through One Port

Fig. 4.41.a shows the sketch of the single-port quad-frequency microstrip patch antenna with polarization diversity. The antenna structure is similar to the dual-port quad-frequency patch antenna but in this case only one coupled line is used to excite the four patch-like modes. This feeding line must be displaced along the y direction to excite the patch-like modes with y polarization ($[0,-1]$ and $[0,+1]$ modes). Moreover, the feeding line must be placed close to the vertical edge of the patch to achieve a proper matching at these modes. A prototype with the same dimensions as the ones presented previously has been manufactured (Fig. 4.41.b). For this case, the patch antenna is fed trough a coupled line displaced 15.00 mm from the centre of the patch in both directions.

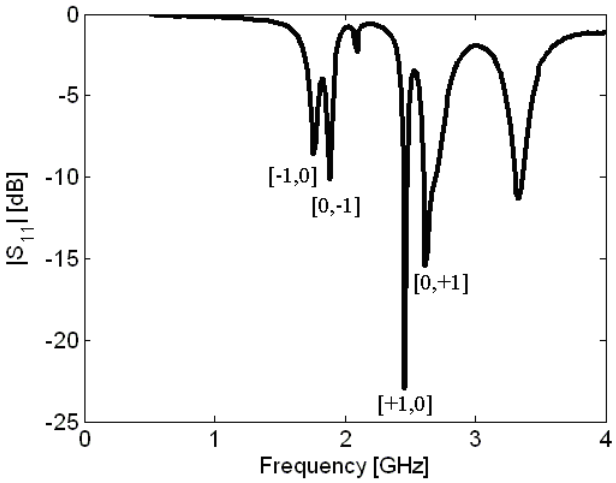

Figure 4.42: Measured reflection coefficient of the single-port quad-frequency microstrip patch antenna with polarization diversity.

The measured reflection coefficient of this antenna is shown in Fig. 4.42. The return losses are -10 dB at $f_{[-1,0]} = 1.76$ GHz, -11 dB at $f_{[0,-1]} = 1.88$ GHz, -24 dB at $f_{[+1,0]} = 2.46$ GHz and -17 dB at $f_{[0,1]} = 2.62$ GHz. The little dip corresponding to the $[-1,-1]$ mode at 2.10 GHz can also be seen. Hence, the resonance frequencies are similar to the previous case and the reflection coefficient is very close to the superposition of the reflection coefficients of boths ports in the dual feeding scheme. Thus, the degree of miniaturization achieved and the ratio between the working frequencies is the same as in the previous case.

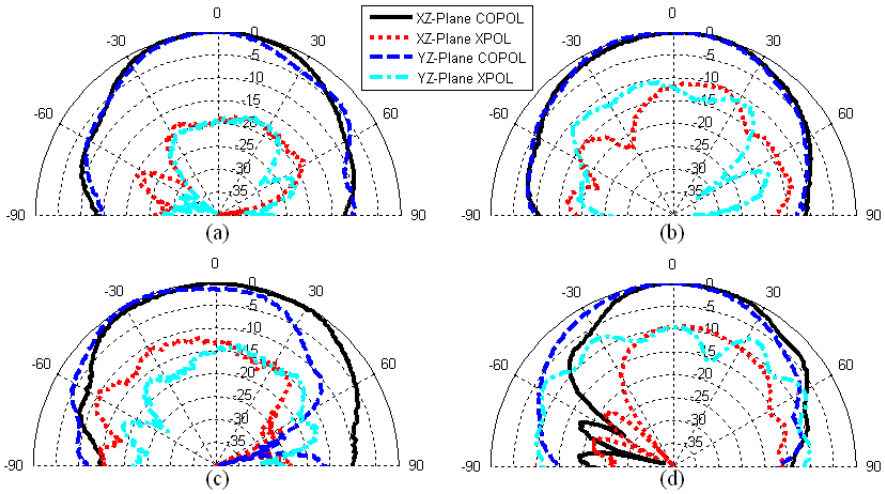

Figure 4.43: Measured radiation patterns of the quad-frequency microstrip patch antenna with polarization diversity fed through one port. (a) $f_{[-1,0]} = 1.76$ GHz (COPOL $= x$). (b) $f_{[+1,0]} = 2.49$ GHz (COPOL $= x$). (c) $f_{[0,-1]} = 1.83$ GHz (COPOL $= y$). (d) $f_{[0,+1]} = 2.62$ GHz (COPOL $= y$).

Fig. 4.43 shows the measured radiation patterns at the four working frequencies. The results are quite similar to the ones obtained with the two-port antenna, achieving four patch-like dipolar modes. The main difference with the two-port prototype is that the cross-polar component has increased. However, this was expected since the displacement of the feeding line makes this antenna asymmetric and the modes with two orthogonal polarization are excited by the same port. It is important to note that four different patch-like modes and polarization diversity has been achieved with a single port. As in the previous prototype, the co-polarization at $f_{[-1,0]}$ and $f_{[+1,0]}$ is oriented along the x axis while it is oriented along the y axis at the other two working frequencies ($f_{[0,-1]}$ and $f_{[0,+1]}$). Measured gains are 5.2 dB at $f_{[-1,0]}$ and $f_{[0,-1]}$, 5.8 dB at $f_{[+1,0]}$ and 5.9 dB at $f_{[0,+1]}$.

4.8.2 Dual-Frequency CP Microstrip Patch Antennas Partially Filled with CRLH Cells

There are two main approaches to achieve CP microstrip patch antennas. The first one consists of exciting two orthogonal half-wavelength modes ($[+1, 0]$ and $[0, +1]$) with equal amplitude and quadrature phase. This can be achieved with two-port patches in which each port is placed at the centre of one side

of the patch and both ports are connected to external circuitry to achieve the quadrature phase. The sign of the relative phase will determine the sense of the polarization (RHCP or LHCP).

The other approach to achieve CP is based on two orthogonal degenerated modes in quadrature. This can be developed with patches with some kind of asymmetry or geometrical modification, such as slots, slightly rectangular patches or elliptical geometries [28]. For all the cases, the dimensions of the antenna are modified such that the resonant frequencies of the two orthogonal modes ($[+1, 0]$ and $[0, +1]$) are close to each other. The antenna is excited at a frequency between both resonant frequencies, such that the amplitudes of the two excited modes are equal. Also, the feeding is placed in a diagonal to excite the two orthogonal modes in phase quadrature.

The main advantages of the first approach are the good axial ratio (AR) and bandwidth. On the other hand, the total size and the complexity of the antenna are increased due to the use of external circuitry (e. g. hybrids) to achieve the phase quadrature between the ports. This drawback is not present in the single-port CP antennas, but they provide limited bandwidths.

Both approaches can be applied to patch antennas filled with CRLH cells to develop dual-frequency CP antennas. In both cases, the dual-frequency performance comes from the fact of exciting the pairs of LH ($[-1, 0]$ and $[0, -1]$) and RH ($[+1, 0]$ and $[0, +1]$) modes with equal amplitude and in quadrature. Examples of both approaches are designed, manufactured and measured. The results are presented in this Subsection.

Dual-Frequency CP Antenna with Two Ports and External Circuitry

This prototype is based on the first approach to achieve a CP patch antenna. It consists of exciting two half-wavelength orthogonal modes with equal amplitude and quadrature phase by using two orthogonal ports and external circuitry. In order to achieve a dual-frequency performance, the dual-frequency patch antenna filled with a 2×2 array of mushroom structures (Section 4.5) is used. Fig. 4.44 shows the sketch of the proposed implementation which is based on the dual-frequency patch fed through two orthogonal coaxial probes. The probes must be fed with the same amplitude and quadrature phase. If the port 1 is fed with 0° and the port 2 is fed with 90°, LHCP is obtained, while RHCP is obtained the other way around. External circuitry is used to obtain the proper feeding at the two ports. It must be taken into account that the feeding circuitry must work correctly at both operating frequencies to achieve a good AR. Dual-band hybrids [132] are proposed to be used as

feeding circuitry for large frequency ratios between the working frequencies and broad-band three-arm hybrids [133] is the optimal solution for small ratios.

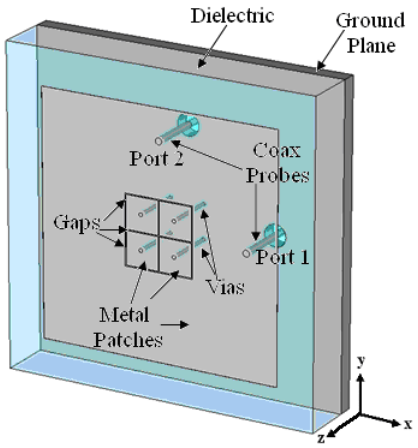

Figure 4.44: Sketch of the dual-frequency CP patch antenna with two orthogonal coaxial probes.

An interesting feature of the patch antennas filled with CRLH cells is that the frequency ratio between the different modes can be set within a wide range of values, as shown in Sections 4.4-4.5. This property can be used to design dual band CP patch antennas with very different frequency ratios, which cannot be achieved with other approaches. For this particular case, there is only one degree of freedom since the patch and the CRLH cells are square (Fig. 4.44). In order to study the variation of the frequency ratio with respect to the patch and mushrooms dimensions, a study based on CST Microwave Studio ® simulations has been made. As concluded in Sections 4.4-4.5, the frequency ratio mainly depends on the patch and cells dimensions. For this reason, two different patch antennas are studied. In both cases, the dimensions of the patch are fixed while the size of the cells is varied. The details of the simulations are as follows: the first patch has $L = W = 46.00$ mm with $h = 10.00$ mm height and the second patch has $L = W = 48.20$ mm over a substatre with $h = 8.00$ mm height, according to Fig. 4.16.a. In both cases the substrate is Polypropylene ($\varepsilon_r = 2.2$), the vias diameter is $d = 0.70$ mm and the gaps are $g = 0.20$ mm. Lastly, the the side of the square cell changes from $L_m = 5.00$ mm to $L_m = 17.00$ mm. The results of the simulations are shown in Fig. 4.45. The range of values that can be obtained is very broad and it goes from very small values (smaller than 1.2) to large values such us 2.2. It is important to note that such small

values cannot be achieved with other approaches.

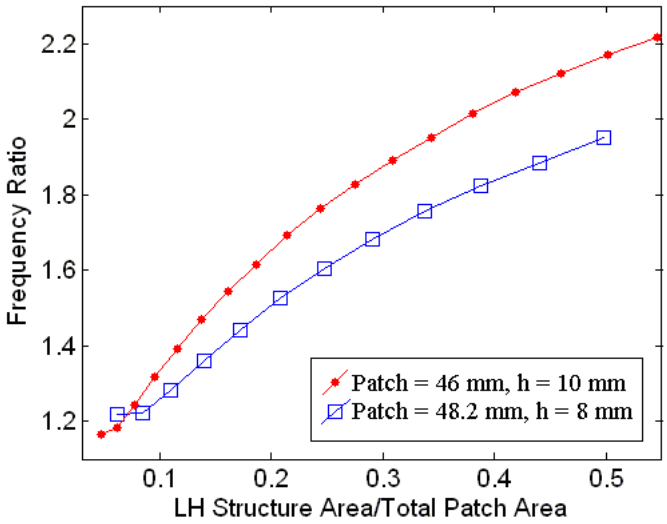

Figure 4.45: Dependence of the frequency ratio between the working frequencies of the dual-band CP patch antenna on the size of the patch and mushroom structures.

As an example, a dual-band CP antenna working at the GSM1800 and UMTS bands is designed, manufactured and measured. These two wireless services are chosen due to their popularity and the small frequency ratio between their bands. The dimensions of the patch antenna are chosen to achieve the working frequencies within the chosen bands. According to Fig. 4.16.a, the patch side is $L = W = 46.00$ mm and the dimensions of the mushrooms are $L_m = W_m = 6.50$ mm, the vias diameter is $d = 0.70$ mm and the separation gap between elements is $g = 0.20$ mm. The substrate is Polypropylene (PP) with $\varepsilon_r = 2.2$ and $h = 10.00$ mm. The coaxial probes are placed at 16.50 mm from the centre.

A prototype of the proposed antenna has been manufactured and its measured $[S]$ parameters are plotted in Fig. 4.46. The measured reflection coefficient at both ports is below -20.5 dB at $f_{-1} = 1.80$ GHz and -10.25 dB at $f_{+1} = 2.11$ GHz. The isolation between both ports is higher than 12 dB at both working frequencies. This isolation can be improved by using proximity coupling feeds, as shown in Subsection 4.8.1. The electrical length of the patch is $\lambda_0/3.62$ at the first working frequency and $\lambda_0/3.09$ at the second working frequency. The ratio between the frequencies is only 1.17.

In this case, a broad-band hybrid coupler is chosen to feed the antenna

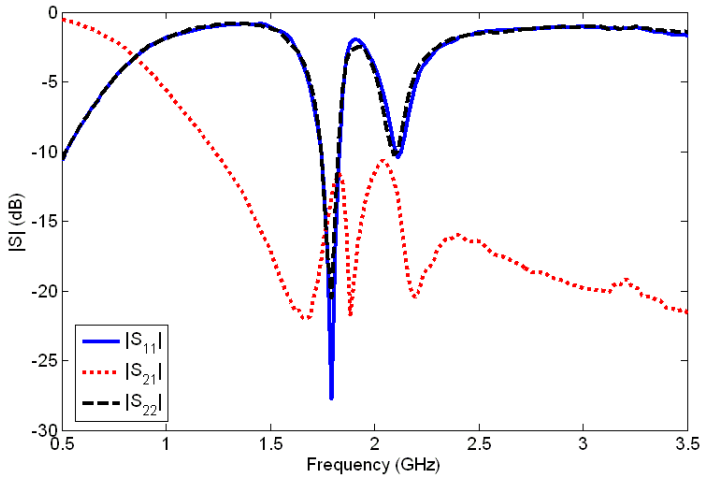

Figure 4.46: Measured $[S]$ parameters of the dual-band CP patch antenna with two orthogonal ports.

because it can cover both working bands [133]. A prototype of the broad-band hybrid has been manufactured and its measured $[S]$ parameters are depicted in Fig. 4.47, considering the port 1 as the input and the ports 3 and 4 the outputs. There is approximately 1.2 dB difference between $|s_{31}|$ and $|s_{41}|$ at both working frequencies. This difference affects the AR of the antenna, leading to worse values than the optimal that can be achieved with an ideal hybrid. On the other hand, there is no error in the phase response of the circuit.

Finally, the broad-band hybrid was connected to the antenna (Fig. 4.48). Fig. 4.49 shows the measured radiation patterns at the two frequencies. Both radiation patterns are similar to the fundamental mode of a conventional patch, as expected. Measured gains are 4.6 dB at f_{-1} and 5.8 dB at f_{+1}. In addition, a roll pattern measured with a linear polarization probe is presented in Fig. 4.50. The roll pattern for both frequencies is always above than -3 dB giving a reasonable circularly polarized wave. The 3 dB AR beamwidth is 194° in the $x-z$ plane and 167° in the $y-z$ plane at the first frequency and 93° in the $x-z$ plane and 72° in the $y-z$ plane at the second one.

A CP patch antenna with the possibility of self-diplexing capability (isolated ports) and alternate or similar senses of polarization (RHCP or LHCP) is presented in Section 5.4 for RFID application. This antenna is based on the same approach presented in this Subsection.

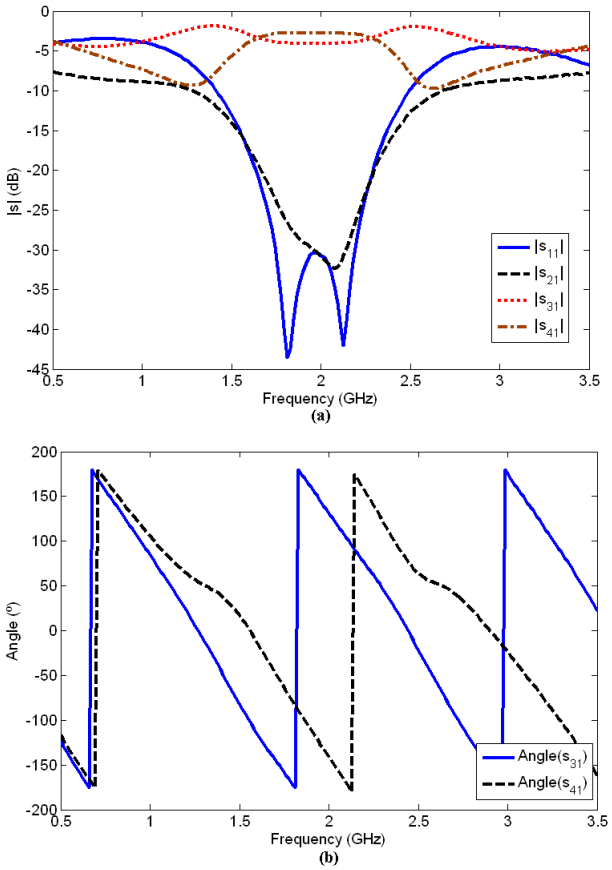

Figure 4.47: Measured $[S]$ parameters of the broad-band hybrid coupler. (a) Magnitude. (b) Phase.

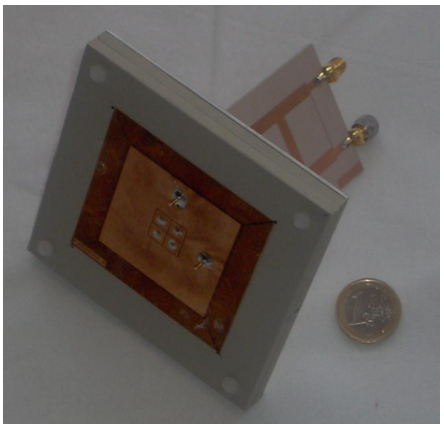

Figure 4.48: Picture of the setup used to measure the dual-band CP patch antenna. The three-arm hybrid coupler is connected to the antenna.

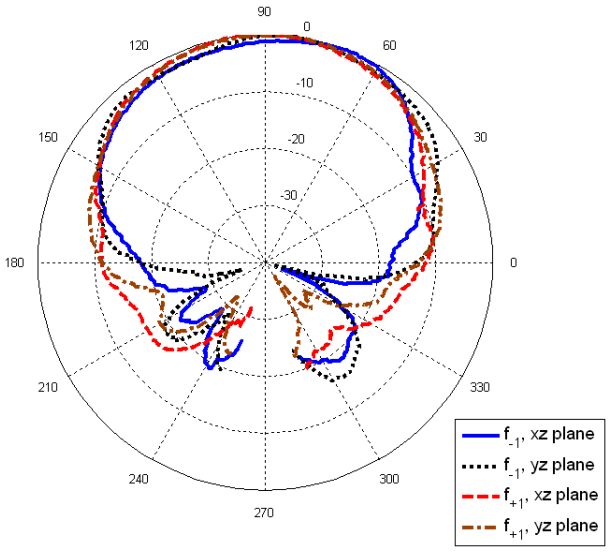

Figure 4.49: Measured radiation patterns of the dual-frequency CP patch antenna with the hybrid coupler connected. (Fig. 4.48).

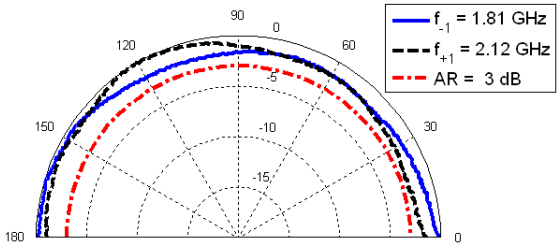

Figure 4.50: Measured roll diagram of the dual-frequency CP patch antenna fed by the hybrid coupler (Fig. 4.48).

Single-Feed Dual-Frequency CP Antennas

Two prototypes based on modified square patches filled with CRLH structures are presented below. Hence, the second approach explained before to achieve CP patch antennas is used.

The first prototype consists of a slightly rectangular microstrip patch with dimensions $L \times W$, being W slightly larger than L. When this patch is fed along one main diagonal, the two orthogonal modes corresponding to the main directions x ($[+1, 0]$ mode) and y ($[0, +1]$ mode) are excited at very close frequencies. The CP is obtained at a frequency, which lies between the resonance frequencies of these two modes, where the two orthogonal modes have equal magnitude and are 90° out-of-phase. Additionally, dual-frequency performance is obtained by filling the patch antenna with a 2×2 array of mushroom structures. This CRLH filling allows exciting the LH modes $[-1, 0]$ and $[0, -1]$ in a similar way that is done for the RH ones ($[+1, 0]$ and $[0, +1]$) and thus, CP is also achieved at an additional frequency. In this way, a single port multifrequency antenna with circular polarization is achieved.

The sketch of this prototype and a picture of a manufactured realization are shown in Fig. 4.51. The dimensions of the prototype are $L = 40.00$ mm, $W = 45.00$ mm, $L_m = 6.80$ mm, the gaps are $g = 0.20$ mm, and the vias diameter is $d = 0.70$ mm. The substrate is PP with $\varepsilon_r = 2.2$ and $h = 8.00$ mm. The feeding approach is a coaxial probe placed in one main diagonal at a distance equals to 13.00 mm from the centre of the patch antenna. The simulated and measured return losses are depicted in Fig. 4.52. High agreement between both results can be observed. CP is obtained at $f_{-1} = 1.75$ GHz and $f_{+1} = 2.23$ GHz.

The measured radiation patterns in the $x - z$ and $y - z$ planes at the two working frequencies are depicted in Fig. 4.53. The expected patch-like radiation pattern is obtained at both frequencies. Moreover, a roll diagram

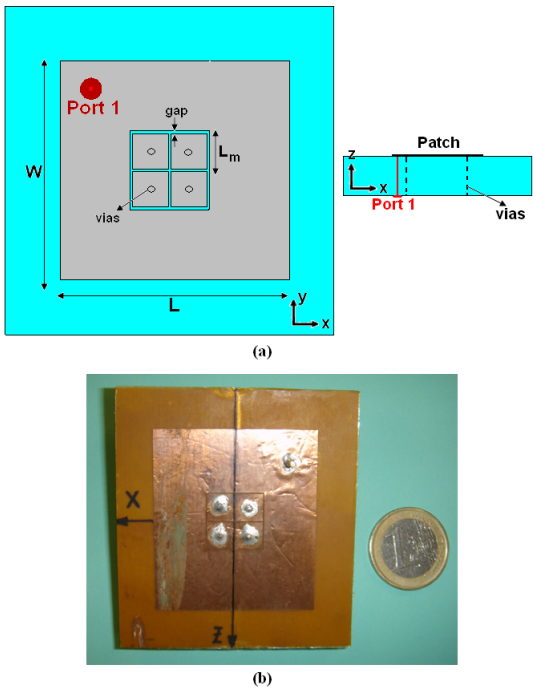

Figure 4.51: Dual-frequency CP slightly rectangular patch antenna filled witch CRLH cells. (a) Sketch of the antenna. (b) Picture of the manufactured prototype.

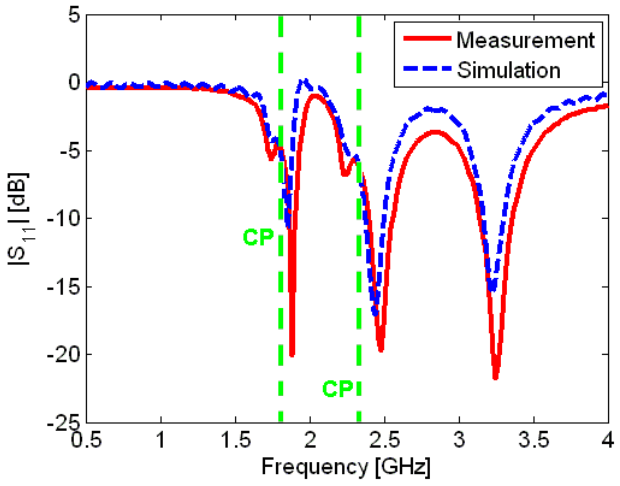

Figure 4.52: Simulated and measured reflection coefficient of the dual-frequency slightly rectangular CP patch antenna (Fig. 4.51).

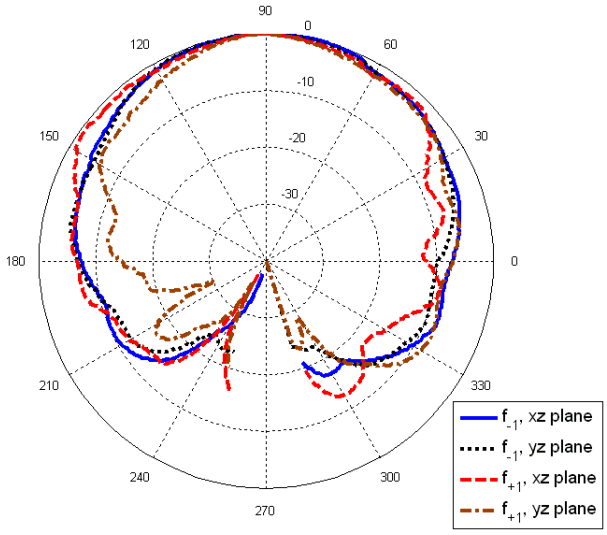

Figure 4.53: Measured radiation patterns ($x-z$ and $y-z$ planes) of the dual-frequency CP patch antenna (Fig. 4.51).

measured with a linear probe is plotted in Fig. 4.54, showing an AR better than 3 dB at both working frequencies. In addition, the 3 dB AR beamwidths have been measured, obtaining 185° in the $x-z$ plane and 220° in the $y-z$ plane at f_{-1} and 43° in the $x-z$ plane and 165° in the $x-z$ plane at f_{+1}.

As commented before, other modifications can be made in the square patch antenna to achieve CP. For example, the second prototype consists of adding stubs in one main dimension of the patch while maintaining the width of the patch equals to its length ($W = L$). The sketch of this antenna and the picture of a manufactured prototype are shown in Fig. 4.55. The dimensions of the antenna are the following: $L = W = 40.00$ mm, $L_{stub} = 12.00$ mm, $W_{stub} = 4.50$ mm, $L_m = 6.80$ mm, the gaps are $g = 0.20$ mm, and the vias diameter is $d = 0.70$ mm. The substrate is PP with $\varepsilon_r = 2.2$ and $h = 8.00$ mm. The feeding probe is placed in a main diagonal and 14.00 mm away from the centre of the patch antenna. Fig. 4.56 shows the simulated and measured reflection coefficient, which are very similar. CP is achieved at $f_{-1} = 1.76$ GHz and $f_{+1} = 2.25$ GHz.

The measured radiation patterns in the two main planes ($x-z$ and $y-z$) are plotted in Fig. 4.57. A patch-like radiation pattern is obtained at both working frequencies, as expected. Furthermore, a roll diagram measured with a linear probe is plotted in Fig. 4.58, showing an AR better than 3 dB at both frequencies. Finally, the 3 dB AR beamwidths have been measured,

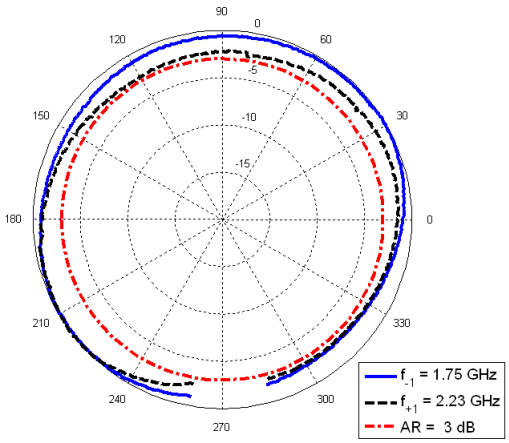

Figure 4.54: Measured roll diagram of the dual-frequency CP slightly rectangular patch antenna (Fig. 4.51).

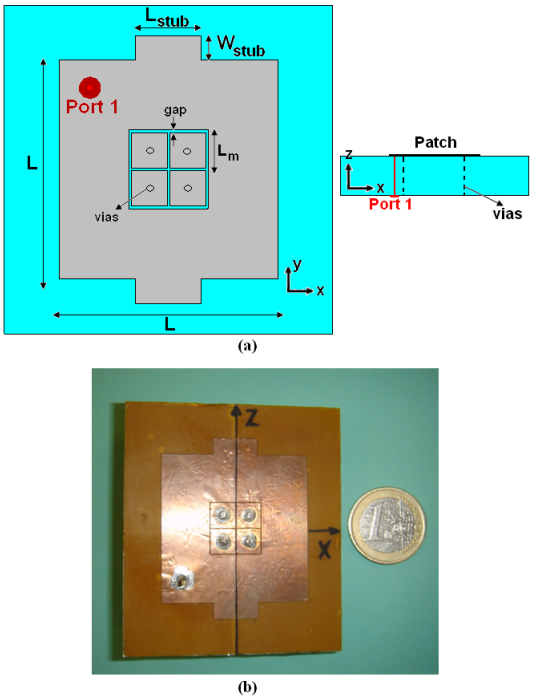

Figure 4.55: Dual-frequency CP patch antenna based on a CRLH-filled square patch with stubs. (a) Sketch of the antenna. (b) Picture of the manufactured prototype.

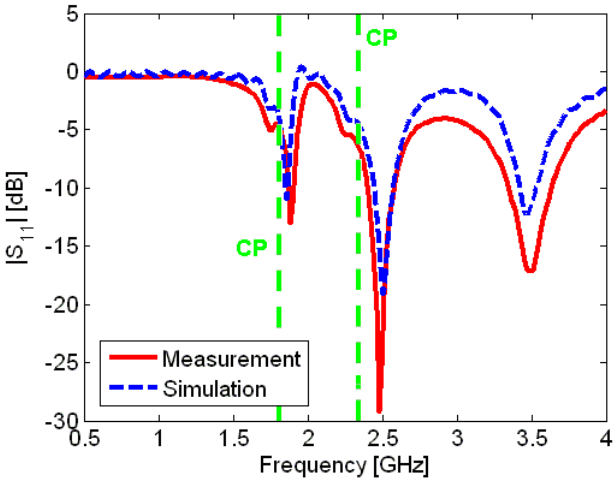

Figure 4.56: Simulated and measured reflection coefficient of the dual-frequency CP patch antenna of Fig. 4.55.

achieving 146° in the $x-z$ plane and 233° in the $y-z$ plane at f_{-1} and 71° in the $x-z$ plane and 162° in the $x-z$ plane at f_{+1}.

4.9 Conclusion

In the present Chapter patch antennas partially filled with CRLH structures have been proposed. Firstly, it has been demonstrated that that the combination of CRLH unit cells with conventional RH TLs provides several degrees of freedom to design resonators with an arbitrary frequency ratio between the resonance frequencies. This technique is very useful for the development of nowadays resonant antennas in which small frequency ratios are demanded. For this reason, this configurarion have been applied to microstrip antennas in order to achieve multifrequency and multifunction single-layer patch antennas. These antennas present two patch-like modes ($n = \pm 1$) and a monopolar one ($n = 0$) between them. The frequency ratio between the different modes can be arbitrarily chosen. This ratio depends on the dimensions of the microstrip patch and the filling CRLH structure. Two different antennas have been implemented by partially filling conventional microstrip patches with CRLH mushroom structures. The first one (Section 4.4) is a triple-frequency and dual-mode patch antenna working at $f_{-1} = 1.06$ GHz, $f_0 = 1.45$ GHz and $f_{+1} = 2.16$ GHz. The first and third modes ($n = \pm 1$) have a patch-like radiation pattern, whilst the mode between them ($n = 0$) has a monopolar

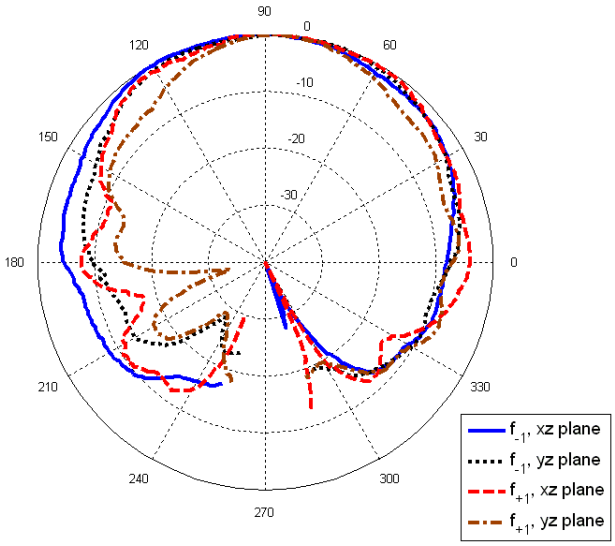

Figure 4.57: Measured radiation patterns of the dual-frequency CP patch antenna with stubs (Fig. 4.55).

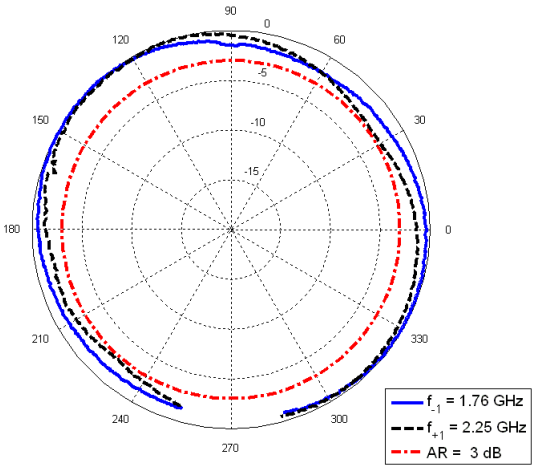

Figure 4.58: Measured roll diagram of the dual-frequency CP patch antenna with stubs (Fig. 4.55).

radiation pattern. The frequency ratio between the patch-like modes is 2.04. The second antenna (Section 4.5) is a dual-frequency microstrip patch antenna with very close working frequencies ($f_{-1} = 1.81$ GHz and $f_{+1} = 2.20$ GHz). In this case, both modes have a patch-like radiation pattern and the ratio between the working frequencies is only 1.21. Prototypes of both antennas have been manufactured and measured, showing good performance. Furthermore, two different simulation tools for the proposed patch antennas have been presented. The first one (Section 4.6) is an equivalent circuit model which allows obtaining the reflection coefficient of the proposed antennas with good accuracy and very low computational load. The second tool (Section 4.7) is a full-wave simulator based on the MPIE-MoM approach. This simulator provides the full-wave solution for the proposed patch antennas, reducing the computation time with respect to commercial solvers and overcoming the problems detected with these commercial solutions.

In Section 4.8 the previous approach has been considered along two dimensions in order to excite modes with orthogonal polarizations. Initially, these orthogonal modes have been used to develop quad-frequency single-layer patch antennas with polarization diversity. Two different kind of quad-frequency patch antennas has been designed, manufactured and measured. The first one has two orthogonal ports with high isolation between them. The working frequencies of the manufactured prototype are 1.76 GHz and 2.49 GHz at the port with polarization along the x axis and 1.88 GHz and 2.64 GHz at the port with orthogonal polarization with respect to the previous one. The measured isolation between the ports is better than 25 dB below 2.5 GHz and 18 dB at the last working frequency. This type of antenna is a good candidate as the radiating element of dual-band transceivers in which the uplink and downlink frequencies for each band are adjacent and the polarizations are orthogonal. Moreover, the high isolation between the ports can avoid the interferences between the transmitter and the receiver. The second kind of quad-frequency patch antennas consists of exciting the four modes with two orthogonal polarizations through only one port. A prototype has been manufactured, showing good performance. This approach is interesting for applications in which frequency and polarization diversity is required (e. g. MIMO systems).

Finally, dual-frequency CP patch antennas have been developed by exciting the modes with orthogonal polarizations in quadrature. Two different feeding approaches have been proposed. The first one is based on a square patch filled with square CRLH cells and two orthogonal ports connected to additional external circuitry (e. g. a branch-line coupler). A prototype of this antenna working at 1.80 GHz and 2.11 GHz has been manufactured and mea-

sured. The second feeding approach consists of making some modifications on a single-port square patch filled with CRLH cells. Two prototypes based on this approach have been designed, manufactured and measured. The first one is based on a slightly rectangular patch filled with CRLH cells. Its working frequencies are 1.75 GHz and 2.23 GHz. The second prototype consists of a square patch antenna with stubs and filled with CRLH cells. The working frequencies of this second prototype are 1.76 GHz and 2.25 GHz. Axial ratios better than 3 dB have been measured at all the working bands for all the manufactured prototypes.

CHAPTER 5

Applications of Metamaterial-Loaded Antennas

5.1 Introduction

In the previous Chapters, several metamaterial-loaded antennas have been proposed. For most of the previous cases, the prototypes were designed to operate at the frequencies of commercial communications systems. For example, the multifrequency patch antennas were designed for the frequencies of mobile communications systems (GSM, DCS and UMTS) and radio navigation systems (GPS). Thus, these antennas can be directly used as radiating elements for the proposed services.

The aim of this Chapter is to study the application of the metamaterial-loaded antennas not as isolated radiating elements, but integrated into systems or antenna arrays. For example, the proposed antennas can be used to enhance the performance of antenna arrays. In Section 5.2 the dual-band dipoles presented in Chapter 3 are used to design log-periodic arrays of printed dipoles with interesting features such us bandwidth broadening with respect to conventional log-periodic arrays.

Moreover, novel antennas based on the designs of previous Chapters are proposed to fulfill the requirements of future communications systems (Cognitive Radio systems) and emerging applications, such us RFID. Particulary, tunable small antennas with wideband tuning are needed for the future portable devices. Hence, tunable LH wire antennas over ground plane are developed for this application in Section 5.3. Finally, a novel scheme for active

RFID systems based on self-diplexed multifrequency patch antennas (two-port patch antennas with high isolation between the ports working at two frequencies) is proposed in Section 5.4.

5.2 Log-Periodic Arrays of Loaded Dipoles

A log-periodic array of printed dipoles consists of a group of dipoles which follows a logarithmic relation with frequency [129]. This configuration is well-known for broadband applications. A novel approach to broaden the bandwidth of a log-periodic array without increasing the number of elements is proposed in this Section. Metamaterial-loading provides additional resonance frequencies in the dipole antenna, as shown in Section 3.2. The proposed approach is based on loading some dipoles of the array with metamaterial particles to achieve additional resonances which broader the bandwidth of the overall antenna.

The strategy to broaden the bandwidth of a log-periodic dipole array is to obtain two additional resonances. One of the additional resonances is placed close to the lowest limit of the bandwidth of the original array. The other additional resonance is set close to the upper limit of the bandwidth of the original array. Moreover, the number of the dipoles is maintained; thus, the dimensions of the array are not increased.

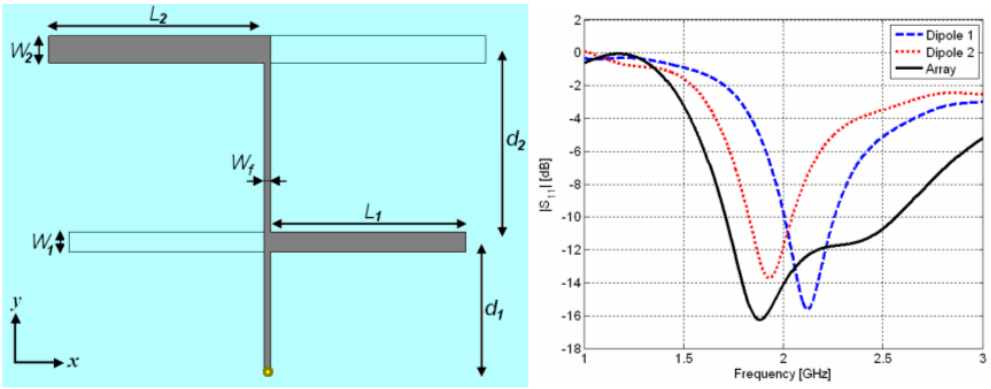

Figure 5.1: Log-periodic array of two antipodal printed dipoles. (a) Top view. (b) Simulated reflection coefficient of the array and the isolated dipoles. The locations of the additional frequencies for the enhanced array are also plotted.

Once the strategy has been presented, some examples are proposed. The

reference antenna is the simplest log-periodic array: the one composed of two dipoles (Fig. 5.1.a). These dipoles are implemented by using an antipodal configuration (each branch of the dipole is printed on one side of a dielectric substrate; the dipole is fed through a parallel plate line). The substrate is FR-4 ($\varepsilon_r = 4.5$, $\tan\delta = 0.015$) with 0.50 mm thickness. The dimensions of the dipoles are $L_1 = 28.50$ mm, $L_2 = 32.00$ mm, $W_1 = 3.00$ mm, $W_2 = 4.00$ mm, $D_1 = 19.75$ mm, $D_2 = 25.00$ mm, $W_f = 1.00$ mm. Fig. 5.1.b shows the reflection coefficient of the dipoles and the log-periodic array. The resonant frequencies of the isolated dipoles are: $f_1 = 2.12$ GHz and $f_2 = 1.93$ GHz. The bandwidth of the dipoles is 12% approximately. The log-periodic array has a reflection coefficient smaller than -10 dB from 1.70 GHz to 2.57 GHz (40% bandwidth).

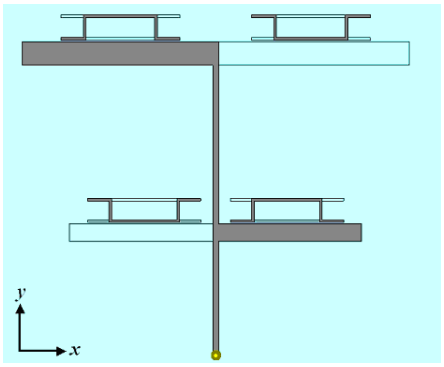

Figure 5.2: Sketch of the log-periodic array of two antipodal printed dipoles loaded with Omega particles.

In this case, the additional resonances must be located close to 1.70 GHz and 2.50 GHz (Fig. 5.1.b) to broader the bandwidth of the overall array. The dipoles of the reference log-periodic array are loaded with Omega particles (Fig. 5.2) to achieve the two additional resonances. The first dipole must resonate at 1.70 GHz (additional resonance) and keep the conventional resonance at 2.20 GHz, while the second dipole must resonate at 1.80 GHz (conventional resonance) and 2.50 GHz (additional resonance). The dimensions of the dipoles are unchanged with respect to the reference array. The first dual-frequency dipole is the same as the one presented in Section 3.2.4. The dimensions of the Omega particles coupled to the second dipole are: $L_p = 3.80$ mm, $W_p = 3 \cdot Lp$, $W_s = 0.40$ mm. The separation gap between the dipoles and the particles is 0.20 mm. The particles are placed at the centre of each branch of the dipoles.

The reflection coefficients (computed with CST Microwave Studio ®) of

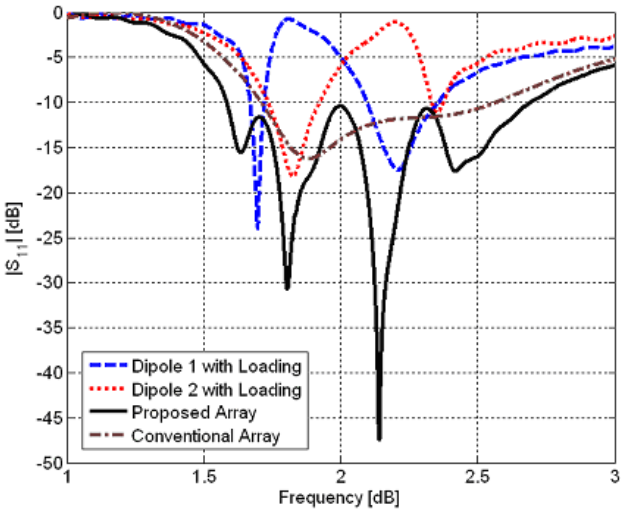

Figure 5.3: Simulated reflection coefficients of the loaded dipoles and array. The reflection coefficient of the conventional array is also plotted.

the dual-band dipoles and the proposed log-periodic array are shown in Fig. 5.3. The dipoles have the desired dual-band operation. The first dipole has the additional resonance at 1.70 GHz, as it was demonstrated in Section 3.2.4. The resonant frequencies of the second loaded dipole are 1.83 GHz and 2.35 GHz. The additional frequency of this second dipole has been placed slightly below 2.50 GHz to achieve a proper matching. Thus, the array bandwidth (reflection coefficient smaller than -10 dB) goes from 1.58 GHz to 2.69 GHz (52% bandwidth). The bandwidth of the proposed array is broader than the one of the conventional array. Moreover, the lower-limit frequency has been shifted down and the upper-limit frequency has been shifted up without increasing the number of dipoles.

Prototypes of the reference and the proposed antennas have been manufactured (Fig. 5.4.a-b). Fig. 5.4.c shows the measured reflection coefficient of both antennas. The bandwidth of the reference array goes from 1.62 GHz to 2.77 GHz. In the case of the proposed antenna, it goes from 1.55 GHz to 2.97 GHz. Thus, the bandwidth of the proposed antenna (62.8% BW) has been increased with respect to the reference one (52.4% BW). Note that both measured bandwidths are broader than the simulated ones.

The same approach can be applied to larger arrays with broader bandwidth. For example, Fig. 5.5 shows a log-periodic array composed of nine dipoles. The measured bandwidth of the unloaded array (considering $|s_{11}| < -10$ dB) goes from 815 MHz to 2.34 GHz (Fig. 5.6), which results in 2.87 : 1

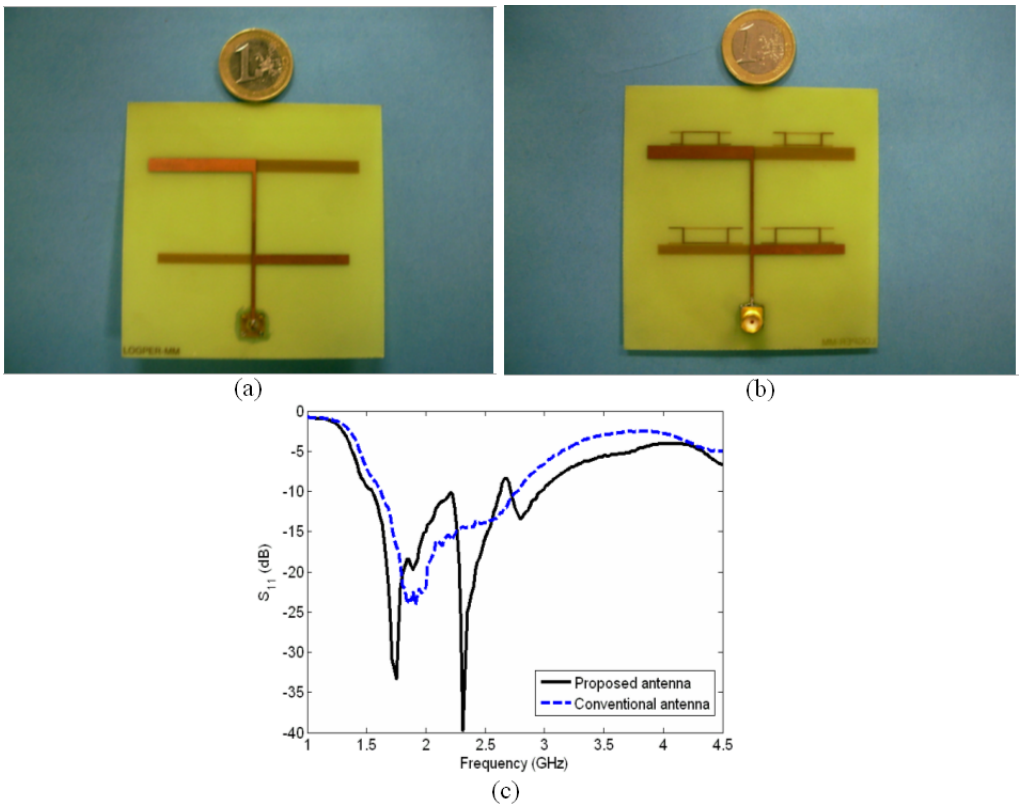

Figure 5.4: Manufactured prototypes of the log-periodic arrays. (a) Picture of the conventional array. (b) Picture of the proposed array. (c) Measured reflection coefficient of both antennas.

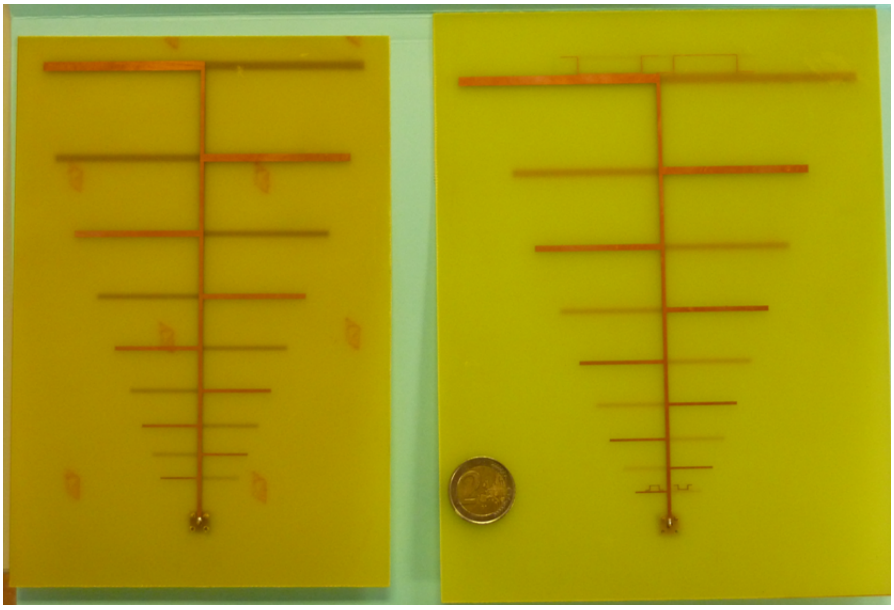

Figure 5.5: Pictures of the log-periodic arrays composed of nine dipoles. Left: conventional array. Right: array loaded with Omega particles.

bandwidth. The first and last dipoles of this array are loaded with Omega particles, as shown in Fig. 5.5. Hence, the bandwidth of this loaded array is 3.45 : 1, shifting the lower limit frequency to 725 MHz and the upper limit frequency to 2.50 GHz (Fig. 5.6).

5.3 LH Wire Antennas with Wideband Tuning and their Application to Cognitive Radio Terminals

5.3.1 Introduction

As it was reviewed in Chapter 3, wire antennas have been traditionally loaded with inductors and capacitors to achieve a proper matching to the source. More recently, wire antennas have been loaded with active components, such as PIN or varactor diodes. This kind of loading can be applied to develop tunable antennas [134]. The typical tuning bandwidth that can be achieved with this technique is around 20% (i.e. the application of this technique to microstrip patch [135] or PIFA antennas [136]). During the last years, novel tun-

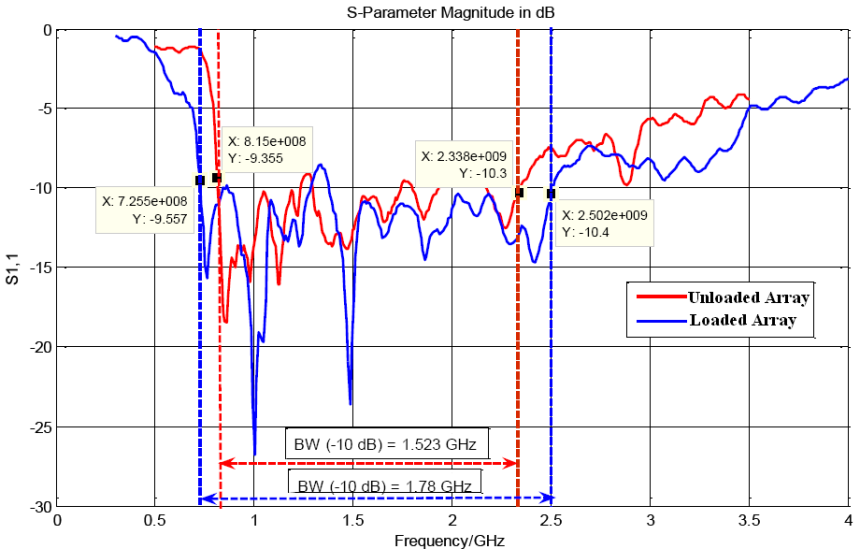

Figure 5.6: Measured reflection coefficients of the conventional and metamaterial-loaded log-periodic arrays composed of nine dipoles.

able antennas have been developed, achieving larger tuning bandwidths such as 44% in antennas for DVB-H application [137] and 62% in slot antennas [138]. These large tuning bandwidths are necessary to cover the huge number of wireless services and standards used nowadays (GSM, DCS, UMTS, GPS, Bluetooth, WiFi, etc.) with only one radiating device [9]. Moreover, small antennas are required to integrate these services into compact handheld devices attractive for the users. However, electrically small antennas are difficult to match to any realistic source because of their very large reactance, as it was commented in Chapter 3. For these reasons, small antennas with large tuning bandwidth and internal matching, i. e., direct matching to the source without an external network, are required for nowadays and future communication systems.

As it has been commented throughout this Thesis, wireless communication systems have grown dramatically during the last years. Due to this fact, the electromagnetic spectrum is used inefficiently: some of the spectrum bands are saturated while others are idle most of the time. For this reason, novel concepts as deregulated spectrum and dynamic allocation of bands are being proposed for future communication systems. One of these proposals is Cognitive Radio (CR) [20] in which a wide bandwidth is deregulated and the elements of the communication system are reconfigurable to operate in a narrow band within the entire free spectrum. In order to implement CR

systems, the terminals must provide a double functionality [21]. The first one is spectrum sensing to determine the best narrowband channel (for example, the one without interferences with other users). The other terminal function consists of providing full-duplex communication at the frequency of the most convenient narrowband channel.

The double functionality of the terminal for CR implies important challenges from antenna engineering point of view [21]. Firstly, the optimal solution to sense the spectrum is a wideband and omnidirectional antenna; however, these antennas are larger than the compact antennas used in handheld terminals. Moreover, a narrowband directive antenna is needed for the communications function. This antenna must be reconfigurable within the entire free spectrum (at least one octave) which is very difficult to achieve with conventional technologies, as it was commented before. Finally, it is important to note that the dimensions of the CR terminal must be small to make it attractive to users. Hence, a directive reconfigurable antenna with wideband tuning and internal matching would be the optimal solution to implement the communications function of the CR terminal.

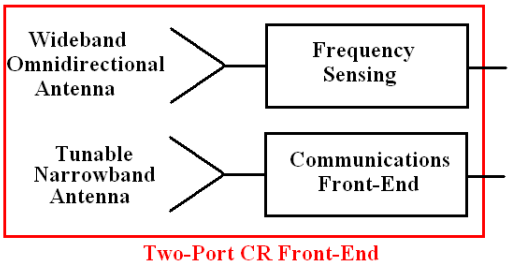

Figure 5.7: General architecture of a CR terminal based on a two-port radiating system.

Some proposals for CR antennas have been presented recently [139, 140]. These are based on two-port systems, as shown in Fig. 5.7. One of the ports provides connectivity to the sensing front-end while the other one is designed to be connected to the communications front-end. Ideally, a high isolation between the two ports should be achieved in these systems.

The goals of the present Section are two. The first one is the development of small antennas with wideband tuning, internal matching and high values of efficiency. These antennas are based on the LH wire antennas over ground plane presented in Section 3.3. It must be taken into account that the resonance frequencies and input impedance of the LH wire antennas depend on the elements of the unit cell. Hence, variable capacitors (e. g. varactor diodes)

can be used to achieve small wire antennas internally matched with wideband tuning. As it was explained before, such antennas are very useful for nowadays and future communications. Hence, the second goal of this Section is the development of a novel compact fully reconfigurable two-port radiating system for a CR terminal with high isolation between the ports. The sensing functionality is achieved with a planar monopole antenna whilst the communications function is implemented with a tunable LH half-loop antenna with wideband tuning. The whole system is fully printed on a dielectric substrate board with small dimensions (60 mm $\times$ 60 mm). Initially, the system is proposed for operation over the bandwidth from 1.5 GHz to 3 GHz (2 : 1 bandwidth) because the band below 3 GHz seems a good candidate for CR systems [21].

The outline of this Section is as follows: the tunable LH monopole antenna is presented in Subsection 5.3.2. After that, a reconfigurable antenna with wideband tuning based on the LH half-loop antenna is obtained in Subsection 5.3.3. Finally, a complete CR system which integrates a printed monopole antenna and a tunable LH half-loop antenna is presented in Subsection 5.3.4.

5.3.2 Tunable LH Monopole Antenna

As the resonant frequencies of the LH monopole antenna depend on the value of the unit cell elements (Section 3.3), a tunable antenna can be developed by replacing the unit cell elements with variable components. In practice, the easiest way to implement this approach is to use variable capacitors, for example varactor diodes, acting as the series capacitances C_L. Then, the resonant frequencies of the monopole antenna will be different for each value of the varactor diodes.

Fig. 5.8 shows the frequency dependence on the value of the series capacitances C_L for the LH monopole antenna presented in Section 3.3.2, computed with CST Microwave Studio ®. In both modes the tuning bandwidth is larger than 50%. The drawback of this approach is that the input impedance strongly depends on the values of the unit cell elements too. The relationship between the value of the series capacitances and the real part of the input impedance for the $n = -1$ mode has been simulated and it is plotted in Fig. 5.9. This magnitude decreases with the capacitance very quickly which makes impossible match this antenna to 50 Ω for most of the operation bandwidth. As the goal is to develop a tunable antenna with wideband tuning and simultaneous internal matching, this approach has to be modified in order to achieve a trade-off between tuning and matching bandwidth.

Two different approaches have been investigated: using asymmetric unit

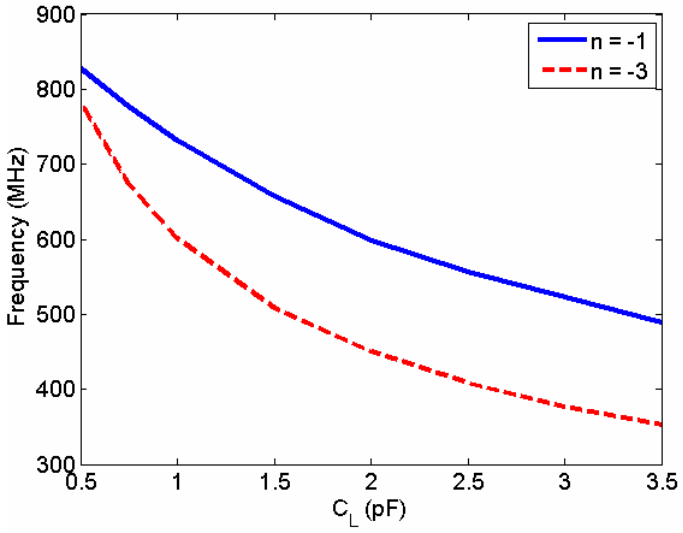

Figure 5.8: Dependence of the resonant frequencies of the LH monopole antenna with the series capacitances of the unit cells (C_L). The other parameters of the antenna are: $L = 50.00$ mm, $N = 2$ unit cells, $a = 25.00$ mm, $d = 10.00$ mm, $r = 0.90$ mm and $L_L = 20$ nH.

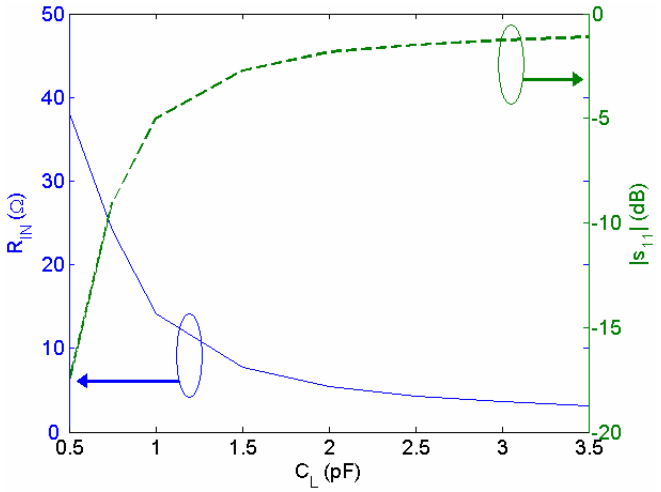

Figure 5.9: Dependence of the input resistance, R_{IN} (continuous line), and $|s_{11}|$ (dashed line) of the LH monopole antenna ($n = -1$ mode) with the series capacitances of the unit cells (C_L). The other parameters of the antenna are: $L = 50.00$ mm, $N = 2$ unit cells, $a = 25.00$ mm, $d = 10.00$ mm, $r = 0.90$ mm and $L_L = 20$ nH.

C_{L1}	C_{L2}	C_{L3}	C_{L4}	Tuning Bandwidth	Matching ($\|s_{11}\| < -10$ dB)
V	V	F	F	9%	Good
F	F	V	V	$< 2\%$	Bad
F	V	V	F	$< 2\%$	Bad
V	F	F	V	$< 2\%$	Bad
F	V	F	V	$< 2\%$	Good
V	F	V	F	18%	Good

Table 5.1: Simulation performance of various configurations of the LH monopole antenna (F: 0.5 pF fixed capacitor, V: variable capacitance)

cells and mixing unit cells with fixed and variable capacitances. In the case of the LH monopole antenna composed of $N = 2$ unit cells, there are four capacitances which gives six different combinations of two variable capacitors and two fixed. All these possibilities have been simulated (CST Microwave Studio ®) and the results are summarized in Table 5.1. The capacitors have been numbered from the one closest to the feed (C_{L1} in Fig. 3.39) to the one closest to the open edge (C_{L4} in Fig. 3.39). The fixed capacitors keep the value of the original LH monopole antenna in Section 3.3.2 ($C_L = 0.5$ pF). The value of the variable capacitors is changed between 0.5 pF and 3.5 pF. In most cases, the frequency of the different modes is almost fixed except for the last case ($C_{L1} = C_{L3} = C_L$ variable and $C_{L2} = C_{L4} = 0.5$ pF), in which an 18% tuning bandwidth has been achieved for the $n = -1$ mode, considering a reflection coefficient lower than -10 dB. This is possible because the real part of the impedance grows with capacitance up to 70 Ω and then remains almost constant, providing a good matching to 50 Ω within all the tuning bandwidth (Fig. 5.10).

Fig. 5.11.a shows the sketch of the proposed tunable LH monopole antenna. The dimensions of the antenna are kept unchanged with respect to the prototype of Section 3.3.2. MV32003 varactor diodes (from Microsemi ®) are used to implement the variable capacitances ($C_{L1} = C_{L3}$). The fixed capacitors ($C_{L2} = C_{L4}$) and the inductors (L_L) are implemented with conventional SMD components. A network with high impedance lines (0.20 mm-width) has been attached to bias the varactor diodes. The capacitance of the varactors is controlled by the control voltage V_R. Two RF-choke inductors ($L_b = 100$ nH) have been inserted in the biasing network. An isolation capacitor ($C_b = 100$ pF) has been connected close to the RF port to block the DC component.

The proposed prototype has been manufactured (Fig. 5.11.b) and measured (Fig. 5.12). The $n = -1$ mode has a tuning range between 777 MHz and 924 MHz, which is 17% approximately. Moreover, the antenna is well matched

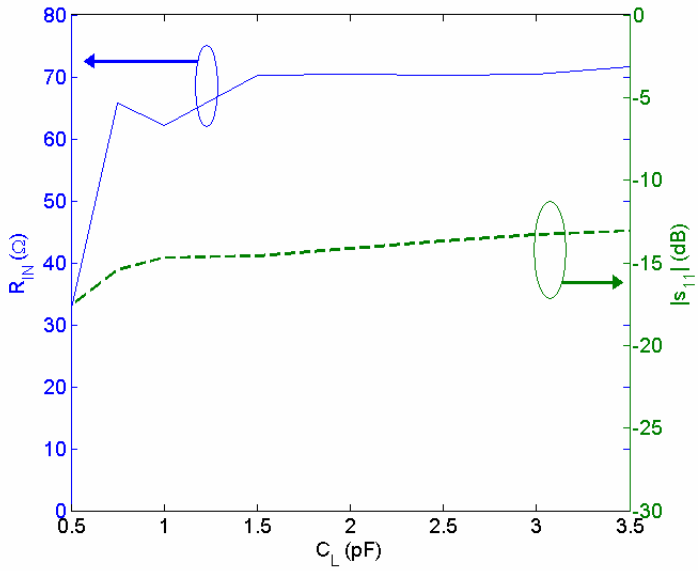

Figure 5.10: Dependence of the input resistance, R_{IN} (continuous line), and $|s_{11}|$ (dashed line) of the LH monopole antenna ($n = -1$ mode) with the variable capacitors ($C_{L1} = C_{L3} = C_L$). The other parameters of the antenna are: $L = 50.00$ mm, $N = 2$ unit cells, $a = 25.00$ mm, $d = 10.00$ mm, $r = 0.90$ mm, $L_L = 20$ nH and $C_{L2} = C_{L4} = 0.5$ pF.

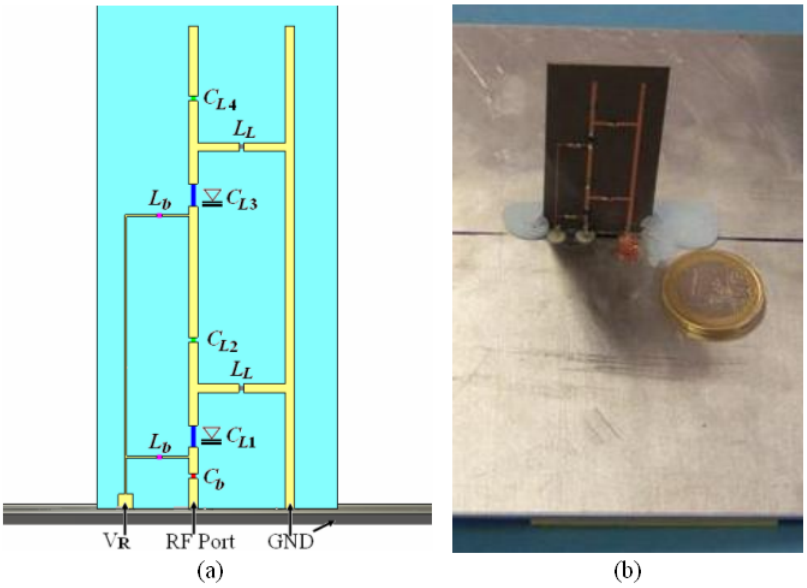

Figure 5.11: Proposed implementation of the tunable LH monopole antenna. (a) Sketch of the antenna. (b) Picture of the manufactured prototype.

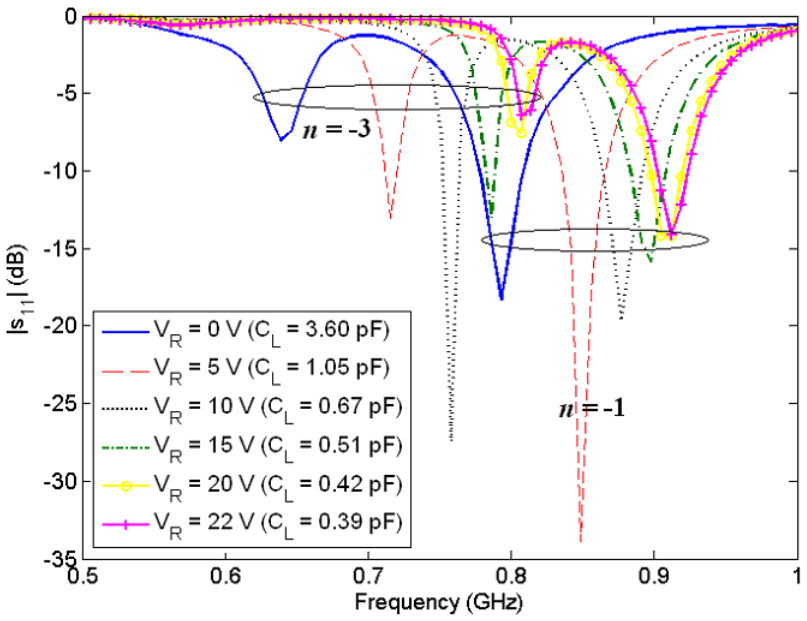

Figure 5.12: Measured $|s_{11}|$ parameter of the tunable LH monopole for different values of the control voltage V_R.

($|s_{11}| < -10$ dB) within the whole bandwidth. The measurement shows a shift towards higher frequencies with respect to the simulation. Nonetheless, the relative bandwidth is almost the same. The frequency of the $n = -3$ mode changes from 639 MHz to 811 MHz and it is well matched ($|s_{11}| < -10$ dB) within the range $695 - 793$ MHz. Considering both modes, an operation range between 695 MHz and 924 MHz is obtained (28% tuning bandwidth) with proper matching. It is important to note that the monopole electrical length varies between $0.11\lambda_0$ at 695 MHz and $0.15\lambda_0$ at 924 MHz.

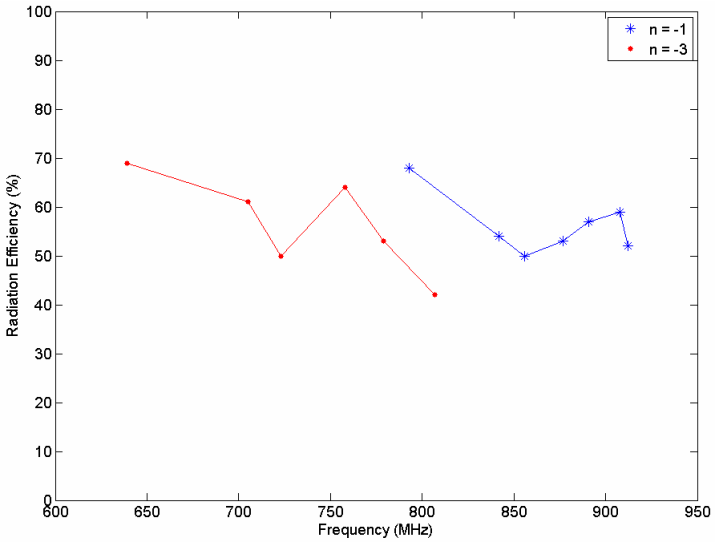

Figure 5.13: Measured radiation efficiency of the tunable LH monopole antenna.

Fig. 5.13 shows the measured radiation efficiency of the manufactured prototype. The Johnston-Geissler method based on the Wheeler Cap principle [14, 120, 119, 118] has been used to measure these values. The radiation efficiency takes values between 50% and 70% within all the operation bandwidth.

5.3.3 Tunable LH Half-Loop Antenna over Ground Plane with Wideband Tuning

In order to make the LH half-loop antenna tunable, an approach similar to the one used in the LH monopole antenna can be applied. In this case, let us consider the LH half-loop antenna presented in Section 3.3.3 but with all the LH capacitances (C_L) variable. The other parameters of the antenna are kept

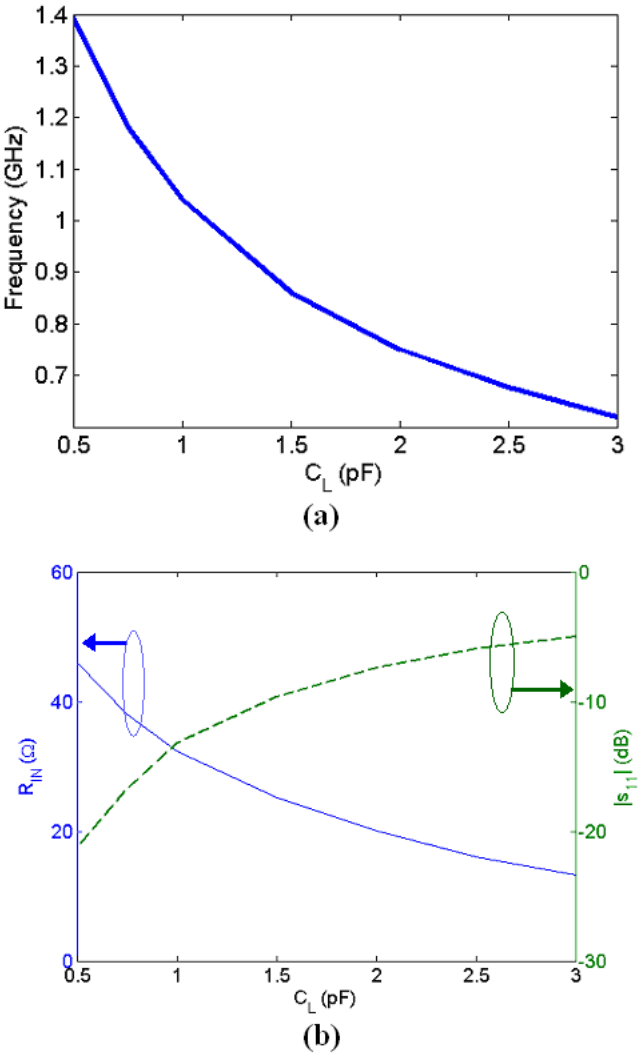

Figure 5.14: Dependence of the LH half-loop antenna over ground plane performance with respect to the series capacitances of the unit cells (C_L). (a) Dependence of the resonance frequency of the $n = 0$ mode. (b) Dependence of the input resistance (R_{IN}, bold line) and $|s_{11}|$ (dashed line) of antenna for the same mode.

unchanged with respect to that example. Fig. 5.14.a shows the dependence of the resonance frequency of the $n = 0$ mode with C_L, computed with CST Microwave Studio ®. In this case the tuning range is broader than the one in the monopole antenna, achieving a potential 2.3 : 1 tuning bandwidth. The dependence of the input resistance and matching to 50 Ω with respect to C_L for the $n = 0$ mode are plotted in Fig. 5.14.b. The input impedance takes values close to 50 Ω for small values of the LH capacitances; however, it decreases for higher values of C_L. This makes that the antenna is well matched (considering $|s_{11}| < -10$ dB) only for values smaller than 1.5 pF. Hence, the antenna working at the $n = 0$ mode is well matched within the range in which the frequency dependence with C_L has the largest slope, as shown in Fig. 5.14. In particular, the antenna is internally matched within a 1.6 : 1 bandwidth which is a considerable improvement over previous approaches.

Potentially, the tuning bandwidth of the half-loop antenna is much wider than the monopole antenna (Section 5.3.2). This is produced by the change of the ending conditions from open circuit to short circuit. This involves a flatter slope in the dependence of the input resistance with the series capacitances. Specifically, for the case of the monopole antenna (Fig. 5.9) the input impedance decreases with the series capacitances very quickly: the ratio between the input resistances is 10.48 for a variation of the capacitances between 0.5 pF and 3 pF. On the other hand, for the case of the half-loop antenna (Fig. 5.14) the ratio between the input resistances is only 3.46 for the same variation of the series capacitances. This fact is the cause for a wider bandwidth in the half-loop case.

The sketch of the proposed tunable LH half-loop antenna is shown in Fig. 5.15. It is based on the LH half-loop antenna presented in the Section 3.38. The dimensions of the antenna are kept unchanged. The LH variable capacitances (C_L) are implemented with MV32003 varactor diodes (from Microsemi ®). The control voltage of the varactors (V_R) is supplied through two 0.20 mm-width lines printed at both sides of the half-loop. RF-choke inductors (L_b = 100 nH) and DC-isolation capacitors (C_b = 100 pF) are attached to the design. All these elements and the LH inductances (L_L) are implemented with SMD components.

The proposed antenna has been manufactured (Fig. 5.16) and measured. The total tuning range of the $n = 0$ mode is 2.35 : 1 (584.8−1376 MHz) which is very similar to the one obtained in simulation (Fig. 5.14.a). Considering good matching ($|s_{11}| < -10$ dB) to 50 Ω, the measured tuning bandwidth of the $n = 0$ mode is 1.64 : 1 (840 − 1376 MHz) as it is shown in Fig. 5.17. The radiation efficiency of this mode has been measured using the Johnston-Geissler method (Fig. 5.18). This magnitude is always above 54% within the

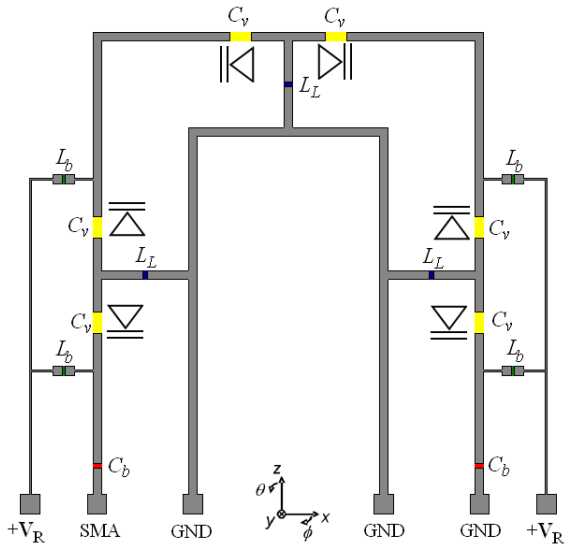

Figure 5.15: Sketch of the tunable LH half-loop antenna over ground plane implementation.

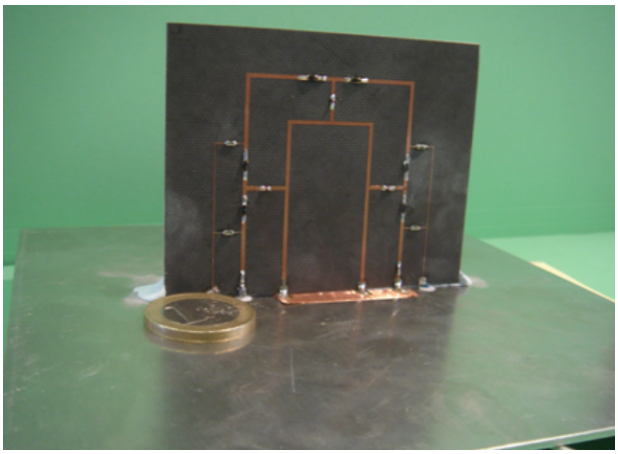

Figure 5.16: Picture of the manufactured tunable LH half-loop antenna over ground plane.

operation bandwidth in which the antenna is well matched (840−1376 MHz). The maximum dimension of the antenna varies between $0.14\lambda_0$ at 840 MHz and $0.23\lambda_0$ at 1376 MHz.

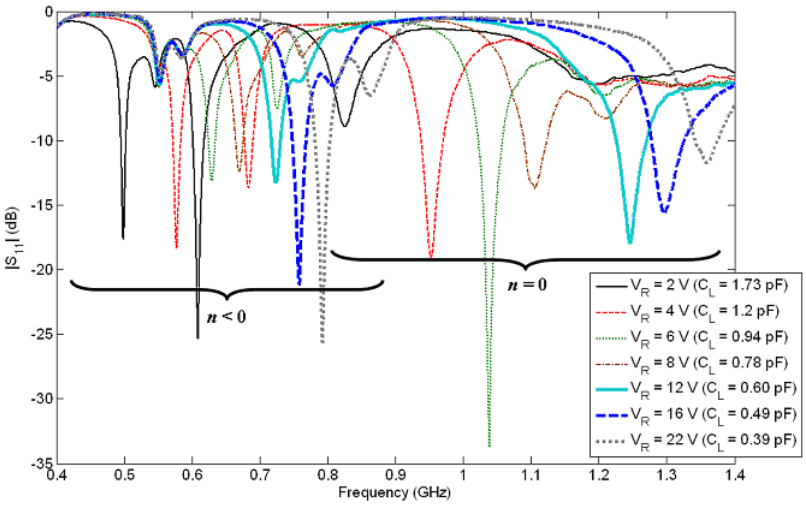

Figure 5.17: Measured reflection coefficient of the tunable LH half-loop antenna for different values of the control voltage V_R.

There are resonances below the $n = 0$ mode which corresponds to the modes with negative indices ($n < 0$). These modes cover the bandwidth 494−804 MHz with proper matching (considering $|s_{11}| < -10$ dB). These modes can be used to extend the tuning bandwidth of this antenna. However, it must be taken into account that the radiation pattern of these modes is monopolar in most of the cases, as shown in Section 3.3.3. Moreover, the radiation efficiency of these modes strongly decreases with decreasing frequency (Fig. 5.18), which makes the efficiency of this modes be below 30% for frequencies lower than 700 MHz. Nevertheless, in applications in which these modes could be useful, the tuning bandwidth of the LH half-loop antenna is potentially larger than 2 : 1.

Finally, the radiation patterns of the tunable prototype have been measured to show that the use of biasing networks does not modify their shapes. As an example, the radiation patterns of the prototype for a control voltage $V_R = 3$ V are shown in Fig. 5.19. The angular margin between $270° \pm 15°$ was not measured due to limitations in the anechoic chamber facility. The $n = -6$ and $n = -2$ modes have the expected monopolar radiation pattern. In the first case a null deeper than −20 dB is observed at the direction orthogonal to the ground plane in both main planes. Moreover, the cross-polarization is

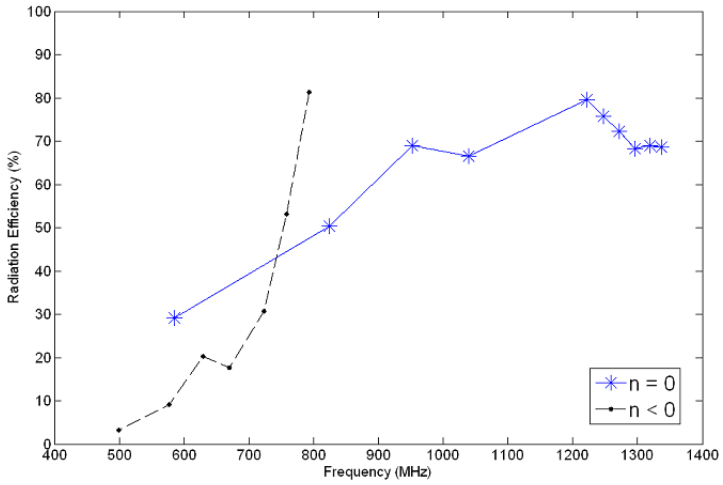

Figure 5.18: Dependence of the measured radiation efficiency of the tunable LH half-loop antenna with frequency.

lower than −13 dB. On the other hand, at f_{-2} the null is around −11 dB in the $x-z$ plane whilst it is deeper than −20 dB in the $y-z$ plane and the cross-polar components are below −13 dB in the $x-z$ plane and −8 dB in the yz plane. The expected radiation pattern with maximum orthogonal to the ground plane is obtained at f_0. In this case the cross-polar component is lower than −14 dB in both planes and the back radiation is low. Again, it is interesting to note that the main component in the $y-z$ plane at this frequency is E_ϕ.

5.3.4 Two-Port Radiating System for Cognitive Radio Terminals based on a LH Half-Loop Antenna with Wideband Tuning

The main objective of the present Subsection is the development of a fully printed radiating system for a CR terminal based on the application of a LH antenna with wideband tuning. Moreover, the following characteristics would be desirable: the whole system must be printed on a unique substrate board with small dimensions (60 mm × 60 mm) to integrate it into a hand-held device. The interface of the system should be composed of two SMA ports with high isolation between them (> 20 dB). Hence, the ports could be directly connected to the sensing and communications front-ends of the CR terminal. Finally, the whole system should work over a wide bandwidth

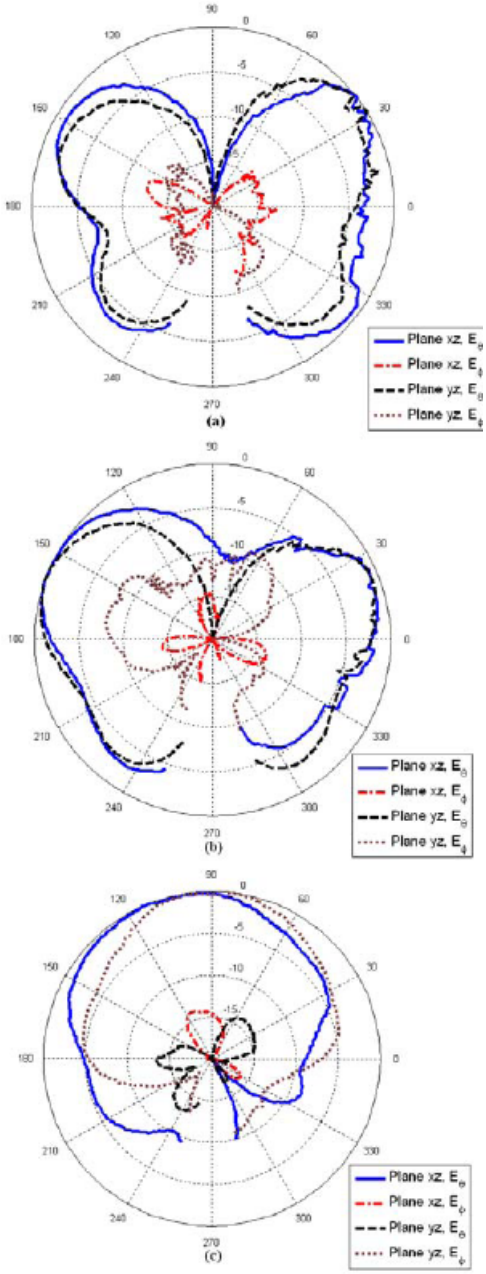

Figure 5.19: Measured radiation patterns of the manufactured tunable LH half-loop antenna for $V_R = 3$ V. (a) $n = -6$ mode. (b) $n = -2$ mode. (c) $n = 0$ mode.

(2 : 1 bandwidth) below 3 GHz because that frequency band seems a good candidate for CR systems [21].

The proposed radiating system for a CR terminal is based on the integration in the same substrate board of a printed monopole antenna and a printed LH half-loop antenna with wideband tuning. The first antenna is used for the spectrum sensing functionality whilst the second one is applied for the full-duplex communications function. The working band has been set from 1.5 GHz to 3 GHz because the physical dimensions of the monopole antenna would be larger than the board dimensions at lower frequencies.

The printed monopole antenna has a "U" geometry. Hence, the half-loop can be printed in the inner part of the monopole. The monopole antenna is fed through a microstrip line with a SMA connector at the end of the line. The ground plane of this antenna and its feeding line is printed on the opposite side of the substrate. The LH half-loop antenna is based on the results presented in the previous Subsections, but some considerations have been taken into account to integrate this antenna into the CR system. First of all, the number of cells has been reduced to two in order to minimize the number of lumped elements. The dimensions of the previous antenna have been recomputed to operate over the desired band. Moreover, the optimal values of the LH inductances to achieve good matching within the working band are very small ($L_L < 1$ nH). For this reason, additional inductors are not used in this case and the LH inductances are provided by direct interconnections between the outer and inner strips of the half-loop. Moreover, the orthogonal ground plane of the LH half-loop antenna has been replaced by a printed ground plane on the opposite side of the printed LH half-loop in order to make a fully printed system which can be integrated into a handheld device. The connections between the LH wires and the ground plane have been implemented with shorting vias. The printed LH half-loop antenna is fed through a SMA connector.

Fig. 5.20 shows the sketch of the system. The substrate is Duroid 5880 ($\varepsilon_r = 2.2$ and $h = 0.787$ mm) and the board dimensions are 60 mm × 60 mm. The dimensions of the monopole antenna are: $L_1 = 3.00$ mm, $L_2 = 3.00$ mm, $L_3 = 22.00$ mm, $L_4 = 37.00$ mm, $L_f = 20.00$ mm, $W_f = 3.60$ mm, $W_1 = 27.20$ mm, $W_2 = 23.50$ mm, $W_3 = 5.50$ mm. The dimensions of the tunable LH half-loop antenna are the following: $L = 14.00$ mm, $W = 8.00$ mm, $d = 2.00$ mm, $r = 0.50$ mm, $L_i = 6.00$ mm, $L_2 = 10.00$ mm, $d_{Cv} = 2.75$ mm, $d_{Cb} = 0.96$ mm, $L_f = 13.31$ mm, $W_f = 5.00$ mm, $r_f = 0.20$ mm, $d_{Lb} = 2.50$ mm, $L_{gnd} = 45.00$ mm and $W_{gnd} = 6.00$ mm. The diameter of the vias is 0.70 mm.

The proposed system has been simulated with CST Microwave Studio ®

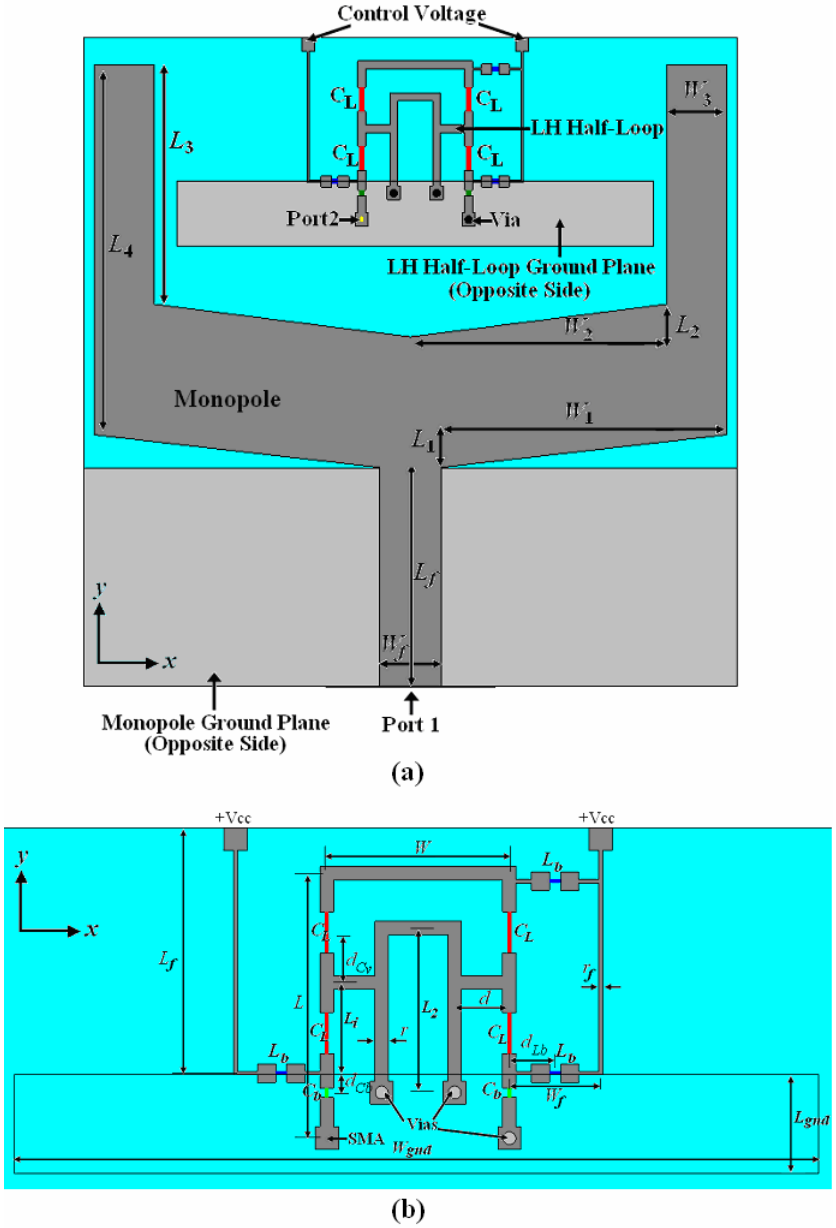

Figure 5.20: Sketch of the proposed system for a CR terminal. (a) Top view. (b) Zoom on the tunable LH half-loop antenna.

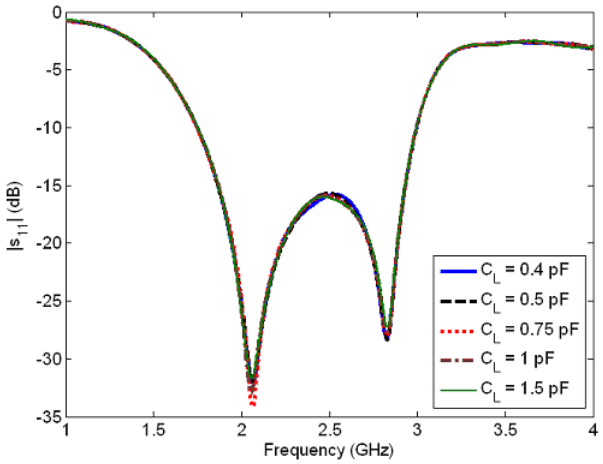

Figure 5.21: Reflection coefficient at the monopole port ($|s_{11}|$) for different values of the LH capacitances (C_L).

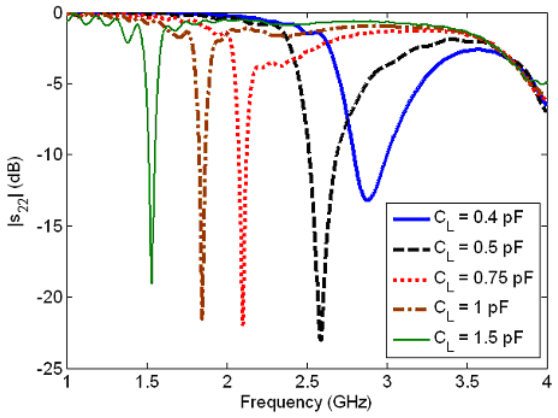

Figure 5.22: Reflection coefficient at the LH half-loop port ($|s_{22}|$) for different values of the LH capacitances (C_L).

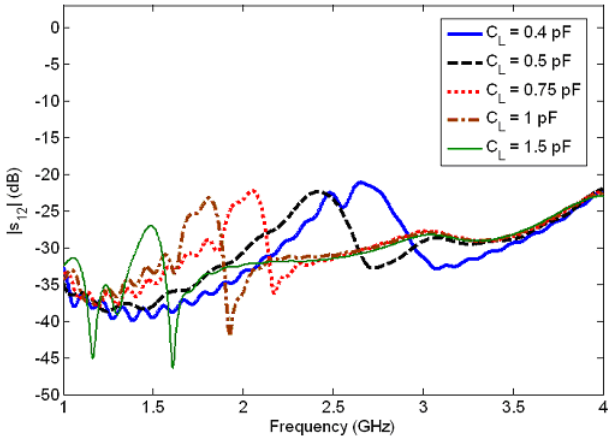

Figure 5.23: Isolation between the ports ($|s_{12}|$) for different values of the LH capacitances (C_L).

for different values of the LH capacitances (C_L). The reflection coefficient of the monopole antenna ($|s_{11}|$) is almost independent with respect to the value of the LH capacitances (Fig. 5.21), as desired. The bandwidth of the monopole, considering $|s_{11}| < -10$ dB, is $1.71:1$ ($1.75-3$ GHz). However, considering a more relaxed condition (e. g. $|s_{11}| < -6$ dB, as in cellular systems) the bandwidth is $1.94:1$ ($1.6-3.1$ GHz). The LH half-lop antenna can be tuned within the target $2:1$ bandwidth ($1.5-3$ GHz) by changing the value of the LH capacitances (Fig. 5.22). The isolation between both ports is higher than 20 dB for all the C_L values, as shown in Fig. 5.23.

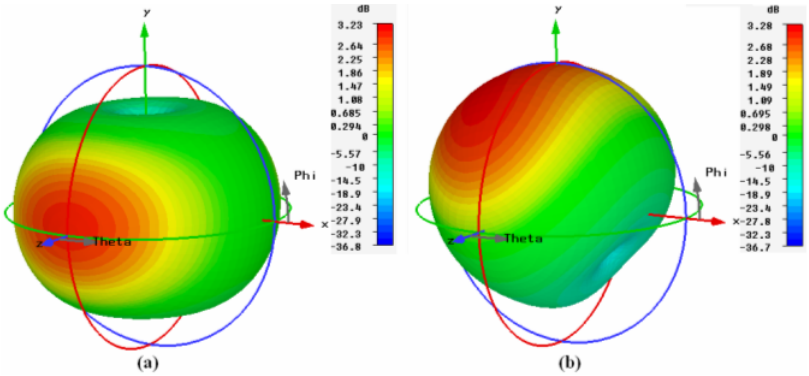

Figure 5.24: Simulated radiation patterns. (a) Port 1 (monopole antenna) at 2.06 GHz. (b) Port 2 (LH half-loop antenna) at 2.59 GHz.

The radiation performance of the system has also been simulated with the same software. The radiation pattern of the monopole antenna is the typical one of a printed monopole antenna, which has a null in the y direction (according to the coordinate system of Fig. 5.20) and is almost omnidirectional in the orthogonal plane ($x-z$), as it is shown in Fig. 5.24.a. It is important to note that the radiation pattern is independent of the value of the variable capacitances (C_L). On the other hand, the LH half-loop antenna has a directional radiation pattern (Fig. 5.24.b), as desired for the communications front-end. The main beam radiates in the y direction. Hence, it can be said that both radiation patterns are orthogonal. The radiation pattern of the LH half-loop is almost independent of the value of the C_L variable capacitances. The simulated radiation efficiency of the LH half-loop antenna at 3 GHz is over 80%. However, it is important to note that the efficiency of this small antenna decreases at lower frequencies because the electrical size of the antenna is considerably smaller.

5.4 Self-Diplexed Patch Antennas for Active RFID Systems

5.4.1 Introduction

In recent years automatic identification procedures have become very popular in many industrial services, purchasing and distribution logistics, manufacturing companies, etc. The barcode labels, that were a revolution in identification systems some years ago, are being found to be inadequate in an increasing number of cases. Barcodes are extremely cheap, but they have a limited storage capacity (only a number) and cannot be reprogrammed. The optimal solution is the storage of data in a memory, which can be read out without mechanical contact (contact-less). These contact-less identification systems are called RFID (Radio Frequency Identification)[22]. Basically it can be said that an RFID system is composed of two devices: the reader and the transponder (or tag). The reader transmits a modulated signal with periods of unmodulated carrier. This is received by the transponder (or tag) that consists of an antenna and an application specific integrated circuit (ASIC). The transponder modulates the received signal with its identification code and sends back the information to the reader.

RFID systems can be classified according to their fundamental parameters such as working frequency, range, electromagnetic coupling, and type of communication between reader and transponder, type of access and ac-

tive or passive systems. Microwave bands (e. g. 2.45 GHz) are being used more and more for RFID systems [22], but the number of commercial RFID systems available at these bands is considerably smaller than the systems working at lower frequencies (e. g. LF or HF bands). Thus, a great effort has to be done to satisfy the increasing demand on RFID components working in the microwave bands. The goal of this Section is the development a dual-frequency active RFID system based on patch antennas working in the microwave bands.

Conventional RFID systems use the same frequency for both radio-links: the reader-transponder link and the transponder-reader link. This approach hinders the design of the reader and it requires higher transmission power from the transponder to allow a proper information reception at the reader side. This implies that the transponder-reader link is power limited due to the very small power that can be generated by the transponder itself. This factor limits the range of operation of the RFID system. Moreover, single-frequency RFID systems have another drawback from the reader point of view. The signal from the transponder is simultaneously received with a leakage from the signal transmitted by the reader. This leakage acts as a large in-band blocker which is very close to the desired signal in frequency band (only $40 - 600$-kHz frequency separation) [141]. This fact makes very difficult to filter out this leakage, making more complicated the design of the reader.

Dual-frequency active RFID systems offer larger capabilities. However, they have not been fully exploited until now due to several drawbacks. The fact of not having self-diplexed dual-frequency antennas (multiport antennas with high isolation between the ports) for arbitrary frequencies has limited the use of active RFID systems to systems based on harmonic interrogation [142, 143]. In these systems, the highest frequency has to be used for the more restricted power link (transponder-reader) making the system more sensitive to propagation losses and reducing both the range associated with the transponder-reader link and the isolation between antenna ports. In order to overcome the previous drawbacks, an optimal solution could be that the reader-transponder link would work at a frequency f_0, while the transponder-reader link would work at a non-harmonic lower frequency (f_0/k,k where is an arbitrary number not forced to be an integer number).

Another matter of great importance in RFID systems deals with power. As the power generated by the transponder is limited, great efforts have been undertaken in the antenna design to look for a proper conjugate impedance matching between the antenna and the RFID ASIC. In this way, the energy transfer between the antenna and transponder would be optimal. Resonant

antennas present a large impedance variation around the resonant condition, which makes them suitable to achieve conjugate impedance matching without any matching network. The resonant antenna then does not work at the resonant condition, as can be seen in [144]. This is of paramount importance for RFID applications where matching networks are usually prohibited. For single frequency systems, we then have slot antennas [145], circular patch antennas [146], PIFA antennas [147], and loaded meander antennas [148]. Additionally, in order to achieve high-radiation efficiency for improving the read range, in [149] a high-efficiency UHF RFID antenna has been proposed. In all these systems, the reader and tag antennas work at the same frequency.

An active RFID system based on self-diplexed antennas filled with CRLH cells is proposed in this Section. The use of self-diplexed dual-frequency resonant antennas increases the capabilities of the RFID system: increases the operation range by reducing the propagation losses, avoids the in-band blocker at the reader and allows conjugate impedance matching at the transponder.

5.4.2 Proposed Active RFID System

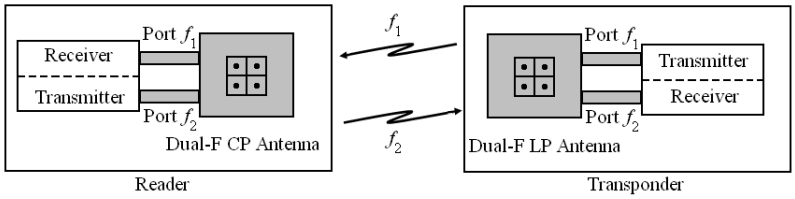

Figure 5.25: Proposed architecture for the RFID active system based on self-diplexed antennas filled with metamaterials.

The operating frequency of an RFID system is the frequency at which the reader transmits. The transmitting frequency of the transponder is disregarded [22]. Then, the realization of dual-frequency antennas for RFID systems is possible. However, very few RFID systems based on dual-frequency performance (i.e. [142] and [143]) have been proposed due to two main reasons. Firstlyn the transponder-reader link is the most critical one in terms of power; these systems work with a harmonic frequency for this link what implies smaller power and larger propagation losses. Secondly, the isolation between transmitter and receiver at both front-ends (reader and transponder) must be large in order to avoid interference coupling between both radio links. Self-diplexed antennas have become a bottle-neck till now so dual-frequency RFID systems have not been very common.

In order to overcome the previous difficulties, a dual-frequency RFID system based on self-diplexed antennas has been proposed. The frequencies in each link are different with any arbitrary ratio between them. The proposed topology is the one shown in Fig. 5.25.

Both antennas are self-diplexed dual-frequency patches. The detailed design of the antennas will be discussed in Subsection 5.4.3. The transponder antenna is a linearly polarized one that receives at f_2 (the higher frequency) while transmits at f_1 (the lower frequency) in order to reduce the propagation losses in the most critical link (transponder-reader). The linear polarization can be the same or orthogonal at each frequency depending on the application. Both cases are considered in this Section. In addition, the transponder antenna must provide a conjugate complex impedance to have the lowest mismatching factor and achieve the maximum power transfer [148]. The mismatching factor is given by

$$M = \frac{4R_a R_c}{|Z_a + Z_c|^2} \tag{5.1}$$

where $Z_c = R_c + j \cdot X_c$ is the ASIC impedance while $Z_a = R_a + j \cdot X_a$ is the antenna impedance.

The reader antenna is a circularly polarized one. It transmits at f_2 (the highest frequency) while receives at f_1 (the lowest frequency). The circular polarizaton helps to overcome the multipath problems and reduce the polarization losses and the link fading. In this case the antenna impedance is matched to the front-end impedance (Z_0). Thus, in this case the design is somewhat different to the transponder case.

5.4.3 Antennas Design

The proposed antennas are based on the multifrequency patch antennas filled with CRLH structures presented in Chapter 4, but some modifications must be made in order to use them for the proposed RFID system. Four design goals are considered:

- Dual-frequency performance.
- Self-diplexing capability: high isolation between the output ports.
- Complex conjugate impedance matching for the transponder antenna.
- Maximum separation between the working frequencies.

The dual-frequency patch antenna filled with a 2×2 array of CRLH cells (Section 4.5) is a proper solution for the transponder antenna. This antenna provides a patch-like radiation pattern at two arbitrary working bands. Moreover, it can provide the same or orthogonal linear polarizations at each port. If the same polarization is required for the RFID application, the antenna must be fed through two ports placed in the middle of one main dimension of the patch (along x or y axes). Thus, the $n = \pm 1$ modes are simultaneously excited. The antenna will operate at f_1 for the $n = -1$ mode and f_2 for the $n = +1$ mode. On the other hand, if orthogonal linear polarizations are required, the antenna must be fed through two ports placed in the middle of the two main dimensions of the patch (x and y axes). In this case, the $[-1, 0]$ (or $[0, -1]$ depending on the port numbering) mode will be excited at f_1 while the $[0, +1]$ (or $[+1, 0]$ for the second port numbering) mode will be used at f_2.

For the case of the reader, the same dual-frequency antenna is valid, but in this case the antenna must be fed through four ports. These ports must be located in the middle of the four sides of the patch (along x and y axes). Thus, the ports are orthogonally placed in pairs. The first pair will be used to excite the $[-1, 0]$ and $[0, -1]$ modes at f_1 simultaneously. These two ports will be connected to the outputs of a branch-line coupler working at f_1 to achieve a 90° phase-shift between them and, thus, circular polarization in the antenna. The other pair of ports will simultaneously excite the $[+1, 0]$ and $[0, +1]$ modes at f_2. Similarly to the previous case, the second pair of ports will be connected to a branch-line coupler but working at f_2.

The type of feeding must be optimized in order to achieve high isolation between the ports. Three feedings commonly used in microstrip patches are considered: coaxial probe, proximity coupled line and aperture coupled line. A set of simulated prototypes considering the previous feeding techniques has been developed in CST Microwave Studio ® to choose the best configuration. The simulations results are summarized in Table 5.2.

Coaxial probes have been used to feed single-port multifrequency patch antennas (e. g. Sections 4.4 and 4.5). However, this feeding technique presents two drawbacks when used for the proposed RFID system. The first one is the inductive behaviour of the feeding that can make the matching difficult, which is particularly harmful when conjugate matching with respect to the RFID ASIC input impedance has to be reached. In addition, the isolation between the antenna probes is very low when two ports are used.

As there are two main goals (maximum isolation between ports and good matching), the coaxial feeding is discarded. The proximity coupled lines can be a suitable feeding technique for the proposed antenna. The patch filled

	Orthogonal ports		Non-orthogonal ports	
Feeding Structure	Without filtering	With filtering lines	Without filtering	With filtering lines
Coaxial	12 dB	Not possible	5 dB	Not possible
Proximity coupled	45 dB	50 dB	8 dB	15 dB
Aperture coupled	30 dB	58 dB	12 dB	25 dB

Table 5.2: Comparison between the isolation levels for different feeding strategies

with CRLH is excited through a coupled line placed between the patch and the ground plane (e. g. Section 4.8.1). Good matching can be achieved by varying the depth of the feeding line under the antenna. This is an easy feeding strategy, but has only one degree of freedom. It must also be taken into account that, for RFID transponders, the impedance should be complex to get conjugate matching. As there is only one parameter to be modified, it is not possible to achieve any arbitrary complex impedance at two different frequencies. In addition, coupled lines have been mainly used as orthogonal feeding ports to obtain self-diplexed patch antennas [150]. Good isolation levels can be achieved by using this approach due to the orthogonality of the excited modes. There are some approaches where isolation can be improved by inserting defected ground plane structures [151] or electromagnetic bandgap (EBG) structures under the feeding lines [152]-[153]. However, these approaches have not been shown as valid when dual-band antennas with the same polarization are built. Finally, all the previous approaches have been designed for real impedances, which is a drawback from the transponder point of view.

The other feeding strategy under study is an aperture coupled line. This arrangement allows independent optimization of the feeding mechanism and the radiating element at the two different frequencies provided by the patch partially filled with CRLH cells. Thus, the number of degrees of freedom is larger and complex impedances at different frequencies at both ports can be achieved, which will be very important for maximum energy transfer at both frequencies. In addition, a good isolation level between both ports is kept. In this case, the parameters considered in the design of the feeding lines are the length and width of the slot and the depth of the coupled microstrip further than the position of the slot. The sketch of the proposed

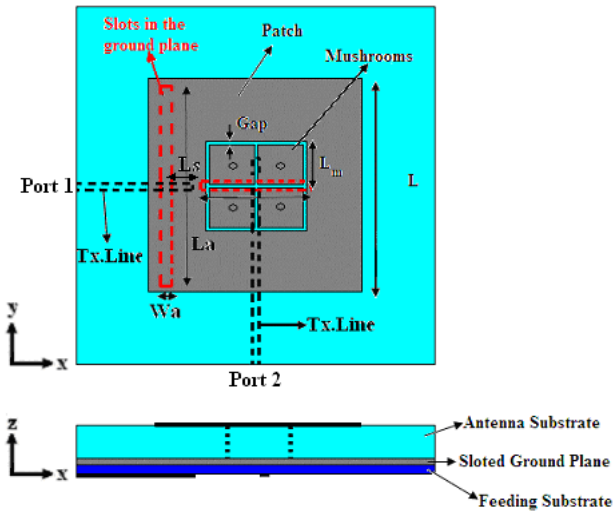

Figure 5.26: Sketch of a self-diplexed linearly polarized patch antenna fed through aperture coupled lines.

dual-frequency, linearly polarized antennas with two ports is seen in Fig. 5.26. In this example, orthogonal polarizations are obtained at each frequency and port. The case for the same polarization at both frequencies and ports is similar, but with one feeding line and its corresponding slot rotated 90° from the others. From Fig. 5.26, it can be seen that two independent slots feed the patch filled with CRLH cells. The vertical slot is related to the higher frequency (f_2), while the horizontal one is associated with the lower frequency (f_1). An increase in the slot length makes the resonant frequency decrease. An increase in the slot width makes the slot line impedance larger, which decreases the reactive antenna impedance and, thus, the resonance frequency. This reactive part can be finally controlled by modifying the length of the microstrip line further than the position of the slot.

The use of filtering feeding lines instead of conventional feeding lines provides higher isolation levels between both ports, even when nonorthogonal modes are excited. These filtering lines are microstrip lines with coupled or connected metamaterial particles to achieve a filtering performance at a desired band.

As it was reviewed in Subsection 2.3.2, if SRRs are coupled at both sides of a microstrip TL, a narrow frequency band above the SRRs resonance frequency is inhibited (notch filter). Moreover, the stopband response can be changed to a passband by periodically inserting metallic vias between the TL and the ground plane. These vias make the structure behave as a LH media

where backward propagation is allowed in a narrow band.

In this way, filtering-feeding lines can be obtained by adding these particles to the antenna feeding TLs. These lines allow the rejection of the antenna non-desired modes and improve the isolation between ports. It must be emphasized that neither the complexity, nor the size of the antenna is increased. In addition, the radiation parameters are kept. For the proposed antennas, two bandpass filtering feeding lines are used. The first one is tuned to the higher frequency (f_2), whilst the second one is tuned to the lower frequency (f_1). In this way, only the desired modes are transmitted or received through each port, achieving a high isolation between both ports.

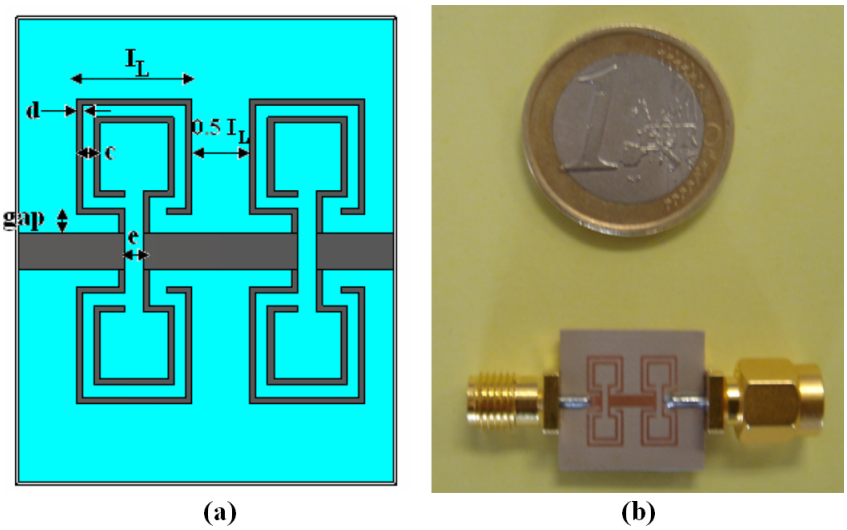

Figure 5.27: (a) Schematic of the bandpass filtering line based on OSRR. (b) Picture of the manufactured circuit.

Bandpass filtering lines based on SRRs and vias to the ground plane are very selective in frequency, but present large insertion losses around 3 dB (mainly due to the vias and its connection to the TL). These losses are not acceptable since the efficiency of the antenna would be noticeably degraded. Then, the so-called open split-ring resonator (OSRR) [154] periodically inserted in the filtering TL is proposed. An OSRR behaves as a series LC circuit in series with the TL. These particles allow obtaining bandpass filtering lines without vias. In order to reduce its size, the topology shown in Fig. 5.27 formed by two pairs of square OSRRs connected to the TL is proposed. It also has a bandpass frequency response tuned by the OSSR characteristic parameters (side of the square I_L, gap between rings c, width of the ring d, spacing between the ring and the microstrip line *gap*, and gap in the mi-

crostrip line e). The selectivity of these filters is lower than the obtained using SRRs and vias, but the insertion losses are also much lower, which is important from the antenna point of view.

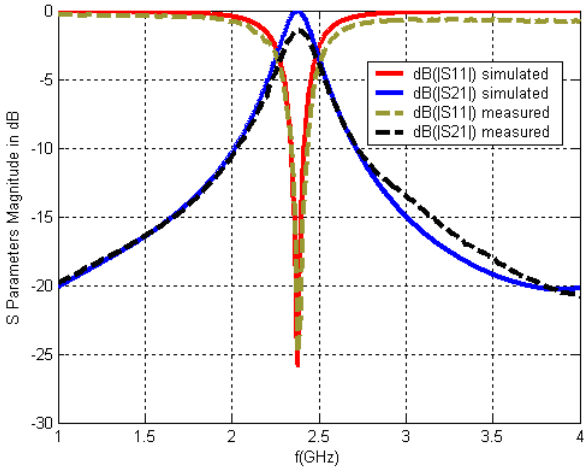

Figure 5.28: Simulation and measurement of the proposed filtering line with two OSRRs.

One filtering line tuned to one of the RFID microwave frequencies (2.45 GHz) has been designed and built. The design parameters are $I_L = 3.9$ mm, $gap = 0.60$ mm, $c = 0.20$ mm, $d = 0.40$ mm, and $e = 0.60$ mm. The substrate is Arlon 1000 ($h = 1.27$ mm and $\varepsilon_r = 10$). Fig. 5.27.b shows a photograph of the manufactured line. Fig. 5.28 shows the simulated (CST Microwave Studio ®) and measured $[S]$ parameters of the proposed structure. High agreement between measurements and simulations can be appreciated. The main advantages of this topology are its construction simplicity (vias are avoided), reduced size, and low insertion losses (around 1.2 dB). Thus, these filtering lines are a proper solution to be used as feeding lines of the self-diplexed antennas.

Considering the results summarized in Table 5.2 for orthogonal ports, it is shown that the isolation is considerably improved when proximity coupled lines or aperture coupled lines in the ground plane are used as the feeding scheme in comparison with the coaxial feeding approach. These values are even improved in both feeding approaches when filtering lines are included, allowing very high isolation levels. In the case of nonorthogonal ports, the isolation is smaller than 10 dB when coaxial probes or proximity coupled lines are used. These results are slightly improved when the feeding lines are coupled through slots in the ground plane. In this case, the filtering feeding

lines technique gives an important improvement with respect to the conventional lines, providing high isolation between the ports. This high isolation level is comparable to the case of orthogonal modes when the filtering lines are coupled to the antenna through slots in the ground plane.

It can be concluded that, according to the isolation levels, there are not any important differences between the proximity coupled and aperture coupled line schemes. In both cases, the use of filtering lines improves the isolation between the ports.

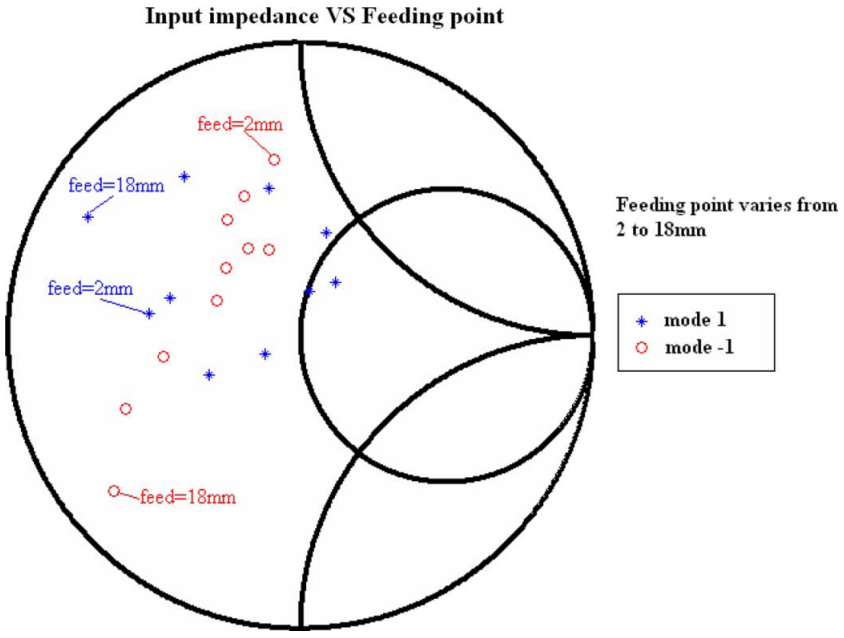

Figure 5.29: Antenna impedance for different positions of the feeding point for a proximity coupled microstrip antenna.

An important parameter to be analysed is the antenna impedance. Proper impedance matching between the antenna and the transmitter or receiver is of paramount importance in RFID systems. For that reason, it is important to have as many degrees of freedom as possible in order to obtain conjugate matching between the transponder and the antenna. When proximity coupled lines are used, the only parameter to be changed is the position of the feeding point. A self-diplexed patch antenna fed through two 50−Ω proximity coupled lines is simulated (CST Microwave Studio ®) for different depths of the feeding line under the patch. This parameter is varied between 2 mm and 18 mm from the edge of the patch towards its center. A study of the antenna impedance variation versus the position of the feeding point has been done

and is shown in Fig. 5.29. The following conclusions can be made:

- Both curves (the higher frequency due to the $n = +1$ mode and the lower one due to the $n = -1$ mode) follow the impedance variation of a resonating antenna.
- The $n = +1$ mode presents two resonant conditions (for depths of the feeding line equals to 2 and 8 mm), while the $n = -1$ mode has only one resonant condition (for a depth of about 12 mm).
- The number of impedances that can be achieved is small and does not usually cover the impedance needed for the transponder.

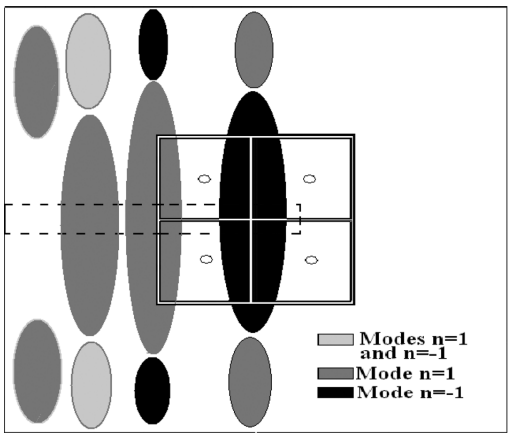

Figure 5.30: Sketch of the position and dimension of the slot under the antenna and the corresponding excited modes.

On the other hand, the coupled slot feeding scheme increases the number of variables to find complex impedance matching. This scheme provides four degrees of freedom to the designer (Fig. 5.26): the position of the slot under the patch, the length and the width of the slot (L_a, W_a), and the stub length of the microstrip line feeding the slot (L_s). The position of the slot under the patch determines the modes to be excited. Fig. 5.30 shows a sketch of the position and dimension of the slot under the antenna and the corresponding excited mode. From that figure, it can be seen that there are areas where the $n = \pm 1$ modes are simultaneously excited. There are other two shadowed areas where only the $n = +1$ or the $n = -1$ mode are excited. It can also be concluded that when the separation from the patch center is small, the $n = -1$ mode is excited for short slot lengths while the $n = +1$ mode is excited for long slot lengths. If the separation from the patch center is

increased: the $n = +1$ mode is excited for short slot lengths while both modes are excited for long slot lengths. Finally, when the slot is located at the center, the $n = -1$ mode is excited for short slots, while the $n = +1$ mode is excited for long slots.

The regions highlighted in Fig. 5.26 show the regions where the antenna resonates. Once the position of the slot is chosen, the parameters L_a, W_a and L_s can be adjusted in order to achieve conjugate impedance matching. An example is shown in Subsection 5.4.4.

Although this feeding structure is somewhat more complicated than the proximity coupled one, it is particularly useful for the dual-frequency linearly polarized transponder antenna since it provides enough degrees of freedom to achieve the desired conjugate complex impedance. On the other hand, the reader antenna only needs a conventional matching to Z_0. Thus, the proximity coupled lines is suitable and easier to manufacture. For the reasons exposed before, the proximity coupled filtering lines approach is proposed to match the reader antenna to the front-end, while the aperture coupled filtering lines technique is proposed for the transponder antennas.

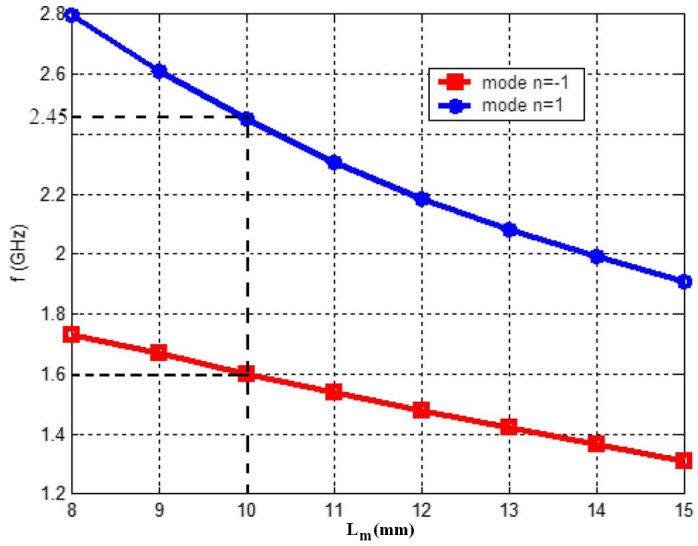

Figure 5.31: Resonance frequencies of the two patch-like modes ($n = \pm 1$) in the CP patch antenna depending on the CRLH cells length (L_m). The maximum frequency separation in the circularly polarized antenna is highlighted with the dashed line.

The last parameter to be analysed for the proposed dual-frequency RFID system is the maximum frequency separation. The RFID frequency is fixed

by the reader-transponder link. ISM band (2.45 GHz) is the first microwave band allowed in RFID. For this reason, the upper frequency of the proposed system f_2 is set to 2.45 GHz. The transponder transmitter frequency is limited by both the linearly polarized transponder antenna and the circularly polarized reader antenna. The second one is more critical since, as the CRLH cells are square, there are not any degrees of freedom to achieve the lowest frequency but the side of the square CRLH cells (L_m). Thus, for a fixed patch dimension L, the side of the square CRLH cell is varied in order to find the maximum separation between the $n = +1$ and $n = -1$ mode. This maximum separation is of paramount importance since it minimizes the losses of the more restricted power limited link, the transponder-reader one. Once that curve is determined, the value of the side of the CRLH cell L_m and the minimum frequency associated with the $n = -1$ mode are obtained. Then, for the proposed circularly polarized antenna with $f_2 = 2.45$ GHz, the maximum frequency separation is computed from Fig. 5.31. This value is maximum for 10−mm square CRLH cells ($L_m = 10.00$ mm), achieving a lower frequency close to 1.65 GHz. Thus, this value is chosen for the transponder-reader link frequency f_1.

5.4.4 Transponder Design Example

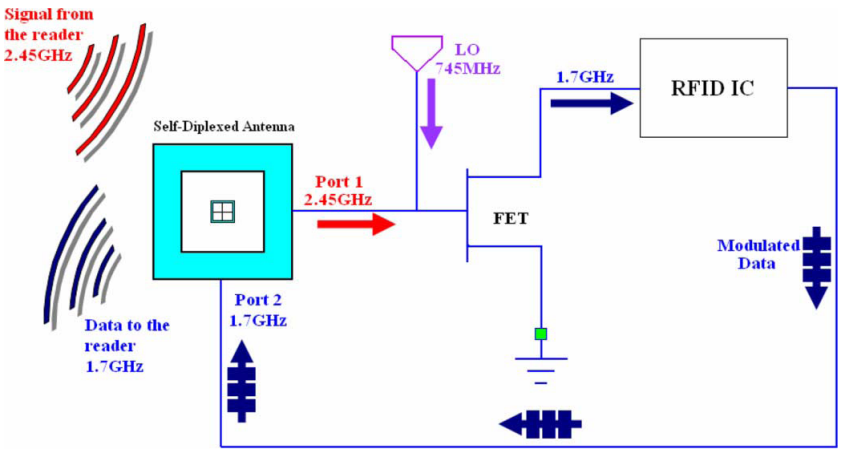

Figure 5.32: Proposed dual-frequency active RFID transponder.

The proposed dual-frequency active RFID transponder consists of the dual-frequency self-diplexed antenna followed by a mixer that directly feeds the RFID ASIC. The schematic can be seen in Fig. 5.32. The signal from the reader at 2.45 GHz is received through the port 1 by the linearly polarized

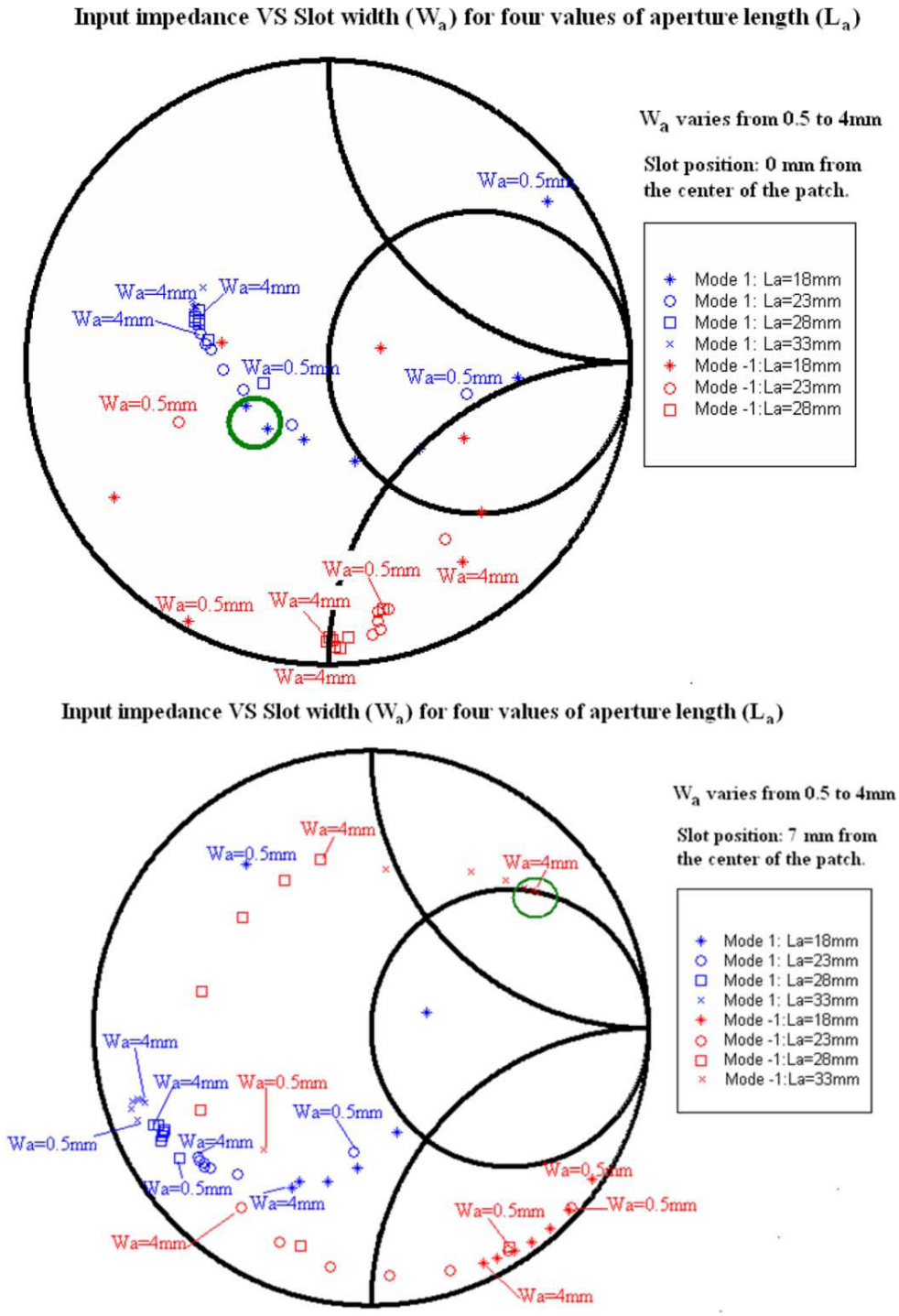

Figure 5.33: Antenna input impedance loci of the $n = -1$ and $n = +1$ modes for different positions of the slots (top: center of the patch, bottom: 7 mm from the center of the patch). The length (L_a) and width (W_a) of the slot are taken as parameters.

dual-frequency antenna. The impedance at this port should be complex and slightly capacitive in order to achieve maximum gain [155]. An impedance around $(20 - j10)\Omega$ is a suitable value to get that maximum gain.

The output of the FET at 1.7 GHz directly feeds the RFID ASIC. This ASIC provides a modulated data at 1.7 GHz that feeds the other port (Port 2) of the linearly polarized self-diplexed antenna. The port 2 must provide a conjugate complex impedance to the RFID ASIC in order to minimize the mismatching factor M. The impedance of the RFID ASICs is around $(20-j150)\Omega$. The antenna impedance at the port 2 must then be around $(20+j150)\Omega$. Thus, for the transponder antenna, a different complex impedance have to be achieved at each antenna port.

It is possible to match any complex impedance with the proposed feeding procedure approach. These values of impedance can be easily obtained at each port by adjusting the slot parameters such as the length L_a, the width W_a, and the position. The port 1 works with the $n = +1$ mode. Then, an impedance around $(20 - j10)\Omega$ has to be achieved at port 1 at 2.45 GHz. According to the lower part of Fig. 5.33, a 3.30×18.00 mm slot placed at the center of the patch has to be made.

The port 2 works with the $n = -1$ mode and an impedance of $(20+j150)\Omega$ has to be achieved at 1.7 GHz. This means a 4.00×33.00 mm slot placed at 7 mm from the center of the patch has to be made to feed the port 2. Lastly, a fine impedance adjustment can be done by using the open stub (L_s) of the microstrip line.

5.4.5 Experimental Results

Transponder Antennas

The proposed antennas for the transponder are based on the dual-frequency linearly-polarized patch antenna fed through two slot-coupled lines. Moreover, the filtering feeding lines presented in Section 5.4.3 are used instead of conventional transmission lines in order to increase the isolation level. The sketch of the proposed antennas can be seen in Fig. 5.34. Without loss of generality and in order to make the measurement of the radiation parameters easier the transponder antennas are matched to 50 Ω in the present Section.

There are two possibilities when choosing the polarization of the proposed RFID linearly polarized antenna: the same linear polarization (horizontal or vertical) at the two working frequencies or orthogonal polarizations (horizontal at one frequency and vertical at the other one). Both schemes are considered in this Section. The design and manufacturing of such antennas

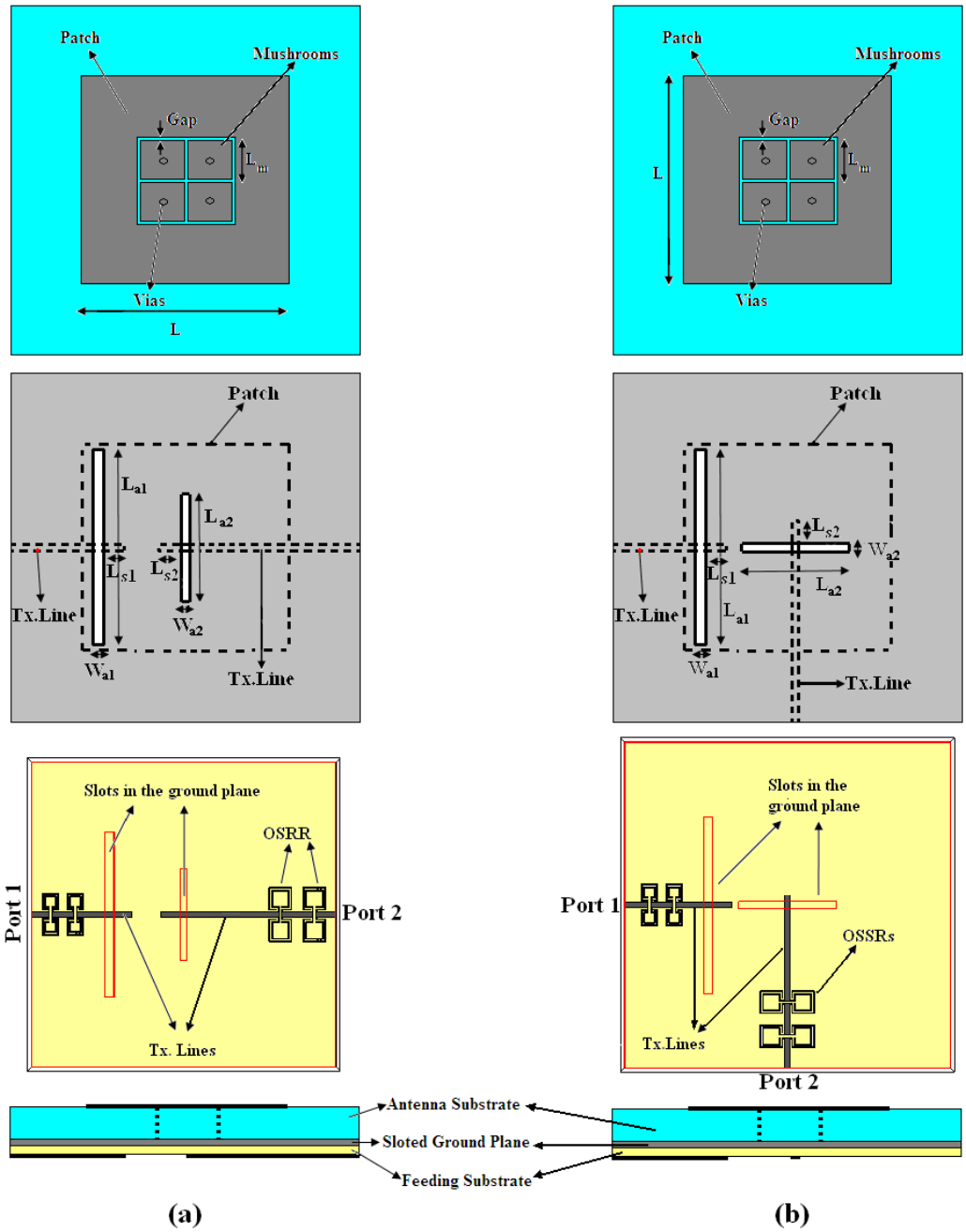

Figure 5.34: Sketch of the proposed self-diplexed dual-frequency linearly-polarized patch antenna for RFID transponder application. (a) Same linear polarization. (b) Orthogonal polarizations.

are similar. The only difference between both schemes comes from the fact that one filtering feeding line and its corresponding slot are rotated 90° with respect to the other filtering line and slot as it is shown in Fig.5.34.

The final dimensions of the prototypes are $L = 40.00$ mm, $L_m = W_m = 6.50$ mm, $gap = 0.35$ mm and vias radii $= 0.35$ mm. The antenna substrate is Polypropylene ($\varepsilon_r = 2.2$) with $h = 8.00$ mm and the feeding substrate is Arlon ® 1000 ($h = 1.27$ mm and $\varepsilon_r = 10$). The feeding microstrip lines are based on $50-\Omega$ transmission lines (1.20−mm width). The parameters of the filter at the port 1 (2.45 GHz) are: $I_L = 3.90$ mm, $gap = 0.60$ mm, $c = 0.20$ mm, $d = 0.40$ mm and $e = 0.60$ mm. The depth of the microstrip line further than the centre of the slot position is $L_{s1} = 6.00$ mm. This line is coupled to the patch through a slot shifted 18.00 mm from the centre of the patch in the horizontal direction. The dimensions of this slot are $W_{a1} = 2.00$ mm and $L_{a1} = 38.00$ mm. On the other hand, the parameters of the filter at the port 2 (1.7 GHz) are: $I_L = 5.20$ mm, $gap = 0.60$ mm, $c = 0.20$ mm, $d = 0.40$ mm and $e = 0.60$ mm. The slot in the ground plane which couples the energy to the patch is centred under the patch and its dimensions are $W_{a2} = 1.50$ mm and $L_{a2} = 21.00$ mm The total length of the stub from the slot to the end of the feeding line is $L_{s2} = 6.00$ mm.

The prototypes of the antennas have been manufactured (see for instance Fig. 5.35) and measured. The filters have been shielded in order to avoid spurious radiation and undesired couplings between elements. The equivalent antennas fed with conventional lines (instead of filtering lines) have been also manufactured and measured in order to show the improvements achieved with the proposed approach.

The measured $[S]$ parameters of the equivalent antennas without filtering lines are shown in Fig. 5.36. The simulated and measured $[S]$ parameters of the self-diplexed antennas are shown in Fig. 5.37. There is a good agreement between them, although there is a little frequency shift due to the permittivity tolerance and the accuracy of the multilayer structure manufacturing process. The results are summarized in Table 5.3.

The antennas are well matched in all the cases. The use of filtering lines keeps the matching at the desired resonance. On the other hand, the filtering lines filter out the non-desired resonances. This can be seen by comparison of Figs. 5.36-5.37. In the reflection coefficients of the antennas without filtering modes (Fig. 5.36) there are resonances at the non-working frequencies of the ports (1.65 GHz at port 1 and 2.45 GHz at port 2). These non-desired resonances are filtered thanks to the use of the filtering lines. For example, in the case of the antenna with the same polarization (Fig. 5.36.b) the reflection coefficient at 1.65 GHz measured at port 1 is -11 dB approximately and

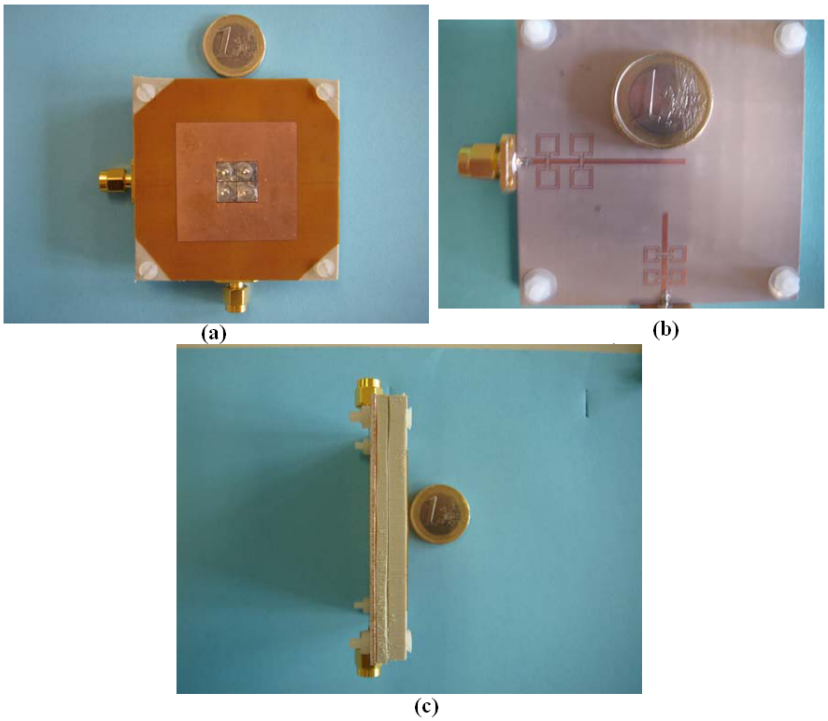

Figure 5.35: Pictures of the manufactured self-diplexed patch antenna with orthogonal polarizations. (a) Top view. (b) Bottom view. (c) Side view.

	Orthogonal ports		Non-orthogonal ports	
Feeding Structure	Without filtering	With filtering lines	Without filtering	With filtering lines
Reflection Coefficient at f_1 (Port 2)	−21 dB	−17 dB	−30 dB	−18 dB
Reflection Coefficient at f_2 (Port 1)	−25 dB	−18 dB	−22 dB	−20 dB
Isolation at f_1	26 dB	41 dB	4 dB	31 dB
Isolation at f_2	26 dB	45 dB	10 dB	48 dB

Table 5.3: Summary of the measured results for the manufactured prototypes with and without filtering lines.

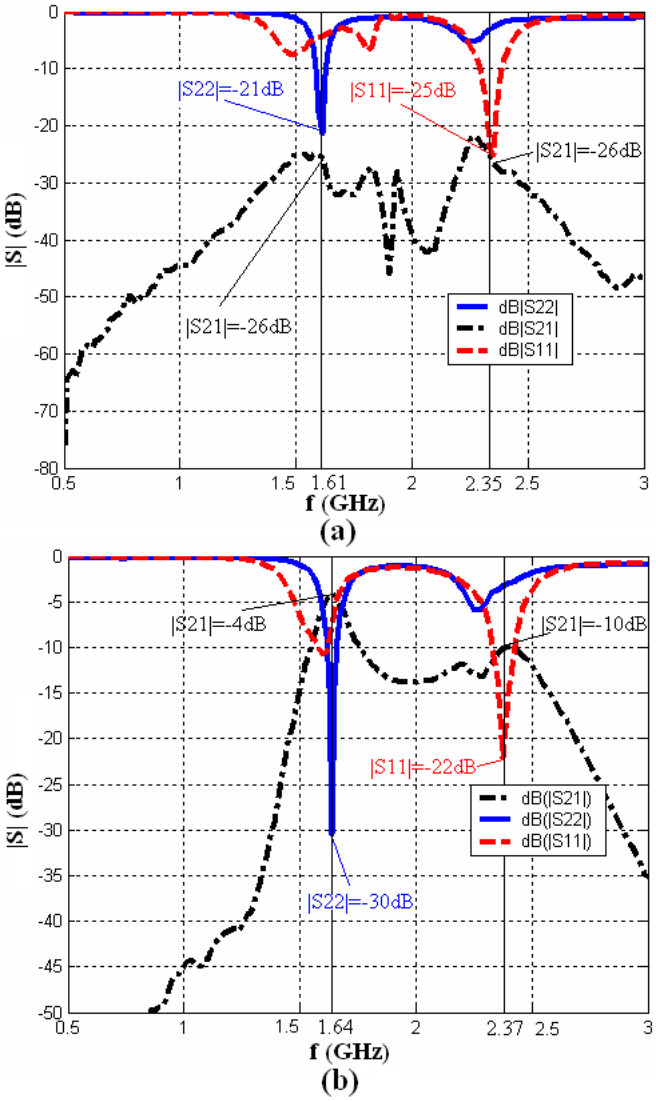

Figure 5.36: Measured $[S]$ parameters of the manufactured aperture coupled linearly-polarized antennas without filtering lines. (a) Orthogonal polarizations. (b) Same polarization.

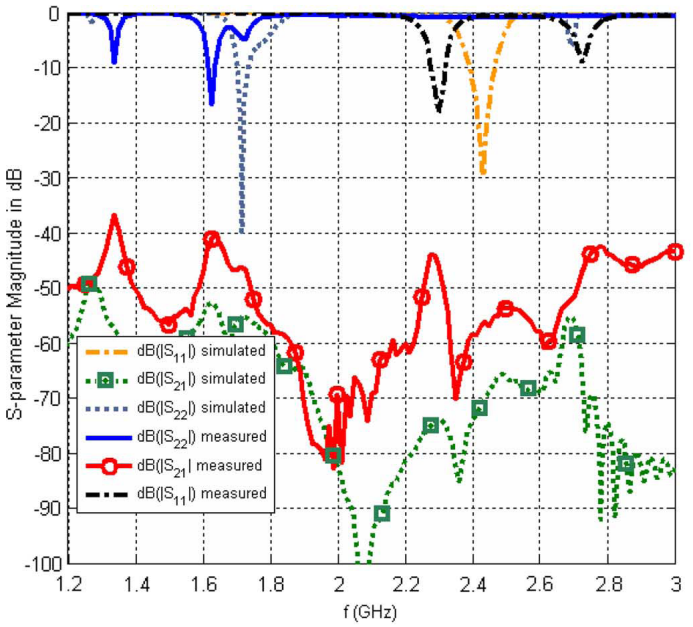

(a)

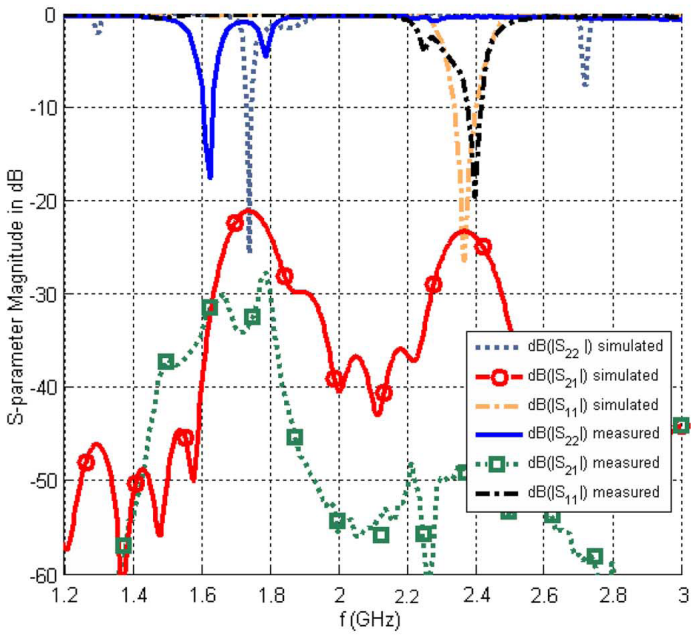

(b)

Figure 5.37: Simulated and measured $[S]$ parameters of the self-diplexed linearly-polarized antennas. (a) Orthogonal polarizations. (b) Same polarization.

	Orthogonal ports		Non-orthogonal ports	
Feeding Structure	Without filtering	With filtering lines	Without filtering	With filtering lines
Port 1: Gain at f_1 (Non-working)	0.4 dB	−15.1 dB	1.6 dB	−15.0 dB
Port 1: Gain at f_2 (Working)	7.0 dB	4.0 dB	3.2 dB	1.4 dB
Port 2: Gain at f_1 (Working)	4.8 dB	4.8 dB	3.3 dB	4.6 dB
Port 2: Gain at f_2 (Non-working)	3.4 dB	−19.3 dB	1.9 dB	−17.7 dB

Table 5.4: Summary of the measured gains for the manufactured prototypes with and without filtering lines.

the reflection coefficient at 2.45 GHz measured at port 2 is −6 dB. These resonances are filtered out in the prototype with filtering lines (Fig. 5.37.b). Moreover, the isolation between the ports is considerably improved by using the filtering lines. For the antenna with orthogonal ports, the isolation is 41 dB at the first working frequency and 45 dB at the second one when filtering lines are used. On the other hand the isolation is 26 dB at both frequencies when these lines are not used. The improvement is even higher for the case with the same linear polarization. In this case, the isolation is 31 dB at the first frequency and 48 dB at the second one for the prototype with filtering lines, while it is only 4 dB at the first frequency and 10 dB at the second frequency for the antenna without filtering lines.

All the prototypes have been measured in an anechoic chamber with the available linearly polarized probe to obtain their radiation patterns and gains. The gain results are summarized in Table 5.4.

The measured gain for the self-diplexed antenna with orthogonal polarizations is 4.8 dB at the lower working frequency and 4.0 dB at the higher one. A comment must be done on this last value since it should be a little higher (a value around 6.5 or 7.0 dB was expected). This value may not have been obtained due to a small shift in filtering lines response. Lastly, the gains at the non-working frequencies (1.63 GHz at port 1 and 2.41 GHz at port 2) are −15.1 dB and −19.3 dB respectively what shows the self-diplexed performance. On the other hand, the equivalent prototype fed with conventional feeding lines (instead of filtering lines) has similar performance at the working frequencies, but it has high gain values at the non-working ones. The

measured gain at the working lower frequency port (port 2) is similar to the self-diplexed case. However, at the non-working frequency the gain is 3.4 dB (instead of −19.3 dB). This shows a very poor diplexing performance when the feeding filtering lines are removed. For the high frequency port (port 1), the measured working gain is 7.0 dB. As in this case the filtering lines have been removed, this value shows that the frequency of the filtering lines in the self-diplexed antenna was somewhat shifted. The gain at the non working frequency is 0.4 dB (instead of −15.1 dB) showing, once again, a very poor diplexing performance.

For the self-diplexed antenna with the same polarization the gain at the working frequencies is 4.6 dB at the first frequency (port 2) and 1.4 dB at the second frequency (port 1). These values are 3.2 dB and 3.3 dB for the antenna with conventional lines. The gain reduction at the second frequency for the self-diplexed antenna may be due to a slight frequency in the filters which increases the insertion losses. The gain of both antennas is lower at the second frequency because there is an energy coupling between the ports. This has also been observed in simulation. Once again the effect of the filtering lines is observed at the non-working frequencies. In this case, the gain at f_1 measured at port 1 is 1.6 dB for the antenna fed with conventional lines. This value is considerably reduced to −15 dB when filtering lines are employed. A similar improvement is achieved (from 1.9 dB to −17.7 dB) for the port 2 at f_2.

The measured radiation pattern of the self-diplexed antennas are shown in Figs. 5.38-5.39. The desired patch-like radiation pattern is obtained in all the cases.

For the self-diplexed antenna with orthogonal polarizations (Fig. 5.38) working at $f_1 = 1.64$ GHz the maximum cross-polarization (XPOL) level (with respect to the normalized 0 dB co-polarization level) in the $x-z$ plane is −14 dB and occurs at around −65°. For the $y-z$ plane the maximum XPOL occurs at around −25° is −14.5 dB. The XPOL level is below −15 dB at broadside in both principal planes. At $f_2 = 2.26$ GHz in the $x-z$ plane, the maximum XPOL level (with respect to the normalized 0 dB co-polarization level), is −7.5 dB and occurs at around −30°. For the $y-z$ plane the maximum cross-polarization occurs at around −15° and is −12 dB. The XPOL component is below −13.5 dB at broadside in both principal planes.

In the case of the self-diplexed antenna with the same linear polarization (Fig. 5.39) the maximum XPOL level (with respect to the normalized 0 dB co-polarization level) is −11 dB for the first working frequency ($f_1 = 1.63$ GHz) in the E-plane ($x-z$ plane) and occurs at around −40°. For the H-plane ($y-z$ plane) the maximum XPOL occurs at around −45° and is also

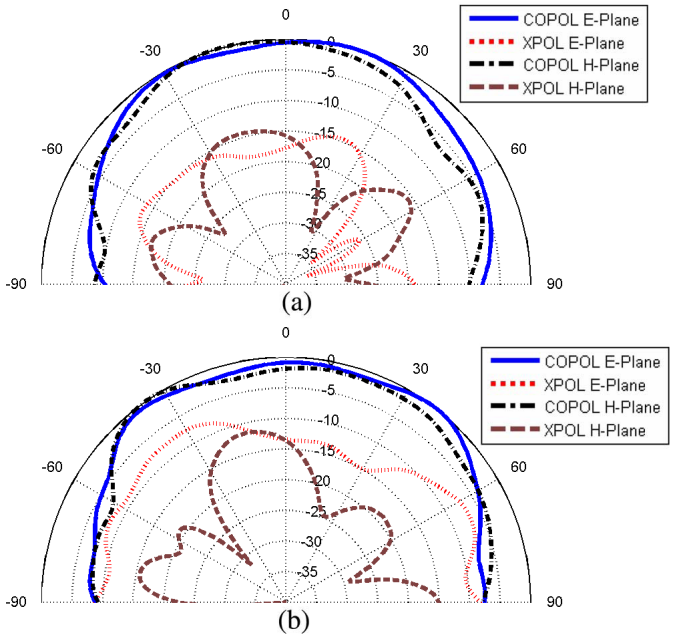

Figure 5.38: Measured radiation patterns of the self-diplexed antenna with orthogonal linear polarizations. (a) f_1. (b) f_2.

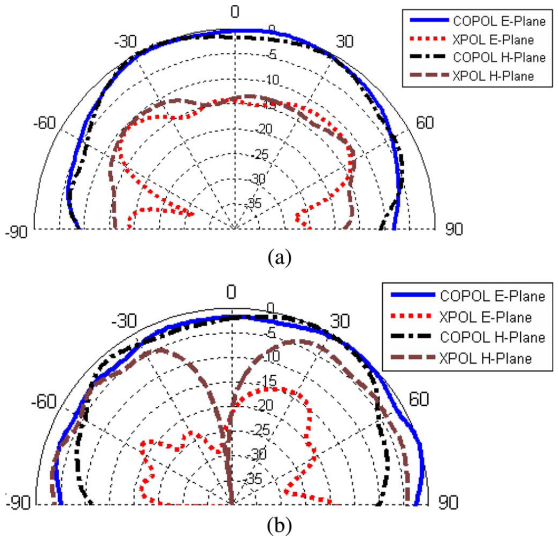

Figure 5.39: Measured radiation patterns of the self-diplexed antenna with the same linear polarization on both ports. (a) f_1. (b) f_2.

−11 dB. The XPOL level is approximately −15 dB at broadside in both principal planes. For the second working frequency (f_2 = 2.41 GHz) in the E-plane, the maximum XPOL level (with respect to the normalized 0 dB co-polarization level), is −15 dB and occurs at around 30°. For the H-plane the maximum cross-polarization occurs at around −45° and is also −5 dB. The high cross-polarization levels are due to the coupling between output ports. Anyway, the XPOL component is below −20 dB at broadside in both principal planes.

Reader Antenna

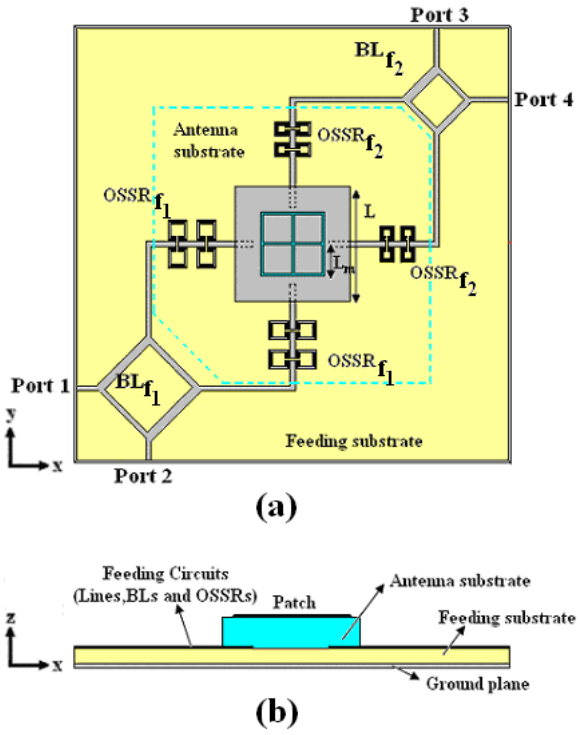

Figure 5.40: Sketch of the self-diplexed circularly polarized antenna for RFID reader application. (a) Top view. (b) Side view.

The proposed antenna for the RFID reader is sketched in Fig. 5.40. It is based on the dual-frequency patch fed through four proximity coupled filtering lines. The filters used for the first pair of orthogonal feeding lines are tuned to the first working frequency of the RFID system (f_1), while the other pair is tuned to the second one (f_2). Each pair of filtering lines is connected

to a conventional branch-line working at the corresponding frequency. Thus, the antenna has four ports, but only one port per frequency is used while the other is connected to a matched load. This allows all the possibilities of operation for a dual-band circularly-polarized antenna with agile polarization capability. The four possible configurations are as follows:

1. RHCP at f_1 and RHCP at f_2 when the ports 1 and 4 are ended with matched loads and the ports 2 and 3 are used as input/output ports.
2. RHCP at the f_1 and LHCP at f_2 when the ports 1 and 3 are ended with matched loads and the ports 2 and 4 are used as input/output ports.
3. LHCP at the f_1 and RHCP at f_2 when the ports 2 and 4 are ended with matched loads and the ports 1 and 3 are used as input/output ports.
4. LHCP at the f_1 and LHCP at f_2 when the ports 2 and 3 are ended with matched loads and the ports 1 and 4 are used as input/output ports.

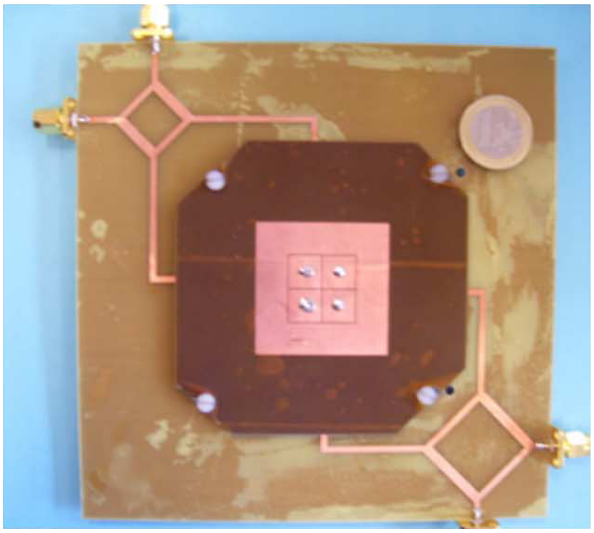

Figure 5.41: Photograph of the RFID reader manufactured prototype.

The proposed dimensions for the reader antenna are $L = 40.00$ mm, $L_m = W_m = 10.00$ mm, $gap = 0.25$ mm and vias radius = 0.35 mm. The antenna substrate is PVC ($\varepsilon_r = 2.9$) with 2.00 mm height which is directly

placed over the feeding substrate which is FR-4 ($\varepsilon_r = 4.5$) with 1.55 mm height. The $50-\Omega$ feeding lines (1.80 mm width) are printed on the top face of this substrate and are ended with a conventional branch-line at each frequency. The parameters of the filters tuned to f_1 (1.63 GHz) are: $I_L = 6.70$ mm, $gap = 0.60$ mm, $c = 0.30$ mm, $d = 0.50$ mm and $e = 0.60$ mm. The offset below the patch of the feeding lines which provides operation at f_1 is 10.00 mm (measured from the edge of the patch). On the other hand, the parameters of the filters at f_2 (2.45 GHz) are: $I_L = 4.80$ mm, $gap = 0.60$ mm, $c = 0.30$ mm, $d = 0.50$ mm and $e = 0.60$ mm. The total length of the lines from the edge of the patch is 10.00 mm.

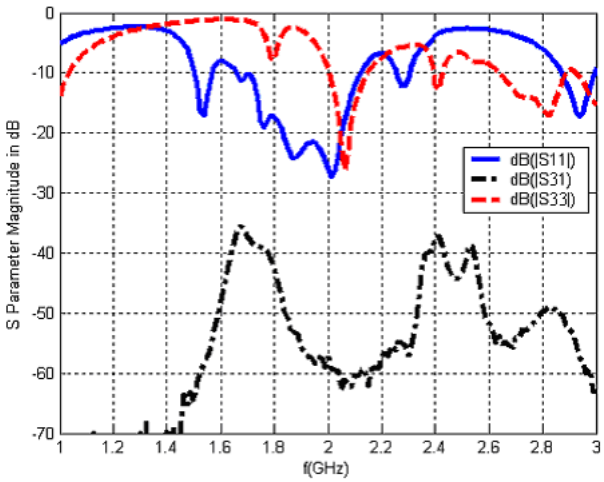

Figure 5.42: Measured $[S]$ parameters of the self-diplexed circularly polarized antenna for RFID reader application.

A prototype of the proposed antenna has been manufactured (Fig. 5.41). The antenna measured $[S]$ parameters are shown in Fig. 5.42. The third configuration has been chosen in order to show an example of dual-frequency with alternate polarizations. The reflection coefficient is -11.5 dB at the port 1 ($f_1 = 1.67$ GHz) and -13 dB at the port 3 ($f_2 = 2.41$ GHz). The isolation between both ports is 35.5 dB at the first frequency and 37.3 dB at the second one. The other configurations have also been measured and the results are very similar to the ones presented.

The measured radiation patterns of this prototype have been measured in an anechoic chamber. As an example, the results for the third configuration are shown (Fig. 5.43). The desired patch-like radiation pattern is obtained in both planes at both frequencies. The measured AR is 0.01 dB at the first

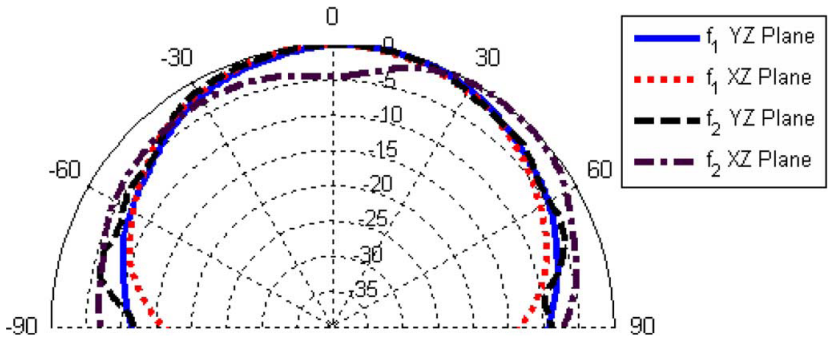

Figure 5.43: Measured radiation pattern of the self-diplexed circularly polarized antenna.

frequency while it is 0.05 dB at the second one. The beamwidths with an AR lower than 3 dB are: 124° at f_1 and 39.5° at f_2 in the $y-z$ plane and 144.5° at f_1 and 10° at f_2 in the $x-z$ plane.

5.5 Conclusion

In this Chapter the application of metamaterial-loaded antennas integrated into systems or antenna arrays has been proposed. First of all, in Section 5.2 dual-frequency printed dipoles loaded with metamaterial particles have been used to broader the bandwidth of log-periodic arrays composed of printed dipoles without increasing the number of elements. This has been obtained by exciting additional resonances provided by metamaterial-loading elements above and below the overall bandwidth of the unloaded array. Two different arrays have been manufactured and measured. The first one is a log-periodic array with two dipoles. The bandwidth of the unloaded array has been broadened (from 52.4% to 62.8%) thanks to the use of metamaterial particles. The same technique has been applied to an array composed of nine dipoles. In this case, the bandwidth has been broadened from 2.87 : 1 to 3.45 : 1.

In Section 5.3 LH antennas over ground plane have been applied to develop antennas with wideband tuning, small dimensions and internal matching. A tunable LH monopole has been designed, manufactured and measured. The manufactured prototype has a 17% tuning bandwidth (777 − 924 MHz) considering only the $n = -1$ mode and 28% (695 − 924 MHz) considering the two LH modes that are excited in the antenna. The measured radiation efficiency takes values between 50% and 70% within all the tuning bandwidth. The maximum dimension varies between $0.11\lambda_0$ at 695 MHz and $0.15\lambda_0$ at

924 MHz. The other tunable antenna is based on the LH half-loop antenna over ground plane. An antenna prototype has been manufactured and measured. The manufactured prototype has a 1.64 : 1 tuning bandwidth with internal matching. The measured radiation efficiency is always above 54% within the working bandwidth. These new kind of small antennas can be used in modern and future communication systems in which reconfiguration over a wide bandwidth is needed. In particular, these antennas are a good candidate for future communications systems such as Cognitive Radios. In order to show this application, a LH half-loop antenna with wideband tuning has been integrated with a broadband printed monopole antenna to develop a complete radiating system for a Cognitive Radio terminal in Section 5.3.4. A prototype operating over a 2 : 1 bandwidth has been designed, achieving high isolation between the ports ($>$ 20 dB) and a monopolar radiation pattern for the sensing function and a directive radiation pattern for the communications function.

Finally, dual-frequency patch antennas partially filled with CRLH cells have been proposed for dual-frequency active RFID systems in Section 5.4. The use of a dual-frequency system allows to reduce the propagation losses in the most critical link (transponder-reader link). Furthermore, it has been proposed the use of a circularly polarized antenna in the reader to overcome the multipath problems and reduce the polarization losses and the link fading. It has been decided to use linearly polarized antennas (with equal or orthogonal polarizations at each frequency) for the transponders in order to simplify the design. A novel feeding approach based on coupled or slot lines with some coupled metamaterial particles has been proposed to increase the isolation between the ports. The transponder antennas have been fed through aperture coupled lines in order to have more degrees of freedom and achieve complex impedances suitable to match the transponder. High isolation levels have been measured in all of the cases: $>$ 30 dB and $>$ 41 dB for the transponder antennas with equal and orthogonal polarizations, respectively, and $>$ 35 dB for the CP reader antenna.

CHAPTER 6

Conclusions and Future Working Lines

6.1 Final Conclusions

In this Thesis metamaterial-loaded printed antennas have been presented. As it has been shown, this kind of antennas are based on a conventional printed antenna loaded with a finite number of metamaterial particles. These loading elements are used to achieved interesting additional features such as multifrequency, multifunctionality and compactness which are fundamental for modern and future communication systems. Moreover, the advantages of printed antennas (light weight, low profile, low cost, easiness of manufacturing, etc.) are maintained. Several types of metamaterial-loaded printed antennas have been developed, each of them for different target applications. All the results have been validated by experimental prototypes. Furthermore, several models based on equivalent circuits and TL theory and a full-wave tool based on the MPIE-MoM approach have been realized to analyse and design the proposed antennas. These models provide accurate results and a small computation time.

First, a low-cost eigenfrequency method has been developed to efficiently compute the dispersion diagram of CRLH structures (Section 2.5). This diagram is a basic tool to analyse and design microwave circuits and antennas based on CRLH structures. The proposed approach drastically reduces the computation time in comparison with the conventional approach. The basic idea consists of computing the dispersion diagram using the resonance fre-

quencies of a CRLH resonator with a finite number of unit cells. The proposed approach has been compared with experimental results and the difference is smaller than 5%.

In Chapter 3, metamaterial-loaded printed wire antennas have been presented. Two different kinds of wire antennas have been proposed. Firstly, printed dipole antennas loaded with metamaterial particles have been proposed. It has been demonstrated that these antennas have a multifrequency performance because additional working bands can be achieved close to the resonance frequencies of the loading particles. Moreover, they present a dipolar-like radiation pattern at the different working frequencies. The approach is valid to design multifrequency dipoles with an arbitrary ratio and is very interesting for nowadays devices in which a small ratio (< 2) between the working frequencies is usually demanded. Furthermore, the additional working bands achieved with the metamaterial loading elements can be set below the band of the unloaded dipole and thus, miniaturization is achieved in that case. Several prototypes with dual-frequency and triple-frequency performance have been designed, manufactured and measured obtaining satisfactory results. Finally, an equivalent circuit model to efficiently simulate this type of antennas has been developed.

The other set of antennas presented in Chapter 3 are LH printed wire antennas over ground plane (Section 3.3). These antennas keep the interesting features of LH wire antennas (small antennas with internal matching and additional radiation characteristics) but a further size reduction is achieved thanks to image theory. Moreover, the problem of the feeding, which was an important disadvantage in previous LH antennas, has been solved by providing a direct SMA connector. Two LH antennas over ground plane have been proposed. The first one is the LH monopole antenna which provides the typical monopolar radiation pattern with onminidirectional shape parallel to the ground plane and minimum radiation in the axis of the monopole. A prototype has been manufactured and measured, achieving a good performance. The second proposed antenna is the LH half-loop antenna over a ground plane. This antenna has the unique feature that a mode with $n = 0$ can be excited. When this antenna is operated at this mode, the currents have a uniform distribution in amplitude and phase. This leads to a radiation pattern with maximum radiation orthogonal to the ground plane, which cannot be obtained with other linear antennas over a ground plane. Moreover, it has an orthogonal polarization in one of the main planes with respect to the monopolar case. A prototype of the LH half-loop antenna has been designed, manufactured and measured. Good results, including high radiation efficiency, have been measured.

In Chapter 4, patch antennas partially filled with CRLH structures have been presented. First, it has been demonstrated that the combination of CRLH unit cells with conventional (RH) structures can be used to achieve resonant structures with an arbitrary ratio between the resonance frequencies. In particular, small frequency ratios can be achieved. Then, this type of resonant structures have been applied to microstrip antennas to achieve multifrequency and multifunction single-layer patch antennas. These antennas present two patch-like modes ($n = \pm 1$) and a monopolar one ($n = 0$) between them. The frequency ratio between the different modes can be arbitrarily chosen. This ratio depends on the dimensions of the microstrip patch the filling CRLH structure. Two different antennas have been implemented by partially filling conventional microstrip patches with CRLH mushroom structures. The first one (Section 4.4) is a triple-frequency and dual-mode patch antenna. The first and third modes ($n = \pm 1$) have a patch-like radiation pattern, while the mode between them ($n = 0$) has a monopolar radiation pattern. The second antenna (Section 4.5) is a dual-frequency microstrip patch antenna with very close working frequencies (1.21 ratio). In this case, both modes have a patch-like radiation pattern. Prototypes of both antennas have been manufactured and measured, showing good performance. Moreover, two different simulation tools for the patch antennas partially filled with CRLH cells have been developed. In Section 4.6 an equivalent circuit model of the proposed antennas has been presented. This model can be used to obtain the reflection coefficient of the proposed antennas with good accuracy and very low computational load. The second approach has been presented in Section 4.7 and is a full-wave simulator based on the MPIE-MoM approach. This simulator provides the full-wave solution for the proposed patch antennas with a reduced computation time.

The approach consisting of partially loading a microstrip patch antennas with CRLH cells has been extended in Section 4.8 to obtain modes with orthogonal polarizations. This approach has been used to develop quad-frequency single-layer patch antennas with polarization diversity and dual-frequency single-layer CP antennas. Two different feeding strategies for quad-frequency antennas have been proposed. The first one consists of using two orthogonal ports with high isolation between them. This approach can be used to design the radiating element of a dual-service transceiver. The second approach consists of feeding the quad-frequency patch antenna through one port. This approach is interesting for applications in which frequency and polarization diversity is simultaneously required (e. g. some advanced MIMO systems). Regarding the dual-frequency CP patch antennas, two different approaches have been proposed. The first one is based on a square patch filled

with square CRLH cells and two orthogonal ports connected to additional external circuitry (e. g. a branch-line coupler). The second one consists of introducing some modifications on a single-port square patch filled with CRLH cells. The first approach provides better AR and bandwidth but it requires additional circuitry which increases the size and complexity of the overall system.

Finally, the application of metamaterial-loaded antennas integrated into systems or antenna arrays has been studied in Chapter 5. The first application consists of using the characteristics of printed dipoles loaded with metamaterial particles to broader the bandwidth of log-periodic arrays of printed dipoles without increasing the number of elements (Section 5.2). This is achieved by obtaining additional resonances above and below the overall bandwidth of the unloaded array. This approach has been applied to two different arrays: a log-periodic array with two dipoles and another one with nine dipoles. In both cases, the loaded and unloaded arrays have been manufactured and measured, obtaining a broader bandwidth in the case of the loaded arrays.

LH antennas over ground plane have been applied to develop antennas with wideband tuning, small dimensions and internal matching in Section 5.3. Two different types of LH tunable antennas have been proposed: the tunable LH monopole antenna and the LH half-loop antenna over ground plane. Prototypes of both antennas have been designed, manufactured and measured. Wideband tunability has been achieved in both cases (28% in the case of the LH monopole antenna and 1.64 : 1 in the case of the LH half-loop antenna). Furthermore, both antennas have reasonable measured radiation efficiencies over the operation bandwidths (between 50% and 80%) with small electrical dimensions ($< 0.23\lambda_0$) and internal matching. These new kind of small antennas are a good candidate as the radiating element of handheld devices for modern and future communication systems in which reconfiguration over a wide bandwidth is needed. In particular, these antennas have been proposed for future communications systems such as Cognitive Radio. In order to show this fact, a LH half-loop antenna with wideband tuning has been integrated with a broadband monopole antenna to develop a complete radiating system for a Cognitive Radio terminal in Section 5.3.4. A design example operating over a 2 : 1 bandwidth has been shown, achieving high isolation between the ports (> 20 dB).

The last application has been the use of the patch antennas partially filled with CRLH cells to the development of self-diplexed antennas for a dual-frequency RFID system (Section 5.4). The lower frequency has been set to the transponder-reader link because is the most critical one in terms of power

and thus, the propagation losses are reduced. Moreover, the use of a circularly polarized antenna in the reader has been proposed to overcome the multipath problems and reduce the polarization losses and the link fading. The antennas of the transponders are linearly polarized to simplify the design. In order to achieve self-diplexing performance, the feeding structures are based on coupled or slot lines with some filtering characteristics achieved by coupling some metamaterial particles. The linearly polarized antennas have been fed through aperture coupled lines in order to have more degrees of freedom to achieve complex impedances suitable to match the transponder. In addition the polarization of the output ports can be the same or orthogonal. Isolation levels of larger than 30 dB have been measured for the equal polarization case and larger than 41 dB for the orthogonal polarization case. For the case of the self-diplexed CP patch antenna for the reader, isolation levels larger than 35 dB have been measured.

6.2 Future Working Lines

As it was commented above, the main goal consisting of the development multifrequency and/or multifunction antennas has been achieved. However, the bandwidth of the different working bands is not the same for most of the cases shown in the previous Chapters. For example, the bandwidth of the additional working bands achieved in the multifrequency printed dipoles (Chapter 3) is narrower than the bandwidth of the conventional band. In the cases in which miniaturization is also achieved, this narrowband behaviour is unavoidable because a small antenna has a high Q factor which implies a narrow bandwidth [12]. Thus, a trade-off between miniaturization and bandwidth has to be chosen. On the other hand, in other cases miniaturization is not achieved but the additional bands also have a narrow bandwidth. In these situations, we consider that the narrow bandwidth is due to the high Q-factor of the metamaterial loading elements. However, a further study must be carried out in order to study the theoretical limit of the bandwidth in each situation and the optimal loading elements necessary to reach that limit.

Another interesting working line is the development of metamaterial-loaded printed antennas at higher frequencies. In the present work, all the examples have been designed, manufactured and measured below 3.5 GHz approximately. For some applications, such as satellite communications, the working bands are at higher frequencies (e. g. X and K bands in satellite communications example). For this reason, it would be interesting the design and manufacturing of metamaterial-loaded printed antennas at higher

frequencies. Initially, it seems that developing these antennas at higher frequencies could be a trivial task because it could be done by just scaling the current prototypes. Nevertheless, it must be taken into account that the elements which compose the metamaterial loading particles (such as gaps or vias) are electrically small which implies tiny elements which cannot be manufactured in some cases at very high frequencies. Hence, the behaviour and dimensions of these antennas must be studied at higher frequencies and alternative metamaterial loading approaches must be proposed in the cases in which the current designs cannot be directly scaled at higher frequencies.

In Chapter 5 the antennas presented in previous Chapters have been applied to future communications systems (Cognitive Radio) and emerging applications (RFID). In both cases, the antennas have been designed considering the requirements of the whole system. Furthermore, for the case of the RFID antennas, an example of a transponder design has been proposed (Section 5.4.4). The final step in both cases will be the evaluation of the performance of the whole system. Hence, this task is a future working line related to both systems.

Finally, related to the application of multifunction microstrip patch antennas, it has been demonstrated the development of self-diplexed multifrequency patch antennas with patch-like radiation pattern and dual-mode multifrequency patch antennas (patch antennas with two patch-like modes and a monopolar one). Patch antennas with monopolar radiation pattern have been extensively used in the field of user terminals for cellular communications [10]. Moreover, monopolar patch antennas have been applied to WLANs. Hence, multifrequency patch antennas with monopolar radiation pattern could be a very interesting radiating element for access points and user terminals due to the increase of standards and bands allowed for wireless communications and WLANs. However, up to the author's knowledge, monopolar patch antennas with multifrequency performance have not been reported yet. Thus, the use of metamaterial loading elements could be a good solution in order to achieve such antennas. Furthermore, the development of self-diplexed monopolar patch antennas could be an interesting objective for future works.

References

[1] D. Manteuffel, A. Bahr, and I. Wolff, "Investigation on integrated antennas for gsm mobile phones," in *AP2000 - Conference on Antennas an Propagation*, Davos, Switzerland, April 2000.

[2] J. E. Padgett, C. G. Gunther, and T. Hattori, "Overview of wireless personal communications," *IEEE Communcations Magazine*, vol. 33, no. 4, pp. 28–41, January 1995.

[3] P. Erätuuli, P. Haapala, and P. Vainikainen, "Dual frequency wire antennas," *Electronics Letters*, vol. 32, no. 12, pp. 1051–1052, June 1996.

[4] Z. D. Liu, P. S. Hall, and D. Wake, "Dual-frequency planar inverted-f antenna," *IEEE Transactions on Antennas and Propagation*, vol. 45, no. 10, pp. 1451–1458, October 1997.

[5] C. T. P. Song, P. S. Hall, H. Ghafouri-Shoraz, and D. Wake, "Triple band planar inverted-f antennas for handheld devices," *Electronics Letters*, vol. 36, no. 2, pp. 112–114, January 2000.

[6] D. Manteuffel, A. Bahr, D. Heberling, and I. Wolff, "Design considerations for integrated mobile phone antennas," in *IEE 11th International Conference on Antennas and Propagation*, Manchester, UK, April 2001, pp. 252–256.

[7] T. Gandara, R. Urban, L. Fregoli, and C. Peixeiro, "Planar inverted-f antennas for small multi-starndard handsets," in *18th International Conference on Applied Electromagnetics and Communications (ICECom 2005)*, Dubrovnik, Croatia, October 2005.

[8] M. Martinez-Vazquez, O. Litschke, M. Geissler, D. Heberling, A. M. Martinez-Gonzalez, and D. Sanchez-Hernandez, "Integrated planar multiband antennas for personal communication handsets," *IEEE Transactions on Antennas and Propagation*, vol. 54, no. 2, Part 1, pp. 384–391, February 2006.

[9] D. Manteuffel and M. Arnold, "Considerations for reconfigurable multi-standard antennas for mobile terminals," in *International Workshop on Antenna Technology: Small Antennas and Novel Metamaterials 2008 (iWAT 2008)*, Chiba, Japan, March 2008, pp. 231–234.

[10] V. González-Posadas, D. Segovia-Vargas, E. Rajo-Iglesias, J. L. Vázquez-Roy, and C. Martín-Pacual, "Approximate analysis of short circuited ring patch antenna working at tm_{01} mode," *IEEE Transactions on Antennas and Propagation*, vol. 54, no. 6, pp. 1875–1879, June 2006.

[11] J. Papapolymerou and J. T. Bernhard, "Guest editorial for the special issue on multifunction antennas and antenna systems," *IEEE Transactions on Antennas and Propagation*, vol. 54, no. 2, Part 1, pp. 314–316, February 2006.

[12] L. J. Chu, "Physical limitations of omnidirectional antennas," *Journal of Applied Physics*, vol. 19, pp. 1163–1175, December 1948.

[13] H. A. Wheeler, "Fundamental limitations of small antennas," *Proceedings of the IRE*, vol. 35, no. 12, pp. 1479–1484, December 1947.

[14] ——, "The radiansphere around a small antenna," *Proceedings of the IRE*, vol. 47, no. 8, pp. 1325–1331, August 1959.

[15] R. E. Collin and S. Rothschild, "Evaluation of antenna q," *IEEE Transactions on Antennas and Propagation*, vol. AP-12, no. 1, pp. 23–27, January 1964.

[16] R. C. Hansen, "Fundamental limitations in antennas," *Proceedings of the IEEE*, vol. 69, no. 2, pp. 170–181, February 1981.

[17] J. S. McLean, "A re-examination of the fundamental limits on the radiation q of electrically small antennas," *IEEE Transactions on Antennas and Propagation*, vol. 44, no. 5, pp. 672–676,, May 1996.

[18] A. D. Yaghjian and S. R. Best, "Impedance, bandwidth, and q of antennas," *IEEE Transactions on Antennas and Propagation*, vol. 53, no. 4, pp. 1298–1324, April 2005.

[19] K. Fujimoto and J. R. James, *Mobile antenna systems handbook*. Boston, MA, USA: Artech House, 2001.

[20] J. Mitola III and G. Q. Maguire Jr., "Cognitive radio: making software radios more personal," *IEEE Personal Communications*, vol. 6, no. 4, pp. 13–18, August 1999.

[21] P. S. Hall, P. Gardner, J. Kelly, E. Ebrahimi, M. R. Hamid, F. Ghanem, F. J. Herraiz-Martínez, and D. Segovia-Vargas, "Reconfigurable antenna challenges for future radio systems," in *Third European Conference on Antennas and Propagation (EuCAP 2009)*, Berlin, Germany, March 2009.

[22] K. Finkenzeller, *RFID Handbook: Fundamentals and application in contactless smart cards and identification.* New York, NY, USA: John Wiley & Sons, 2003.

[23] S. Ahson and M. Ilyas, *RFID Handbook: Applications, Technology, Security, and Privacy.* New York, NY, USA: CRC Press, 2008.

[24] C. Caloz and T. Itoh, *Electromagnetic Metamaterials: Transmission Line Theory and Microwave Applications.* New York, NY, USA: IEEE-Wiley, 2004.

[25] G. V. Eleftheriades and K. G. Balmain, *Negative-Refraction Metamaterials: Fundamental Principles and Applications.* Hoboken, NJ, USA: IEEE-Wiley, 2005.

[26] N. Engheta and R. W. Ziolkowski, *Metamaterials: Physics and Engineering Explorations.* New York, NY, USA: IEEE-Wiley, 2006.

[27] R. Marqués, F. Martín, and M. Sorolla, *Metamaterials with Negative Parameters: Theory, Design and Microwave Applications.* Hoboken, NJ, USA: IEEE-Wiley, 2008.

[28] R. Garg, P. Barthia, I. Bahl, and A. Ittipiboon, *Microstrip Antenna Design Handbook.* Norwood, MA, USA: Artech House, 2001.

[29] J. R. James and P. S. Hall, *Handbook of Microstrip Antennas*, P. Peregrinus, Ed. London, UK: IEE-Peter Peregrinus, 1989.

[30] V. Veselago, "The electrodynamics of substances with simultaneously negative values of ε and μ," *Soviet Physics Uspekhi*, vol. 10, no. 4, pp. 509–514, 1968.

[31] D. R. Smith, W. J. Padilla, D. C. Vier, S. C. Nemat-Nasser, and S. Schultz, "Composite medium with simultaneously negative permeability and permitivity," *Physics Review Letters*, vol. 84, no. 18, pp. 4184–4187, May 2000.

[32] J. B. Pendry, A. J. Holden, D. J. Robins, and W. J. Stewart, "Low frequency plasmons in thin-wire structures," *Journal of Physics: Condensed Matter*, vol. 10, pp. 4785–4809, 1998.

[33] ——, "Magnetism from conductors and enhanced nonlinear phenomena," *IEEE Transactions on Microwave Theory and Techniques*, vol. 47, no. 11, pp. 2075–2084, November 1999.

[34] R. A. Shelby, D. R. Smith, and S. Schultz, "Experimental verification of a negative index of refraction," *Science*, vol. 292, no. 292, pp. 77–79, April 2001.

[35] A. A. Houck, J. B. Brock, and I. L. Chuang, "Experimental observations of a left-handed material that obeys snell's law," *Physics Review Letters*, vol. 90, no. 13, p. 137401, April 2003.

[36] J. D. Baena, J. Bonache, F. Martín, R. Marqués, F. Falcone, T. Lopetegui, M. A. G. Laso, J. García-García, I. Gil, M. Flores Portillo, and M. Sorolla, "Equivalent circuit models for split ring resonators and complementary split ring resonators coupled to planar transmission lines," *IEEE Transactions on Microwave Theory and Techniques*, vol. 53, no. 4, pp. 1451–1461, April 2005.

[37] I. Bahl and P. Bhartia, *Microwave Solid State Circuit*. New York, NY, USA: IEEE-Wiley, 1988.

[38] R. Marqués, F. Mesa, J. Martel, and F. Medina, "Comparative analysis of edge- and broadside-coupled split ring resonators for metamaterial design: Theory and experiment," *IEEE Transactions on Antennas and Propagation*, vol. 51, no. 10, pp. 2572–2581, October 2003.

[39] L. Ran, J. Huangfu, H. Chen, X. Zhang, K. Cheng, T. M. Grzegorczyk, and J. A. Kong, "Experimental study on several left-handed metamaterials," *Progress in Electromagnetic Research (PIER)*, vol. 51, pp. 249–279, 2005.

[40] H. S. Chen, L. X. Ran, J. T. Huangfu, X. M. Zhang, K. S. Chen, T. M. Grzegorczyk, and J. A. Kong, "Magnetic properties of s-shaped split-ring resonators," *Progress in Electromagnetic Research (PIER)*, vol. 51, pp. 231–247, 2005.

[41] A. K. Iyer and G. V. Eleftheriades, "Negative refractive index metamaterials supporting 2-d waves," in *2002 IEEE-MTT International Microwave Symposium Digest*, vol. 2, Seattle, WA, USA, June 2002, pp. 412–415.

[42] A. A. Oliner, "A periodic-structure negative-refractive-index medium without resonant elements," in *2002 IEEE-AP-S USNC/URSI National Radio Science Meeting*, San Antonio, TX, USA, June 2002, p. 41.

[43] C. Caloz and T. Itoh, "Application of the transmission line theory of left-handed (lh) materials to the realization of a microstrip lh transmission line," in *2002 IEEE-AP-S USNC/URSI National Radio Science Meeting*, vol. 2, San Antonio, TX, USA, June 2002, pp. 412–415.

[44] D. M. Pozar, *Microwave Engineering*. Reading, MA, USA: Wiley, 1993.

[45] I. Lin, M. DeVincentis, C. Caloz, and T. Itoh, "Arbitrary dual-band components using composite right/left-handed transmission lines," *IEEE Transactions on Microwave Theory and Techniques*, vol. 52, no. 4, pp. 1142–1149, April 2004.

[46] C. Caloz, H. Okabe, T. Iwai, and T. Itoh, "Transmission line approach of left-handed (lh) materials," in *2002 IEEE-AP-S USNC/URSI National Radio Science Meeting*, vol. 1, San Antonio, TX, USA, June 2002, p. 39.

[47] C. Caloz, A. Sanada, and T. Itoh, "Microwave applications of transmission-line based negative refraction index structures," in *Asia-Pacific Microwave Conference*, vol. 3, Seoul, Korea, November 2003, pp. 1708–1713.

[48] A. Sanada, K. Murakami, S. Aso, H. Kubo, and I. Awai, "A via-free microstrip left-handed transmission line," in *2004 IEEE-MTT International Symposium*, Fort Worth, TX, USA, June 2004, pp. 301–304.

[49] A. Grbic and G. V. Eleftheriades, "Experimental verification of backward wave radiation from a negative refractive index metamaterial," *Journal of Applied Physics*, vol. 92, no. 9, pp. 5930–5935, November 2002.

[50] ——, "Leaky cpw-based slot antenna arrays for millimeter-wave applications," *IEEE Transactions on Antennas and Propagation*, vol. 50, no. 11, pp. 1494–1504, November 2002.

[51] M. A. Antoniades and G. V. Eleftheriades, "A cps leaky-wave antenna with reduced beam squinting using nri-tl metamaterials," *IEEE Transactions on Antennas and Propagation*, vol. 56, no. 3, pp. 708–721, March 2008.

[52] A. Sanada, C. Caloz, and T. Itoh, "Planar distributed structures with negative refractive index," *IEEE Transactions on Microwave Theory and Techniques*, vol. 52, no. 4, pp. 1252–1263, April 2004.

[53] G. V. Eleftheriades, A. K. Iyer, and P. C. Kremer, "Planar negative refraction index media using periodically l-c loaded transmission lines," *IEEE Transactions on Microwave Theory and Techniques*, vol. 50, no. 12, pp. 2702–2712, December 2002.

[54] A. Grbic and G. V. Eleftheriades, "Dispersion analysis of a microstrip-based negative refraction index periodic structure," *IEEE Microwave and Wireless Components Letters*, vol. 13, no. 4, pp. 155–157, April 2003.

[55] F. Elek and G. V. Eleftheriades, "A two-dimensional uniplanar transmission-line metamaterial with a negative index of refraction," *New Journal of Physics*, vol. 7, pp. 1–18, August 2005.

[56] D. Sievenpiper, L. Zhang, F. J. Broas, N. G. Alexopulos, and E. Yablonovitch, "High-impedance electromagnetic surfaces with a forbidden frequency band," *IEEE Transactions on Microwave Theory and Techniques*, vol. 47, no. 11, pp. 2059–2074, November 1999.

[57] M. Gil, J. Bonache, J. Selga, J. García-García, and F. Martín, "Broadband resonant type metamaterial transmission lines," *IEEE Microwave and Wireless Components Letters*, vol. 17, no. 2, pp. 97–99, February 2007.

[58] F. J. Herraiz-Martínez, V. González-Posadas, F. Iñigo-Villacorta, and D. Segovia-Vargas, "Low-cost approach based on an eigenfrequency method to obtain the dispersion diagram in crlh structures," *IEEE Antennas and Wireless Propagation Letters*, vol. 17, no. 1, pp. 13–15, January 2007.

[59] B. C. Wadell, *Transmission Line Design Handbook*. Norwood, MA, USA: Artech House, 1991.

[60] L. Liu, C. Caloz, and T. Itoh, "Dominant mode (dm) leaky-wave antenna with backfire-to-endfire scanning capability," *Electronics Letters*, vol. 38, no. 23, pp. 1414–1416, 2000.

[61] A. Lai, C. Caloz, and T. Itoh, "Composite right/left-handed transmisión line metamaterials," *IEEE Microwave Magazine*, vol. 5, no. 3, pp. 34–50, September 2004.

[62] S. Lim, C. Caloz, and T. Itoh, "Metamaterial-based electronically-controlled transmission line structure as a novel leaky-wave antenna

with tunable angle and beamwidth," *IEEE Transactions on Microwave Theory and Techniques*, vol. 52, no. 12, pp. 2678–2690, December 2004.

[63] ——, "A reflecto-directive system using a composite right/left-handed (crlh) leaky-wave antenna and heterodyne mixing," *IEEE Microwave and Wireless Components Letters*, vol. 14, no. 4, pp. 183–185, April 2004.

[64] S. Hrabar and G. Jankovic, "Scanning leaky-wave antenna based on a waveguide filled with plasma-like eng metamaterial," in *2006 IEEE MELECON*, Benalmádena (Málaga), Spain, May 2006.

[65] F. P. Casares-Miranda, C. Camacho-Peñalosa, and C. Caloz, "High-gain active composite right/left-handed leaky-wave antenna," *IEEE Transactions on Antennas and Propagation*, vol. 54, no. 8, pp. 2292–2300, August 2006.

[66] Y. Sugio, T. Makimoto, S. Nishimura, and H. Nakanishi, "Analysis for gain enhancement of multiple-reflection line antenna with dielectric plates," *Electronics and Communications in Japan (Part I: Communications)*, vol. 74, no. 5, pp. 80–112, January 1991.

[67] N. G. Alexopoulos and D. R. Jackson, "Fundamental superstrate (cover) effects on printed circuit antennas," *IEEE Transactions on Antennas and Propagation*, vol. 32, no. 8, pp. 807–815, August 1984.

[68] D. R. Jackson and N. G. Alexopoulos, "Gain enhancement methods for printed circuit antennas," *IEEE Transactions on Antennas and Propagation*, vol. 33, no. 9, pp. 976–987, September 1985.

[69] Y. Vardaxoglou and F. Capolino, "Review of highly-directive flat-plate antenna technology with metasurfaces and metamaterials," in *36th European Microwave Conference*, Manchester, UK, September 2006, pp. 963–966.

[70] L. Zhang, H. Contopanagos, N. G. Alexopoulos, and E. Yablonovitch, "An electromagnetic bandgap resonator antenna," in *1998 IEEE Antennas and Propagation Society International Symposium*, vol. 1, Atlanta, GA, USA, June 1998, pp. 186–189.

[71] L. Zhang, N. G. Alexopoulos, and E. Yablonovitch, "Microstrip line fed slot antenna with pbg superstrate," in *1999 IEEE Antennas and Propagation Society International Symposium*, vol. 3, Orlando, FL, USA, July 1999, pp. 1924–1927.

[72] M. Thevenot, C. Cheype, A. Reineix, and B. Jecko, "Directive photonic-bandgap antennas," *IEEE Transactions on Microwave Theory and Techniques*, vol. 47, no. 11, pp. 2115–2122, November 1999.

[73] Y. J. Lee, J. Yeo, R. Mittra, and W. S. Park, "Design of a high-directivity electromagnetic band gap (ebg) resonator antenna using a frequency- selective surface (fss) superstrate," *Microwave and Optical Technology Letters*, vol. 43, no. 6, pp. 462–467, December 2004.

[74] P. Lee, Y. J. W. Yeo, and R. Mittra, "Directivity enhancement of printed antennas using a class of metamaterial superstrates," *Electromagnetics*, vol. 26, pp. 203–218, 2006.

[75] A. P. Feresidis, G. Goussetis, S. Wang, and J. C. Vardaxoglou, "Artificial magnetic conductor surfaces and their application to low-profile high-gain planar antennas," *IEEE Transactions on Antennas and Propagation*, vol. 53, no. 1, pp. 209–215, January 2005.

[76] S. Wang, A. P. Feresidis, G. Goussetis, and Y. C. Vardaxoglou, "'high-gain subwavelength resonant cavity antennas based on metamaterial ground planes," *IEE Proceedings: Microwaves, Antennas and Propagation*, vol. 153, no. 1, pp. 1–6, February 2006.

[77] S. Enoch, G. Tayeb, P. Sabouroux, N. Guerin, and P. Vincent, "A metamaterial for directive emission," *Physics Review Letters*, vol. 89, no. 21, p. 213902, November 2002.

[78] K. C. Gupta, "Narrow beam antenna using an artificial dielectric medium with permittivity less than unity," *Electronics Letters*, vol. 7, no. 1, pp. 16–18, January 1971.

[79] S. J. Franson and R. W. Ziolkowski, "Gigabit per second data transfer in high-gain metamaterial structures at 60 ghz," *IEEE Transactions on Antennas and Propagation*, vol. 57, no. 10, pp. 2913–2925, October 2009.

[80] ——, "Confirmation of zero-n behavior in a high gain grid structure at millimeter-wave frequencies," *IEEE Antennas and Wireless Propagation Letters*, vol. 8, pp. 387–390, 2009.

[81] S. Hrabar, D. Bonefacic, and D. Muha, "Numerical and experimental investigation of horn antenna with embedded enz metamaterial lens," in *19th International Conference on Applied Electromagnetics and Communications (ICECom 2007)*, Duvrobnik, Croatia, September 2007.

[82] ——, "Enz-based shortened horn antenna - an experimental study," in *2008 IEEE AP-S International Symposium*, San Diego, CA, USA, July 2008.

[83] ——, "Application of wire-based metamaterials for antenna miniaturization," in *Third European Conference on Antennas and Propagation (EuCAP 2009)*, Berlin, Germany, March 2009.

[84] E. Saenz, R. Gonzalo, I. Ederra, J. C. Vardaxoglou, and P. de Maagt, "Resonant meta-surface superstrate for single and multi-frequency dipole antenna arrays," *IEEE Transactions on Antennas and Propagation*, vol. 56, no. 4, pp. 951–960, April 2008.

[85] P. M. T. Ikonen, E. Saenz, R. Gonzalo, and S. A. Tretyakov, "Modeling and analysis of composite antenna superstrates consisting on grids of loaded wires," *IEEE Transactions on Antennas and Propagation*, vol. 55, no. 10, pp. 2692–2700, October 2007.

[86] E. Saenz, I. Ederra, P. de Maagt, and R. Gonzalo, "Highly efficient dipole antenna with planar meta-surface," *Electronics Letters*, vol. 43, no. 16, pp. 850–851, August 2007.

[87] E. Saenz, I. Ederra, R. Gonzalo, S. Pivnenko, O. Breinbjerg, and P. de Maagt, "Coupling reduction between dipole antenna elements by using a planar meta-surface," *IEEE Transactions on Antennas and Propagation*, vol. 57, no. 2, pp. 383–394, February 2009.

[88] G. S. Smith, "Efficiency of electrically small antennas combined with matching networks," *IEEE Transactions on Antennas and Propagation*, vol. AP-40, no. 5, pp. 369–373, May 1977.

[89] R. W. Ziolkowski and A. Kipple, "Application of double negative metamaterials to increase the power radiated by electrically small antennas," *IEEE Transactions on Antennas and Propagation*, vol. 51, no. 10, pp. 2626–2640, October 2003.

[90] R. W. Ziolkowski and A. Erentok, "Metamaterial-based efficient electrically small antennas," *IEEE Transactions on Antennas and Propagation*, vol. 54, no. 7, pp. 2113–2130, July 2006.

[91] A. Erentok and R. W. Ziolkowski, "Metamaterial-inspired efficient electrically small antennas," *IEEE Transactions on Antennas and Propagation*, vol. 56, no. 3, pp. 691–707, March 2008.

[92] P. Jin and R. W. Ziolkowski, "Low-q, electrically small, efficient near-field resonant parasitic antennas," *IEEE Transactions on Antennas and Propagation*, vol. 57, no. 9, pp. 2548–2563, September 2009.

[93] A. Sanada, M. Kimura, I. Awai, H. Kubo, C. Caloz, and T. Itoh, "A planar zeroth-order resonator antenna using a left-handed transmission line," in *34th European Microwave Conference*, Amsterdam, The Netherlands, October 2004, pp. 1341–1343.

[94] C. Caloz and A. Rennings, "Overview of resonant metamaterial antennas," in *Third European Conference on Antennas and Propagation (EuCAP 2009)*, Berlin, Germany, March 2009.

[95] A. Rennings, T. Liebig, S. Otto, C. Caloz, and I. Wolff, "Highly directive resonator antennas based on composite right/left-handed (crlh) transmission lines," in *Second International ITG Conference on Antennas (INICA '07)*, Munich, Germany, March 2007.

[96] C. Caloz, T. Itoh, and A. Rennings, "Crlh metamaterial leaky-wave and resonant antennas," *IEEE Antennas and Propagation Magazine*, vol. 50, no. 5, pp. 25–39, October 2008.

[97] A. Rennings, T. Liebig, S. Abielmona, C. Caloz, and P. Waldow, "Triband and dual-polarized antenna based on composite right/left-handed transmission line," in *37th European Microwave Conference*, Munich, Germany, October 2007.

[98] S. Otto, A. Rennings, C. Caloz, and P. Waldow, "Dual mode zeroth order ring resonator with tuning capability and selective mode excitation," in *35th European Microwave Conference*, Paris, France, October 2005.

[99] S. Otto, A. Rennings, C. Caloz, P. Waldow, and T. Itoh, "Composite right/left-handed λ-resonator ring antenna for dual-frequency operationy," in *2005 IEEE International Symposium on Antennas and Propagation*, Washington DC, USA, July 2005.

[100] A. Rennings, S. Otto, T. Liebig, C. C., and I. Wolff, "Dual-band composite right/left-handed ring antenna with linear/circular polarization capability," in *First European Conference on Antennas and Propagation (EuCAP 2006)*, Nice, France, November 2006.

[101] M. Schüßler, J. Freese, and R. Jakoby, "Design of compact planar antennas using lh-transmission lines," in *2004 IEEE-MTT International Microwave Symposium Digest*, Fort Worth, TX, USA, June 2004, pp. 209–212.

[102] M. Schüßler, C. Damm, J. Freese, and R. Jakoby, "Performance evaluation of periodically lc loaded small patch antennas," in *First European Conference on Antennas and Propagation (EuCAP 2006)*, Nice, France, November 2006.

[103] C. J. Lee, K. M. K. H. Leong, and T. Itoh, "Design of resonant small antenna using composite right/left-handed transmission line," in *2005 IEEE Antenna and Propagation Society International Symposium*, Washington DC, USA, July 2005.

[104] ——, "Composite right/left-handed transmission line based compact resonant antennas for rf module integration," *IEEE Transactions on Antennas and Propagation*, vol. 54, no. 8, pp. 2283–2291, August 2006.

[105] A. Lai, K. M. K. H. Leong, and T. Itoh, "Infinite wavelength resonant antennas with monopolar radiation pattern based on periodic structures," *IEEE Transactions on Antennas and Propagation*, vol. 55, no. 3, pp. 868–876, March 2007.

[106] ——, "Dual mode compact microstrip antenna based on fundamental backward wave," in *2005 Asia-Pacific Microwave Conference*, Suzhou, China, December 2005.

[107] F. Qureshi, M. A. Antoniades, and G. V. Eleftheriades, "A compact and low-profile metamaterial ring antenna with vertical polarization," *IEEE Microwave and Wireless Components Letters*, vol. 4, pp. 333–336, 2005.

[108] M. A. Antoniades and G. V. Eleftheriades, "A folded-monopole model for electrically small nri-tl metamaterial antennas," *IEEE Antennas and Wireless Propagation Letters*, vol. 7, pp. 425–428, 2008.

[109] G. V. Eleftheriades, M. A. Antoniades, and F. Qureshi, "Antenna applications of negative-refractive-index transmission-line structures," *IET Microwave, Antennas and Propagation*, vol. 1, no. 1, pp. 12–22, February 2007.

[110] G. V. Eleftheriades, A. Grbic, and M. Antoniades, "Negative-refractive-index metamaterials and enabling electromagnetic applications," in *2002 IEEE International Symposium on Antennas and Propagation*, vol. 2, Monterey, CA, USA, June 2002, pp. 1399–1402.

[111] J. Zhu and G. V. Eleftheriades, "A compact transmission-line metamaterial antenna with extended bandwidth," *IEEE Antennas and Wireless Propagation Letters*, vol. 8, pp. 295–298, 2009.

[112] N. Engheta, "An idea for thin subwavelength cavity resonators using metamaterials with negative permittivity and permeability," *IEEE Antennas and Wireless Propagation Letters*, vol. 1, pp. 10–13, 2002.

[113] A. Alù, F. Bilotti, N. Engheta, and L. Vegni, "Sub-wavelength, compact, resonant patch antennas loaded with metamaterials," *IEEE*

Transactions on Antennas and Propagation, vol. 55, no. 1, pp. 13–25, January 2007.

[114] F. Bilotti, A. Alù, and L. Vegni, "Design of miniaturized metamaterial patch antennas with μ-negative loading," *IEEE Transactions on Antennas and Propagation*, vol. 56, no. 6, pp. 1640–1647, June 2008.

[115] K. Fujimoto, "'a loaded antenna system applied to vhf portable communication equipment," *IEEE Transactions on Vehicular Technology*, vol. VT-17, no. 1, pp. 6–12, October 1968.

[116] A. W. Rudge, K. Milne, A. D. Olver, and P. Knight, *The handbook of Antenna Design (vol. 1 and 2)*. London, UK: IEE-Peter Peregrinus, 1986.

[117] H. Choo, R. Rogers, and H. Ling, "'on the wheeler cap measurement of the efficiency of microstrip antennas," *IEEE Transactions on Antennas and Propagation*, vol. 53, no. 7, pp. 2328–2332, July 2005.

[118] P. Miskovsky, J. M. González-Arbesú, and J. Romeu, "Antenna radiation efficiency measurement in an ultrawide frequency range," *IEEE Antennas and Wireless Propagation Letters*, vol. 8, pp. 72–75, 2009.

[119] M. Geissler, O. Litschke, D. Heberling, P. Waldow, and I. Wolff, "An improved method for measuring the radiation efficiency of mobile devices," in *2003 IEEE Antennas Propagation Society International Symposium*, vol. 4, Columbus, OH, USA, June 2003, pp. 743–746.

[120] R. H. Johnston and J. G. McRory, "An improved small antenna radiation- efficiency measurement method," *IEEE Antennas and Propagation Magazine*, vol. 40, no. 5, pp. 40–48, October 1998.

[121] C.-M. Su, H. Chen, and K. Wong, "Printed dual-band dipole antenna with u-slotted arms for 2.4/5.2 ghz wlan operation," *Electronics Letters*, vol. 38, no. 22, pp. 1308–1309, October 2002.

[122] Y. F. Liu, Q. Xue, C. Chan, and C. H. Olver, "A novel dual-band printed-dipole antenna using crr structure," *Microwave and Optical Technology Letters*, vol. 41, no. 2, pp. 105–106, April 2004.

[123] H. Iizuka, P. S. Hall, and A. Lucas Borja, "Dipole antenna with left-handed loading," *IEEE Antennas and Wireless Propagation Letters*, vol. 5, pp. 483–485, 2006.

[124] H. Iizuka and P. S. Hall, "'left-handed dipole antennas and their implementations," *IEEE Transactions on Antennas and Propagation*, vol. 55, no. 5, pp. 1246–1253,, May 2007.

[125] A. Lucas Borja, P. S. Hall, Q. Liu, and H. Iizuka, "Omnidirectional loop antenna with left-handed loading," *IEEE Antennas and Wireless Propagation Letters*, vol. 6, pp. 495–498, 2007.

[126] Q. Liu, P. S. Hall, and A. Lucas Borja, "Dipole with left handed loading with optimised efficiency," in *Second European Conference on Antennas and Propagation (EuCAP 2007)*, Edinburgh, UK, November 2007.

[127] ——, "Efficiency of electrically small dipole antennas loaded with left-handed transmission lines," *IEEE Transactions on Antennas and Propagation*, vol. 3009-3017, no. 10, p. 57, October 2009.

[128] P. S. Hall and Q. Liu, "Dual mode reconfigurable loop antenna with left handed loading," in *Metamaterials 2008*, Pamplona, Spain, September 2008.

[129] C. A. Balanis, *Antenna Theory: Analysis and Design.* New York, NY, USA: Wiley-Interscience, 2005.

[130] J. R. Mosig and F. E. Gardiol, "General integral equation formulation for microstrip antennas and scatterers," *IEE Proceedings H: Microwaves, Antennas and Propagation*, vol. 132, no. 7, pp. 424–432, December 1985.

[131] J. R. Mosig, *Numerical Techniques for Microwave and Millimeter-wave Passive Structures.* New York, NY, USA: IEEE-Wiley, 1989, ch. Integral Equation Technique, pp. 133–213.

[132] I. H. Lin, C. Caloz, and T. Itoh, "A branch-line coupler with two arbitrary operating frequencies using left-handed transmission lines," in *2003 IEEE MTT-S International Microwave Symposium Digest*, Philadelphia, PA, USA, June 2003.

[133] H. H. Howe, *Stripline Circuit Desing.* Norwood, MA, USA: Artech House, 1974.

[134] D. J. Roscoe, L. Shafai, A. Itippiboon, M. Cuhaci, and R. Douville, "Tunable dipole antennas," in *1993 Antennas and Propagation Society International Symposium*, vol. 2, no. 28, Ann Arbor, MI, USA, June-July 1993, pp. 672–675.

[135] P. Bhartia and I. J. Bahl, "A frequency agile microstrip antenna," in *1982 Antennas and Propagation Society International Symposium*, vol. 20, Albuquerque, NM, USA, May 1982, pp. 304–307.

[136] K. L. Virga and Y. Rahmat-Samii, "Low-profile enhanced-bandwidth pifa antennas for wireless communications packaging," *IEEE Trans-*

actions on Microwave Theory and Techniques, vol. 45, no. 10, pp. 1879–1888, October 1997.

[137] M. Komulainen, M. Berg, H. Jantunen, and E. Salonen, "Compact varactor-tuned meander line monopole antenna for dvb-h signal reception," *Electronics Letters*, vol. 43, no. 24, pp. 1324–1326, November 2007.

[138] C. R. White and G. M. Rebeiz, "A slot-ring antenna with an octave of tunability," in *2007 IEEE AP-S International Symposium*, Honolulu, HI, USA, June 2007, pp. 5841–5845.

[139] E. Ebrahimi and P. S. Hall, "A dual port wide-narrowband antenna for cognitive radio," in *Third European Conference on Antennas and Propagation (EuCAP 2009)*, Berlin, Germany, March 2009.

[140] F. Ghanem, P. S. Hall, and J. R. Kelly, "Two port frequency reconfigurable antenna for cognitive radios," *Electronics Letters*, vol. 45, no. 11, pp. 534–536, May 2009.

[141] A. Safarian, A. Shameli, A. Roufugaram, M. Roufugaram, and F. De Flaviis, "Rf identification (rfid) reader front ends with active blocker rejection," *IEEE Transactions on Microwave Theory and Techniques*, vol. 57, no. 5, Part 2, pp. 1320–1329, May 2009.

[142] C. W. Pobanz and T. Itoh, "A microwave noncontact identification transponder using subharmonic interrogation," *IEEE Transactions on Microwave Theory and Techniques*, vol. 43, no. 7, pp. 1673–1679, July 1995.

[143] L. Cabriá, J. A. Garcia, E. Malaver, and A. Tazón, "A phemt frequency doubling active antenna with bpsk modulation capability," *IEEE Antennas and Wireless Propagation Letters*, vol. 3, pp. 310–313, 2004.

[144] D. Segovia-Vargas, D. Castro-Galán, L. E. García-Muñoz, and V. González-Posadas, "Broadband active receiving patch with resistive equalization," *IEEE Transactions on Microwave Theory and Techniques*, vol. 56, no. 1, pp. 56–64, January 2008.

[145] S. Y. Chen and P. Hsu, "Cpw-fed folded slot antenna for 5.8 ghz rfid tags," *Electronics Letters*, vol. 40, no. 24, pp. 1516–1517, November 2004.

[146] S. K. Padhi, N. C. Karmakar, C. L. Law, and S. Aditya, "A dual polarized aperture coupled circular patch antenna using a c-shaped coupling slot," *IEEE Transactions on Antennas and Propagation*, vol. 51, no. 12, pp. 3295–3298, December 2003.

[147] M. Hirvonen, P. Pursula, K. Jaakola, and K. Laukkanen, "Planar inverted f-antenna for radio frequency identification," *Electronics Letters*, vol. 40, no. 14, pp. 848–850, July 2004.

[148] K. V. Seshagiri Rao, P. V. Nikitin, and S. F. Lam, "Antenna design for uhf rfid tags: A review and practical application," *IEEE Transactions on Antennas and Propagation*, vol. 53, no. 12, pp. 3870–3876, December 2005.

[149] S. Serkan Basat, S. Bhattacharya, L. Yang, A. Rida, M. Tentzeris, and J. Laskar, "Design of a novel high-efficiency uhf rfid antenna on flexible lcp substrate with high read-range capability," in *2006 IEEE Antennas and Propagation International Symposium*, Albuquerque, NM, USA, June 2006.

[150] H. Iwasaki, "Proximity coupled linearly polarised patch antenna for dual frequency use," *Electronics Letters*, vol. 31, no. 15, pp. 1212–1213, July 1995.

[151] Y. Chung, S.-S. Jeon, D. Ahn, J.-I. Choi, and T. Itoh, "High isolation dual-polarized patch antenna using integrated defected ground structure," *IEEE Microwave and Wireless Components Letters*, vol. 14, no. 1, pp. 4–6, January 2004.

[152] Y. Hao and C. Parini, "Isolation enhancement of anisotropic uc-pbg microstrip diplexer patch antenna," *IEEE Antennas and Wireless Propagation Letters*, vol. 1, pp. 135–137, 2002.

[153] L. Inclán-Sánchez, J. L. Vázquez-Roy, and E. Rajo-Iglesias, "High isolation proximity coupled multilayer patch antenna for dual-frequency operation," *IEEE Transactions on Antennas and Propagation*, vol. 56, no. 4, pp. 1180–1183, April 2008.

[154] J. Martel, J. Bonache, R. Marqués, F. Martín, and F. Medina, "Design of wide-band semi-lumped bandpass filters using open split ring resonators," *IEEE Antennas and Wireless Propagation Letters*, vol. 17, no. 1, pp. 28–30, January 2007.

[155] D. Segovia-Vargas, D. Manceras, D. Castro, and V. González-Posadas, "A microstrip mixer receiving antenna for maximum conversion gain for mobile applications," in *2005 IEEE Antennas and Propagation Society International Symposium*, vol. 2A, Washington, DC, USA, July 2005, pp. 217–220.

List of Publications and Awards

Awards

- May 2007: Carlos III University of Madrid Extraordinary Award as the first student of his class.
- May 2007: Spanish Education and Science Ministry (MEC) Official Grant (FPU) for funding his doctoral research activity.
- June 2007: 27th AEIT/COIT (Official Association of Spanish Telecommunication Engineers) Best Thesis Dissertation Award.
- June 2007: Finalist of the IEEE AP-S (Antennas and Propagation Society) *Student Paper Contest*.
  IEEE AP-S International Symposium 2007, Honolulu, HW, USA.
- September 2007: : Finalist of the 2007 ReSA (Spanish Network of Antennas) *Young Scientist Award*.
  22nd URSI National Symposium, La Laguna, Tenerife, Spain.
- February 2008: Short-Term Scientific Mission funded by the European Action COST ic0603 ASSIST (Antenna Systems & Sensors for Information Society Technologies).
  Host institution: LEMA-EPFL. Directed by Prof. Juan R. Mosig.
- September 2008: Finalist of the 2008 ReSA (Spanish Network of Antennas) *Young Scientist Award*.
  23rd URSI National Symposium, Madrid, Spain.

Peer Reviewed Journal Publications

- F. J. Herraiz-Martínez, V. González-Posadas, F. Iñigo-Villacorta and D. Segovia-Vargas, "Low-cost Approach based on an Eigenfrequency Method to obtain the Dispersion Diagram in CRLH Structures", *IEEE Microwave and Wireless Components Letters*, pp. 13-15, Vol. 17, January 2007.
- E. Ugarte-Muñoz, F. J. Herraiz-Martínez, V. González-Posadas and D. Segovia-Vargas, "Patch Antenna based on Metamaterials for a RFID Transponder", *Radioengineering*, pp. 66-71, Vol. 17, No. 2, June 2008.
- F. J. Herraiz-Martínez, L. E. García-Muñoz, V. González-Posadas and D. Segovia-Vargas, "Multi-frequency and Dual Mode Patch Antennas Partially Filled with Left-Handed Structures", *IEEE Transactions on Antennas and Propagation*, pp. 2527-2539, Vol. 58, No. 8, Part 2, August 2008.
- F. J. Herraiz-Martínez, L. E. García-Muñoz, D. González-Ovejero, V. González-Posadas and D. Segovia-Vargas, "Dual-frequency printed dipole loaded with Split Ring Resonators", *IEEE Antennas and Wireless Propagation Letters*, vol. 8, pp. 137-140, 2009.
- F. J. Herraiz-Martínez, E. Ugarte-Muñoz, V. González-Posadas, L. E. García-Muñoz and D. Segovia-Vargas, "Self-Diplexed Patch Antennas based on Metamaterials for RFID Active Systems", *IEEE Transactions on Microwave Theory and Techniques*, Special Issue on RFID, vol. 57, no. 5, part 2, pp. 1330 - 1340, May 2009.
- D. Segovia-Vargas, F. J. Herraiz-Martínez, E. Ugarte-Muñoz, J. Montero-de-Paz, V. González-Posadas and L. E. García-Muñoz, "Multifrequency Printed Antennas Loaded with Metamaterial Particles", *Radioengineering*, vol. 18, no. 2, pp. 129 - 143, June 2009, **invited paper**.
- B. Andrés-García, L. E. García-Muñoz , F. J. Herraiz-Martínez, V. González-Posadas and D. Segovia-Vargas, "Filtering Lens Structure based on SRRs in the Low THz Band", *Progress in Electromagnetics Research*, PIER 93, pp. 71 -90, 2009.
- V. González-Posadas, J. L. Jiménez-Martín, F. J. Herraiz-Martínez, L. E. García-Muñoz and D. Segovia-Vargas, "Design of dual-frequency SRR-loaded dipole with equivalent circuit approach", *Electronics Letters*, vol. 45, no. 19, pp. 964-966, September 2009.
- F. J. Herraiz-Martínez, P. S. Hall, Q. Liu and D. Segovia-Vargas, "Left-Handed Wire Antennas over Ground Plane with Wideband Tuning", *IEEE Transactions on Antennas and Propagation*, submitted.

- F. J. Herraiz-Martínez, D. Segovia-Vargas, E. Ugarte-Muñoz and V. González-Posadas, "Multifrequency Microstrip Patch Antennas with Multiple Polarizations", *IEEE Transactions on Antennas and Propagation*, submitted.

Book Chapters

- F. J. Herraiz-Martínez, D. Segovia-Vargas, E. Ugarte-Muñoz, L. E. García-Muñoz and V. González-Posadas, "Multifrequency and Multifunction Metamaterial-loaded Printed Antennas", *Microwave and Millimeter Wave Technologies*, ISBN 978-953-7619-X-X, Ed. In Tech.

Patents

- D. Segovia-Vargas, V. González-Posadas, L. E. García-Muñoz, F. J. Herraiz-Martínez, F. Moyano-Carmona, E. Ugarte-Muñoz and J. Sanmartín-Jara, "Antena apilada multifrecuencia con metamateriales", Número de solicitud: P200930859, fecha de solicitud: 16 de Octubre de 2009.

Invited Tutorials

- D. Segovia-Vargas, F. J. Herraiz-Martínez and V. González-Posadas, "Tutorial on Multifrequency Patch Antennas based on Metamaterial Structures", *IEEE International Seminar*, Zagreb, Croatia, 27th September 2007.

Invited Conference Papers

- P. S. Hall, P. Gardner, J. Kelly, E. Ebrahimi, M. R. Hamid, F. Ghanem, F. J. Herraiz-Martínez and D. Segovia-Vargas, "Reconfigurable Antenna Challenges for Future Radio Systems", *EuCAP 2009 (Third European Conference on Antennas and Propagation)*, Berlin, Germany, March 2009.
- F. J. Herraiz-Martínez, E. Ugarte-Muñoz, J. Montero-de-Paz, P. S. Hall and D. Segovia-Vargas, "Applications of Metamaterial Loaded Printed Antennas", *YSMM'09 (Third Young Scientist Meeting on Metamaterials)*, Leganés (Madrid), Spain, July 2009.
- E. Ugarte-Muñoz , F. J. Herraiz-Martínez, J. Montero-de-Paz, L. E. García-Muñoz and D. Segovia-Vargas, "Planar superstrate for dual-frequency RHCP-LHCP array", *META'10 (Second International Conference on Metamaterials, Photonic Crystals and Plasmonics)*, Cairo, Egypt, February 2010.

Conference Papers

- F. J. Herraiz-Martínez, V. González-Posadas and D. Segovia-Vargas, "Análisis y Diseño de Resonadores CRLH aplicado a Antenas Miniaturizadas", *21st URSI National Symposium*, Oviedo, Spain, September 2006.
- F. J. Herraiz-Martínez, V. González-Posadas and D. Segovia-Vargas, "Multi-frequency Microstrip Patch Antennas Based on Metamaterial Structures", *YSMM'06 (Young Scientist Meeting On Metamaterials 2006)*, Sevilla, Spain, November 2006.
- F. J. Herraiz-Martínez, V. González-Posadas and D. Segovia-Vargas, "Multi-frequency Microstrip Patch Antennas Based on Metamaterial Structures", *IEEE AP-S International Symposium 2007*, Honolulu, HW, USA, June 2007.
- F. J. Herraiz-Martínez, V. González-Posadas and D. Segovia-Vargas, "Antenas Multifrecuencia basadas en Parches Rellenos de Estructuras Left-Handed", *22nd URSI National Symposium*, La Laguna, Tenerife, Spain, September 2007.
- E. Ugarte-Muñoz, F. J. Herraiz-Martínez, V. González-Posadas and D. Segovia-Vargas, "Self-Diplexed Antenna based on Metamaterials for RFID Application", *ICECom 2007 (19th International Conference on Applied Electromagnetics and Communications)*, Dubrovnik, Croatia, September 2007.
- O. García-Pérez, F. J. Herraiz-Martínez, V. González-Posadas and D. Segovia-Vargas, "Design of a Dual-Band Active Filter using CRLH Structures", *ICECom 2007 (19th International Conference on Applied Electromagnetics and Communications)*, Dubrovnik, Croatia, September 2007.
- F. J. Herraiz-Martínez, V. González-Posadas and D. Segovia-Vargas, "Multifunction Patch Antennas Filled with Metamaterial Structures", *37th European Microwave Conference*, Munich, Germany, October 2007.
- F. J. Herraiz-Martínez, V. González-Posadas and D. Segovia-Vargas, "Compact dual-mode and triple-frequency circular patch antenna based on metamaterial structures", *Metamaterials 2007 (First International Conference on Advanced Electromagnetic Materials in Microwave and Optics)*, Rome, Italy, October 2007.
- F. J. Herraiz-Martínez, V. González-Posadas and D. Segovia-Vargas, "A dual-band circularly polarized antenna based on a microstrip patch

filled with left-handed structures", *EuCAP 2007 (Second European Conference on Antennas and Propagation)*, Edinburgh, UK, November 2007.

- D. Segovia-Vargas, S. Arcas, F. J. Herraiz-Martínez, F. Iñigo and V. González-Posadas, "Hexagonal Metallo-Dielectric Periodic Structure: Characterization and Application", *EuCAP 2007 (Second European Conference on Antennas and Propagation)*, Edinburgh, UK, November 2007.
- F. J. Herraiz-Martínez, L. E. García-Muñoz, V. González-Posadas and D. Segovia-Vargas, "Multi-function Microstrip Patch Antennas Partially Filled with Left-Handed Structures", *COST ASSIST Workshop*, Cyprus, April 2008.
- F. J. Herraiz-Martínez, L. E. García-Muñoz, V. González-Posadas and D. Segovia-Vargas, "Multi-frequency Printed Dipoles Loaded with Metamaterial Particles", *COMITE 2008 (14th Conference on Microwave Techniques)*, Prague, Czech Republic, April 2008.
- F. J. Herraiz-Martínez, D. Segovia-Vargas, L. E. García-Muñoz and V. González-Posadas, "Dual-frequency Printed Dipole Loaded with Metamaterial Particles", *IEEE AP-S International Symposium 2008*, San Diego, California, USA, July 2008.
- E. Ugarte-Muñoz, F. J. Herraiz-Martínez, J. Montero de Paz and D. Segovia-Vargas, "Antena microstrip basada en metamateriales para transpondedores RFID", *23rd URSI National Symposium*, Madrid, Spain, September 2008.
- F. J. Herraiz-Martínez, L. E. García-Muñoz, V. González-Posadas and D. Segovia-Vargas, "Dipolos impresos multifrecuencia cargados con partículas metamateriales", *23rd URSI National Symposium*, Madrid, Spain, September 2008.
- F. J. Herraiz-Martínez, L. E. García-Muñoz, V. González-Posadas and D. Segovia-Vargas, "Bandwidth broadening of dual-frequency printed dipoles loaded with Split Ring Resonators", *Metamaterials 2008 (Second International Conference on Advanced Electromagnetic Materials in Microwave and Optics)*, Pamplona, Spain, September 2008.
- E. Ugarte-Muñoz, F. J. Herraiz-Martínez, V. González-Posadas and D. Segovia-Vargas, "Patch Antennas Partially Filled with CRLH cells for Self-Diplexed Antennas for RFID Application", *38th European Microwave Conference*, Amsterdam, The Nederlands, October 2008.
- F. J. Herraiz-Martínez, L. E. García-Muñoz, V. González-Posadas and D. Segovia-Vargas, "Analysis of Metamaterial Loaded Antennas using

MoM Computational Tools", *VI EIEC (6th Iberian Meeting on Computational Electromagnetism)*, Chiclana de la Frontera, Cádiz, Spain, October 2008.

- F. J. Herraiz-Martínez, S. López-Peña, J. R. Mosig, L. E. García-Muñoz, V. González-Posadas and D. Segovia-Vargas, "Analysis of Patch Antennas Partially Filled with LH Cells using the MPIE-MoM Approach", *COST ASSIST Workshop on "Antenna Systems & Sensors for Information Society Technologies"*, Dublin, Ireland, October 2008.
- F. J. Herraiz-Martínez, L. E. García-Muñoz, V. González-Posadas, D. Segovia-Vargas, D. González-Ovejero and C. Craeye, "Arrays of Dual-Band Printed Dipoles Loaded with Metamaterial Particles", *EuCAP 2009 (Third European Conference on Antennas and Propagation)*, Berlin, Germany, March 2009.
- F. J. Herraiz-Martínez, P. S. Hall, Q. Liu and D. Segovia-Vargas, "Tunable Left-Handed Monopole and Loop Antennas", *IEEE AP-S International Symposium 2009*, Charleston, South Carolina, USA, June 2009.
- F. J. Herraiz-Martínez, P. S. Hall and D. Segovia-Vargas, "Sistema Compacto de Dos Puertos para Terminales de Cognitive Radio", *24th URSI National Symposium*, Santander, Cantabria, Spain, September 2009.
- E. Ugarte-Muñoz, F. J. Herraiz-Martínez, V. González-Posadas, L. E. García-Muñoz and D. Segovia-Vargas, "Técnicas de diseño de antenas de polarización circular empleando metamateriales", *24th URSI National Symposium*, Santander, Cantabria, Spain, September 2009.
- J. Montero-de-Paz, E. Ugarte-Muñoz, F. J. Herraiz-Martínez, V. González-Posadas, L. E. García-Muñoz and D. Segovia-Vargas, "Antenas multifrecuencia con SRRs parásitos en banda X", *24th URSI National Symposium*, Santander, Cantabria, Spain, September 2009.
- E. Ugarte-Muñoz, F. J. Herraiz-Martínez, V. González-Posadas and D. Segovia-Vargas, "Design Techniques for Circularly Polarized Antennas using Metamaterial Structures", *39th European Microwave Conference*, Rome, Italy, September-October 2009.
- F. J. Herraiz-Martínez, P. S. Hall and D. Segovia-Vargas, "Application of the Left-Handed Half-Loop Antenna with Wideband Tuning to a Cognitive Radio Terminal", *EuCAP 2010 (Fourth European Conference on Antennas and Propagation)*, accepted.
- F. J. Herraiz-Martínez, E. Ugarte-Muñoz, V. González-Posadas and D. Segovia-Vargas, "A Dual-Frequency Patch Antenna with Monopolar

Radiation Pattern", *IEEE AP-S International Symposium 2010*, accepted.